Doctoral Thesis

Inclusive modeling of hydrate formation in sand sediment for sub-seabed CO₂ storage

（海底下二酸化炭素貯留のための砂層内ハイドレート
生成に関する包括的モデル構築の研究）

于 涛 Tao YU

Supervisor   Professor Toru SATO

Department of Ocean Technology, Policy and Environment

Graduate School of Frontier Sciences

The University of Tokyo

February 2016

CONTENTS

LIST OF FIGURES

LIST OF TABLES

1 INTRODUCTION

1.1 Background

Global warming has been identified as one of the most serious global environmental issues for the last several decades. According to the Climate Change 2014 by IPCC [1-1], the globally averaged combined land and ocean surface temperature anomaly has risen by around 0.85 °C from 1880 to 2012. Moreover, it is likely to rise by 2.6 ~ 4.8 °C by the end of the 21st century. As a result, the temperature rise causes the thaw of the mountain glaciers and snow cover globally, leading to the sea level change. Over the period from 1901 to 2010, the globally averaged sea level has risen by 0.19 m, and will further rise by around 0.07 ~ 0.36 m by 2050, and around by 0.09 ~ 0.69 m by 2080 [1-2].

As the main cause for global warming, greenhouse gas emissions (such as CO_2, CH_4, N_2O, etc.) into the atmosphere have increased significantly during the past few decades. Especially, continued emissions of CO_2 gas by human activities will cause further warming and long-lasting changes in all components of the climate system, increasing the likelihood of severe, pervasive and irreversible impacts for human beings and ecosystems [1-1]. Therefore, in order to limit the climate change and prevent the global warming, substantial and sustained reduction in CO_2 emissions is considered to be necessary and emergent, of which CO_2 capture and storage (CCS) is expected to be one of the most effective strategies [1-3].

For the storage of a large amount of CO_2 gas, onshore and shallow offshore storages are considered to be the most common methods for CCS [1-4]. In these methods, CO_2 gas is usually injected into the deep saline aquifers located at 800 ~ 3000 m below the seafloor in the ocean [1-5], with three main CO_2 trapping mechanisms as geochemical trapping, geological trapping, and hydrodynamic trapping basically [1-6]. Although CO_2 storage in the deep saline aquifers has been regarded as a feasible and effective way to trap anthropogenic CO_2 gas, there is a social concern that it may have inadequate safe storage life span [1-7] because the stored CO_2 may not remain stable beneath the seafloor, and the leakage of CO_2 gas may cause some environment issues such as ocean acidification [1-8], leading to negative impacts on marine organisms and the ecosystem [1-9].

In order to reduce the major risk of CO_2 leakage from the deep saline aquifers, a novel approach of CO_2 storage in the deep saline aquifers using the sealing effect of gas hydrate (hereinafter referred to as hydrate sealing) was proposed by Koide et al. [1-10], as shown in Fig 1-1. In this

method, if a leakage occurs at the sub-seabed storage sites, and CO_2 gas seeps out of the cap rock which is considered to be the first seal, the leaked CO_2 gas migrates upward and tends to form CO_2 hydrate at the base of the hydrate stability zone, creating a low-permeability secondary cap layer which can greatly restrict further upward CO_2 flow [1-10]. The potential of the hydrate sealing process has been studied and proved by Tohidi et al. [1-9], and hydrate formation providing an effective seal has been found to reduce the risk of CO_2 leakage significantly for CO_2 storage in the deep saline aquifers.
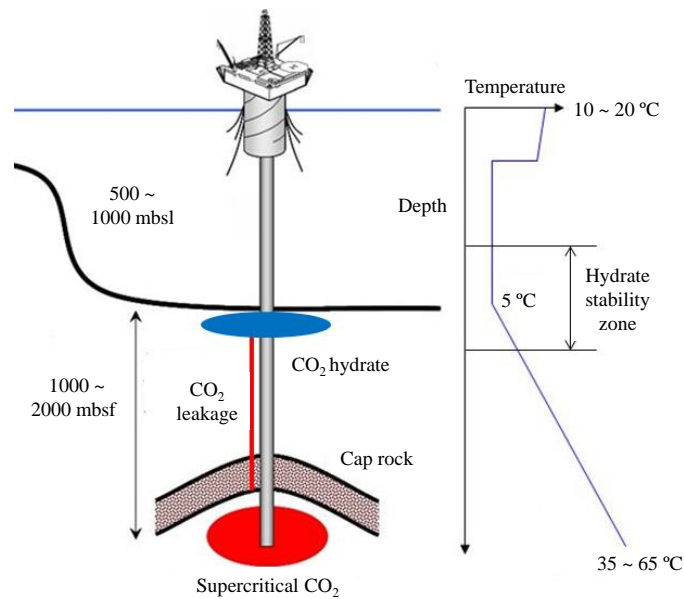
Fig. 1- 1 The schematic diagram of CO_2 storage in the deep saline aquifers using the sealing effect of gas hydrate proposed by Koide et al. [1-10]

On the other hand, as a new countermeasure for CCS, CO_2 storage in the sub-seabed sand sediment in the form of gas hydrate (hereinafter referred to as hydrate storage) was proposed by Inui et al. [1-11], as shown in Fig. 1-2. In this method, CO_2 gas is injected into the sub-seabed sediment at the depth of about hundreds of meters beneath the seafloor under the water column of more than 300 m, where the sediment is composed by sand-mud alternate layers under the condition of low temperature and high pressure. After injection, CO_2 gas selectively flows into the sand layers whose permeability is $10 \sim 100$ times higher than the surrounding mud layers, and forms CO_2 hydrate gradually. This method has the following features: (a) there are many storage sites all over the world due to the broad distribution of sand-mud alternate layers offshore; (b) a huge amount of CO_2 hydrate can form effectively due to the large pore space and wide contact area between CO_2 and water in the sand layers; (c) CO_2 hydrate can be stored safely in the marine

sediment due to the solid form of hydrate; and (d) the risk of CO_2 leakage can be reduced to a great extent due to the permeability reduction in the hydrate reservoirs which function as impermeable layers.

However, after CO_2 hydrate formation, the permeability of the sand layers near the injection wells drops sharply because the solid hydrate occupies the pore space of the sand sediment, which may cause the blockage of the gas flow, and hinder the further injection of CO_2 gas. In order to store a large amount of CO_2 gas in the sub-seabed sand sediment in the form of gas hydrate, it is important and essential to avoid such large permeability reduction, and ensure the gas front expands over a wide area.
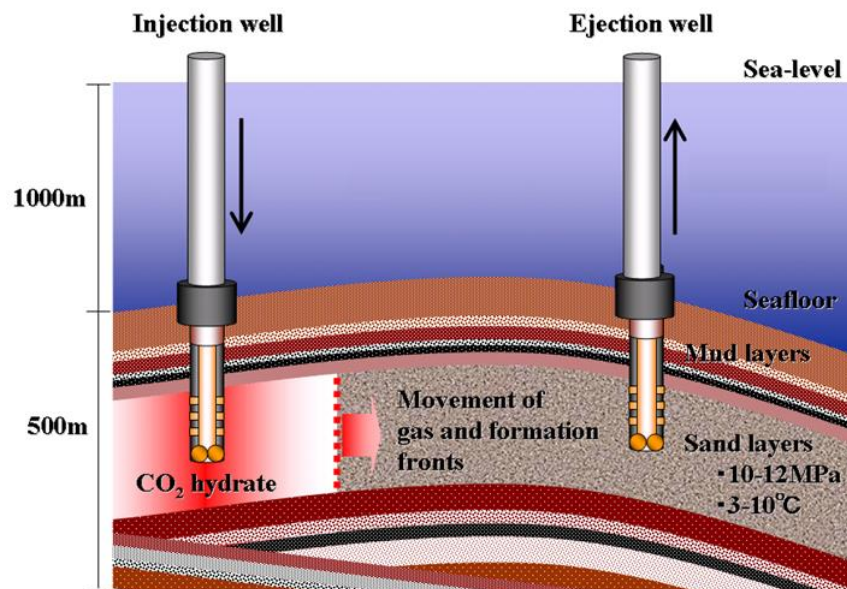
Fig. 1- 2 The schematic diagram of CO_2 storage in the sub-seabed sand sediment in the form of gas hydrate proposed by Inui et al. [1-11]

1.2 Previous Study

In order to evaluate the potential and feasibility of hydrate sealing and hydrate storage, it requires comprehensive understanding of the kinetics of CO_2 hydrate formation, and precise assessment of hydrate formation rate. Therefore, firstly, general reviews of previous studies on kinetic models for CO_2 hydrate formation are provided in this study.

As the first work which accounts for the fact that the growth of gas hydrate particles is a

crystallization and mass transfer process, the model proposed by Englezos et al. [1-12] has remained for more than ten years as the most complete kinetic model available in the open literature for hydrate growth.

$$\left(\frac{dn}{dt}\right)_p = K^* A_p \left(f - f_{eq}\right),$$

(1-1)

where n is the moles of gas consumed in hydrate formation, K^* is the overall rate constant around a hydrate particle [mol/m²/Pa/s], A_p is the particles surface area [m²], and $\left(f - f_{eq}\right)$ is the fugacity difference between dissolved gas and its three-phase equilibrium point [Pa]: i.e. the overall driving force.

Although this model is a mechanistic one with a simple form, it has far-reaching influence on other improved models proposed by the subsequent researchers (Skovborg and Rasmussen [1-13], Herri et al. [1-14][1-15], Gnanendran and Amin [1-16], Ribeiro and Lage [1-17], etc.).

In 2011, Inui [1-18] conducted a series of experiments on CO_2 hydrate formation in the lab-scale sand sediment under the condition of gas-liquid two-phase flow to figure out the phenomena of the gas flow blockage. Then, Inui [1-18] developed a one-dimensional simulator using a new kinetic model for CO_2 hydrate formation in the sand sediment proposed by Inui et al. [1-11] in order to reveal the blockage mechanism of the gas flow due to hydrate formation. Inui [1-18] also proposed a new concept of "rupture", which means fresh surface appearing on the hydrate film. In this theory, CO_2 hydrate forms and accumulates at the gas-liquid interface. However, under certain circumstances, rupture occurs on the hydrate film, resulting in the appearance of fresh gas-liquid interface where new hydrate can form. The kinetic model proposed by Inui et al. [1-11] is shown as below:

$$Q_H = k_f x A_I \left(f_G^{CO_2} - f_{eq}^{CO_2}\right) + \left(1-x\right) A_I \frac{\left(f_G^{CO_2} - f_{eq}^{CO_2}\right)}{\left(\frac{h}{k_d}\right) + \left(\frac{1}{k_f}\right)} + k_f^l A_S \left(f_A^{CO_2} - f_{eq}^{CO_2}\right),$$

(1-2)

where k_f and k_f^l are the intrinsic rate constants of CO_2 hydrate formation at the gas-liquid interface and in the aqueous phase [mol/m²/Pa/s], respectively. k_d is CO_2 diffusion constant in the hydrate film [mol/m/Pa/s]. A_I and A_S are the gas-liquid interfacial area and the sand surface area where CO_2 hydrate formation takes place [m²/m³], respectively. x is the rupture ratio: i.e.

the ratio of the fresh surface at the gas-liquid interface [-], and h is the average thickness of the hydrate film [m]. Besides, $f_G^{CO_2}$, $f_A^{CO_2}$, and $f_{eq}^{CO_2}$ are CO_2 fugacity in the gas phase, in the aqueous phase, and at the three-phase equilibrium point [Pa], respectively.

In this kinetic model, hydrate formation morphologies in the sand sediment were considered to consist of three different parts: from the fresh surface (rupture), from the growth of the hydrate film, and from dissolved CO_2 in the aqueous phase. Especially for the part of dissolved CO_2 in the aqueous phase without the gas-liquid interface, Inui et al. [1-11] considered that CO_2 hydrate only formed on the surface of the sand particles in their model. Besides, Inui et al. [1-11] treated the intrinsic rate constants of CO_2 hydrate formation at the gas-liquid interface and in the aqueous phase as different parameters, for which the value of k_f was about three orders larger than that of k_f^l. Moreover, for the rupture ratio x, Inui et al. [1-11] assumed that it would not change with time, and treated it as a constant value.

Afterward, based on the concept of rupture, Takahashi et al. [1-19] proposed another kinetic model, in which hydrate formation morphologies in the sand sediment without gas-liquid two-phase flow were only considered to consist of two different parts: from the fresh surface (rupture), and from the growth of the hydrate film. However, unlike Inui et al. [1-11], Takahashi et al. [1-19] assumed that dissolved CO_2 moved towards the gas-liquid interface in the aqueous phase, and formed hydrate on the aqueous-phase side of the hydrate film at the gas-liquid interface. The kinetic model proposed by Takahashi et al. [1-19] is shown as below:

$$Q_H = k_f x A_I \left(f_G^{CO_2} - f_{eq}^{CO_2} \right) + k_f \left(1 - x \right) A_I \left(f_I^{CO_2} - f_{eq}^{CO_2} \right),$$ (1-3)

where $f_I^{CO_2}$ is CO_2 fugacity at the gas-liquid interface [Pa], which is given as below:

$$f_I^{CO_2} = \frac{h_A k_d f_G^{CO_2} + h_A h k_f f_{eq}^{CO_2} + h k_A C_A^{CO_2}}{h_A k_d + h_A h k_f + h k_A / H},$$ (1-4)

where h_A is a thin layer of water in which CO_2 diffusion takes place [m], k_A is the normalized CO_2 diffusion coefficient in the aqueous phase [mol/m/s], $C_A^{CO_2}$ is CO_2 concentration in the aqueous phase [mol/mol], and H is Henry's constant [Pa].

In addition, for the rupture ratio x, Takahashi et al. [1-19] considered that it should be related to

the average thickness of the hydrate film h. In their theory, with the increase of h, the hydrate film is more likely to fracture due to the volume expansion of the solid hydrate under non-flow condition, and fresh surface (rupture) appears. Therefore, their rupture ratio model describes the inverse correlation of x decreasing monotonically with the increase of h as below:

$$x = \exp\left(-ah^2\right), \tag{1-5}$$

where a is a coefficient which can be determined by parameter-fitting with the experimental data [m^{-2}].

Then, Takahashi et al. [1-19] used their models and conducted numerical simulations of CO_2 hydrate formation in the sand sediment without gas-liquid two-phase flow in order to determine the unknown parameters of k_d and a in their models.

Later, Nakashima [1-20] used the kinetic model proposed by Inui et al. [1-11] and developed a two-dimensional numerical simulator by modifying a gas-liquid two-phase flow code, TOUGH+HYDRATE v1.0 [1-21], to replicate the experimental results of Inui et al. [1-11]. Moreover, Nakashima [1-20] proposed a new rupture ratio model under the condition of gas-liquid two-phase flow as below:

$$x = \chi p_G M_A, \tag{1-6}$$

where χ is a coefficient which means the inverse of the velocity [s/m], p_G is the dynamic pressure of the gas phase to the water surface [Pa], and M_A is the mobility of the aqueous phase [m/Pa/s].

As shown in Fig. 1-3 (a), in this model, Nakashima [1-20] assumed that only under the condition of gas-liquid two-phase flow could the rupture occur on the hydrate film. In addition, the more rapidly the gas phase was flowing, the larger the rupture ratio became (Fig. 1-3 (b)). However, even the gas phase was flowing, if the water saturation dropped to a certain extent: i.e. the irreducible water saturation state, the aqueous phase would lose its mobility, and the rupture could not occur (Fig. 1-3 (c)). In a similar way, even the water saturation was large enough to support its mobility, if the gas phase could not flow, there would still be no rupture on the hydrate film (Fig. 1-3 (d)).
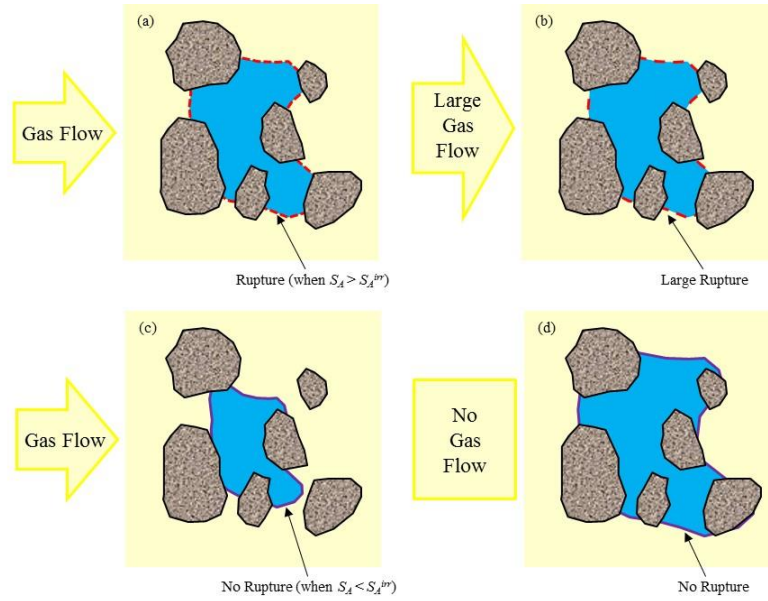
Fig. 1- 3 The schematic diagram of the rupture ratio model proposed by Nakashima [1-20]

Then, Nakashima [1-20] used this model and conducted numerical simulations of CO_2 hydrate formation in the sand sediment with gas-liquid two-phase flow by the numerical simulator. The calculation results were consistent with the experimental data of Inui et al. [1-11] in one case, but had some errors in the other case.

Recently, in order to match the calculation results to the experiments better, Yu et al. [1-22] modified the rupture ratio model proposed by Nakashima [1-20] by changing the dynamic pressure of the gas phase p_G to the momentum density of the gas phase ρ_G as below:

$$x = \chi \rho_G M_A. \tag{1-7}$$

In this model, unlike Nakashima [1-20], Yu et al. [1-22] considered that the contribution of the gas phase to the rupture ratio was made by the force generated by the momentum difference of the gas flow instead of the energy generated by the pressure difference of the gas flow.

Then, Yu et al. [1-22] used this model and conducted numerical simulations of CO_2 hydrate formation in the sand sediment with gas-liquid two-phase flow using the numerical simulator developed by Nakashima [1-20]. Their calculation results showed good consistency with the experimental data of Inui et al. [1-11] in both the two cases.

1.3 Objective of This Study

As mentioned above, CO_2 storage in the deep saline aquifers using the sealing effect of gas hydrate (hydrate sealing) and CO_2 storage in the sub-seabed sand sediment in the form of gas hydrate (hydrate storage) are regarded as emerging technologies for CCS with many advantages. However, open literatures related to the formation process of CO_2 hydrate in the sand sediment are limited. In addition, the blockage mechanism of the gas flow due to hydrate formation has not been revealed clearly yet.

Therefore, before these technologies can be promoted to the commercial application, lack of the knowledge about the storage potential of hydrate sealing and hydrate storage will still be the bottleneck. In order to reach the target of conducting field experiments, it is necessary to build a numerical simulator which can fully describe the complicated physical and chemical phenomena of gas-liquid two-phase flow and CO_2 hydrate formation in the sub-seabed sand sediment.

Although previous studies on CO_2 hydrate formation behavior in the sand sediment under the condition of gas-liquid two-phase flow were generally reviewed in this study, hydrate formation morphologies have not been classified by locations in the sand sediment completely. Besides, CO_2 hydrate formation in the aqueous phase either on the surface of the sand particles or on the aqueous-phase side of the hydrate film has been taken into account in these models, but not both. Furthermore, the rupture ratio models should have different forms depending on hydrate formation morphologies.

Therefore, based on the studies of the previous researchers, an inclusive model for CO_2 hydrate formation, which includes different hydrate formation morphologies at different locations in the sand sediment, is proposed in this study. Besides, a new rupture ratio model related to the geometric shapes of the sand particles, which can be explained both physically and geometrically, is also introduced. Then, numerical simulations are conducted using these new models to replicate the experimental results of Inui et al. [1-11]. Moreover, the calculation results are compared with the experimental data so that unknown parameters in the models can be determined by parameter-fitting. In addition, in order to validate the inclusive model proposed in this study, numerical simulations of CO_2 hydrate formation in the lab-scale sediment by liquid CO_2 injection are carried out using the model parameters determined in this study under the experimental conditions. Finally, conclusions are drawn for the whole study, and suggestions are made for the future work.

2 MODELING OF GAS-LIQUID TWO-PHASE FLOW AND CO₂ HYDRATE FROMATION IN LAB-SCALE SAND SEDIMENT

In this chapter, the basic structure of the numerical simulator used in this study, including governing equations and models for gas-liquid two-phase flow and CO_2 hydrate formation, especially an inclusive model for CO_2 hydrate formation, are introduced in detail.

2.1 Introduction of the Numerical Simulator

2.1.1 About TOUGH+HYDRATE

The numerical simulator used in this study is made by modifying a gas-liquid two-phase flow code, TOUGH+HYDRATE v1.0 [1-21], which was developed by the Lawrence Berkeley National Laboratory. This simulator can describe the mass balance for water, gas, hydrate and heat under the condition of gas-liquid two-phase flow using the finite difference method.

In the original TOUGH+HYDRATE code, a series of four primary variables (P, T, S_G and S_A) are solved iteratively by Newton-Raphson method using four governing equations (mass balance equations for aqueous, gas and hydrate phases as well as heat balance equation) as below, respectively:

$$\frac{\partial\left(\phi(S_G\rho_G X_G^{H_2O} + S_A\rho_A X_A^{H_2O})\right)}{\partial t} = \mathbf{F}_G X_G^{H_2O} + \mathbf{F}_A X_A^{H_2O} - Q_H X_H^{H_2O},$$

(2-1)

$$\frac{\partial\left(\phi(S_G\rho_G X_G^{CO_2} + S_A\rho_A X_A^{CO_2})\right)}{\partial t} = \mathbf{F}_G X_G^{CO_2} + \mathbf{F}_A X_A^{CO_2} + \mathbf{J}_G + \mathbf{J}_A,$$
$$- Q_H X_H^{CO_2} + Q_{inj}^{CO_2}$$

(2-2)

$$\frac{\partial\left(\phi S_H\rho_H\right)}{\partial t} = Q_H^{hyd},$$

(2-3)

$$\frac{\partial\left((1-\phi)\rho_R C_R T + \sum_{\beta\equiv A,G,H}\phi S_\beta\rho_\beta U_\beta\right)}{\partial t} = -\lambda_m\nabla T + \sum_{\beta\equiv A,G}h_\beta(\mathbf{F}_\beta + \mathbf{J}_\beta)$$
$$+ \sum_{\beta\equiv A,G}h_\beta Q_\beta + Q_H\Delta H_H + Q_{sol}^{CO_2}\Delta H_{sol}^{CO_2}$$

(2-4)

9

where the subscripts of the variables A, G, and H represent aqueous phase, gas phase, and hydrate phase, respectively. The superscripts of the variables H_2O, CO_2, and hyd represent H_2O, CO_2, and CO_2 hydrate as components, respectively.

Other variables are described as below. S_β is the volume fraction (i.e. saturation) of phase $\beta \equiv A$, G, H [m^3/m^3], ρ_β is the density of phase $\beta \equiv A$, G, H [kg/m^3], and X_β^κ is the mass fraction of the component $\kappa \equiv H_2O$, CO_2, hydrate in phase $\beta \equiv A$, G, H [kg/kg]. $\mathbf{F}_\beta$ is the flux term of phase $\beta \equiv A$, G [kg/m^3/s], $\mathbf{J}_\beta$ is the diffusion term of phase $\beta \equiv A$, G [kg/m^3/s], Q_β is the source/sink term of phase $\beta \equiv A$, G [kg/m^3/s], h_β is the specific enthalpy of phase $\beta \equiv A$, G [J/kg], and U_β is the specific internal energy of phase $\beta \equiv A$, G, H [J/kg]. T is the absolute temperature [K], and λ_m is the composite thermal conductivity [W/m/K]. ϕ is the porosity of the porous medium [-], ρ_R is the density of the porous medium [kg/m^3], and C_R is the specific heat capacity of the porous medium [J/kg/K]. Q_H is the total hydrate formation rate [kg/m^3/s], and ΔH_H is the enthalpy change during hydrate formation/dissociation [J/kg]. $Q_{sol}^{CO_2}$ is CO_2 dissolution rate in the aqueous phase [kg/m^3/s], $\Delta H_{sol}^{CO_2}$ is the enthalpy change during CO_2 gas dissolution [J/kg], and $Q_{inj}^{CO_2}$ is CO_2 injection rate [kg/m^3/s].

In addition, the flux terms in the governing equations follow the Darcy's law, which are given as below:

$$\mathbf{F_A} = -k_S \frac{k_{rA}\rho_A}{\mu_A}(\nabla P_A - \rho_A\mathbf{g})\phi S_A, \tag{2-5}$$

$$\mathbf{F_G} = -k_S \frac{k_{rG}\rho_G}{\mu_G}(\nabla P_G - \rho_G\mathbf{g})\phi S_G, \tag{2-6}$$

$$P_c = P_A - P_G, \tag{2-7}$$

where k_S is the absolute permeability of the porous medium [m^2], $k_{r\beta}$ is the relative permeability of phase $\beta \equiv A$, G [-], and μ_β is the viscosity of phase $\beta \equiv A$, G [Pa·s]. P_β is the pressure of phase $\beta \equiv A$, G [Pa], P_c is the capillary pressure [Pa], and $\mathbf{g}$ is the acceleration of gravity [m/s^2].

Based on the governing equations mentioned above, four primary variables of P, T, S_G and S_A are solved iteratively using the fully implicit method for three-phase coexistence condition (gas phase, aqueous phase and hydrate phase). Then, the other parameters are determined

automatically when the primary variables are settled.

However, the original TOUGH+HYDRATE code is mainly used for the simulations of the system behavior in methane hydrate-bearing geologic media (i.e. in the permafrost or in the deep ocean sediments), and the mass fraction of methane in the aqueous phase is not considered as a primary variable but determined based on the equilibrium concentration at the given pressure and temperature condition, because methane gas can barely dissolve into the aqueous phase. This may not be a critical problem for the simulations of methane hydrate formation and dissociation, but this approximation has a great risk to yield to misleading results in the simulations of CO_2 gas injection into the pure water. For this reason, an addition governing equation: i.e. the mass balance equation for CO_2 gas dissolved in the aqueous phase was added to the original code by Nakashima [1-20] in order to determine CO_2 mass fraction in the aqueous phase as a fifth primary variable $X_A^{CO_2}$ as below:

$$\frac{\partial \left(\phi S_A \rho_A X_A^{CO_2} \right)}{\partial t} = Q_{sol}^{CO_2} + \mathbf{F}_A X_A^{CO_2} + \mathbf{J}_A^{CO_2} - Q_H X_H^{CO_2} , \tag{2-8}$$

where $X_H^{CO_2}$ is CO_2 mass fraction in CO_2 hydrate [kg/kg], which is calculated by the chemical formula of CO_2 hydrate ($CO_2 \cdot 5.75 H_2O$).

In summary, by using five governing Equations (2-1) ~ (2-4) and (2-8), a set of five primary variables (P, T, S_G, S_A and $X_A^{CO_2}$) are solved iteratively in the modified version of TOUGH+HYDRATE, which builds the basic structure of the code.

In addition, the calculation scheme of the modified version of TOUGH+HYDRATE used in this study is shown in Fig. 2-1.
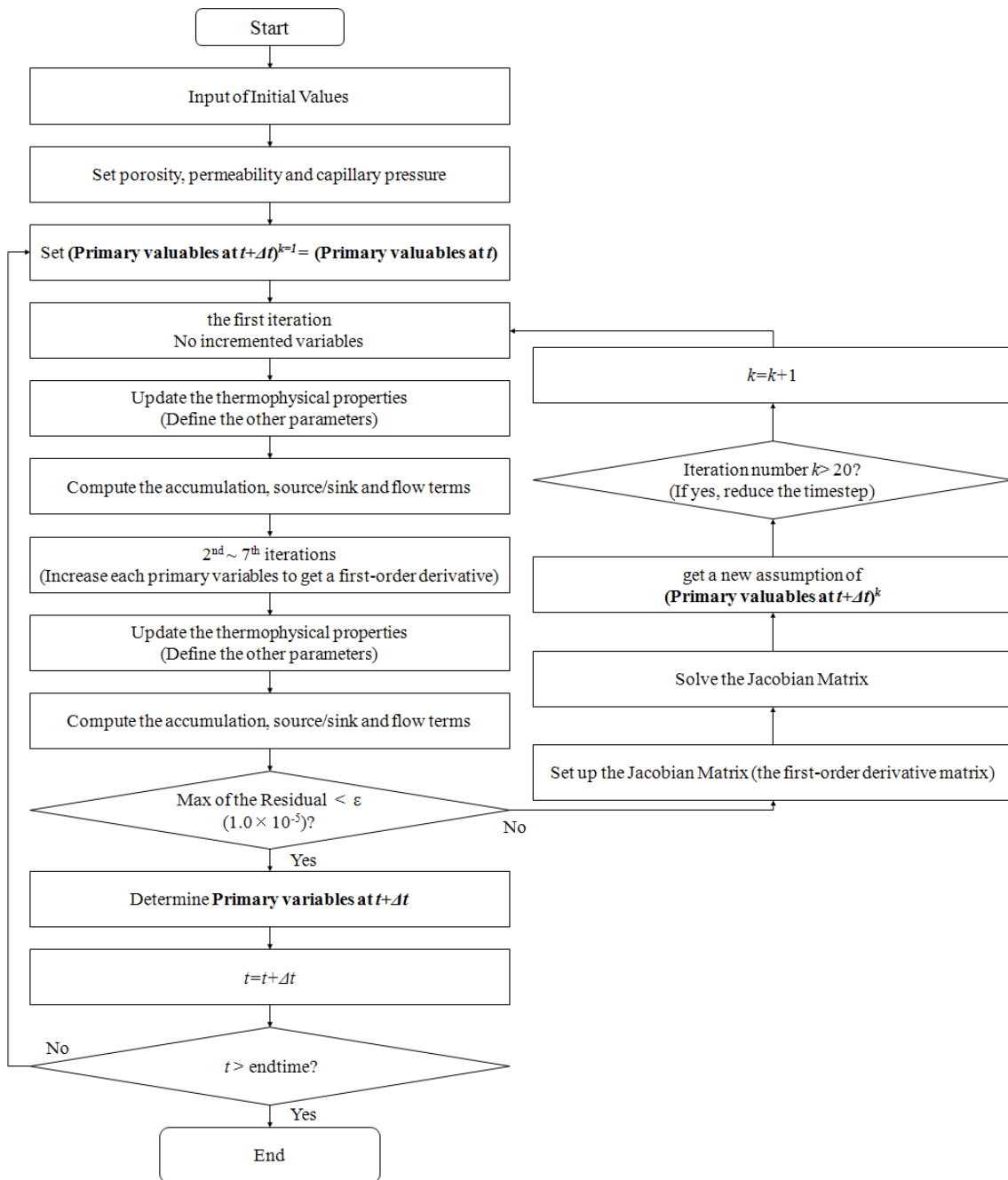
Fig. 2- 1 The calculation scheme of the modified version of TOUGH+HYDRATE used in this study [1-21]

2.1.2 Relative permeability and capillary pressure models

As shown in Equations (2-5) and (2-6), it is considered that gas-liquid two-phase flow follows the Darcy's law in this study, and the Darcy's velocity depends on the relative permeability and capillary pressure greatly. Based on a review of various models proposed by the previous

researchers (van Genuchten [2-1], Milly et al. [2-2], Stone [2-3], Brooks and Corey [2-4], etc.), the Brooks and Corey models [2-4] were adopted by Nakashima [1-20] for the broad application.

First, by using the irreducible water saturation S_A^{irr} [m^3/m^3] and the residual gas saturation S_G^{res} [m^3/m^3], the water saturation S_A [m^3/m^3] is normalized to the effective water saturation S_e [m^3/m^3] as below:

$$S_e = \frac{S_A - S_A^{irr}}{1 - S_A^{irr} - S_G^{res}}, \tag{2-9}$$

where the irreducible water saturation S_A^{irr} is set to be 0.39 [m^3/m^3] according to Inui [1-18], who adopted the experimental results of Sakamoto et al. [2-5], and the residual gas saturation S_G^{res} is set to be 0.02 [m^3/m^3] according to Rutqvist et al. [2-6].

Then, by using the effective water saturation S_e, the relative permeability models used in this study are given as below:

$$k_{rG} = k_{rG}^0 \left(1 - S_e\right)^{n_{rG}} \left(1 - S_e^2\right), \tag{2-10}$$

$$k_{rA} = (S_e)^{n_{rA}}, \tag{2-11}$$

where k_{rG}^0 is called the end point of the relative permeability for gas phase [-] (i.e. the relative permeability for gas phase when water saturation drops below the irreducible water saturation). According to the literatures reviewed, a range of 0.063~0.5 for k_{rG}^0 were measured and used by other researchers (Sakamoto et al. [2-7], Ott et al. [2-8]). However, in order to simplify this model, $k_{rG}^0 = 1$ is adopted in this study.

Besides, the exponents of n_{rG} and n_{rA} in the models are treated as unknown parameters, whose optimum values will be determined by parameter-fitting comparing with the experimental data. As a special case, by setting n_{rG} and n_{rA} to be 2 and 4, respectively, Equations (2-10) and (2-11) become the generalized Corey model [2-4]. The curves of relative permeability models for gas phase and aqueous phase with the change of water saturation are shown in Fig. 2-2.
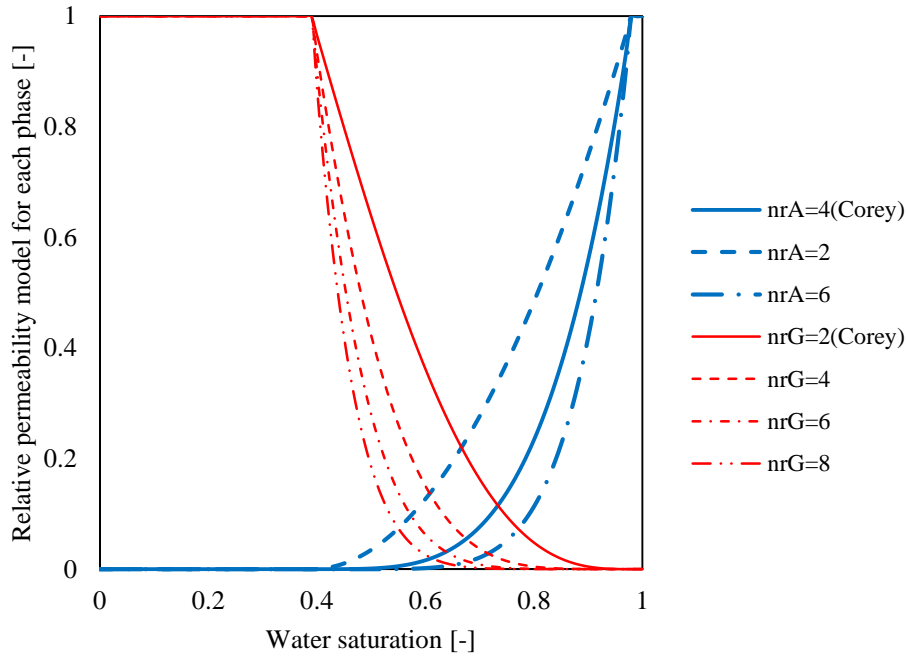
Fig. 2- 2 The curves of relative permeability models for gas phase and aqueous phase with the change of water saturation

In addition, the capillary pressure model is given by using the effective water saturation S_e according to Brooks and Corey [2-4] as below:

$$P_c = -P_d (S_e)^{n_{Pc}},$$ (2-12)

where P_d is the initial capillary pressure at the moment when gas begins to flow [Pa], which can be calculated by Young-Laplace equation as below:

$$P_d = \frac{4\sigma \cos \theta}{d},$$ (2-13)

where σ is the surface tension of the aqueous phase [N/m], set as 75 N/m referring to the Chronological Scientific Tables [2-9]. θ is the contact angle of the sand particles [rad], and d is the main pore radius of the sand sediment [μm], set as 1.23 rad and 56 μm, respectively, referring to Sakamoto et al. [2-7]. Then, P_d can be calculated as P_d = 1.79 kPa by Equation (2-13).

Besides, the exponent of n_{Pc} in Equation (2-12) is treated as an unknown parameter in this

study, which will be determined by parameter-fitting.

2.1.3 CO₂ gas dissolution rate model

During the process of gas-liquid two-phase flow, CO_2 gas dissolves into the aqueous phase through the gas-liquid interface gradually. CO_2 gas dissolution rate model can be described as Equation (2-14), and the driving force is the difference between CO_2 equilibrium mass fraction X_A^{eq} [kg/kg] and CO_2 mass fraction in the aqueous phase $X_A^{CO_2}$ [kg/kg].

$$Q_{sol}^{CO_2} = k_t A_I \left(X_A^{eq} - X_A^{CO_2} \right),$$ (2-14)

where k_t is CO_2 mass transfer coefficient at the gas-liquid interface [m/s], whose value is set as 2.0×10^{-6} m/s by Inui [1-18] and Nakashima [1-20]. However, in this study, k_t is treated as an unknown parameter, and will be determined by parameter-fitting. Besides, A_I is the gas-liquid interfacial area [m²/m³].

2.1.4 Gas-liquid interfacial area model

Gas-liquid interfacial area in variably saturated porous media has a significant influence on mass transfer processes, such as gas dissolution in the aqueous phase, volatilization, and evaporation [2-10]. Recently, Molly et al. [2-11] used a promising technology – synchrotron X-ray microtomography for the direct investigation of the gas-liquid interfacial area in sandy porous media. They found a totally smooth interfacial area and water saturation correlation based on the experimental data, and proposed an empirical model for estimating the gas-liquid interfacial area. In this study, the empirical model proposed by Molly et al. [2-11] is adopted and modified as below:

$$A_I = \begin{cases} A_S \left[(-0.9112) S_A + 0.9031 \right] & S_A^{irr} \leq S_A \leq 0.991 \\ 0 & 0.991 < S_A \leq 1 \end{cases},$$ (2-15)

where A_S is the surface area of the porous media [m²/m³]: i.e. sand surface area in this study.

In this model, the gas-liquid interfacial area is proportional to the surface area of the porous media, and inversely proportional to the water saturation. The specific gas-liquid interfacial area

A_I/A_S as a function of water saturation S_A is shown in Fig. 2-3.
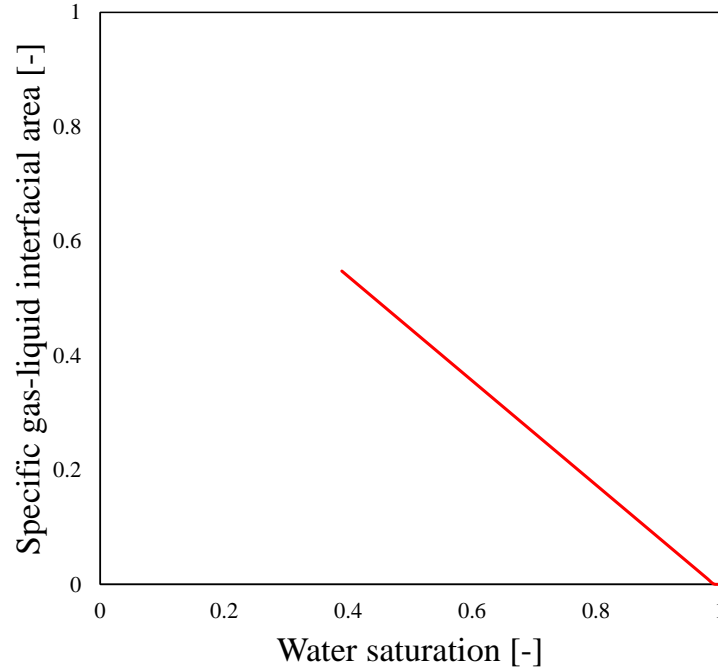
Fig. 2- 3 The specific gas-liquid interfacial area A_I/A_S as a function of water saturation S_A

2.1.5 Sand surface area model

The sand surface area A_S used in Equation (2-15) for the calculation of gas-liquid interfacial area A_I, is given by Kozeny and Carman model [2-12] as below:

$$A_S = \sqrt{\frac{\phi^3}{5k_S}}.$$

(2-16)

For the porosity ϕ and absolute permeability k_S of the sand sediment, the average values of the experimental data obtained by Sakamoto et al. [2-5] using the same Toyoura sand are adopted in this study.

2.1.6 Mass diffusion models

$\mathbf{J}_\beta$ in Equations (2-2) and (2-4) is the mass diffusion term of phase $\beta \equiv A$, G. In the original TOUGH+HYDRATE code, only the mass diffusion term of the gas phase was included. However, the mass diffusion term of the aqueous phase was not taken into account. In this study, the mass

diffusion term of the aqueous phase was also introduced using the method according to Fuller et al. [2-13] by Nakashima [1-20] as below:

$$\mathbf{J}_G = -\phi S_G \tau_G D_G^{CO_2} \rho_G \nabla X_G^{CO_2} , \qquad (2\text{-}17)$$

$$\mathbf{J}_A = -\phi S_A \tau_A D_A^{CO_2} \rho_A \nabla X_A^{CO_2} , \qquad (2\text{-}18)$$

where τ_β is the tortuosity factor for phase $\beta \equiv A$, G [-], which can be calculated internally by Millington and Quirk model [2-14]. $D_G^{CO_2}$ is CO_2 diffusion coefficient in the gas phase [m²/s], determined by Riazi and Whiton model [2-15], and $D_A^{CO_2}$ is CO_2 diffusion coefficient in the aqueous phase [m²/s], which can be calculated by the following method according to Wilke and Chang [2-16]:

$$D_A^{CO_2} = 7.4 \times 10^{-9} \frac{\left(\varphi M_{H_2O}\right)^{1/2} T}{\eta_{H_2O} V_{CO_2}^{0.6}} , \qquad (2\text{-}19)$$

where φ is called the association parameter [-], set as 2.6 in this study. V_{CO_2} is the molar volume of CO_2 [cm³/mol], given as 34 cm³/mol. M_{H_2O} is the molar mass of H_2O [g/mol], and η_{H_2O} is the viscosity of H_2O [Pa·s] at the absolute temperature T, which can be calculated as below:

$$\eta_{H_2O} = -0.4199 \ln\left(T - 273.15\right) + 2.2057 . \qquad (2\text{-}20)$$

2.1.7 Heat flux and diffusion models

The heat balance in this study is solved by using Equation (2-4), the five terms on the right side of which represent (a) heat exchange due to the temperature gradient, (b) heat transfer due to the flux and diffusion of the fluids, (c) injection and exhaust heat due to the source and sink of the fluids, (d) CO_2 hydrate formation heat, and (e) CO_2 gas dissolution heat, respectively. For the composite thermal conductivity λ_m in the first term, a random model which is often used in the hydrate-bearing sand sediment is adopted in this study [2-17] as below:

$$\lambda_m = \lambda_G^{\phi S_G} \lambda_A^{\phi S_A} \lambda_H^{\phi S_H} \lambda_S^{1-\phi} , \qquad (2\text{-}21)$$

17

where λ_G is the thermal conductivity of the gas phase [W/m/K], which can be calculated by the empirical equation proposed by Chung et al. [2-18]. λ_A is the thermal conductivity of the aqueous phase [W/m/K], which can be determined by the model of O'Sullivan et al. [2-19] and the modified model of Falta et al. [2-20] (in the case of low water saturation).

For CO_2 hydrate formation heat ΔH_H in the fourth term, Kamath model [2-21] is adopted as below:

$$\Delta H_H = 28.38 \times \left(19199 - \frac{14.95}{T} \right).$$

(2-22)

In addition, CO_2 gas dissolution heat $\Delta H_{sol}^{CO_2}$ in the fifth term is determined according to Himmelblau and Babb [2-22].

2.2 Modeling of CO₂ Hydrate Formation in the Sand Sediment

2.2.1 Equilibrium curve for CO₂ hydrate formation

The equilibrium curve is very important for the determination of hydrate formation and dissociation conditions. In this study, Kamath model [2-21] for the calculation of CO_2 hydrate equilibrium pressure $P_{eq}^{CO_2}$ is adopted as below, and the equilibrium curve is shown in Fig. 2-4.

$$P_{eq}^{CO_2} = \exp\left(\alpha - \frac{\beta}{T} \right) \times 10^3$$

(2-23)

$$\begin{pmatrix} \alpha = 18.59, \beta = 3161 & 248.15\text{K} < T \leq 273.15\text{K} \\ \alpha = 44.58, \beta = 10246 & 273.15\text{K} < T < 298.15\text{K} \end{pmatrix}.$$
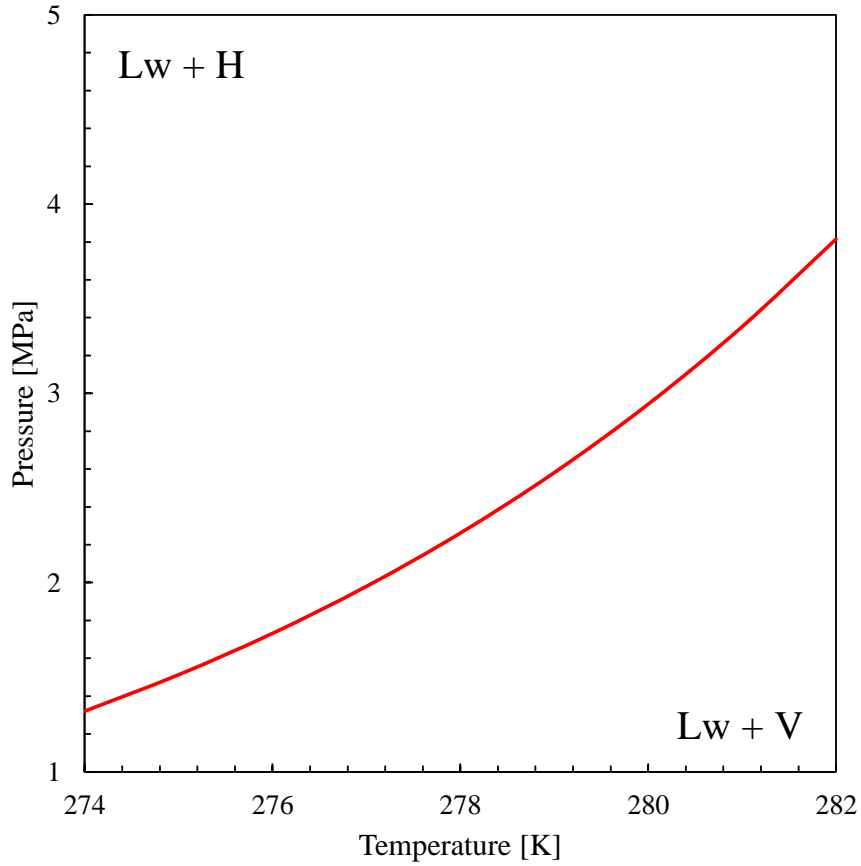
Fig. 2- 4 The equilibrium curve for CO_2 hydrate formation used in this study

2.2.2 Inclusive model for CO_2 hydrate formation in the sand sediment

As mentioned in Section 1.3, in CO_2 hydrate formation models proposed by the previous researchers (Inui et al. [1-11], Takahashi et al. [1-19]), hydrate formation morphologies have not been classified by locations completely. Besides, for CO_2 hydrate formation in the aqueous phase, only one part (either on the surface of the sand particles or on the aqueous-phase side of the hydrate film) has been taken into account in their models. For these reasons, previous models used so far cannot fully describe the complex process of CO_2 hydrate formation in the sand sediment, and need to be improved. Therefore, in this study, an inclusive model for CO_2 hydrate formation in the sand sediment is proposed as below:

$$Q_H = \delta Q_{H1} + Q_{H2} + Q_{H3}.$$
(2-24)

As shown in Fig. 2-5, in this model, hydrate formation morphologies in the sand sediment are

19

assumed to consist of three different parts: (a) on the gas front, (b) on the hydrate film behind the gas front, and (c) on the surface of the sand particles behind the gas front, where the corresponding hydrate formation rates are Q_{H1}, Q_{H2}, and Q_{H3} [kg/m³/s], respectively.
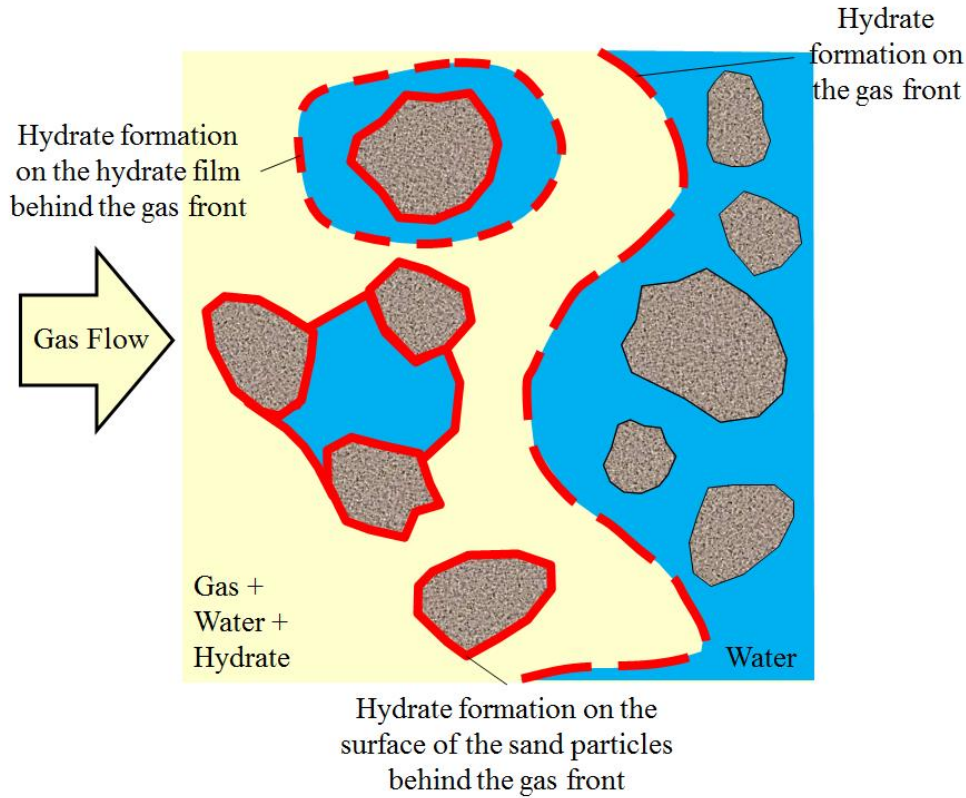
Fig. 2- 5 The schematic diagram of hydrate formation morphologies in the sand sediment proposed in this study

δ in the model is a "switch", which is used to determine whether the gas front exists in a computational cell or not. It is defined as below:

$$\delta = \begin{cases} 1 & \cdots \quad \text{in a computational cell where the gas front exists} \\ 0 & \cdots \quad \text{elsewhere} \end{cases} . \qquad (2\text{-}25)$$

In order to determine whether the gas front exists in a computational cell ($\delta = 1$) or not ($\delta = 0$) during the simulation, the following method is introduced in this study. First, the conceptions of computational cells for the aqueous phase (hereinafter referred to as water cell) and for the gas phase (hereinafter referred to as gas cell) are defined. A water cell is a computational cell, which the gas front has not passed by yet: i.e. the cell located in the forward side of the gas front. While

a gas cell is a computational cell, which the gas front exists in or has already passed by: i.e. the cell located on the gas front or in the backward side of the gas front. The division between a water cell and a gas cell is a threshold value of gas saturation: i.e. the residual gas saturation S_G^{res} (a very small value such as 0.01). If the gas saturation within a computational cell is no larger than the residual gas saturation: i.e. $S_G \leq S_G^{res}$, then, this cell is treated as a water cell. On the contrary, if the gas saturation within a computational cell is larger than the residual gas saturation: i.e. $S_G > S_G^{res}$, then, this cell is treated as a gas cell.

At the beginning of the simulation, all the δ switches within the calculation domain are set to be "off state": i.e. $\delta = 0$. Then, during the calculation, the simulator searches a particular gas cell automatically at every time iteration: the gas cell that has a water cell as its neighbor in the same line along the gas flow direction. After this cell is found, it is considered to be a cell where the gas front exists, and the switch within this cell will "turn on": i.e. $\delta = 1$ (only a gas cell can change to the gas front cell). For other computational cells, the switches still remain "off state": i.e. $\delta = 0$. Therefore, it is assumed that there is only one computational cell where the gas front exists in each line along the gas flow direction, and the combination of these particular gas cells is treated as the gas front. The schematic diagram for the determination of a computational cell where the gas front exists (orange cells), as well as the conceptions of a water cell (green cells) and a gas cell (pink cells) is shown in Fig. 2-6.
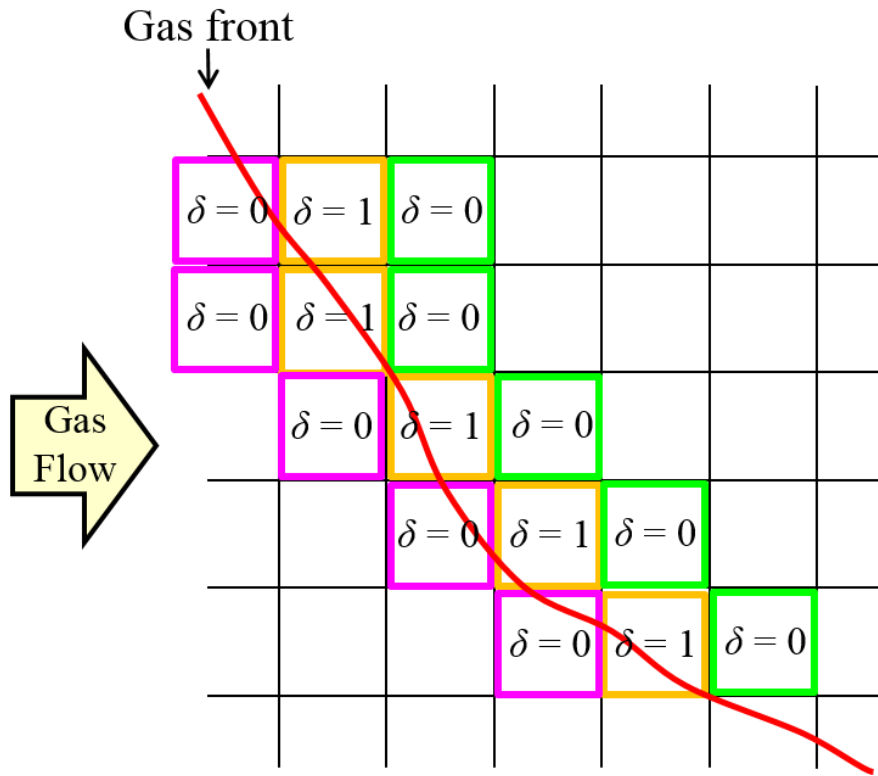
Fig. 2- 6 The schematic diagram for the determination of a computational cell where the gas front exists

It is worth mentioning that when the angle between the gas front and the cross section of the calculation domain is too steep, there may be two computational cells where the gas front exists in a line along the gas flow direction at the same time. This method can only detect the former ones (orange cells) as the gas front cells, while the latter ones (pink cells) are only treated as normal gas cells. This approximate method may lead to a slight error in the calculation. However, this phenomenon is only likely to occur near the boundary where there is a steep angle between the gas front and the cross section of the calculation domain, which is considered to be rare during the simulation based on the Darcy's law.

2.2.2.1 Hydrate formation rate on the gas front

As shown in Fig. 2-7, hydrate forms on the gas front at two different locations: one is at the fresh surface (rupture), and the other one is at the gas-liquid interface of the existing hydrate film (the growth of the hydrate film). For the growth of the hydrate film, CO_2 gas is provided both by the diffusion of CO_2 gas through the hydrate film, and by the diffusion of dissolved CO_2 in the aqueous phase to the gas-liquid interface of the hydrate film. Besides, the gas-liquid interface is

not covered by the hydrate film completely. Under certain circumstances, rupture occurs on the hydrate film, resulting in the appearance of fresh gas-liquid interface where new hydrate can form.
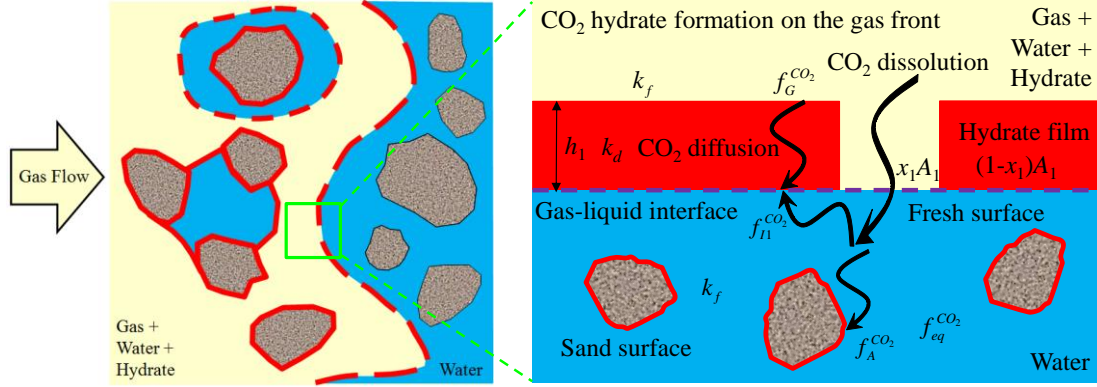
Fig. 2- 7 The schematic diagram of hydrate formation morphologies on the gas front

In addition, as the gas flows, a part of CO_2 hydrate on the gas front may be captured by the sand particles, and separated from the gas front. This part of hydrate should be taken as the loss of the formation amount, and converted into a negative formation rate as $-Q_{H1 \to 3}$. Therefore, hydrate formation rate on the gas front is considered to be composed of the fresh surface formation (rupture), the growth of the hydrate film, and the formation loss due to the capture of the sand particles, which is given as below:

$$Q_{H1} = M_H k_f x_1 A_1 \left(f_G^{CO_2} - f_{eq}^{CO_2} \right) + M_H k_f \left(1 - x_1 \right) A_1 \left(f_{I1}^{CO_2} - f_{eq}^{CO_2} \right) - Q_{H1 \to 3}, \qquad (2\text{-}26)$$

where M_H is the molar mass of CO_2 hydrate [kg/mol], k_f is the intrinsic rate constant of CO_2 hydrate formation [mol/m²/Pa/s], A_1 is the gas-liquid interfacial area on the gas front where CO_2 hydrate formation takes place [m²/m³], and x_1 is the rupture ratio on the gas front where fresh surface appears [-]. Besides, $f_G^{CO_2}$, $f_{I1}^{CO_2}$, and $f_{eq}^{CO_2}$ are CO_2 fugacity in the gas phase, at the gas-liquid interface on the gas front, and at the three-phase equilibrium point [Pa], respectively.

① Gas-liquid interfacial area on the gas front A_1

The gas-liquid interfacial area on the gas front A_1 is the specific surface area of the gas-liquid interface where CO_2 hydrate formation takes place under the condition of gas-liquid two-phase flow. It is assumed that A_1 within a computational cell is given as below:

$$A_1 = \frac{\phi A_0}{V_0} = \frac{\phi}{\sqrt{\left(\left|\frac{u_G}{U_G}\right|\Delta x\right)^2 + \left(\left|\frac{v_G}{U_G}\right|\Delta y\right)^2 + \left(\left|\frac{w_G}{U_G}\right|\Delta z\right)^2}} ,$$

$$= \frac{\phi|U_G|}{\sqrt{\left(|u_G|\Delta x\right)^2 + \left(|v_G|\Delta y\right)^2 + \left(|w_G|\Delta z\right)^2}}$$

(2-27)

where A_0 is the cross sectional area of the computational cell on the gas front [m^2], V_0 is the volume of the computational cell [m^3], and U_G is the gas phase velocity [m/s]. Δx, Δy, and Δz are the sizes of the computational cell on the x axis, y axis, and z axis [m], respectively. u_G, v_G, and w_G are the component velocities of U_G on the x axis, y axis, and z axis [m/s], respectively.

② Rupture ratio on the gas front x_1

As the gas front passes by the equator of a sand particle, fresh surface (rupture) appears on the gas front after a part of hydrate film on the gas front is captured by the sand particle, as shown in Fig. 2-8.
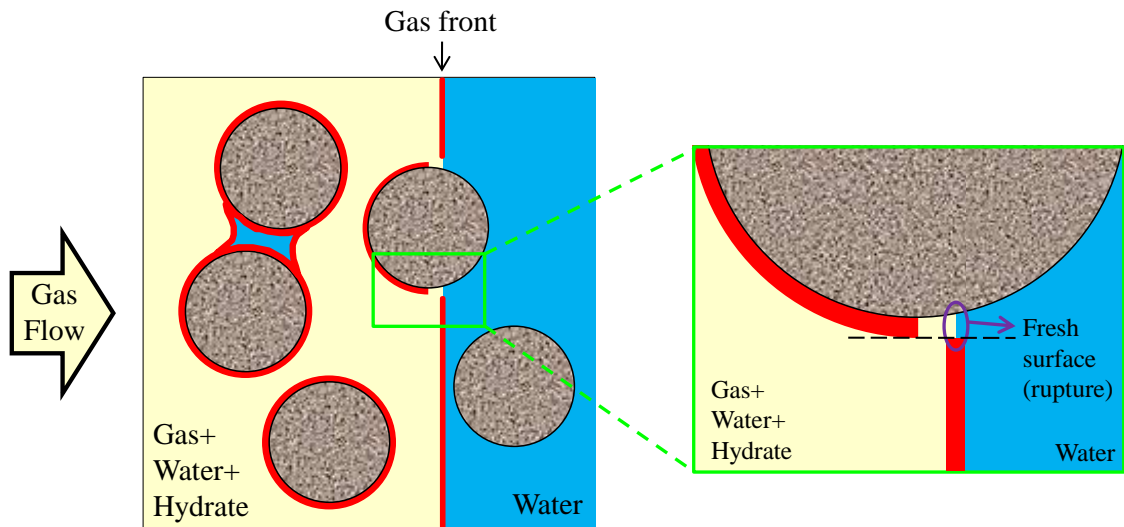
Fig. 2- 8 The schematic diagram of fresh surface (rupture) appearing on the gas front

For the determination of rupture ratio on the gas front x_1, the following method is introduced in this study, as shown in Fig. 2-9. First, the average radius of the cross sectional area of the sand particle is assumed to be $\bar{R}$, which can be calculated by using the radius of the sand particle r as below:

$$\overline{R} = \frac{1}{4}\pi r^2 \cdot \frac{1}{r} = \frac{\pi}{4}r. \tag{2-28}$$
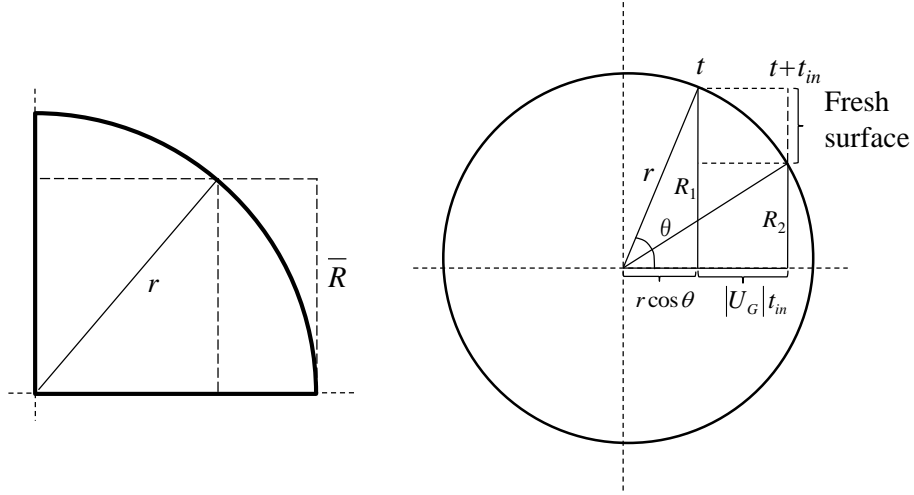
Fig. 2- 9 The schematic diagram for the determination of rupture ratio on the gas front

Then, the following equation can be obtained:

$$r\cos\theta = \sqrt{r^2 - \overline{R}^2} = \frac{\sqrt{16 - \pi^2}}{4}r. \tag{2-29}$$

It is assumed that the sand particle is spherical. At time t, the radius of the cross sectional area of the sand particle where the gas front exists is assumed to be R_1, and at time $t + t_{in}$, the radius is assumed to be R_2, as can be seen in Fig. 2-9. Therefore, the following equations can be obtained:

$$R_1^2 = r^2 \sin^2\theta, \tag{2-30}$$

$$R_2^2 = r^2 - \left(r\cos\theta + |U_G|t_{in}\right) = r^2 \sin^2\theta - 2r\cos\theta \cdot |U_G|t_{in} - |U_G|^2 (t_{in})^2, \tag{2-31}$$

where t_{in} is the microscale induction time for hydrate formation at the fresh surface on the gas front, as shown in Fig. 2-9, which is very short, so $(t_{in})^2$ can be neglected in this study. Therefore, R_2 is rewritten as below:

$$R_2^2 = r^2 \sin^2 \theta - 2r \cos \theta \cdot |U_G| t_{in}. \tag{2-32}$$

As a result, the fresh surface generated by one sand particle from time t to $t + t_{in}$ is a circle, as shown in Fig. 2-10, the area a_{fresh} of which can be calculated as below:

$$a_{fresh} = \pi \left(R_1^2 - R_2^2 \right) = 2\pi \cdot r \cos \theta \cdot |U_G| t_{in} = \frac{\pi \sqrt{16 - \pi^2}}{2} r \cdot |U_G| t_{in}. \tag{2-33}$$
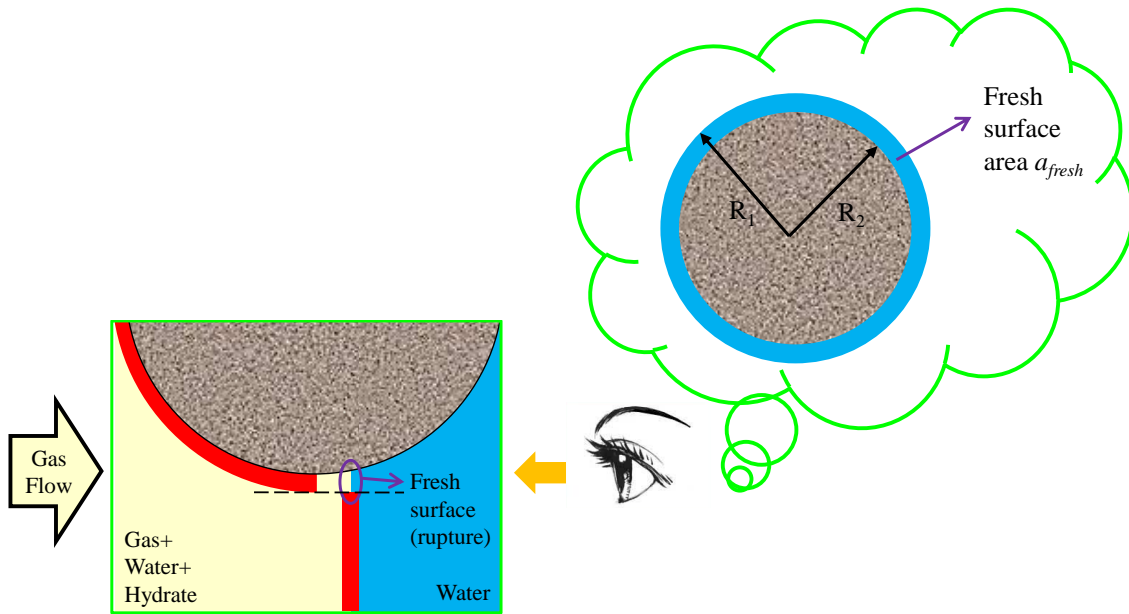
Fig. 2- 10 The schematic diagram for the determination of fresh surface area on the gas front

Assume n is the number of the sand particles on the gas front within a computational cell, which is given as below:

$$n = \frac{(1 - \phi) A_0}{\pi \overline{R}^2} = \frac{16}{\pi^3} \cdot \frac{(1 - \phi)}{r^2} \cdot A_0. \tag{2-34}$$

As the gas front moves, it is assumed that fresh surface appears only for half the number of the sand particles on the gas front, because rupture occurs after the gas front passes by the equators of the spherical sand particles. Therefore, the total fresh surface area on the gas front A_{fresh} should be calculated as below:

$$A_{fresh} = a_{fresh} \cdot \frac{n}{2} = \frac{4\sqrt{16-\pi^2}}{\pi^2 r} \cdot (1-\phi) \cdot |U_G| t_{in} \cdot A_0. \tag{2-35}$$

As a result, the rupture ratio on the gas front x_1 can be defined as below:

$$x_1 = \frac{A_{fresh}}{\phi A_0} = \frac{4\sqrt{16-\pi^2}}{\pi^2} \cdot t_{in} \cdot \frac{(1-\phi)}{\phi} \cdot \frac{|U_G|}{r}. \tag{2-36}$$

Assume $\alpha = \frac{4\sqrt{16-\pi^2}}{\pi^2} \cdot t_{in}$, then,

$$x_1 = \alpha \frac{(1-\phi)}{\phi} \cdot \frac{|U_G|}{r}, \tag{2-37}$$

where α is the function of geometrical factor and microscale induction time [s], which can be determined by parameter-fitting for the real irregular sand particles.

③ CO₂ fugacity at the gas-liquid interface on the gas front $f_{I1}^{CO_2}$

As shown in Fig. 2-11, for the growth of the hydrate film, it is assumed that hydrate formation rate at the gas-liquid interface of the hydrate film equals to the total sum of CO_2 diffusion rates which come from both the gas phase and aqueous phase to the gas-liquid interface of the hydrate film on the gas front (in the case of $C_A^{CO_2} > C_{I1}^{CO_2}$) as below:

$$\frac{\partial n_I}{\partial t} = \frac{\partial n_G}{\partial t} + \frac{\partial n_A}{\partial t}. \tag{2-38}$$
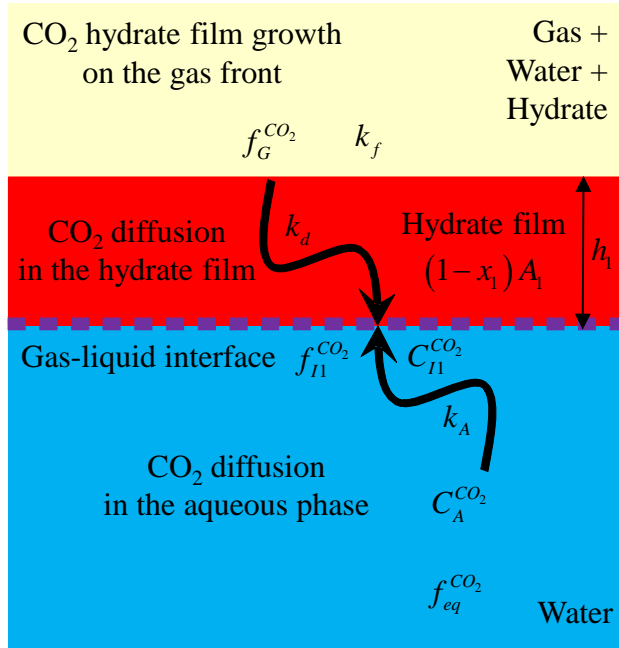
Fig. 2- 11 The schematic diagram of hydrate film growth on the gas front

By the introduction of CO_2 fugacity at the gas-liquid interface on the gas front $f_{I1}^{CO_2}$, hydrate formation rate at the gas-liquid interface of the hydrate film $\partial n_I / \partial t$ can be described as below:

$$\frac{\partial n_I}{\partial t} = k_f \left(1 - x_1\right) A_1 \left(f_{I1}^{CO_2} - f_{eq}^{CO_2} \right). \tag{2-39}$$

According to the Henry's law and the definition of fugacity, $f_{I1}^{CO_2}$ is given by

$$f_{I1}^{CO_2} = \Phi H C_{I1}^{CO_2}, \tag{2-40}$$

where Φ is the fugacity coefficient [-], which is a function of pressure P and temperature T. H is Henry's constant [Pa], and $C_{I1}^{CO_2}$ is CO_2 concentration at the gas-liquid interface on the gas front [mol/mol].

For CO_2 diffusion rate in the hydrate film $\partial n_G / \partial t$, the driving force is the difference between CO_2 fugacity in the gas phase, and that at the gas-liquid interface on the gas front.

$$\frac{\partial n_G}{\partial t} = \frac{k_d}{h_1} \left(1 - x_1\right) A_1 \left(f_G^{CO_2} - f_{I1}^{CO_2} \right), \tag{2-41}$$

where k_d is CO_2 diffusion constant in the hydrate film [mol/m/Pa/s], which is treated as an unknown parameter in this study. h_1 is the average thickness of the hydrate film on the gas front [m], which is given as below:

$$h_1 = \frac{\phi S_{H1}}{(1-x_1) A_1},$$

(2-42)

where S_{H1} is CO_2 hydrate saturation on the gas front [m³/m³], which can be calculated by the integral of hydrate formation rate on the gas front Q_{H1}. Besides, the integral interval is from the start time 0 of the simulation to the current time T_{cur}.

$$S_{H1} = \frac{1}{\rho_H} \int_0^{T_{cur}} Q_{H1} dt.$$

(2-43)

On the other hand, for CO_2 diffusion rate in the aqueous phase $\partial n_A / \partial t$, the driving force is the difference between CO_2 concentration in the aqueous phase, and that at the gas-liquid interface on the gas front.

$$\frac{\partial n_A}{\partial t} = \frac{k_A}{h_A} (1-x_1) A_1 \left(C_A^{CO_2} - C_{I1}^{CO_2} \right),$$

(2-44)

where h_A is a thin layer of water in which CO_2 diffusion takes place [m], set as 1.0×10^{-6} m in this study, according to Takahashi et al. [1-19]. k_A is the normalized CO_2 diffusion coefficient in the aqueous phase [mol/m/s], which is given as below:

$$k_A = D_A^{CO_2} \frac{\rho_{H_2O}}{M_{H_2O}}.$$

(2-45)

By the combination of Equations (2-38) ~ (2-41) and Equation (2-44), CO_2 mass transfer at the gas-liquid interface of the hydrate film on the gas front can be described as below:

$$
k_f \left(1-x_1\right) A_1 \left(\Phi H C_{I1}^{CO_2} - f_{eq}^{CO_2}\right)
$$
$$
= \frac{k_d}{h_1}\left(1-x_1\right) A_1 \left(f_G^{CO_2} - \Phi H C_{I1}^{CO_2}\right) + \frac{k_A}{h_A}\left(1-x_1\right) A_1 \left(C_A^{CO_2} - C_{I1}^{CO_2}\right). \tag{2-46}
$$

By solving the equation above, $C_{I1}^{CO_2}$ can be obtained as below:

$$
C_{I1}^{CO_2} = \frac{h_A k_d f_G^{CO_2} + h_A h_1 k_f f_{eq}^{CO_2} + h_1 k_A C_A^{CO_2}}{\Phi H \left(h_A k_d + h_A h_1 k_f\right) + h_1 k_A}. \tag{2-47}
$$

During the numerical simulation, $C_{I1}^{CO_2}$ is calculated at each time step, and substituted into Equation (2-40), so CO$_2$ fugacity at the gas-liquid interface on the gas front $f_{I1}^{CO_2}$ can be calculated as below:

$$
f_{I1}^{CO_2} = \frac{h_A k_d f_G^{CO_2} + h_A h_1 k_f f_{eq}^{CO_2} + h_1 k_A C_A^{CO_2}}{h_A k_d + h_A h_1 k_f + h_1 k_A / \Phi H}. \tag{2-48}
$$

It is worth mentioning that Fig. 2-11 only describes the case of $C_A^{CO_2} > C_{I1}^{CO_2}$, in which CO$_2$ diffusion in the aqueous phase only takes place in one direction (from the aqueous phase to the gas-liquid interface of the hydrate film). In fact, CO$_2$ diffusion in the aqueous phase can happen in both two directions (the aqueous phase $\rightleftharpoons$ the gas-liquid interface of the hydrate film), as shown in Fig. 2-12. For the case of $C_A^{CO_2} < C_{I1}^{CO_2}$, it is assumed that hydrate film dissociates, and CO$_2$ gas dissolves into the aqueous phase due to the low CO$_2$ concentration in the aqueous phase, resulting in CO$_2$ diffusion from the gas-liquid interface of the hydrate film to the aqueous phase inversely. Equation (2-44) has taken this part of CO$_2$ diffusion into consideration as well, so it can describe CO$_2$ diffusion in the aqueous phase in both two directions on the gas front.
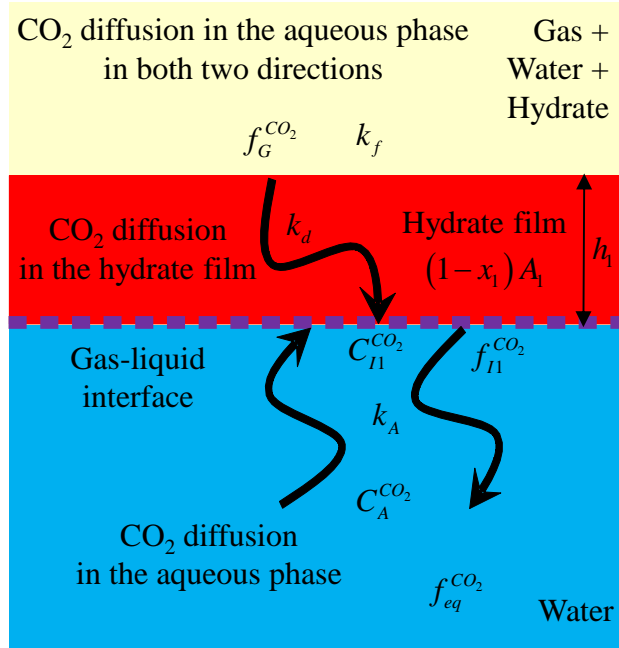
Fig. 2- 12 The schematic diagram of CO_2 diffusion in the aqueous phase in both two directions on the gas front

④ Hydrate formation rate $Q_{H1\to3}$: transferred from Q_{H1} to Q_{H3}

The part of hydrate film on the gas front captured by the sand particles after the gas front passes by should be considered as the formation loss in the form of a negative formation rate as $-Q_{H1\to3}$. The derivation process of $Q_{H1\to3}$ can be calculated through the following procedures.

As shown in Fig. 2-13, at time t, a volume element dV of the hydrate film on the gas front can be calculated as below:

$$dV = ds \cdot h_1 = \frac{\pi\sqrt{16-\pi^2}}{2}rh_1 \cdot |U_G|dt , \tag{2-49}$$

where ds is the area element of the hydrate film on the gas front [m^2], which can be calculated by the radii of the cross sectional area of the sand particle, R_1 and R_2.
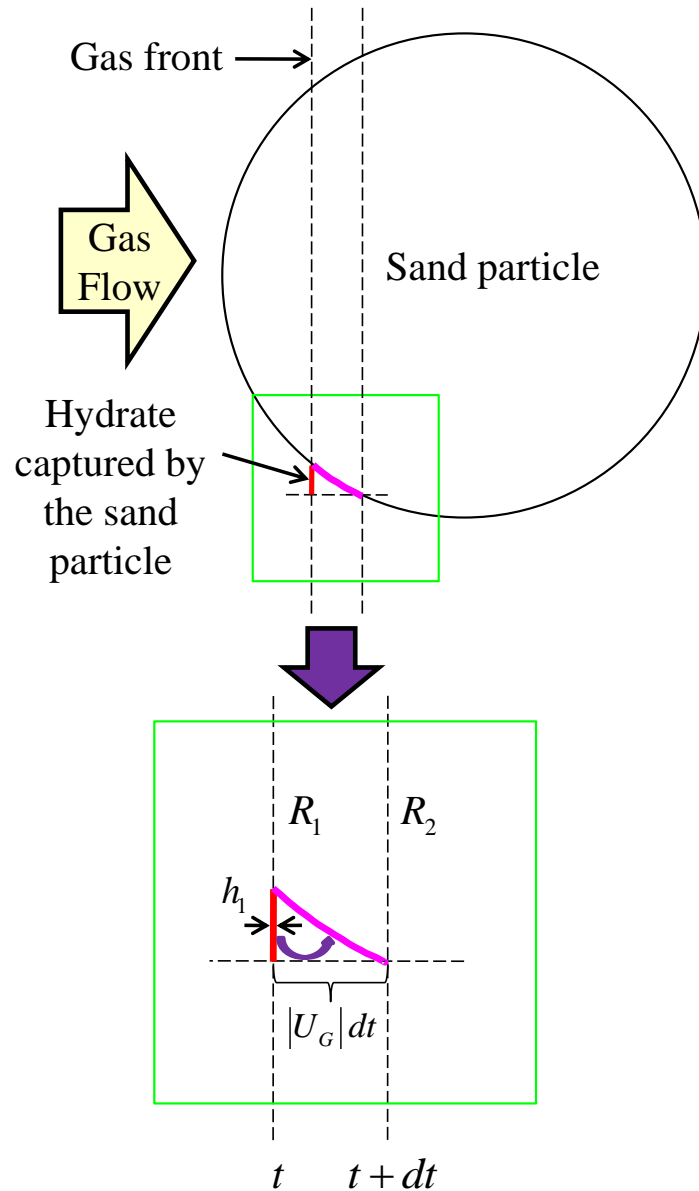
Fig. 2- 13 The schematic diagram for the determination of hydrate formation rate $Q_{H1\rightarrow3}$:
transferred from Q_{H1} to Q_{H3}

At time $t + dt$, this part of hydrate is captured by the sand particle completely, and transferred to part of Q_{H3}. For all the sand particles on the gas front, it is assumed that only half of them capture hydrate film, and the other half generate ruptures, so the total volume $dV_{H1\rightarrow3}$ of the hydrate film captured by the sand particles in a computational cell during the time element dt is calculated as below:

$$dV_{H1\rightarrow3} = \frac{n}{2} \cdot dV = \frac{4\sqrt{16-\pi^2}}{\pi^2} \cdot (1-\phi) \cdot \frac{h_1}{r} \cdot A_0 \cdot |U_G| dt. \tag{2-50}$$

Then, the saturation of the hydrate film captured by the sand particles on the gas front $dS_{H1\rightarrow3}$ can be calculated as below:

$$dS_{H1\rightarrow3} = \frac{dV_{H1\rightarrow3}}{\phi V_0} = \frac{4\sqrt{16-\pi^2}}{\pi^2} \cdot \frac{(1-\phi)}{\phi^2} \cdot \frac{h_1}{r} \cdot A_1 \cdot |U_G| dt ,$$

(2-51)

where $A_1 = \dfrac{\phi A_0}{V_0}$.

Therefore, the corresponding hydrate formation rate transferred from Q_{H1} to Q_{H3} can be obtained as below:

$$Q_{H1\rightarrow3} = \rho_H \cdot \frac{dS_{H1\rightarrow3}}{dt} = \rho_H \cdot \frac{4\sqrt{16-\pi^2}}{\pi^2} \cdot \frac{(1-\phi)}{\phi^2} \cdot \frac{h_1}{r} \cdot A_1 \cdot |U_G| .$$

(2-52)

Assume $\gamma = \dfrac{4\sqrt{16-\pi^2}}{\pi^2} \approx 1.0$, then, $Q_{H1\rightarrow3}$ becomes

$$Q_{H1\rightarrow3} = \gamma \cdot \rho_H \cdot \frac{(1-\phi)}{\phi^2} \cdot \frac{h_1}{r} \cdot A_1 \cdot |U_G| ,$$

(2-53)

where γ is a dimensionless geometrical factor of the sand particles [-]. It is an unknown parameter for the real irregular sand particles, but in order to reduce the number of unknown parameters in this study, γ is set to be 1.0.

2.2.2.2 Hydrate formation rate on the hydrate film behind the gas front

As shown in Fig. 2-14, hydrate forms on the hydrate film behind the gas front at two different locations: one is at the fresh surface (rupture), and the other one is at the gas-liquid interface of the existing hydrate film (the growth of the hydrate film). The corresponding hydrate formation rate is given as below:

$$Q_{H2} = M_H k_f x_2 A_2 \left(f_G^{CO_2} - f_{eq}^{CO_2} \right) + M_H k_f \left(1 - x_2 \right) A_2 \left(f_{I2}^{CO_2} - f_{eq}^{CO_2} \right), \tag{2-54}$$

where A_2 is the gas-liquid interfacial area behind the gas front where CO_2 hydrate formation takes place [m^2/m^3], x_2 is the rupture ratio on the hydrate film behind the gas front where fresh surface appears [-], and $f_{I2}^{CO_2}$ is CO_2 fugacity at the gas-liquid interface behind the gas front [Pa].
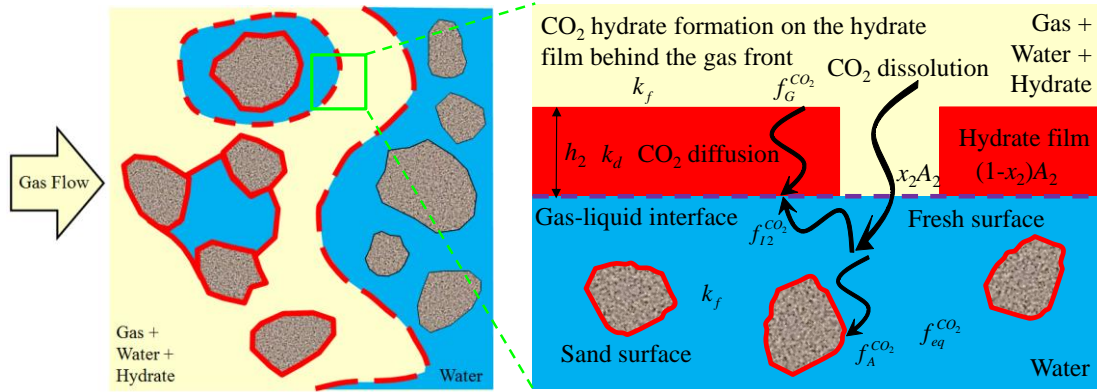
Fig. 2- 14 The schematic diagram of hydrate formation morphologies on the hydrate film behind the gas front

① Gas-liquid interfacial area behind the gas front A_2

As the gas front passes by, the water saturation behind the gas front approaches to the irreducible state gradually. For the gas-liquid interfacial area behind the gas front, Molly et al. [2-11] proposed an empirical model as mentioned in Equation (2-15), which describes a linear correlation of gas-liquid interfacial area and water saturation, and is modified as below:

$$A_2 = \begin{cases} A_S \left[\left(-0.9112 \right) S_A + 0.9031 \right] & S_A^{irr} \leq S_A \leq 0.991 \\ 0 & 0.991 < S_A \leq 1 \end{cases}. \tag{2-55}$$

Especially, for a computational cell where the gas front exists, the gas-liquid interfacial area behind the gas front should be calculated by using the actual water saturation S_A^* behind the gas front within the same cell instead of the average water saturation S_A of the whole cell: i.e.

$$A_2^* = \begin{cases} A_S \left[\left(-0.9112\right) S_A^* + 0.9031 \right] & S_A^{irr} \leq S_A^* \leq 0.991 \\ 0 & 0.991 < S_A^* \leq 1 \end{cases}.$$

(2-56)

However, it is difficult to determine S_A^* due to the complex three-dimensional shapes of the computational cell behind the gas front. Therefore, an approximate method is introduced in this study, as shown in Fig. 2-15. To start with, for S_A^* of the first computational cell in each line along the gas flow direction, it is assumed that it equals to the irreducible water saturation: i.e. $S_A^* = S_A^{irr}$. Then, for other computational cells, it is assumed that it equals to the water saturation of the cell just behind the one where the gas front exists within the same line along the gas flow direction: i.e. $S_A^* = S_A'$.
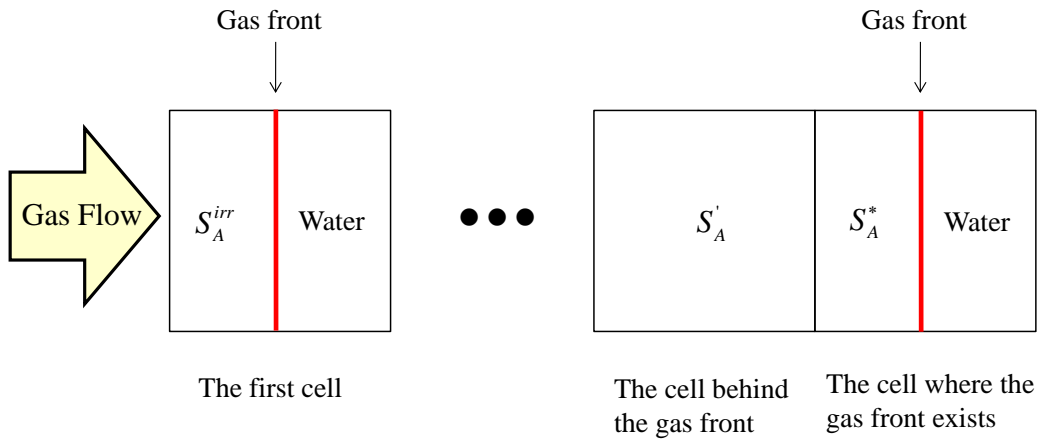
Fig. 2- 15 The schematic diagram for the determination of actual water saturation behind the gas front within a computational cell

② Rupture ratio behind the gas front x_2

After the gas front passes by, hydrate formation takes place at the gas-liquid interface behind the gas front, as shown in Fig. 2-16 (a). As the thickness of the hydrate film grows to a certain extent, the film fractures due to the volume expansion of the solid hydrate, and fresh surface (rupture) appears where new hydrate can form, as shown in Fig. 2-16 (b). Takahashi et al. [1-19] proposed a model which describes the inverse correlation of the rupture ratio decreasing monotonically with the increase of the average thickness of the hydrate film as mentioned before, and it is also adopted in this study.

$$x_2 = \exp\left(-\beta h_2^2\right),$$ (2-57)

where β is an unknown coefficient which can be determined by parameter-fitting with the experimental data [m^{-2}], and h_2 is the average thickness of the hydrate film behind the gas front [m]. The correlation between x_2 and h_2 by different β is shown in Fig. 2-17.
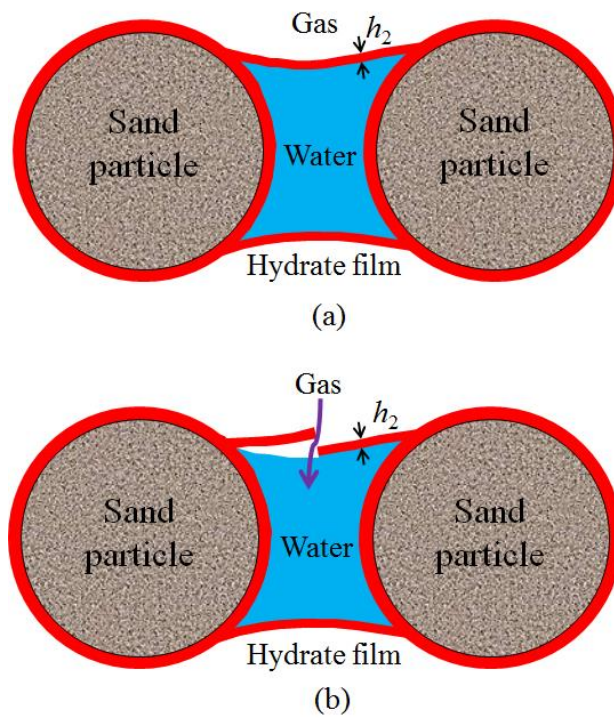
Fig. 2- 16 The schematic diagram for the determination of rupture ratio on the hydrate film behind the gas front
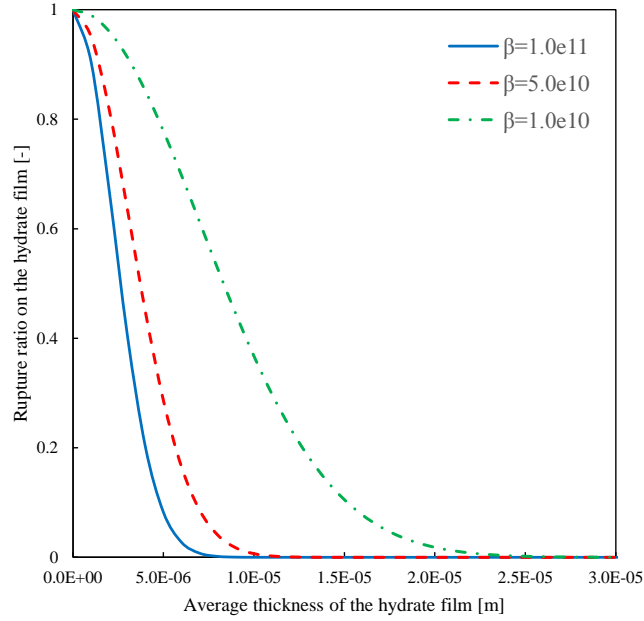
Fig. 2- 17 The correlation between the rupture ratio on the hydrate film and the average thickness of the hydrate film by different β

In addition, the average thickness of the hydrate film behind the gas front h_2 is given as below:

$$h_2 = \frac{\phi S_{H2}}{(1-x_2) A_2} , \tag{2-58}$$

where S_{H2} is CO_2 hydrate saturation on the hydrate film behind the gas front [m³/m³], which can be calculated by the integral of the hydrate formation rate on the film behind the gas front Q_{H2}. Besides, the integral interval is from the start time 0 of the simulation to the current time T_{cur}.

$$S_{H2} = \frac{1}{\rho_H} \int_0^{T_{cur}} Q_{H2} dt . \tag{2-59}$$

③ CO_2 fugacity at the gas-liquid interface behind the gas front $f_{I2}^{CO_2}$

The schematic diagram of hydrate film growth behind the gas front is shown in Fig. 2-18. As introduced in Section 2.2.2.1, it is also considered that hydrate formation rate at the gas-liquid interface of the hydrate film equals to the total sum of CO_2 diffusion rates which come from both the gas phase and aqueous phase to the gas-liquid interface of the hydrate film behind the gas front (in the case of $C_A^{CO_2} > C_{I2}^{CO_2}$). Therefore, CO_2 concentration and fugacity at the gas-liquid

interface behind the gas front are given as below, respectively:

$$C_{I2}^{CO_2} = \frac{h_A k_d f_G^{CO_2} + h_A h_2 k_f f_{eq}^{CO_2} + h_2 k_A C_A^{CO_2}}{\Phi H \left(h_A k_d + h_A h_2 k_f \right) + h_2 k_A}, \tag{2-60}$$

$$f_{I2}^{CO_2} = \frac{h_A k_d f_G^{CO_2} + h_A h_2 k_f f_{eq}^{CO_2} + h_2 k_A C_A^{CO_2}}{h_A k_d + h_A h_2 k_f + h_2 k_A / \Phi H}. \tag{2-61}$$
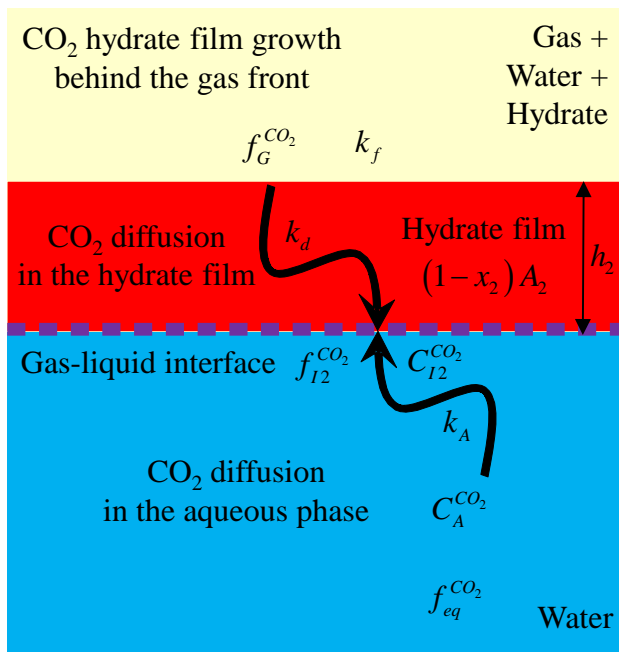
Fig. 2- 18 The schematic diagram of hydrate film growth behind the gas front

Likewise, the equations above can also describe CO_2 diffusion in the aqueous phase in both two directions behind the gas front (the aqueous phase $\rightleftharpoons$ the gas-liquid interface of the hydrate film), as shown in Fig. 2-19.
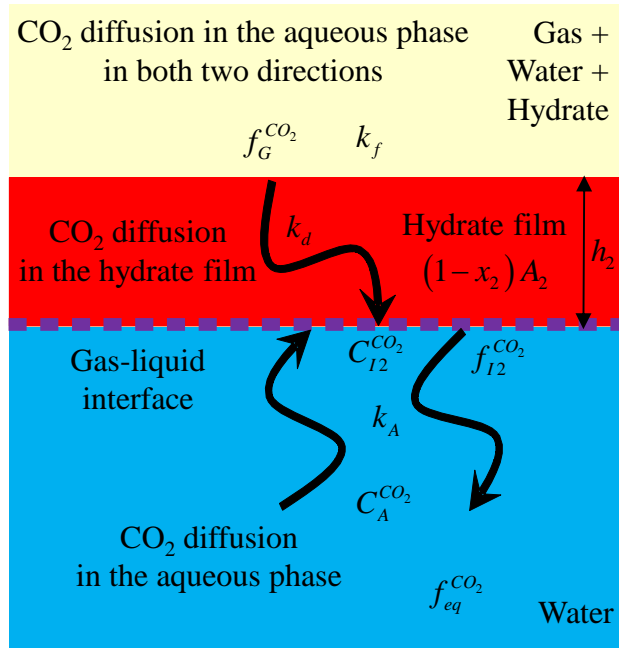
Fig. 2- 19 The schematic diagram of CO_2 diffusion in the aqueous phase in both two directions behind the gas front

2.2.2.3 Hydrate formation rate on the surface of the sand particles behind the gas front

As shown in Fig. 2-20, hydrate forms on the surface of the sand particles behind the gas front from two different parts: one is dissolved CO_2 in the aqueous phase, and the other one is the part of hydrate captured by the sand particles as mentioned in Section 2.2.2.1. Therefore, Q_{H3} is given as below:

$$Q_{H3} = M_H k_f A_S \left(f_A^{CO_2} - f_{eq}^{CO_2} \right) + \delta Q_{H1 \to 3} ,$$

(2-62)

where $f_A^{CO_2}$ is CO_2 fugacity in the aqueous phase [Pa].
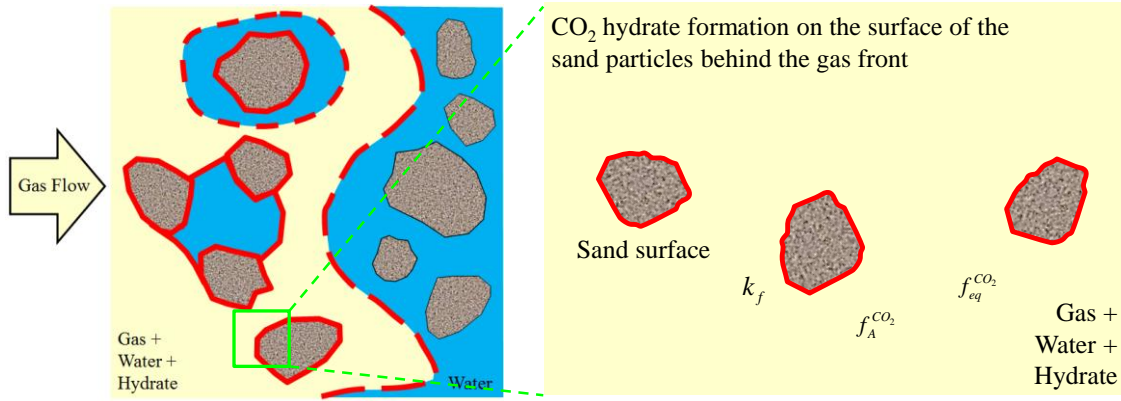
Fig. 2- 20 The schematic diagram of hydrate formation morphologies on the surface of the sand particles behind the gas front

2.2.3 Modified permeability reduction model

After CO_2 hydrate forms in the sand sediment, the flow resistance increases due to the existence of the solid hydrate in the pore space. In this study, the increase of the flow resistance induced by hydrate formation is represented by the permeability reduction of the sand sediment in appearance. However, since hydrate formation morphologies are classified by locations in this study: i.e. on the gas front, on the hydrate film, and on the surface of the sand particles behind the gas front, it is considered that CO_2 hydrate formation with different morphologies should have different contributions to the permeability reduction. Therefore, a modified permeability reduction model is proposed as below:

$$k_S = k_{S,0} K_{H1} K_{H2} K_{H3},$$ (2-63)

where $k_{S,0}$ is the absolute permeability of the sand sediment without hydrate [m²], and K_{H1}, K_{H2}, and K_{H3} are the permeability reduction coefficients of hydrate formation on the gas front, on the hydrate film, and on the surface of the sand particles behind the gas front [-], respectively.

Because CO_2 hydrate film on the gas front is assumed to be very thin, it is considered that CO_2 hydrate formation on the gas front has no influence on the permeability reduction, and the permeability reduction coefficient K_{H1} is given by

$$K_{H1} = 1.$$ (2-64)

Because CO_2 hydrate on the hydrate film behind the gas front is likely to form between the sand particles or in the pore space of the sand sediment, it is considered to have a great effect on the permeability reduction. For the calculation of the permeability reduction coefficient K_{H2}, the model proposed by Masuda et al. [2-17] is adopted in this study as below:

$$K_{H2} = (1 - S_{H2})^N,$$ (2-65)

where N is the permeability reduction exponent of hydrate formation behind the gas front [-], which is usually treated as an unknown parameter in the previous studies (Inui et al. [1-11], Nakashima [1-20], etc.). In this study, it will be determined by parameter-fitting.

Because CO_2 hydrate on the surface of the sand particles behind the gas front is only considered to coat the sand particle and become part of it, it is supposed to have less effect on the permeability reduction. For the calculation of the permeability reduction coefficient K_{H3}, the following method is introduced in this study.

First, it is assumed that hydrate only forms on the surface of the sand particles in a computational cell. After hydrate formation, the porosity of the cell changes from ϕ to ϕ^* because solid hydrate occupies the pore space of the sand sediment, as shown in Fig. 2-21. The relationship between ϕ and ϕ^* can be described as below:

$$\phi^* = \phi(1 - S_{H3}),$$ (2-66)

where S_{H3} is CO_2 hydrate saturation on the surface of the sand particles behind the gas front, which can be calculated as below:

$$S_{H3} = S_H - S_{H1} - S_{H2}.$$ (2-67)

On the other hand, the sand surface area also changes from A_S to A_S^* after hydrate formation, and the relationship between them can be described as below:

$$A_S^* = A_S \left(\frac{1-\phi^*}{1-\phi} \right)^{\frac{2}{3}} = A_S \left[\frac{1-\phi(1-S_{H3})}{1-\phi} \right]^{\frac{2}{3}}. \tag{2-68}$$

Therefore, the permeability reduction coefficient K_{H3} can be calculated by the permeability change before and after hydrate formation: i.e. $k_{S,0}$ and k_S, using Kozeny and Carman model [2-12] as below:

$$K_{H3} = \frac{k_S}{k_{S,0}} = \frac{\frac{c_K \phi^{*3}}{A_S^{*2}}}{\frac{c_K \phi^3}{A_S^2}} = \left(\frac{\phi^*}{\phi} \right)^3 \left(\frac{A_S}{A_S^*} \right)^2 = (1-S_{H3})^3 \left[\frac{1-\phi}{1-\phi(1-S_{H3})} \right]^{\frac{4}{3}}, \tag{2-69}$$

where c_K is Kozeny coefficient [-].

Before hydrate formation on the surface of the sand particles
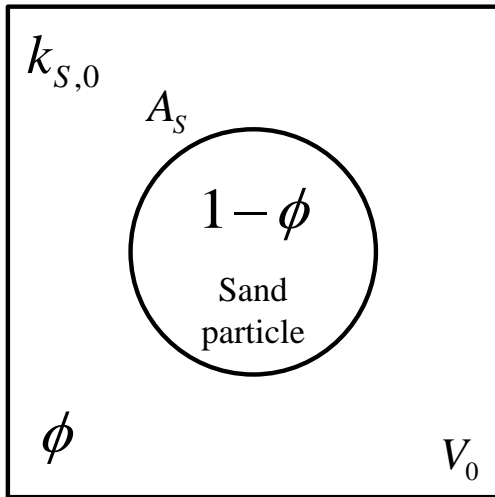
After hydrate formation on the surface of the sand particles
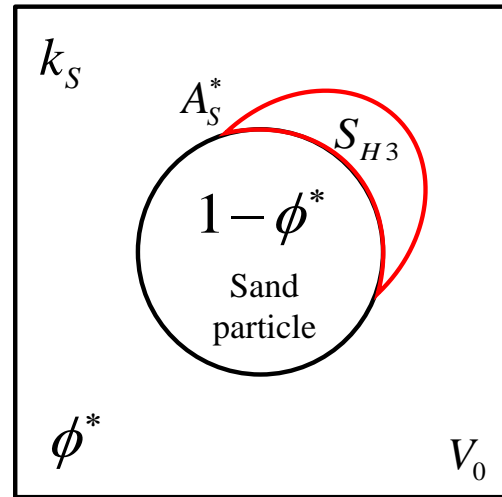
Fig. 2- 21 The schematic diagram for the determination of permeability reduction coefficient of hydrate formation on the surface of the sand particles behind the gas front K_{H3}

2.3 Summary

In this chapter, governing equations and models used for gas-liquid two-phase flow and CO_2 hydrate formation in the numerical simulator, especially the inclusive model for CO_2 hydrate formation, have been described in detail.

In the next chapter, numerical simulations of gas-liquid two-phase flow and CO_2 hydrate formation in the sand sediment will be conducted in order to determine the unknown parameters in the models.

3 DETERMINATION OF MODEL PARAMETERS

As mentioned in Chapter 2, there are several model parameters in the numerical simulator which have been treated as unknown parameters in this study. In this chapter, these unknown parameters are determined by parameter-fitting comparing with the experimental data.

3.1 CO₂ Hydrate Formation without Gas-liquid Two-phase Flow

In this section, experiments of CO_2 hydrate formation in the lab-scale sand sediment without gas-liquid two-phase flow carried out by Inui [1-18] are introduced at first. Then, based on the experiments, simulations of CO_2 hydrate formation in the sand sediment without gas-liquid two-phase flow under the experimental conditions are conducted using the numerical simulator. Finally, unknown parameters are determined by comparing the simulation results with the experimental data.

3.1.1 Experiment outline of CO₂ hydrate formation without gas-liquid two-phase flow

In order to determine the intrinsic rate constant of CO_2 hydrate formation k_f and CO_2 diffusion constant in the hydrate film k_d, which are both important parameters in the inclusive model for CO_2 hydrate formation as mentioned in Section 2.2.2, experiments of CO_2 hydrate formation in the lab-scale sand sediment without gas-liquid two-phase flow were conducted by Inui [1-18]. For the easy understanding of this study, the experiment outline is introduced in brief as below.

3.1.1.1 Experimental apparatus and procedures

The experimental apparatus used by Inui [1-18] was the same as that used by Sakamoto et al. [2-5], which mainly consisted of a reaction vessel, a cooling unit, fluid injection and discharge parts. The reaction vessel was made of high-pressure stainless steel with the internal diameter of 50 mm and the depth of 200 mm. Besides, one thermocouple was placed at the center of the reaction vessel in order to measure the temperature change in the sand sediment with time. The schematic diagram of the experimental apparatus is shown in Fig. 3-1.
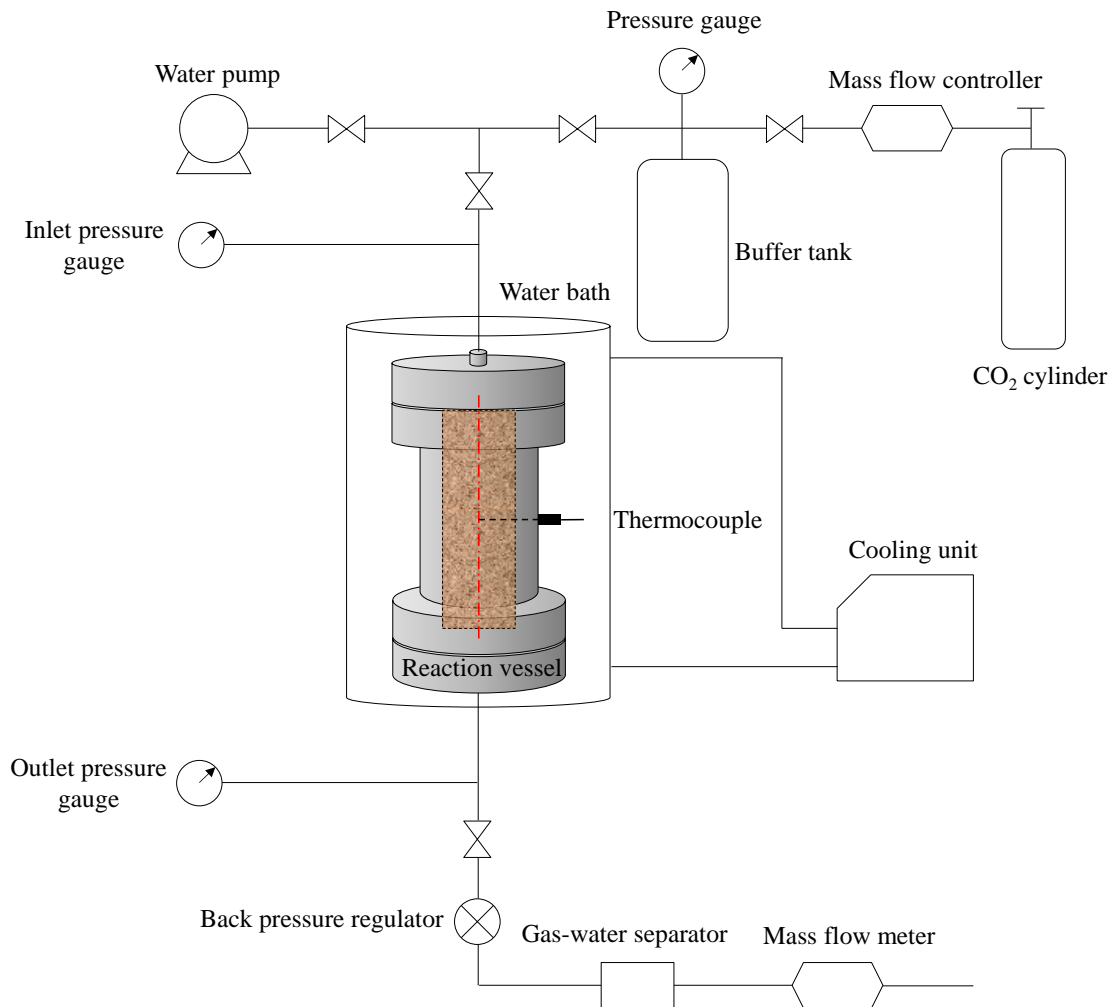
Fig. 3- 1 The schematic diagram of the experimental apparatus for CO_2 hydrate formation in the sand sediment without gas-liquid two-phase flow [1-18]

The experimental procedures are summarized in brief according to Inui [1-18], with the illustration of the experimental apparatus as below.

1) First, water-saturated sand sediment was prepared by filling Toyoura sand and pure water into the reaction vessel. Besides, in order to eliminate the air bubbles inside the sand sediment, the reaction vessel was beaten lightly with a wooden hammer at the side during the sand filling.

2) After the sand sediment was set up, a certain amount of water was extracted from the outlet of the reaction vessel to set the initial water saturation in the sand sediment as 62%.

3) CO_2 gas was supplied from CO_2 cylinder to the buffer tank in which the pressure was much higher than the experimental value.

4) After adjusting the back pressure regulator to the experimental value, CO_2 gas was supplied from the buffer tank to the reaction vessel until the pressure reached the experimental value.

5) The reaction vessel was bathed in the cooling unit at the experimental temperature, and the experiments were started.

6) CO_2 hydrate formation was confirmed by the temperature rise detected by the thermocouple placed at the center of the reaction vessel.

7) For gas consumption due to hydrate formation, only that part of CO_2 gas was supplied from the buffer tank to the reaction vessel.

8) The pressure in the buffer tank was measured with time during the experiments, and the amount of CO_2 gas consumption was calculated by the pressure drop in the buffer tank.

9) After 12 hours since hydrate formation, one cycle of the experiments was completed.

3.1.1.2 Initial experimental conditions

The initial pressure and temperature conditions for five experimental cases – Case 1 ~ Case 5 are listed in Table 3-1.

Table 3- 1 Initial experimental conditions for Case 1 ~ Case 5 [1-18]

	Initial pressure [MPa]	Initial temperature [K]
Case 1	2.5	275.95
Case 2	3.1	276.05
Case 3	3.1	278.85
Case 4	3.1	278.65
Case 5	3.5	278.65

3.1.2 Simulation outline of CO_2 hydrate formation without gas-liquid two-phase flow

In this section, the simulation outline of CO_2 hydrate formation in the lab-scale sand sediment without gas-liquid two-phase flow is explained in detail, including physical parameters, computational mesh, and initial simulation conditions.

3.1.2.1 Physical parameters

The physical parameters of Toyoura sand, stainless steel (for the reaction vessel), and CO_2 hydrate are listed in Table 3-2.

Table 3- 2 Physical parameters of each material

	Density [kg/m^3]	Specific heat [J/kg/K]	Thermal conductivity [W/m/K]
Toyoura sand	2.65×10^3	8.0×10^2	7.0
Stainless steel	7.85×10^3	4.8×10^2	15.0
CO_2 hydrate	1.11×10^3	2.1×10^3	0.49

For the physical parameters of Toyoura sand, the values used by Konno et al. [3-1] and Ikegawa [3-2] are adopted in this study. For the stainless steel, the values are obtained from the Chronological Scientific Tables [2-9]. Besides, the density of CO_2 hydrate is given by Aya et al. [3-3], and the specific heat and the thermal conductivity refer to the values of methane hydrate (Gupta et al. [3-4]).

3.1.2.2 Computational mesh

The computational mesh used for numerical simulations of CO_2 hydrate formation without gas-liquid two-phase flow in this study is designed as an axisymmetric cylinder with the radius of 25 mm and the height of 200 mm, simulating the lab-scale sand sediment. Along the radial direction, it is divided into 17 cells, of which 16 cells have a length of 1.5 mm, and 1 cell has a length of 1.0 mm (only for the outermost cell). On the other hand, along the height direction, it is divided into 100 cells equally with a height of 2.0 mm.

Besides, a thin layer of cells which represents the stainless steel is placed around the cells of the calculation domain either with a length of 0.1 mm or a height of 0.1 mm, respectively. The pressure and temperature in these cells are set to be constant, and cannot change with time in order to simulate the reaction vessel bathed in the cooling unit. Therefore, a total number of 1836 cells (18 cells in the radial direction and 102 cells in the height direction) is used for the computational mesh in Case 1 ~ Case 5. The schematic diagram of the computational mesh is shown in Fig. 3-2.
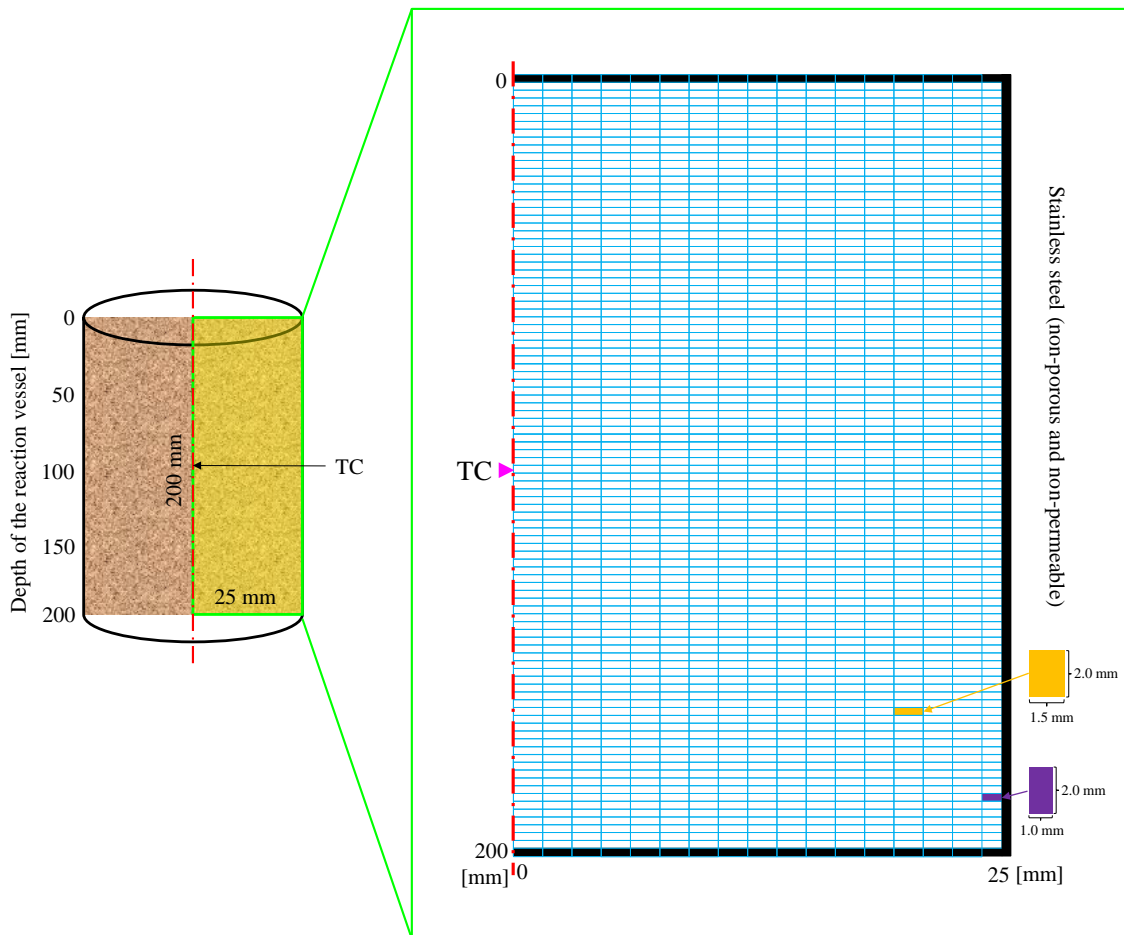
Fig. 3- 2 The schematic diagram of the computational mesh for CO_2 hydrate formation without gas-liquid two-phase flow

3.1.2.3 Initial simulation conditions

As mentioned before, the initial water saturation of the sand sediment is set as 0.62 m^3/m^3 in the simulation. In addition, the solubility of CO_2 gas in the aqueous phase is set to be the saturated concentration at the experimental pressure and temperature conditions in advance.

Besides, the porosity and absolute permeability of the sand sediment are determined by the average values of the experimental data obtained by Sakamoto et al. [2-5] using the same Toyoura sand, set as 0.356 and 1.78×10^{-11} m^2, respectively, in this study. However, the boundary cells which represent the stainless steel are considered to be non-porous and non-permeable: i.e. the porosity and absolute permeability are both set as 0 in this study. In addition, as mentioned before, since the reaction vessel is bathed in the cooling unit at the experimental temperature, the temperature of the boundary cells is assumed to be constant and cannot change with time, which

is set to be the initial temperature invariably during the simulation.

On the other hand, in this study, with the severe change of pressure and temperature, physical and chemical behaviors in the sand sediment, such as hydrate formation rate, CO_2 gas dissolution rate and so on, may also change significantly during the simulation. In order to reproduce these complicated phenomena, the time step in the iterative process of the implicit method needs to be determined properly in the calculations. Therefore, the time step is set to be variable in this study. In the case of convergence within 4 iteration loops, the time step becomes 2 times automatically. On the contrary, if the calculations cannot be convergent within 20 iteration loops, the time step is reduced to 1/4 automatically. Besides, the initial time step is set as 0.01 s, and the total calculation time is set as 1000 s in Case 1 ~ Case 5.

3.1.3 Simulation results and discussions

In this section, numerical simulations of CO_2 hydrate formation in the lab-scale sand sediment without gas-liquid two-phase flow are conducted in order to determine the intrinsic rate constant of CO_2 hydrate formation k_f and CO_2 diffusion constant in the hydrate film k_d, as introduced in Chapter 2 by comparing the calculation results with the experimental data.

3.1.3.1 Sensitivity analysis on unknown parameters for CO_2 hydrate formation

For the calculation of hydrate formation rate in the sand sediment, the inclusive model as proposed in Equation (2-24) is adopted in this study. However, since there is no gas-liquid two-phase flow in the sand sediment, the movable gas front doesn't exist. Therefore, it is considered that $\delta = 0$ is for no movable gas front, and Equation (2-24) can be simplified as below:

$$Q_H = Q_{H2} + Q_{H3}, \tag{3-1}$$

where Q_{H2} and Q_{H3} proposed in Equation (2-54) and (2-62) can also be simplified as below:

$$Q_{H2} = M_H k_f x_2 A_2 \left(f_G^{CO_2} - f_{eq}^{CO_2} \right) + M_H k_f \left(1 - x_2 \right) A_2 \left(f_{I2}^{CO_2} - f_{eq}^{CO_2} \right), \tag{3-2}$$

$$Q_{H3} = M_H k_f A_S \left(f_A^{CO_2} - f_{eq}^{CO_2} \right). \tag{3-3}$$

In order to determine k_f and k_d, numerical simulations are conducted under different experimental conditions, as listed in Table 3-1 for Case 1 ~ Case 5. Besides, since the rupture ratio on the hydrate film x_2 also plays an important part in the hydrate formation rate on the hydrate film behind the gas front, the coefficient β in Equation (2-57) is treated as a third unknown parameter in this study, which will be determined by parameter-fitting with experimental data as same as k_f and k_d.

First, preliminary simulations are conducted in order to understand the difference between the calculation results and the experimental data, and predict the ranges of the unknown parameters. Then, accurate simulations are conducted in order to carry out the sensitivity analysis, and obtain the optimum values for the unknown parameters.

Since the variation trends are found to be almost the same in Case 1 ~ Case 5 by changing the values of the unknown parameters, only the calculation results of Case 1 are used as an example to conduct the sensitivity analysis on unknown parameters for CO_2 hydrate formation. As a result, the fitting parameters of k_f (5.0×10^{-10} mol/m^2/Pa/s, 5.0×10^{-9} mol/m^2/Pa/s, and 5.0×10^{-8} mol/m^2/Pa/s), k_d (5.0×10^{-19} mol/m/Pa/s, 5.0×10^{-18} mol/m/Pa/s, and 5.0×10^{-17} mol/m/Pa/s), and β (5.0×10^{12} m^{-2}, 5.0×10^{13} m^{-2}, and 5.0×10^{14} m^{-2}): i.e. total seven combinations of Case 1A ~ Case 1G are selected in this study. The simulation conditions for the sensitivity analysis on unknown parameters for CO_2 hydrate formation in Case 1are listed in Table 3-3.

In addition, the comparisons between the calculation results and the experimental data in Case 1A ~ Case 1G are shown in Fig. 3-3 ~ Fig. 3-9, respectively. For all these figures, the first ones represent the temperature change detected at the center of the reaction vessel, and the second ones represent the amount of CO_2 gas consumption due to hydrate formation, respectively.

Table 3-3　The simulation conditions for the sensitivity analysis on unknown parameters for CO_2 hydrate formation in Case 1

| | | k_f [mol/m^2/Pa/s] | | |
		5.0×10^{-10}	5.0×10^{-9}	5.0×10^{-8}
k_d [mol/m/Pa/s] $(\beta = 5.0 \times 10^{13})$	5.0×10^{-19}		Case 1D	
	5.0×10^{-18}	Case 1A	Case 1B	Case 1C
	5.0×10^{-17}		Case 1E	
β [m^{-2}] $(k_d = 5.0 \times 10^{-18})$	5.0×10^{12}		Case 1F	
	5.0×10^{13}	(Case 1A)	(Case 1B)	(Case 1C)
	5.0×10^{14}		Case 1G	

① Sensitivity analysis on the intrinsic rate constant of CO_2 hydrate formation k_f

　As shown in Case 1A (Fig. 3-3), Case 1B (Fig. 3-4), and Case 1C (Fig. 3-5), k_f is varied from 5.0×10^{-10} mol/m^2/Pa/s to 5.0×10^{-8} mol/m^2/Pa/s, while k_d and β are fixed at 5.0×10^{-18} mol/m/Pa/s and 5.0×10^{13} m^{-2}, respectively. From the first figures, it can be seen that with the increase of k_f, the temperature change detected at the early stage of CO_2 hydrate formation becomes much more obvious. On the other hand, as shown in the second figures, the amount of CO_2 gas consumption due to hydrate formation increases during the whole period, but the increasing extent at the early stage is much more significant than that at the late stage, which means k_f mainly has a great effect on CO_2 hydrate formation at the early stage.

② Sensitivity analysis on CO_2 diffusion constant in the hydrate film k_d

　As shown in Case 1B (Fig. 3-4), Case 1D (Fig. 3-6), and Case 1E (Fig. 3-7), k_d is varied from 5.0×10^{-19} mol/m/Pa/s to 5.0×10^{-17} mol/m/Pa/s, while k_f and β are fixed at 5.0×10^{-9} mol/m^2/Pa/s and 5.0×10^{13} m^{-2}, respectively. From the first figures, it can be seen that with the increase of k_d, the temperature during the whole period, especially at the late stage, also increases obviously. Besides, for the amount of CO_2 gas consumption due to hydrate formation, the calculation result is much smaller than the experimental data in Case 1D; while in Case 1E, the calculation result exceeds the experimental data significantly, which means k_d mainly has a great effect on CO_2 hydrate formation at the late stage.

③ Sensitivity analysis on the coefficient β in the rupture ratio model behind the gas front

As shown in Case 1B (Fig. 3-4), Case 1F (Fig. 3-8), and Case 1G (Fig. 3-9), β is varied from 5.0×10^{12} m^{-2} to 5.0×10^{14} m^{-2}, while k_f and k_d are fixed at 5.0×10^{-9} mol/m^2/Pa/s and 5.0×10^{-18} mol/m/Pa/s, respectively. From all these figures, it can be seen that with the increase of β, both the temperature detected at the center of the reaction vessel and the amount of CO_2 gas consumption due to hydrate formation drop sharply. The reason is that the rupture ratio x_2 may drop too sharply at the early stage. At the early stage, CO_2 hydrate is more likely to form at the fresh surface of the gas-liquid interface rather than on the existing hydrate film, resulting in the obvious temperature rise. Then, with the decrease of x_2, the growth of the hydrate film becomes dominant, whose rate is much smaller than that at the fresh surface, so the temperature drops gradually at the late stage. However, if β is set to be too large as shown in Case 1G, x_2 drops sharply, depressing CO_2 hydrate formation at the fresh surface which has a great contribution to the temperature rise at the early stage. On the contrary, if β is set to be a smaller value as shown in Case 1F, x_2 drops much more slowly, causing CO_2 hydrate formation at the fresh surface to play an important part during the whole period. The result is that both the calculation results of the temperature change detected at the late stage and CO_2 gas consumption due to hydrate formation exceed the experimental data significantly.

④ Parameter-fitting results and discussions

Based on the sensitivity analysis on the unknown parameters for CO_2 hydrate formation, the optimum values of k_f, k_d, and β are determined as 5.0×10^{-9} mol/m^2/Pa/s, 5.0×10^{-18} mol/m/Pa/s, and 5.0×10^{13} m^{-2}, respectively, as the figures shown in Case 1B where the calculation results are almost consistent with the experimental data.

As can be seen in Fig. 3-4, for the amount of CO_2 gas consumption due to hydrate formation, the calculation result shows good consistency with the experimental data. However, for the temperature change detected at the center of the reaction vessel, the calculation result of the temperature rise at the early stage of CO_2 hydrate formation is not so obvious as the experimental data. One possible reason is that before hydrate formation, CO_2 gas in the reaction vessel might be in the supersaturation state, so at the beginning of CO_2 hydrate formation, the temperature reached a high peak in very short time due to the severe hydrate formation rate. However, the experimental data before CO_2 hydrate formation has been lost, resulting in no way to verify this hypothesis. Therefore, the supersaturation state of CO_2 gas has not been considered during the calculations. Instead, the solubility of CO_2 gas in the aqueous phase is set to be the saturated concentration at the experimental pressure and temperature conditions in advance as mentioned before. Besides, the amount of CO_2 gas consumption due to hydrate formation is fitted

preferentially in this study.
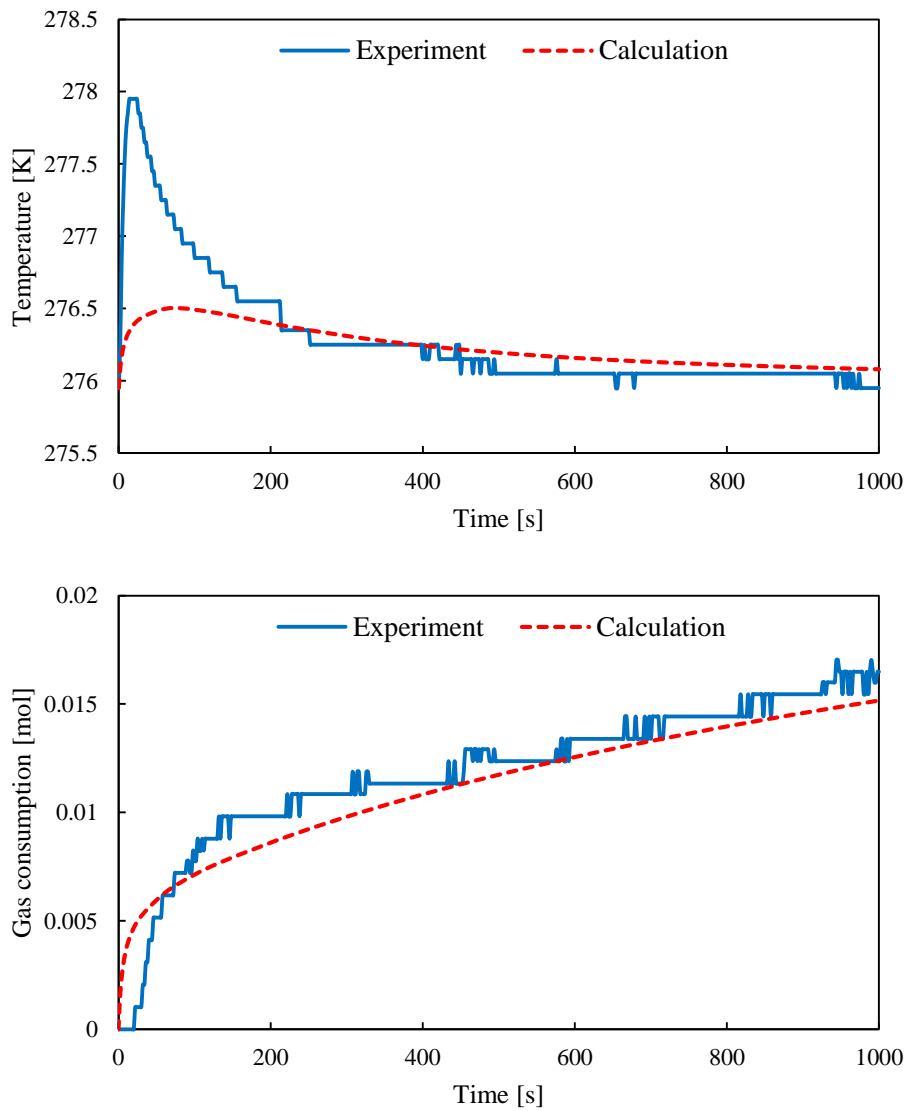
Fig. 3- 3 The comparisons between the calculation results and the experimental data in Case 1A
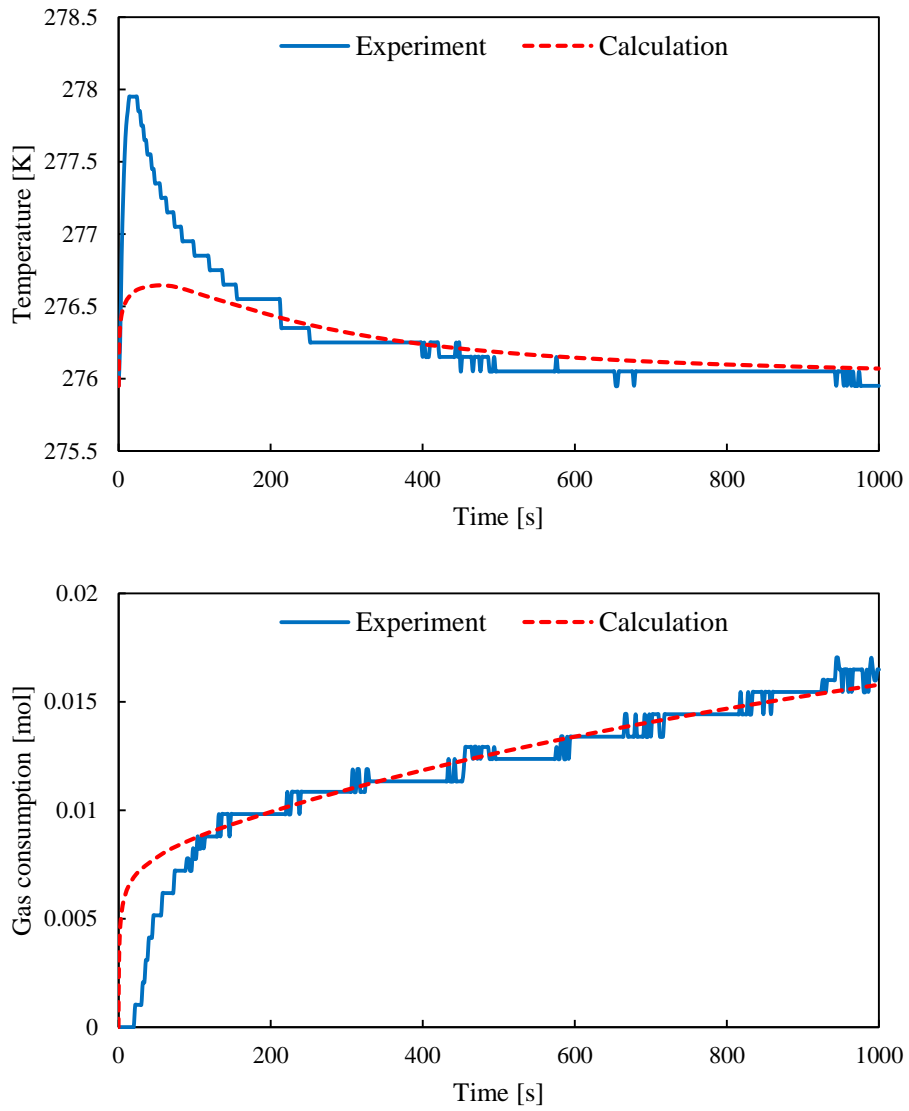
Fig. 3- 4 The comparisons between the calculation results and the experimental data in Case 1B
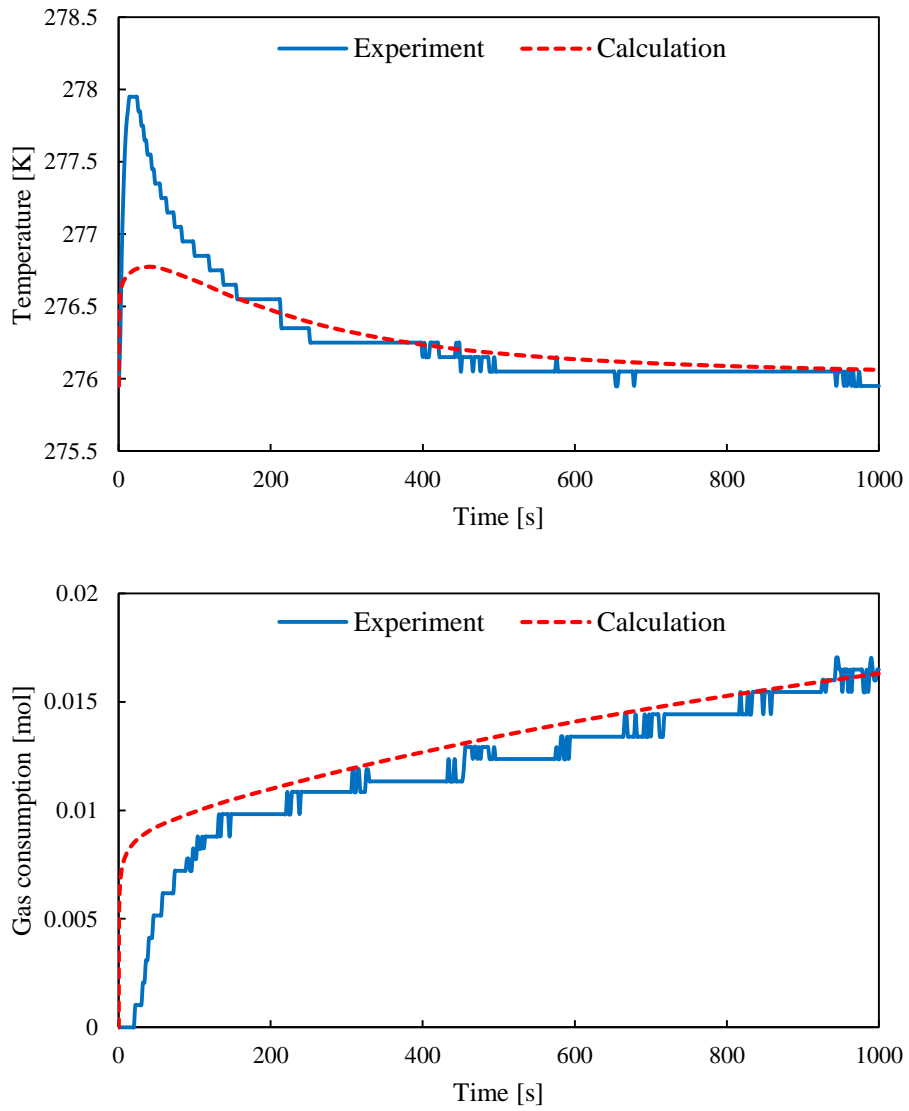
Fig. 3- 5 The comparisons between the calculation results and the experimental data in Case 1C
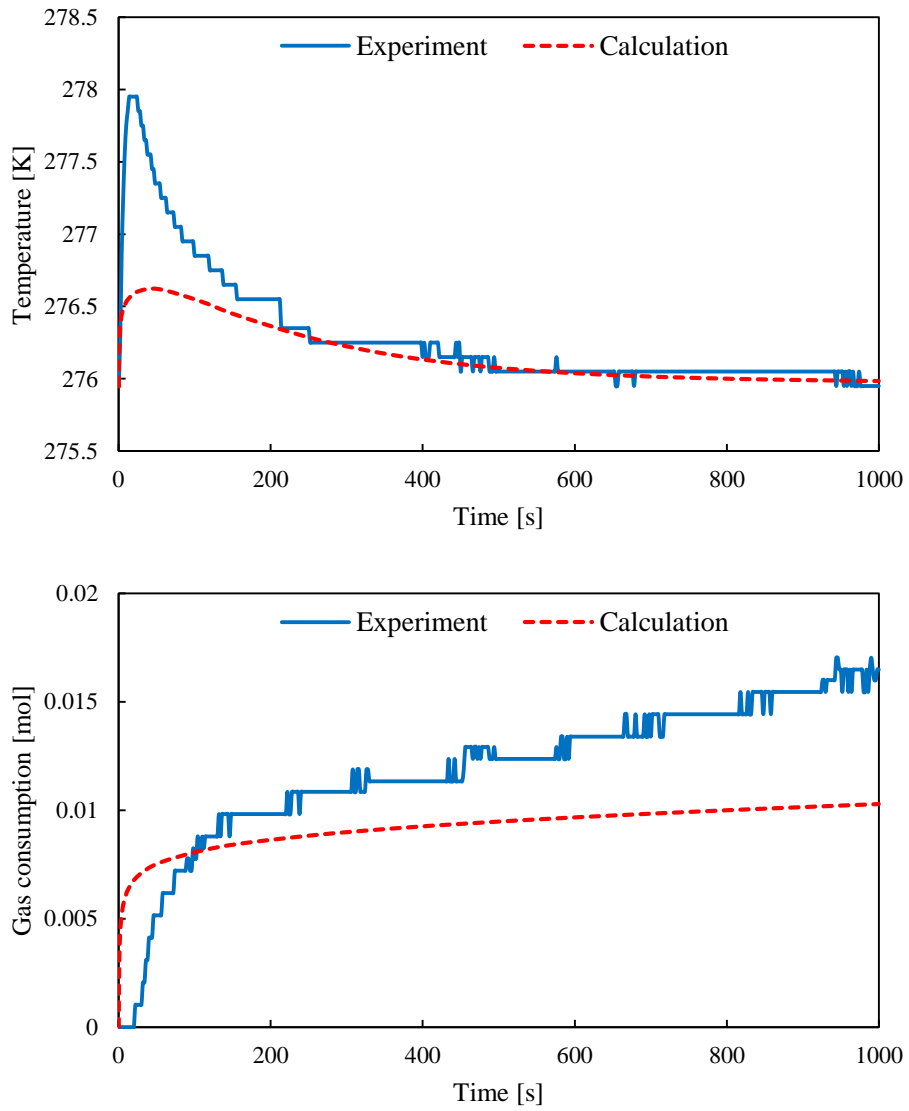
Fig. 3- 6 The comparisons between the calculation results and the experimental data in Case 1D
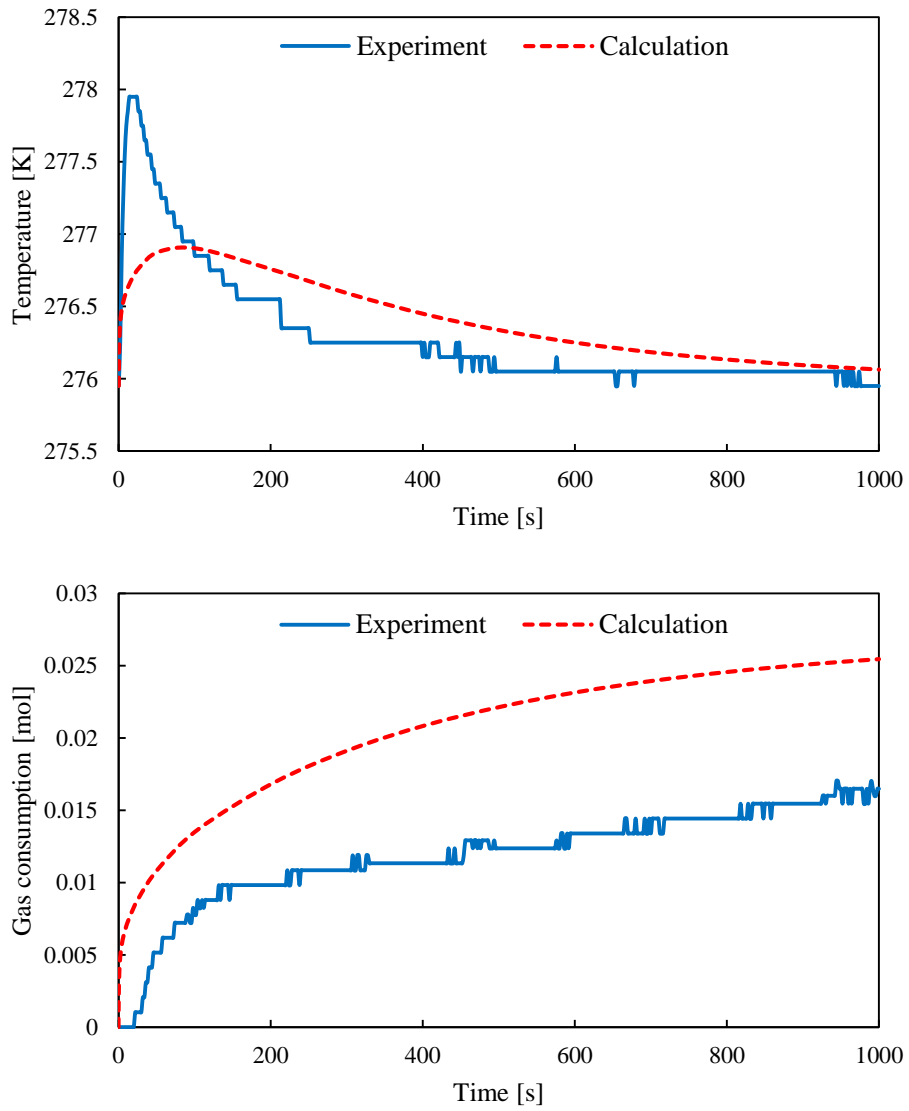
Fig. 3- 7 The comparisons between the calculation results and the experimental data in Case 1E
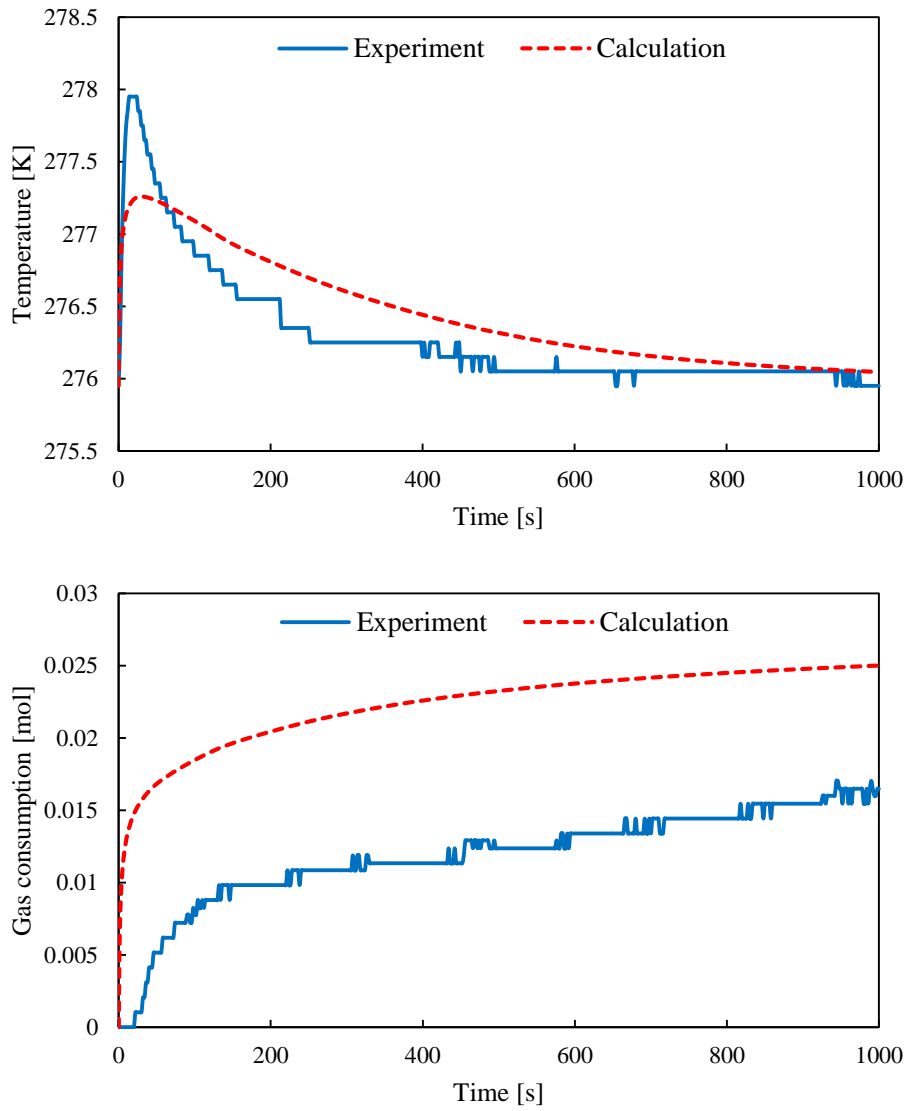
Fig. 3- 8 The comparisons between the calculation results and the experimental data in Case 1F
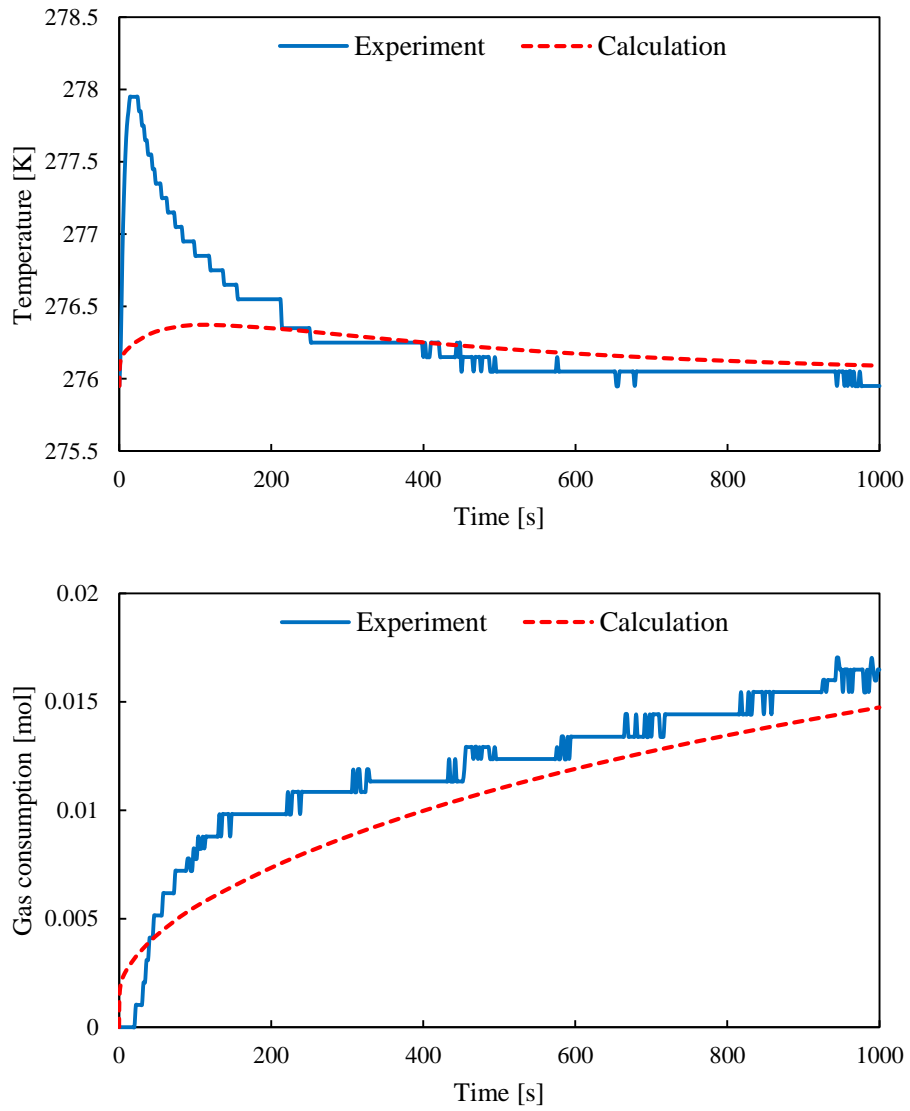
Fig. 3- 9 The comparisons between the calculation results and the experimental data in Case 1G

3.1.3.2 The determination of k_f, k_d, and β

The parameter-fitting results for k_f, k_d, and β in Case 1 ~ Case 5 are listed in Table 3-4. In addition, the fitting curves for the temperature change detected at the center of the reaction vessel, and the amount of CO_2 gas consumption due to hydrate formation are shown in Fig. 3-10 ~ Fig. 3-14, respectively.

Table 3- 4 The parameter-fitting results for k_f, k_d, and β in Case 1 ~ Case 5

	k_f [mol/m^2/Pa/s]	k_d [mol/m/Pa/s]	β [m^{-2}]
Case 1	5.0×10^{-9}	5.0×10^{-18}	5.0×10^{13}
Case 2	1.0×10^{-9}	2.0×10^{-18}	8.0×10^{13}
Case 3	5.0×10^{-9}	5.0×10^{-18}	2.0×10^{13}
Case 4	2.0×10^{-9}	1.0×10^{-18}	1.0×10^{13}
Case 5	5.0×10^{-9}	3.5×10^{-18}	3.0×10^{13}
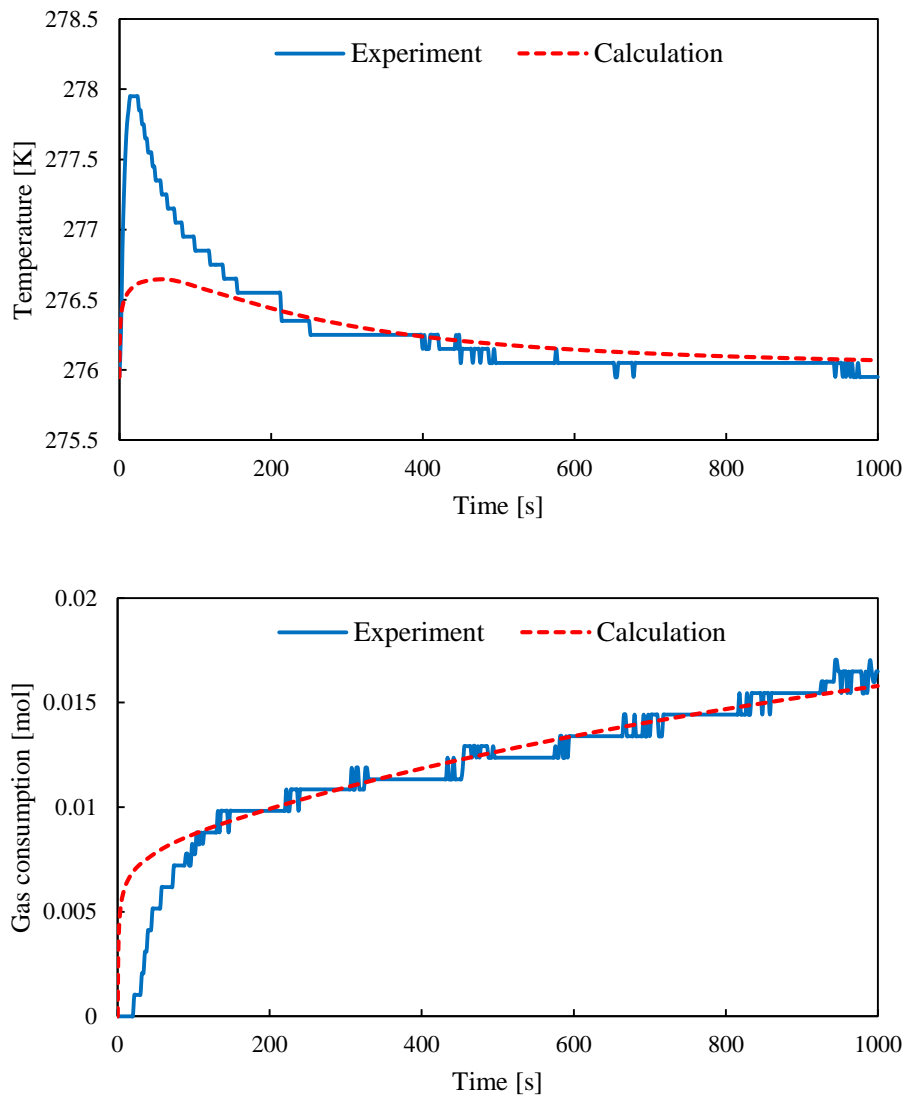
Fig. 3- 10 The fitting curves for the temperature change detected at the center of the reaction vessel, and the amount of CO_2 gas consumption due to hydrate formation in Case 1
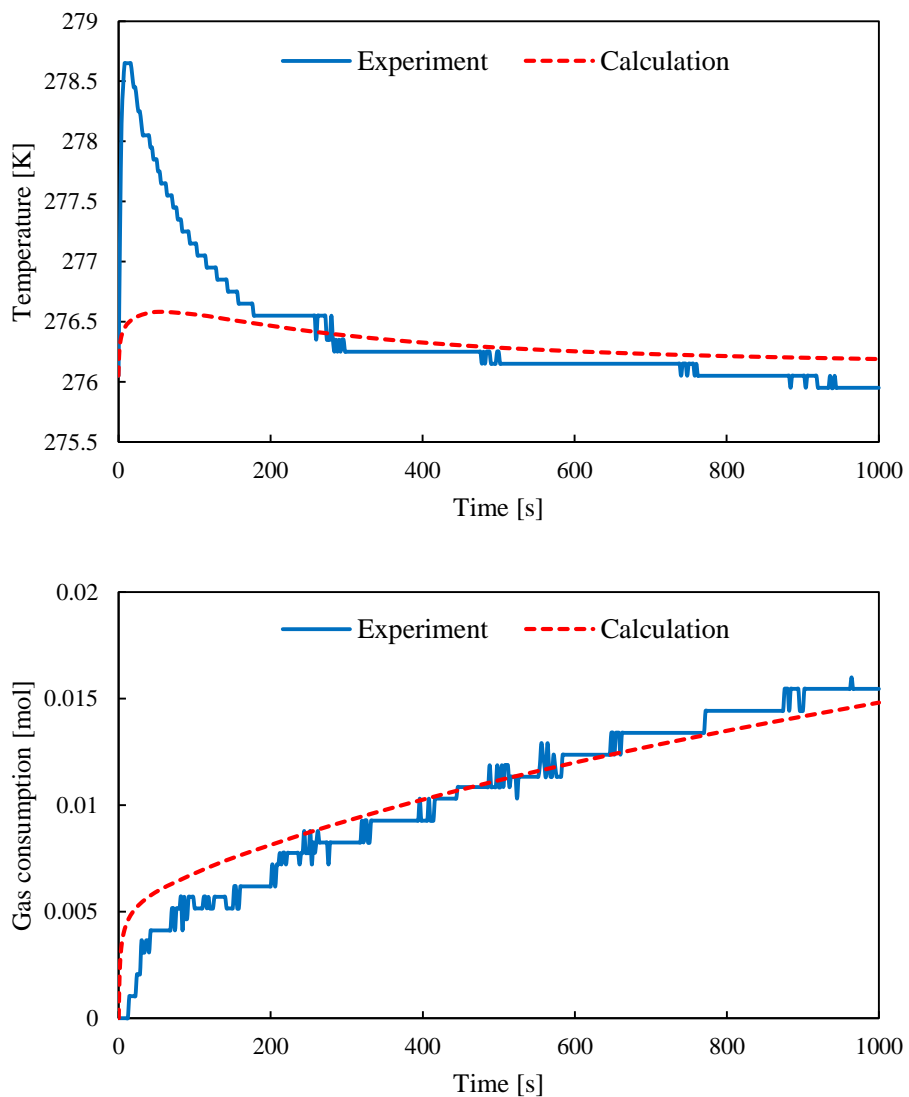
Fig. 3- 11 The fitting curves for the temperature change detected at the center of the reaction vessel, and the amount of CO_2 gas consumption due to hydrate formation in Case 2
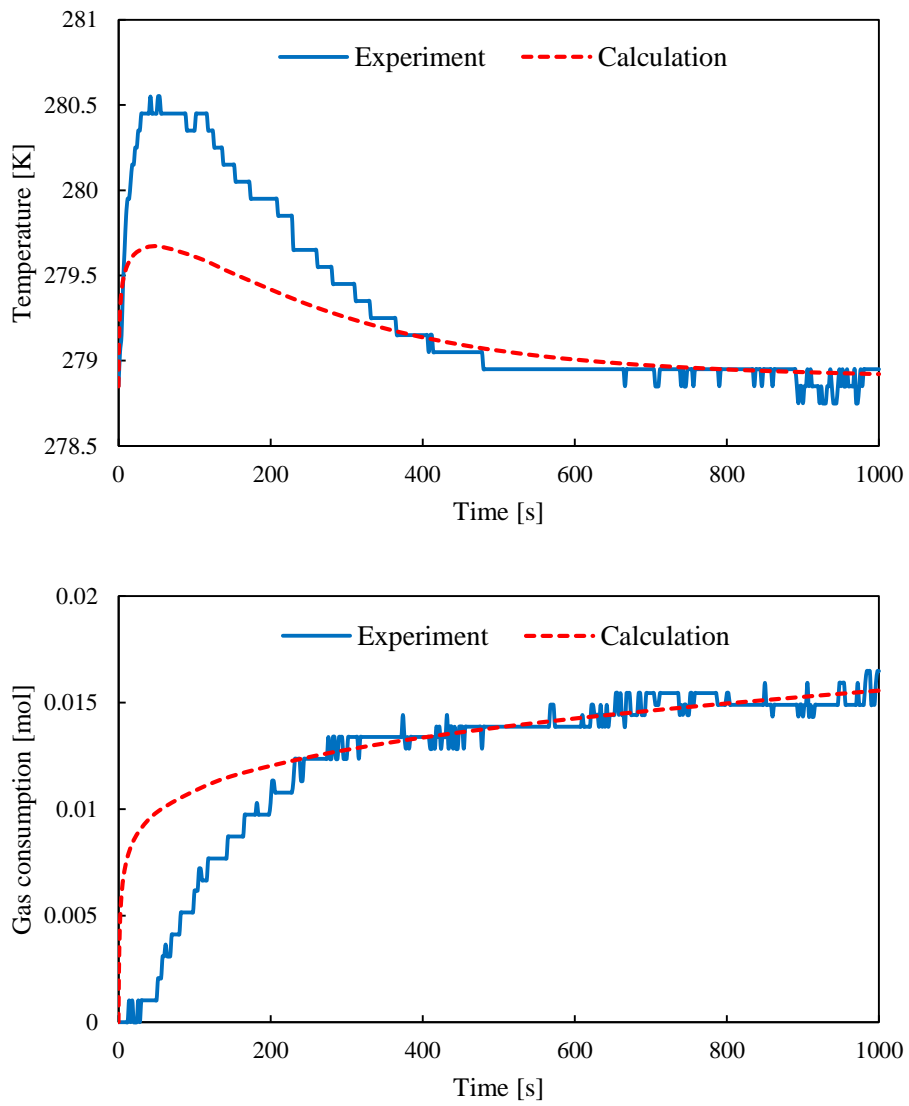
Fig. 3- 12 The fitting curves for the temperature change detected at the center of the reaction vessel, and the amount of CO_2 gas consumption due to hydrate formation in Case 3
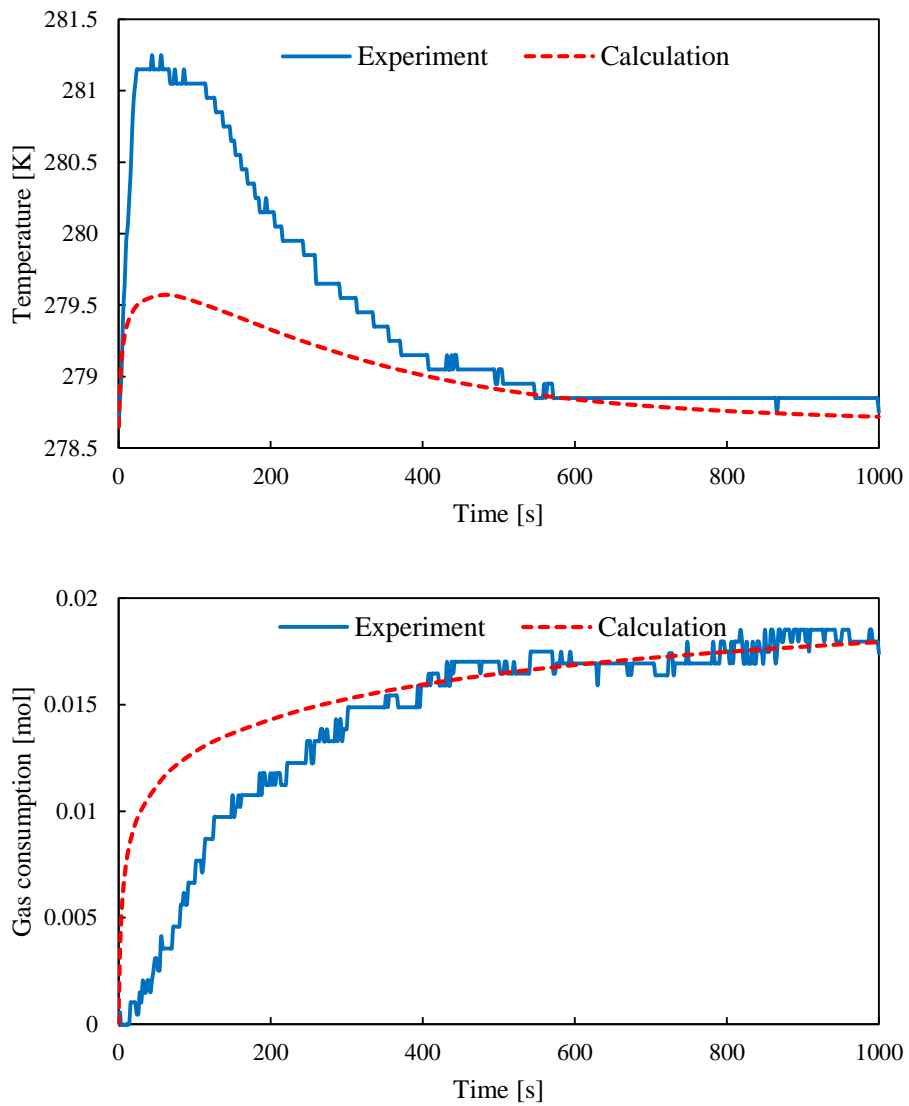
Fig. 3- 13 The fitting curves for the temperature change detected at the center of the reaction vessel, and the amount of CO_2 gas consumption due to hydrate formation in Case 4
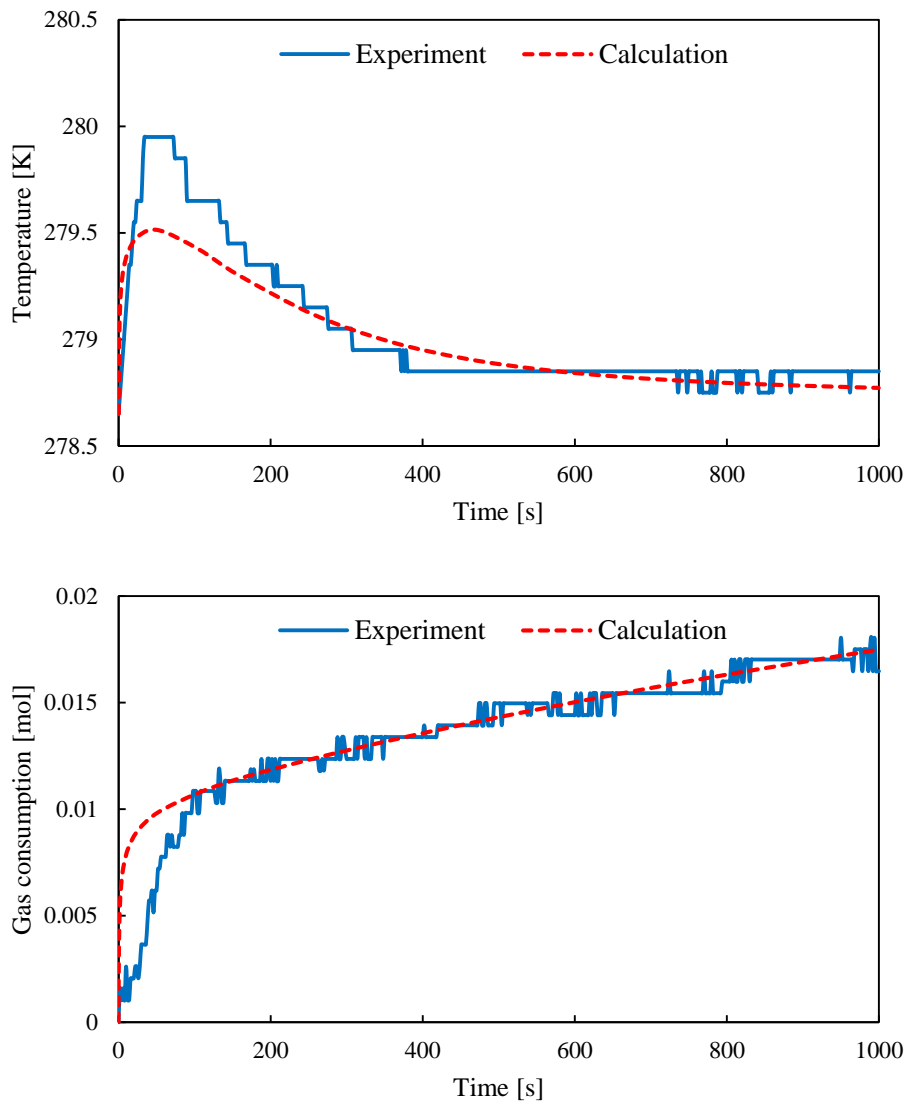
Fig. 3- 14 The fitting curves for the temperature change detected at the center of the reaction vessel, and the amount of CO_2 gas consumption due to hydrate formation in Case 5

For the determination of k_f and k_d, Arrhenius equation is often adopted, which gives the dependence of the rate constant k of a chemical reaction on the absolute temperature T as below:

$$k = k_0 \exp\left(-\frac{\Delta E}{RT}\right), \tag{3-4}$$

where k_0 is the pre-exponential factor [mol/m²/Pa/s], ΔE is the activation energy [J/mol], and R is the universal gas constant [J/mol/K], given as 8.314 J/mol/K. In addition, if the natural logarithm is taken to both sides of Equation (3-4), k_0 and ΔE can be determined by Arrhenius plot, which displays the logarithm of rate constant $\ln k$ plotted against inverse temperature $1/T$ as below:

$$\ln k = \ln k_0 - \frac{\Delta E}{RT}. \tag{3-5}$$

In order to investigate the temperature dependence of k_f and k_d, the fitting results extracted from Case 1 ~ Case 5 are plotted by Equation (3-5), as shown in Fig. 3-15 and Fig. 3-16.
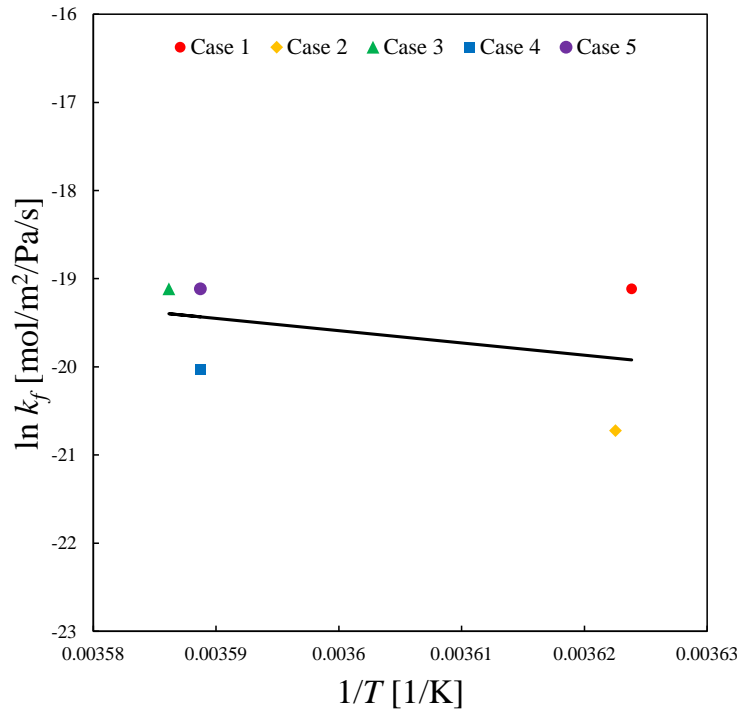
Fig. 3- 15 Arrhenius plot for the intrinsic rate constant of CO_2 hydrate formation k_f

66
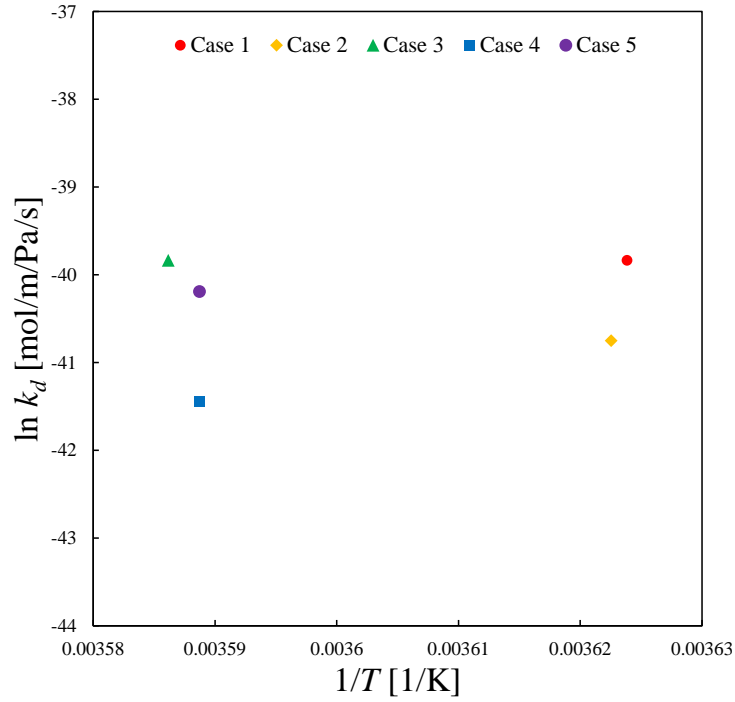
Fig. 3- 16 Arrhenius plot for CO_2 diffusion constant in the hydrate film k_d

As can be seen in Fig. 3-15, the temperature dependence of k_f has been confirmed, with the pre-exponential factor k_0 as 1.73×10^{13} mol/m^2/Pa/s, and the activation energy ΔE as 115.6 kJ obtained from the approximate curve, respectively. Besides, the range of k_f fitted in this study ($1.0 \times 10^{-9} \sim 5.0 \times 10^{-9}$ mol/m^2/Pa/s) shows good consistency with the values fitted by Clark and Bishnoi [3-5] ($3.214 \times 10^{-9} \sim 6.423 \times 10^{-9}$ mol/m^2/Pa/s), which validates the parameter-fitting results in this study. On the other hand, it is assumed that k_d has no temperature dependence, as can be seen in Fig. 3-16, so the average value of k_d in Case 1 ~ Case 5 is adopted in this study, given as 3.30×10^{-18} mol/m/Pa/s. In addition, the rupture ratio model coefficient behind the gas front β under non-flow condition is determined by an order of 10^{13} m^{-2} ($1.0 \times 10^{13} \sim 8.0 \times 10^{13}$ m^{-2}) in this study.

For the validation, numerical simulations using k_f and k_d obtained from Arrhenius plot are re-conducted in Case 1 ~ Case 5, and the validation results are shown in Fig. 3-17 ~ Fig. 3-21, respectively. As can be seen in the figures, the validation results almost agree with the experimental data. Therefore, k_f and k_d obtained in this section will be used in the numerical simulations of CO_2 hydrate formation with gas-liquid two-phase flow in the next section.
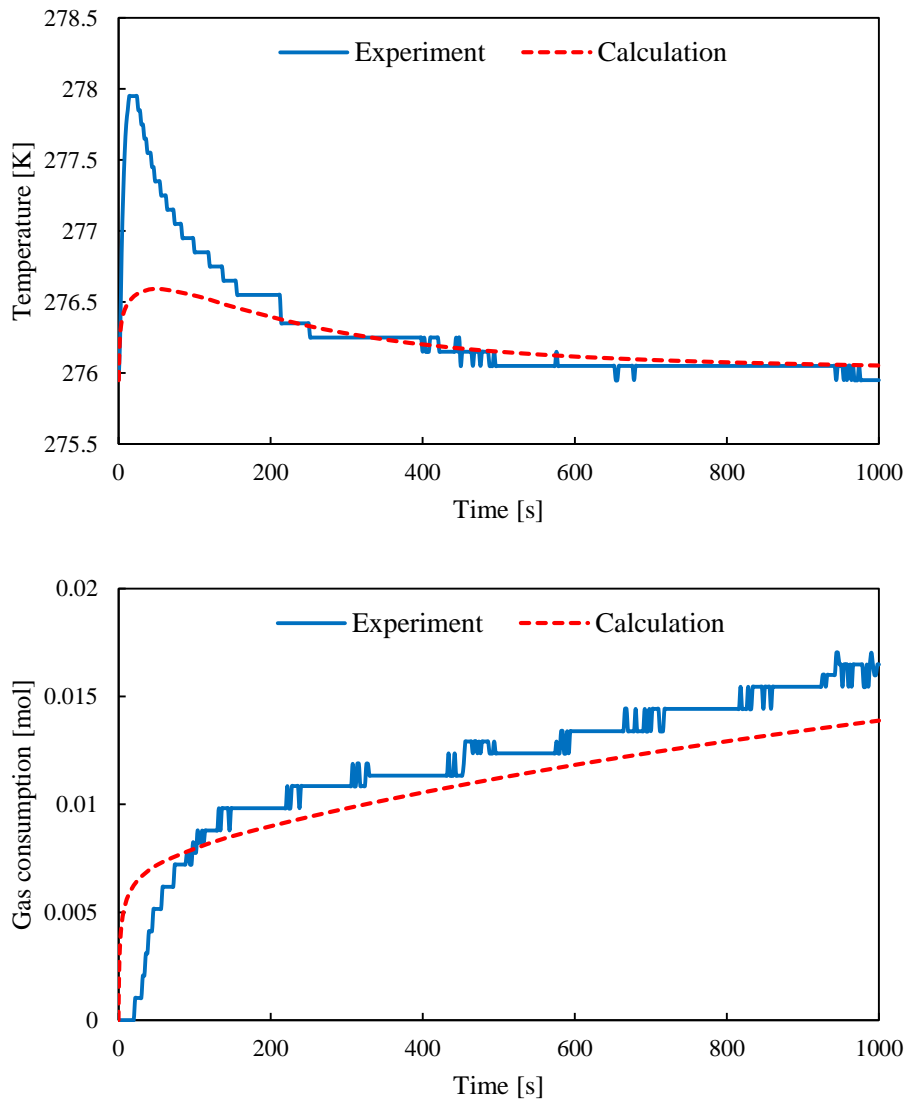
Fig. 3- 17 The validation results using k_f and k_d obtained from Arrhenius plot in Case 1
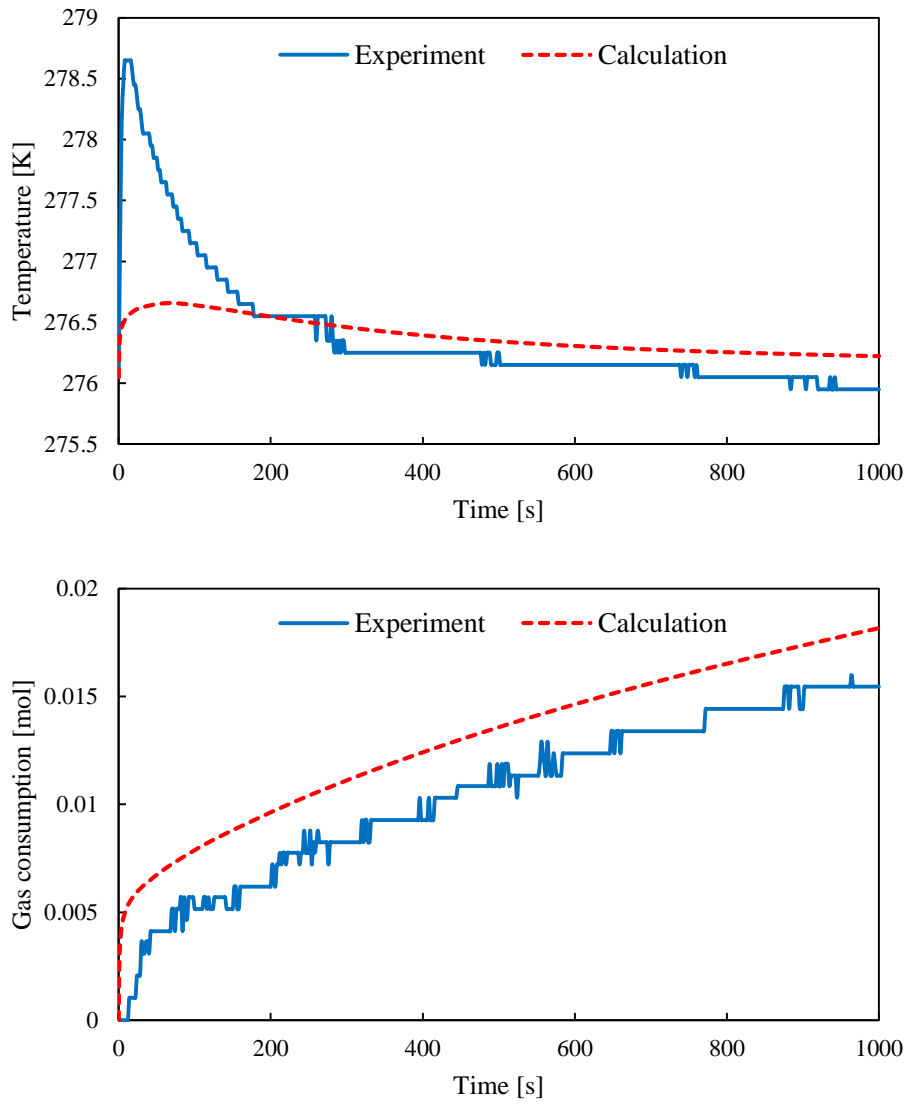
Fig. 3- 18 The validation results using k_f and k_d obtained from Arrhenius plot in Case 2
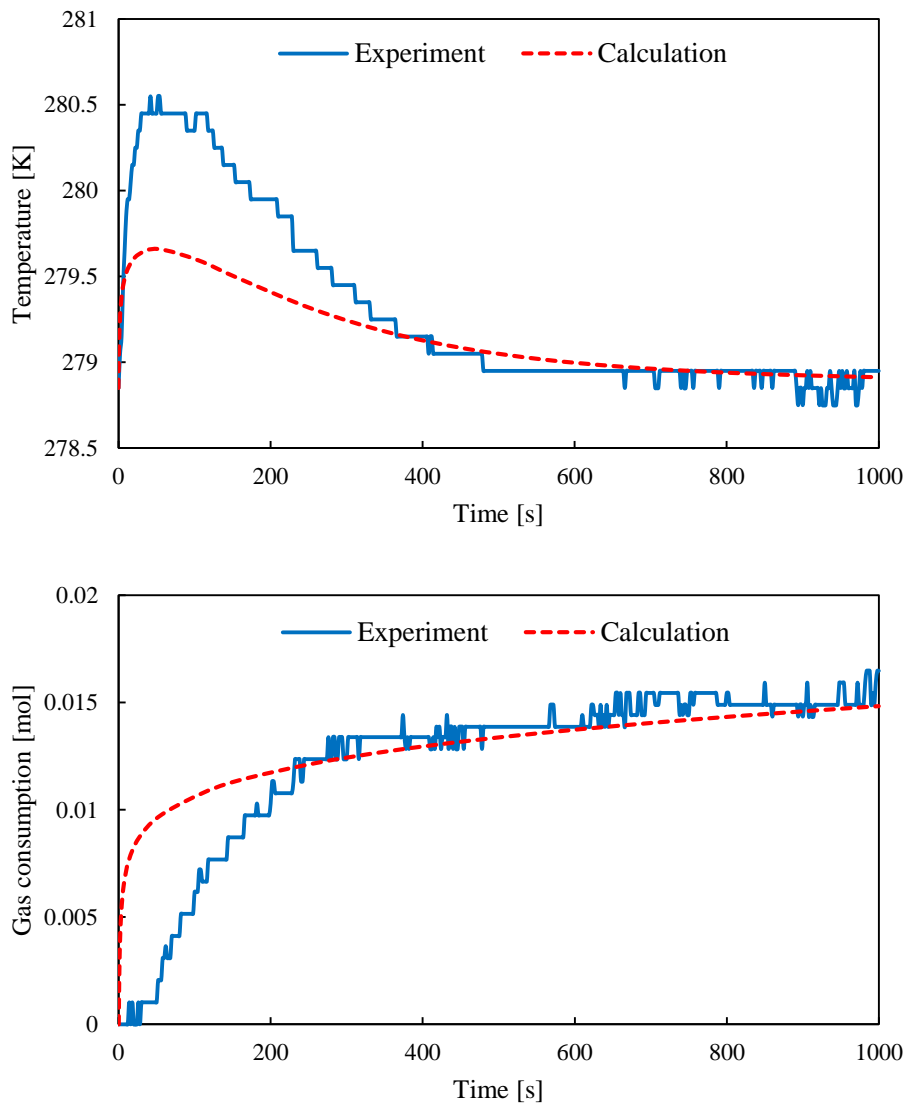
Fig. 3- 19 The validation results using k_f and k_d obtained from Arrhenius plot in Case 3
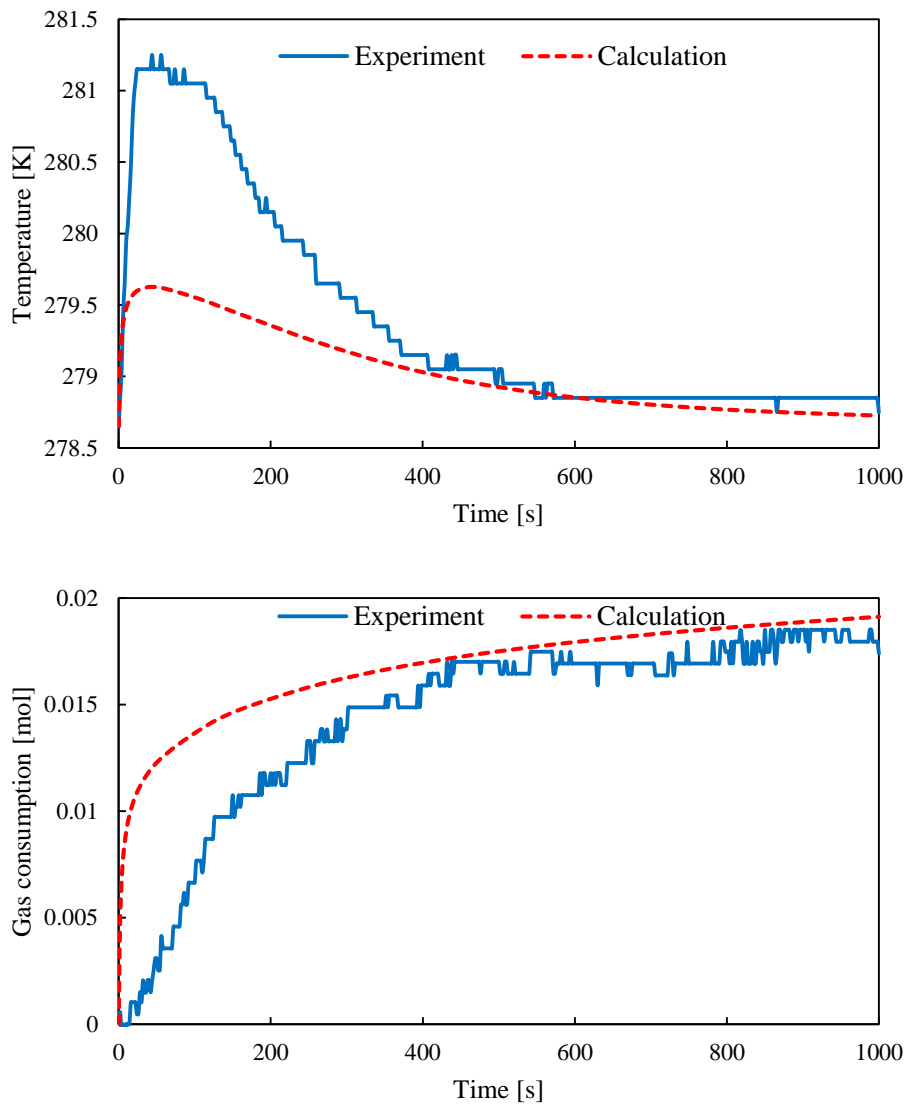
Fig. 3- 20 The validation results using k_f and k_d obtained from Arrhenius plot in Case 4
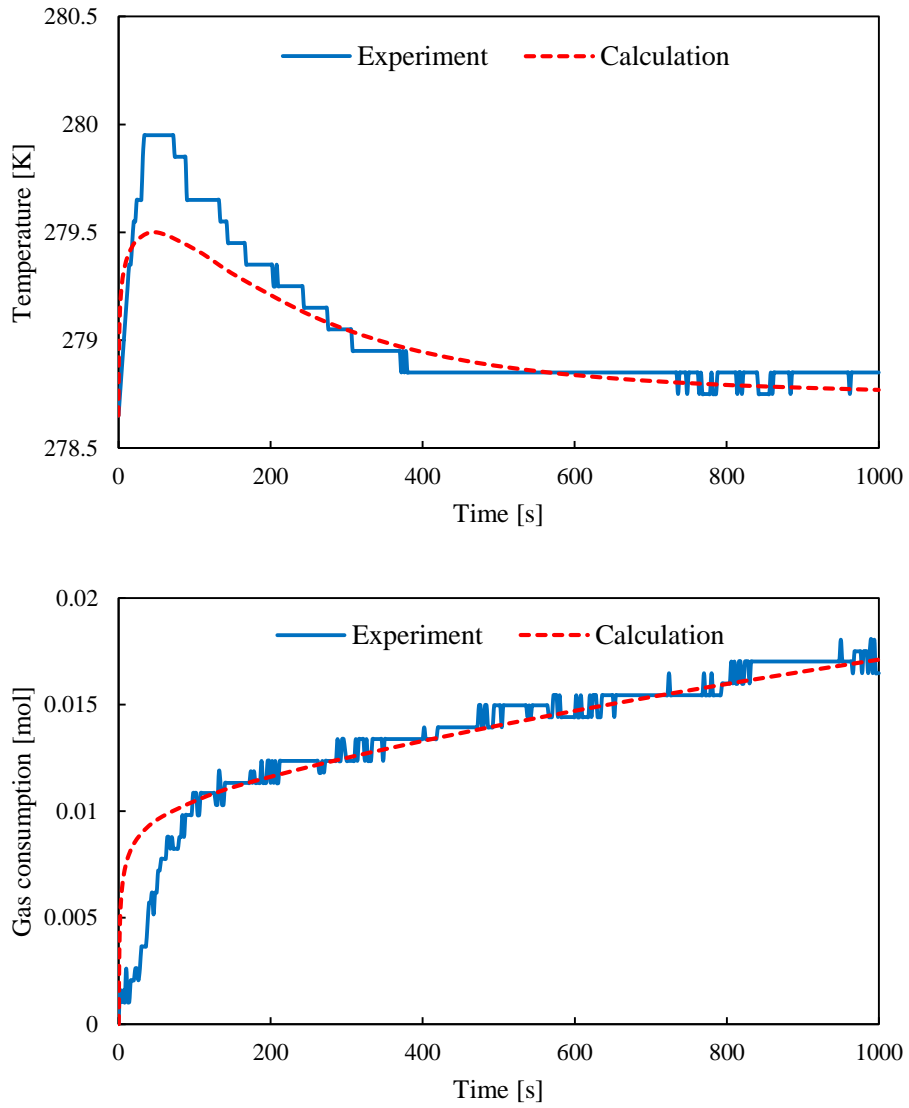
Fig. 3- 21 The validation results using k_f and k_d obtained from Arrhenius plot in Case 5

3.2 CO$_2$ Hydrate Formation with Gas-liquid Two-phase Flow

In this section, experiments of CO$_2$ hydrate formation in the lab-scale sand sediment with gas-liquid two-phase flow carried out by Inui [1-18] are introduced at first. Then, based on the experiments, simulations of gas-liquid two-phase flow and CO$_2$ hydrate formation in the sand sediment under the experimental conditions are conducted using the numerical simulator. Finally, unknown parameters are determined by comparing the simulation results with the experimental data.

3.2.1 Experiment outline of CO$_2$ hydrate formation with gas-liquid two-phase flow

In order to reveal the blockage mechanism of hydrate storage, experiments of CO$_2$ gas injection into the lab-scale water-saturated sand sediment and CO$_2$ hydrate formation in the sand sediment with gas-liquid two-phase flow, simulating the sub-seabed sand sediment, were conducted by Inui [1-18]. For the easy understanding of this study, the experiment outline is introduced in brief as below.

3.2.1.1 Experimental apparatus and procedures

The experimental apparatus used by Inui was the same as that introduced in Section 3.1.1.1, except that there was no buffer tank between CO$_2$ cylinder and the reaction vessel. Besides, seven thermocouples (hereinafter referred to as T1 ~ T7 from the inlet to the outlet of the reaction vessel) were placed along the axis inside the reaction vessel with the interval of 20 mm vertically to measure the temperature changes in the sand sediment with time instead of one. On the other hand, a differential pressure gauge was placed between the inlet and outlet of the reaction vessel in order to measure the differential pressure between them. The schematic diagram of the experimental apparatus is shown in Fig. 3-22.
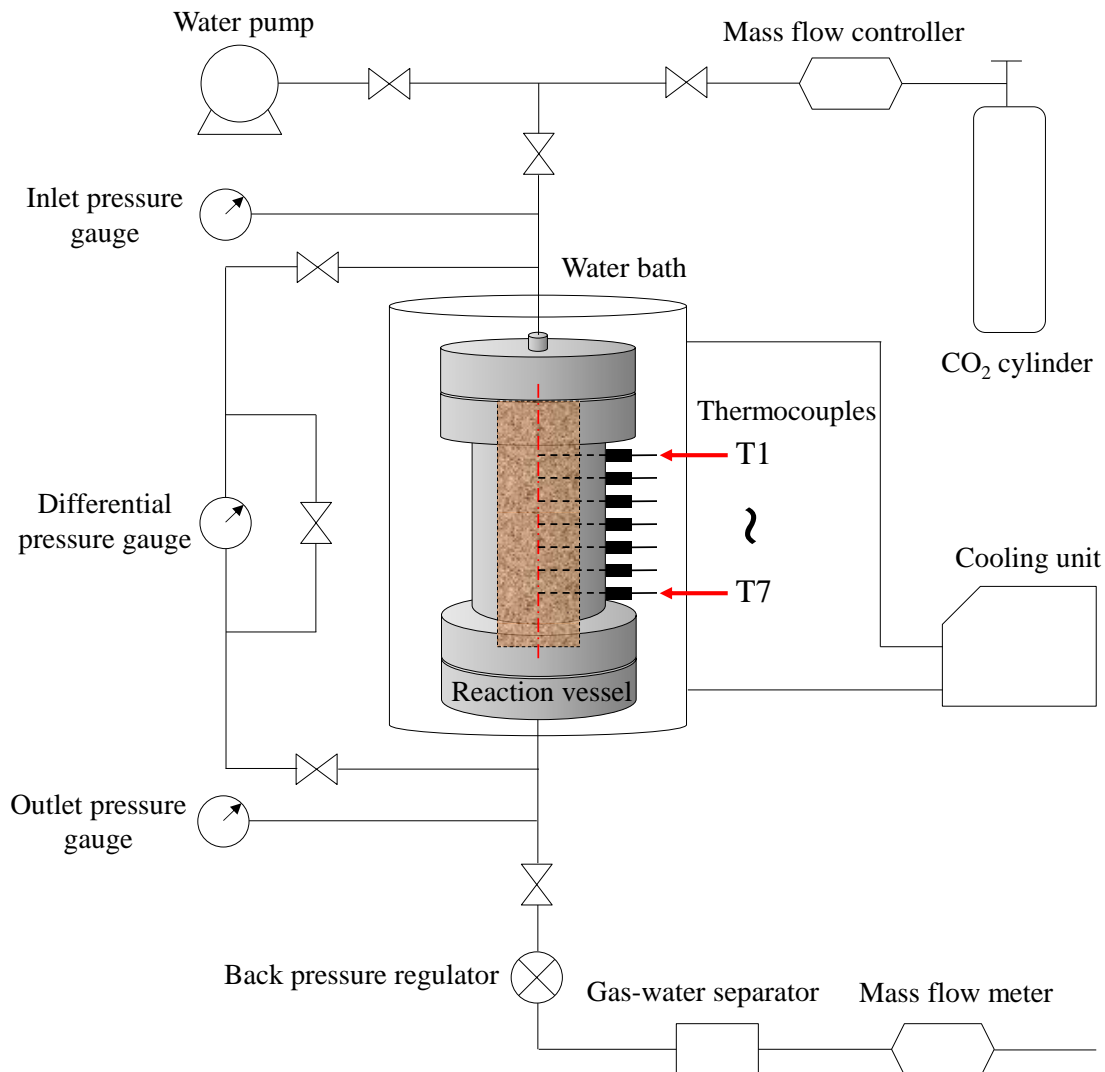
Fig. 3- 22 The schematic diagram of the experimental apparatus for CO_2 hydrate formation in the sand sediment with gas-liquid two-phase flow [1-18]

The experimental procedures are summarized in brief according to Inui [1-18] as below.

1) First, water-saturated sand sediment was prepared as introduced in Section 3.1.1.1.
2) After the sand sediment was set up, the reaction vessel was bathed in the cooling unit at the experimental temperature. Then, water was injected from the inlet of the reaction vessel at a constant rate by the water pump.
3) After the temperature values detected at T1 ~ T7 dropped to the experimental temperature set by the cooling unit and became stable during water injection, the back pressure valve was adjusted in order to set the pressure at the outlet of the reaction vessel to the experimental value.

4) When the pressure inside the reaction vessel became stable, CO_2 gas was injected from the CO_2 cylinder into the reaction vessel at a constant rate through the mass flow controller, and the experiments were started.

5) During the process of CO_2 gas injection, hydrate formed in the sand sediment gradually, and the following data were measured:
   (a) the amount of discharged water from the outlet of the reaction vessel per minute;
   (b) the temperature changes detected at T1 ~ T7 due to CO_2 dissociation and hydrate formation;
   (c) the differential pressure between the inlet and outlet of the reaction vessel due to the blockage of the gas flow.

6) At the moment when gas was discharged from the outlet of the reaction vessel, CO_2 gas injection was stopped, and one cycle of the experiments was completed.

7) After the experiments, hydrate formed in the sand sediment was dissociated, and the amount of discharged gas from the outlet of the reaction vessel was measured by the mass flow meter.

3.2.1.2 Initial experimental conditions

The initial experimental conditions for two experimental cases – Case 6 and Case 7 are listed in Table 3-5.

Table 3- 5 Initial experimental conditions for Case 6 and Case 7 [1-18]

		Case 6	Case 7
Initial temperature	[K]	275.15	278.15
Initial pressure	[MPa]	3.1	3.1
CO_2 gas injection rate	[Nml/min]	300	300
End time of induction stage	[min]	4.6	3.4
End time of CO_2 gas injection	[min]	19.1	20.6

3.2.2 Simulation outline of CO_2 hydrate formation with gas-liquid two-phase flow

In this section, the simulation outline of CO_2 hydrate formation in the lab-scale sand sediment with gas-liquid two-phase flow is explained in detail, including physical parameters, computational mesh, and initial simulation conditions.

3.2.2.1 Physical parameters

The physical parameters of Toyoura sand, stainless steel, and CO_2 hydrate are the same as those listed in Table 3-2.

3.2.2.2 Computational mesh

The computational mesh used for numerical simulations of CO_2 hydrate formation with gas-liquid two-phase flow in this study is almost the same as that introduced in Section 3.1.2.2, except that a thin layer of cells with a height of 0.1 mm, which represents the gas injection layer, is inserted between the sand layer and the top stainless steel layer to simulate CO_2 gas injection. Besides, the cell in the bottom stainless steel layer next to the axis is set to be water-saturated with constant pressure and temperature in order to represent the water discharging point at the bottom of the reaction vessel with a diameter of 3 mm. Therefore, a total number of 1854 cells (18 cells in the radial direction and 103 cells in the height direction) is used for the computational mesh in Case 6 and Case 7. The schematic diagram of the computational mesh is shown in Fig. 3-23.
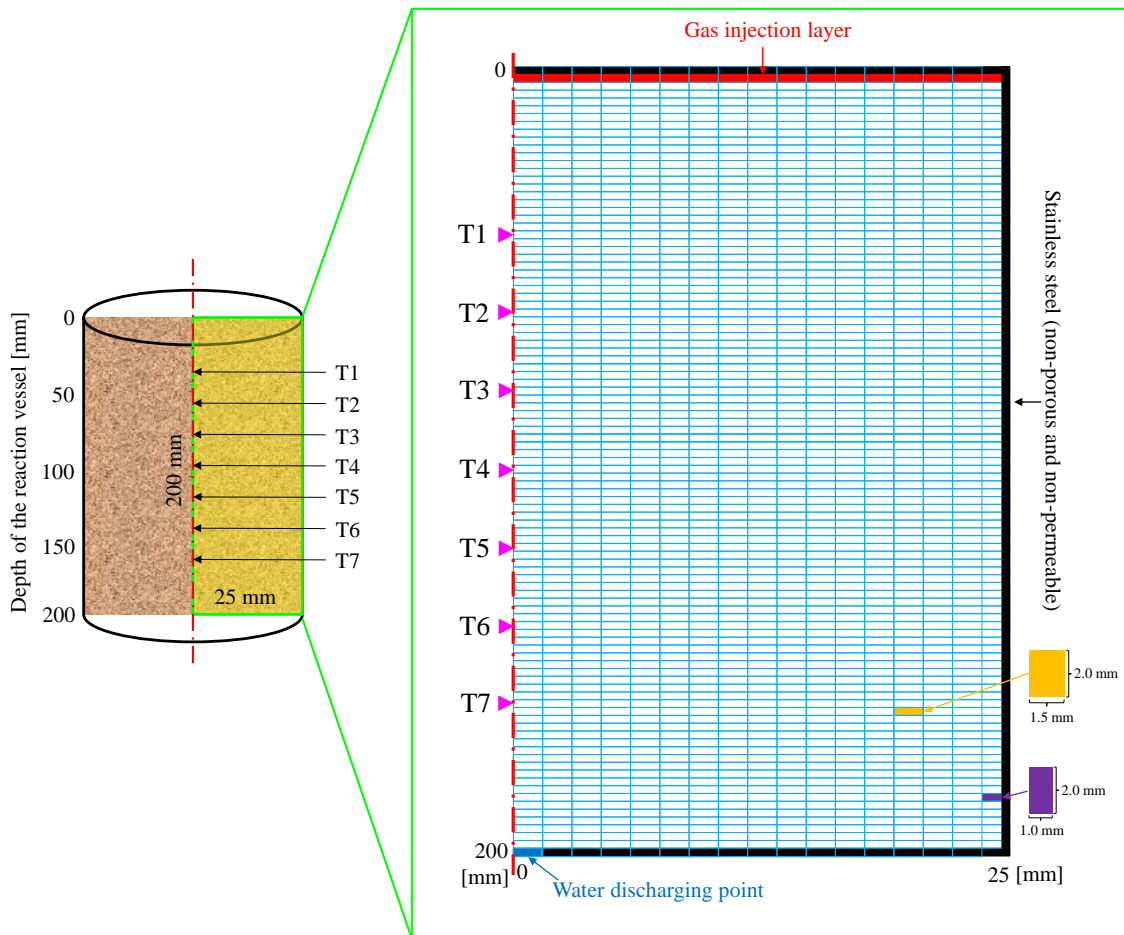
Fig. 3- 23 The schematic diagram of the computational mesh for CO_2 hydrate formation with gas-liquid two-phase flow

3.2.2.3 Initial simulation conditions

The porosity and absolute permeability of the sand sediment are determined by the average values of experimental data obtained by Sakamoto et al. [2-5] using the same Toyoura sand, set as 0.38 and 1.78×10^{-11} m^2, respectively, in this study.

Since the sand sediment is water-saturated, for the first time step when gas flows into the computational cell, the water saturation in the cell may change to the plus side and exceed 1 in the iteration process, which causes the calculation termination during the simulation. In order to solve this problem, the initial water saturation in the sand sediment is set as 0.99 m^3/m^3 in this study: i.e. the initial gas saturation is set as 0.01 m^3/m^3 instead of 0. Moreover, the hypothetical amount of CO_2 gas in the sand sediment is set to be smaller than the residual gas saturation 0.02 m^3/m^3, so it has no influence on the gas-liquid two-phase flow. On the other hand, when the gas

saturation in the cell drops below 0.01 m^3/m^3, the gas-liquid interfacial area is adjusted to 0 automatically in the simulator, so there is no CO_2 gas dissociation and hydrate formation in this cell.

In addition, the initial time step is set as 0.01 s. Meanwhile, the induction stage (before CO_2 hydrate formation) are set as 4.6 min and 3.4 min in Case 6 and Case 7, respectively, as listed in Table 3-5, and the formation stage (after CO_2 hydrate formation) are set as 14.5 min and 17.2 min in Case 6 and Case 7, respectively.

3.2.3 Simulation results and discussions

In this section, numerical simulations of the induction stage (including only the process of gas-liquid two-phase flow) and the formation stage (including both the processes of gas-liquid two-phase flow and CO_2 hydrate formation) are conducted, respectively, in order to determine the unknown model parameters introduced in Chapter 2 by comparing the calculation results with the experimental data.

3.2.3.1 Sensitivity analysis on unknown parameters for gas-liquid two-phase flow

As mentioned in Section 2.1, unknown parameters for gas-liquid two-phase flow are included in the relative permeability and capillary pressure models as well as CO_2 gas dissolution rate model, which are n_{rG} and n_{rA} in Equations (2-10) and (2-11), n_{P_c} in Equation (2-12), and k_t in Equation (2-14), respectively.

For the aqueous phase flow, since the sand sediment is nearly water-saturated before CO_2 gas injection, it can hardly be seen that the change of n_{rA} in the relative permeability model for the aqueous phase has a great influence on the behavior of the gas-liquid two-phase flow according to Nakashima [1-20]. So n_{rA} is set as 4, for which the generalized Corey model [2-4] is adopted in this study. However, if n_{rG} is set as 2, which is also the same value as that in the generalized Corey model [2-4], CO_2 gas may become more likely to flow than the actual situation even under a small pressure difference. Besides, n_{P_c} and k_t may also have influence on the differential pressure and the amount of discharged water. Therefore, for the simplification of unknown parameters for gas-liquid two-phase flow, only three parameters: n_{rG}, n_{P_c}, and k_t are fitted in this study.

Likewise, first, preliminary simulations are conducted in order to understand the difference

between the calculation results and the experimental data, and predict the ranges of the unknown parameters. Then, accurate simulations are conducted in order to carry out the sensitivity analysis, and obtain the optimum values for the unknown parameters.

As a result, the fitting parameters of n_{rG} (4, 8, and 12), n_{P_c} (no capillary pressure, 0.1, and 1), and k_t (0.5×10^{-17} m/s, 1.5×10^{-17} m/s, and 2.5×10^{-17} m/s): i.e. total seven combinations of Case 6(7)A ~ Case 6(7)G are selected in this study. The simulation conditions for the sensitivity analysis on unknown parameters for gas-liquid two-phase flow are listed in Table 3-6.

In addition, the comparisons between the calculation results and the experimental data in Case 6A ~ Case 6G and Case 7A ~ Case 7G are shown in Fig. 3-24 ~ Fig. 3-30 and Fig. 3-31 ~ Fig. 3-37, respectively. For all these figures, the first two ones represent the temperature changes detected at T1 ~ T3, the third ones represent the differential pressure between the inlet and outlet of the reaction vessel, and the fourth ones represent the amount of discharged water from the outlet of the reaction vessel, respectively.

Table 3- 6 The simulation conditions for the sensitivity analysis on unknown parameters for gas-liquid two-phase flow

		n_{rG} [-]		
		4	8	12
n_{P_c} [-] $\left(k_t = 1.5 \times 10^{-7}\right)$	No capillary pressure		Case 6(7)D	
	0.1	Case 6(7)A	Case 6(7)B	Case 6(7)C
	1		Case 6(7)E	
k_t [m/s] $\left(n_{P_c} = 0.1\right)$	0.5×10^{-7}		Case 6(7)F	
	1.5×10^{-7}	(Case 6(7)A)	(Case 6(7)B)	(Case 6(7)C)
	2.5×10^{-7}		Case 6(7)G	

① Sensitivity analysis on the exponent n_{rG} in the relative permeability model

As shown in Case 6(7)A (Fig. 3-24 and Fig. 3-31), Case 6(7)B (Fig. 3-25 and Fig. 3-32), and Case 6(7)C (Fig. 3-26 and Fig. 3-33), n_{rG} is varied from 4 to 12, while n_{P_c} and k_t are fixed at 0.1 and 1.5×10^{-7} m/s, respectively. From the third figures, it can be seen that the differential pressure becomes larger with the increase of n_{rG}, for which the gas flow velocity decreases on the contrary due to the relative permeability reduction according to Equation (2-10). This also

explains the reason that obvious temperature rises detected at T3 can be seen in the second figures in Case 6A and Case 7A, but not in Case 6C and Case 7C where the gas flow moves much more slowly. On the other hand, for the amount of discharged water, with the increase of the differential pressure, the driving force of the gas flow which pushes the water out of the sand sediment becomes stronger, so a slight increase can be seen in the fourth figures from Case 6(7)A to Case 6(7)C.

② Sensitivity analysis on the exponent n_{P_c} in the capillary pressure model

As shown in Case 6(7)B (Fig. 3-25 and Fig. 3-32), Case 6(7)D (Fig. 3-27 and Fig. 3-34), and Case 6(7)E (Fig. 3-28 and Fig. 3-35), n_{P_c} is varied from 0.1 to 1 as well as no capillary pressure, while n_{rG} and k_t are fixed at 8 and 1.5×10^{-7} m/s, respectively. From the third figures, it can be seen that the differential pressure is the lowest when the capillary pressure is not considered in the calculations. While with the increase of n_{P_c}, the differential pressure also rises significantly. However, little differences can be seen in the second and fourth figures, which means n_{P_c} has a great influence on the differential pressure, but not so much on the temperature changes and the amount of discharged water.

③ Sensitivity analysis on the mass transfer coefficient k_t in CO₂ gas dissolution rate model

As the shown in Case 6(7)B (Fig. 3-25 and Fig. 3-32), Case 6(7)F (Fig. 3-29 and Fig. 3-36), and Case 6(7)G (Fig. 3-30 and Fig. 3-37), k_t is varied from 0.5×10^{-7} m/s to 2.5×10^{-7} m/s, while n_{rG} and n_{P_c} are fixed at 8 and 0.1, respectively. From the fourth figures, it can be seen that the amount of discharged water decreases sharply with the increase of k_t. The reason is that if k_t is too large, more CO₂ gas dissolves into the aqueous phase through the gas-liquid interface, and the gas flow velocity becomes small, which makes the driving force not strong enough to push the water out of the sand sediment. This also explains the reason that the differential pressure drops in the third figures from Case 6(7)F to Case 6(7)G. On the other hand, with a larger amount of dissolved CO₂ gas in the aqueous phase, the dissolution heat increases as well, so obvious temperature rises detected at T1 can be seen in Case 6(7)G rather than in Case 6(7)F.

④ Parameter-fitting results and discussions

Based on the sensitivity analysis on the unknown parameters for gas-liquid two-phase flow, the optimum values of n_{rG}, n_{P_c}, and k_t are determined as 8, 0.1, and 1.5×10^{-7} m/s, respectively, as the figures shown in Case 6B and Case 7B where the calculation results show good consistency

with the experimental data. In addition, contour maps of CO_2 gas saturation, CO_2 mass fraction in the aqueous phase, and temperature at the end of the induction stage in Case 6B and Case 7B are shown in Fig. 3-38 and Fig. 3-39, respectively.

During the induction stage, as the gas front moves down towards the outlet of the reaction vessel, CO_2 gas dissolves into the aqueous phase through the gas-liquid interface gradually. After the gas front passes by, water-unsaturated zone appears in the sand sediment behind the gas front. Small temperature rises detected at T1 and T2 during this stage are due to the dissolution heat of CO_2 gas in the aqueous phase. From the figures of the differential pressure in Case 6B and Case 7B, it can be seen that the calculation results are a little higher than the experimental data at the beginning of gas injection, and tend towards the experimental data gradually. This may be caused by the gas-liquid interfacial area model used in this study, whose value increases with the decrease of the water saturation linearly as mentioned in Section 2.1.4. When a tiny amount of CO_2 gas flows into a computational cell at the beginning of the calculation, the gas-liquid interfacial area is also very small. However, in the actual process of gas injection, the gas front should have much larger gas-liquid interfacial area. For this reason, the calculated amount of CO_2 gas dissolved in the aqueous phase is less than the actual amount at the beginning of gas injection, resulting in the gap of the differential pressure between the calculation results and the experimental data.

As shown in Fig. 3-38 and Fig. 3-39, the gas front moves horizontally towards the outlet with CO_2 gas dissociation into the aqueous phase gradually, and nearly arrives at the one-third location of the reaction vessel. On the other hand, since the temperature of the boundary cells is set to be constant in order to simulate the reaction vessel bathed in the cooling unit, heat generated by CO_2 gas dissociation near the boundary transfers to the boundary cells which have lower temperature, causing the temperature in the center of the reaction vessel to become much higher than that near the boundary.

In the next section, n_{rG}, n_{P_c}, and k_t determined in this section will be treated as known parameters, and adopted to determine other unknown parameters in the numerical simulations of CO_2 hydrate formation with gas-liquid two-phase flow. Besides, the calculation results of Case 6B and Case 7B, as shown in Fig. 3-38 and Fig. 3-39, will be used as initial conditions for the simulation processes during the formation stage.
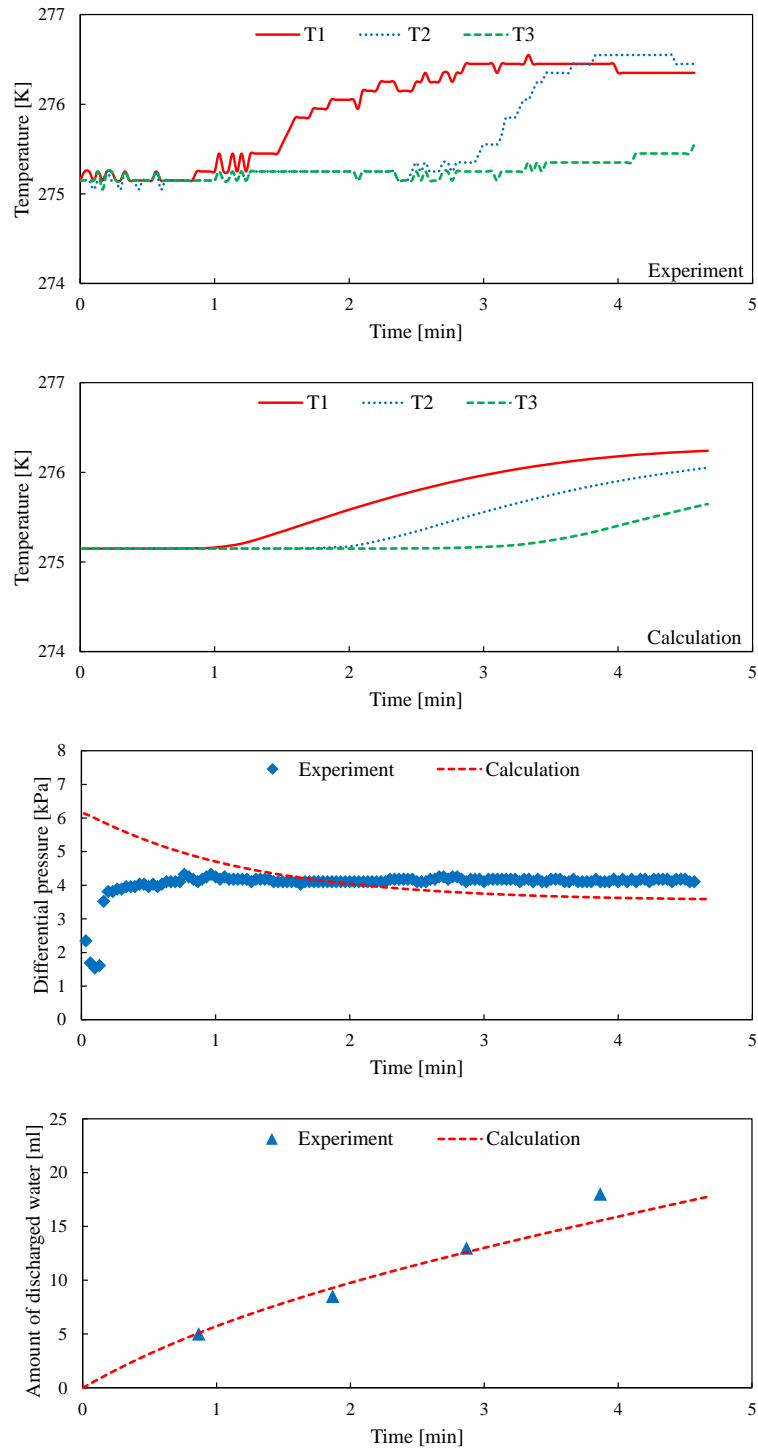
Fig. 3- 24 The comparisons between the calculation results and the experimental data in Case
6A (Induction stage)

(First two) The temperature changes detected at T1~T3

(Third) The differential pressure between the inlet and outlet of the reaction vessel

(Fourth) The amount of discharged water from the outlet of the reaction vessel
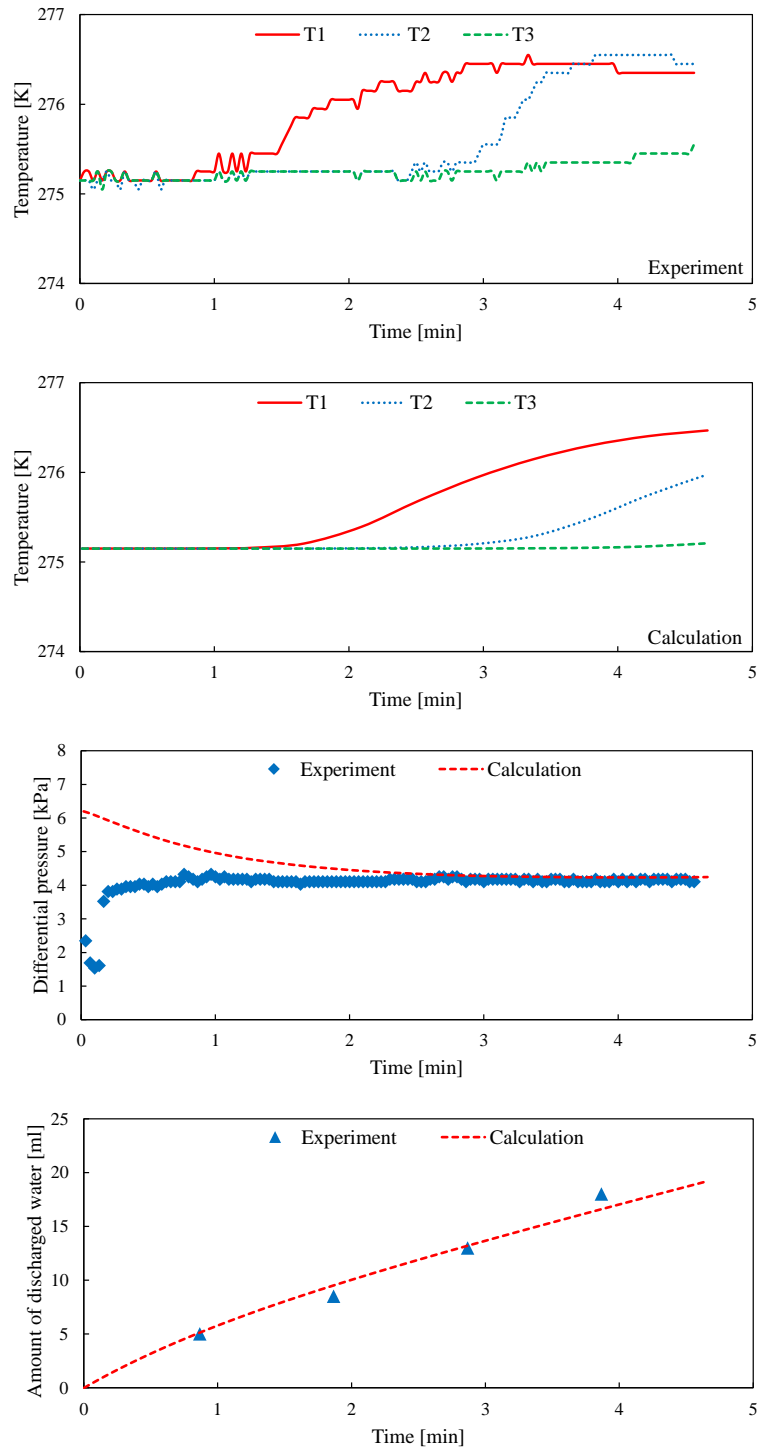
Fig. 3- 25 The comparisons between the calculation results and the experimental data in Case
6B (Induction stage)

(First two) The temperature changes detected at T1~T3

(Third) The differential pressure between the inlet and outlet of the reaction vessel

(Fourth) The amount of discharged water from the outlet of the reaction vessel
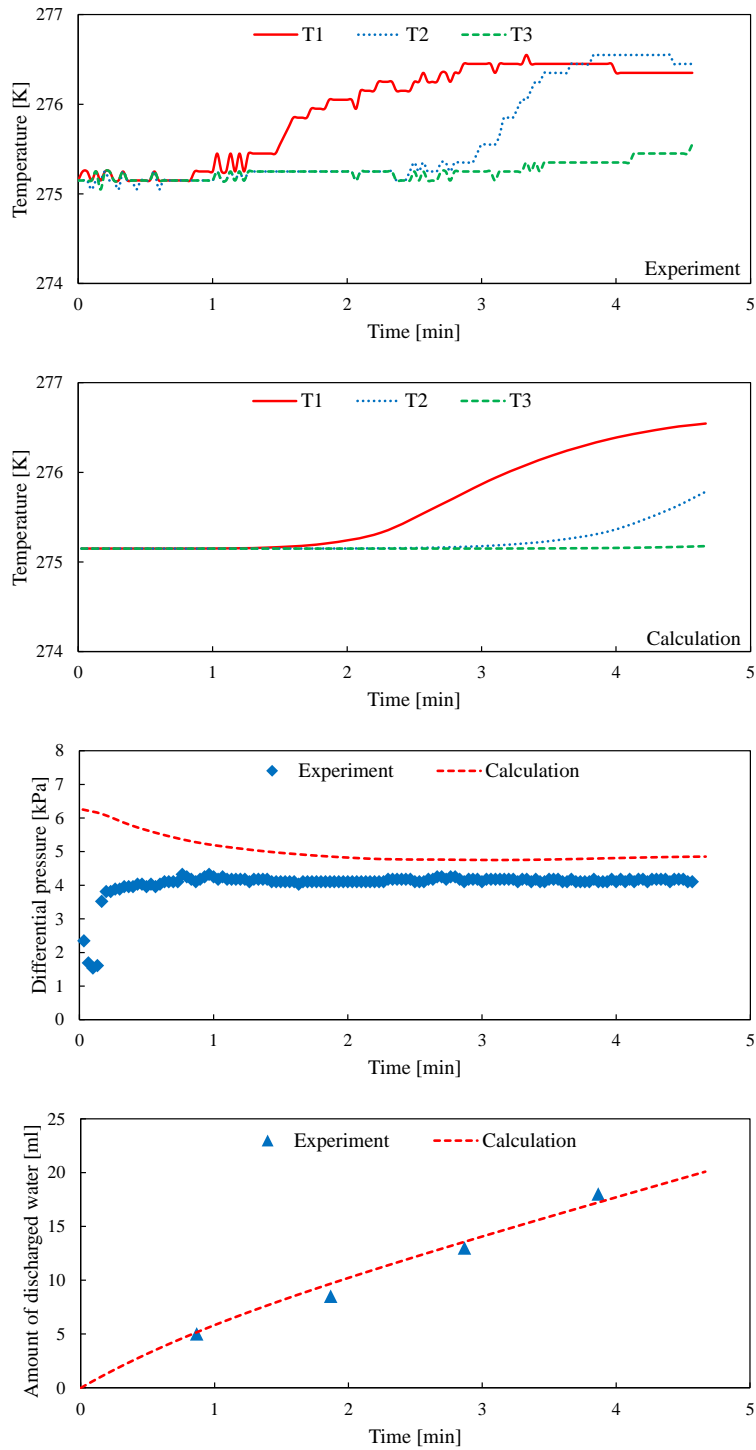
Fig. 3- 26 The comparisons between the calculation results and the experimental data in Case
6C (Induction stage)

(First two) The temperature changes detected at T1~T3

(Third) The differential pressure between the inlet and outlet of the reaction vessel

(Fourth) The amount of discharged water from the outlet of the reaction vessel
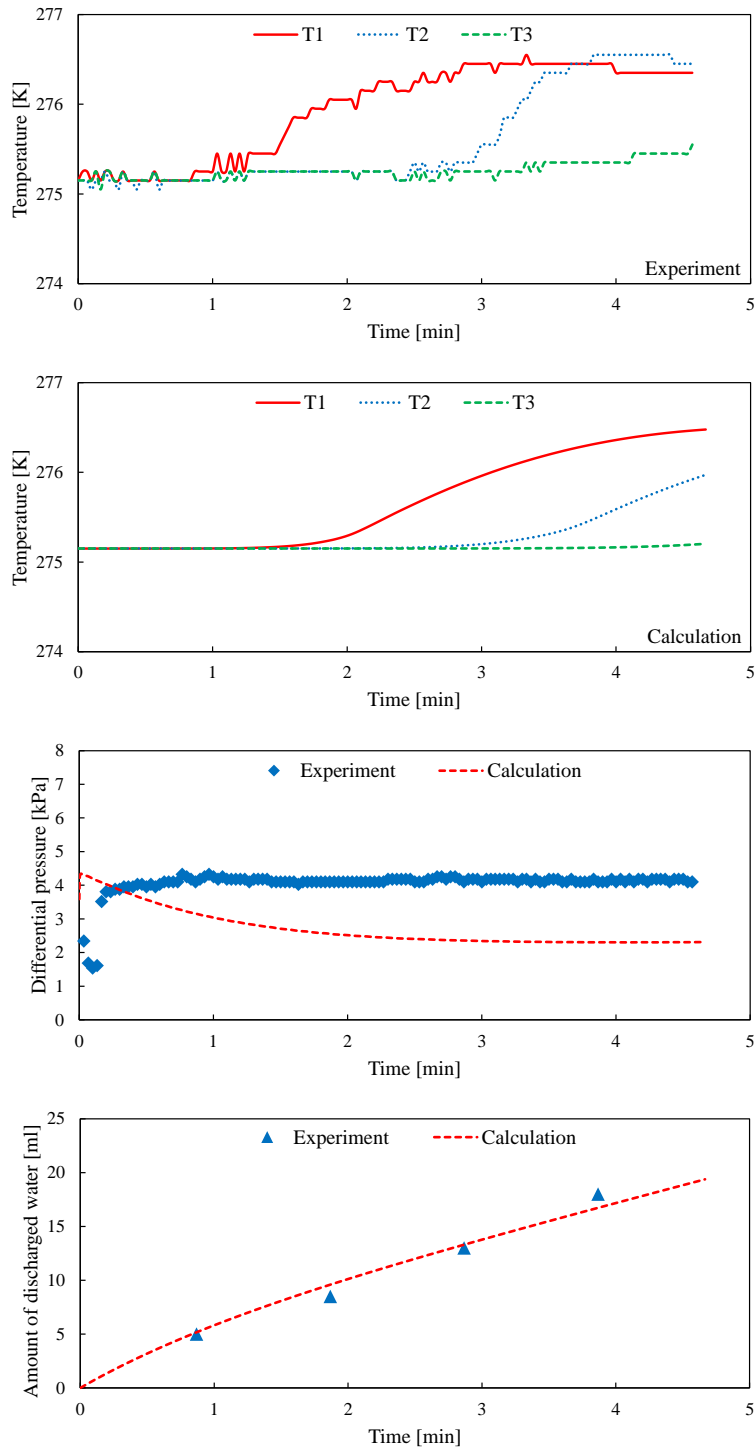
Fig. 3- 27 The comparisons between the calculation results and the experimental data in Case 6D (Induction stage)

(First two) The temperature changes detected at T1~T3

(Third) The differential pressure between the inlet and outlet of the reaction vessel

(Fourth) The amount of discharged water from the outlet of the reaction vessel
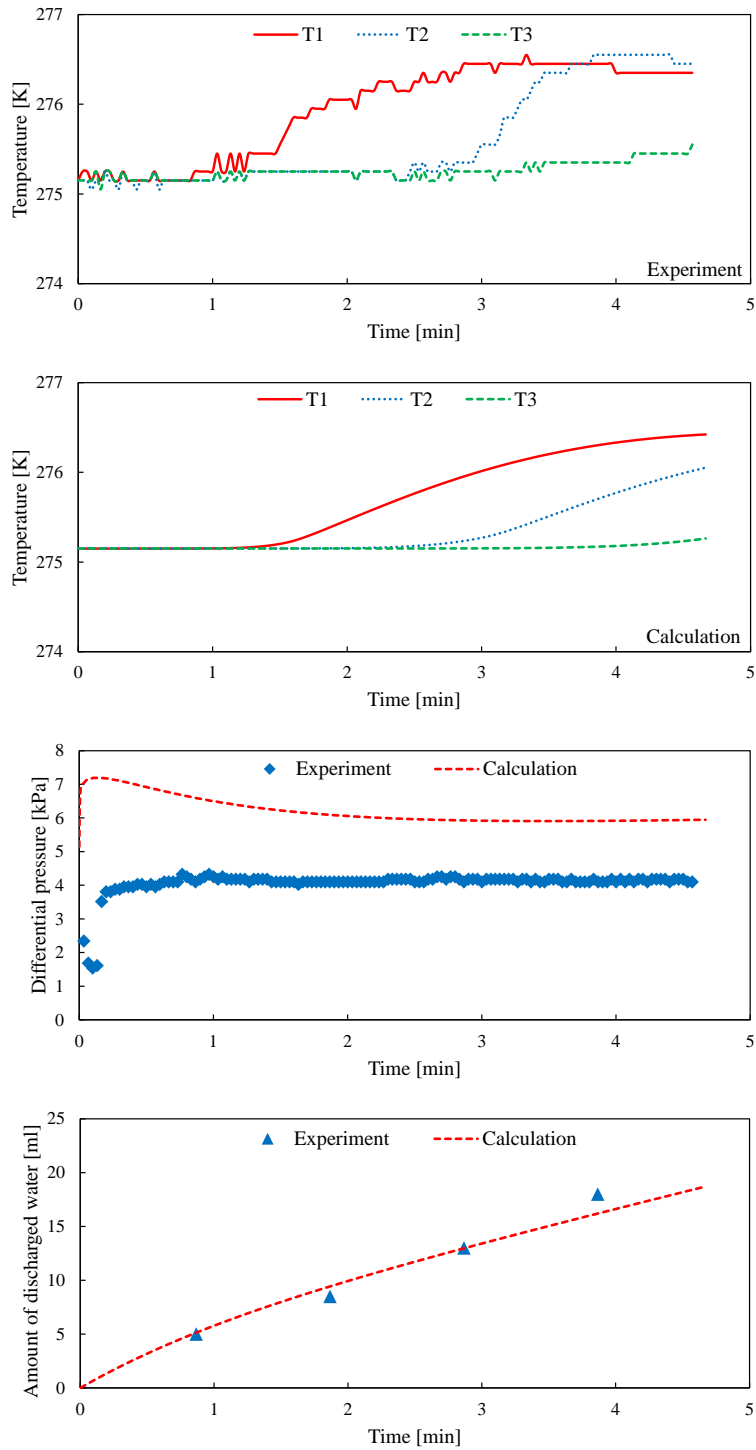
Fig. 3- 28 The comparisons between the calculation results and the experimental data in Case 6E (Induction stage)

(First two) The temperature changes detected at T1~T3

(Third) The differential pressure between the inlet and outlet of the reaction vessel

(Fourth) The amount of discharged water from the outlet of the reaction vessel

86
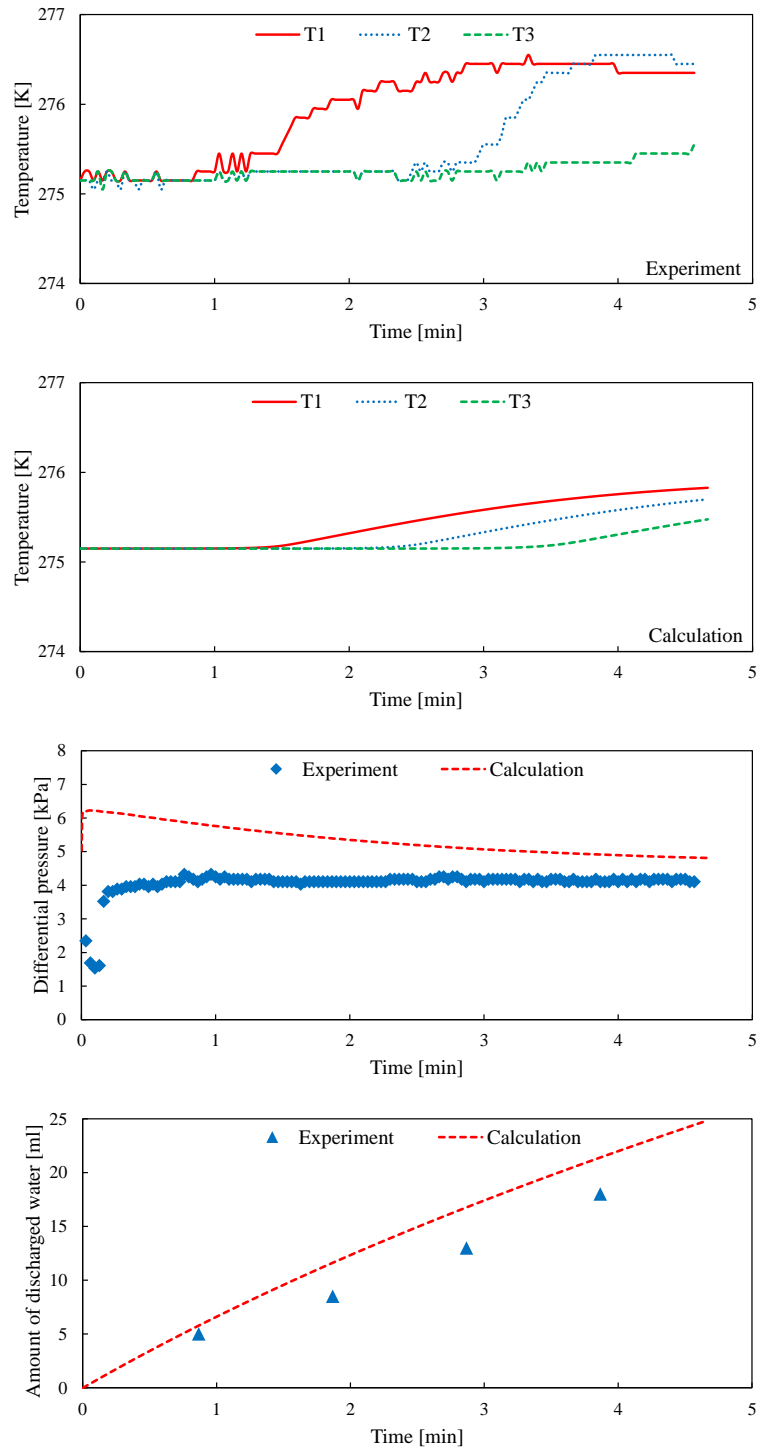
Fig. 3- 29 The comparisons between the calculation results and the experimental data in Case 6F

(Induction stage)

(First two) The temperature changes detected at T1~T3

(Third) The differential pressure between the inlet and outlet of the reaction vessel

(Fourth) The amount of discharged water from the outlet of the reaction vessel
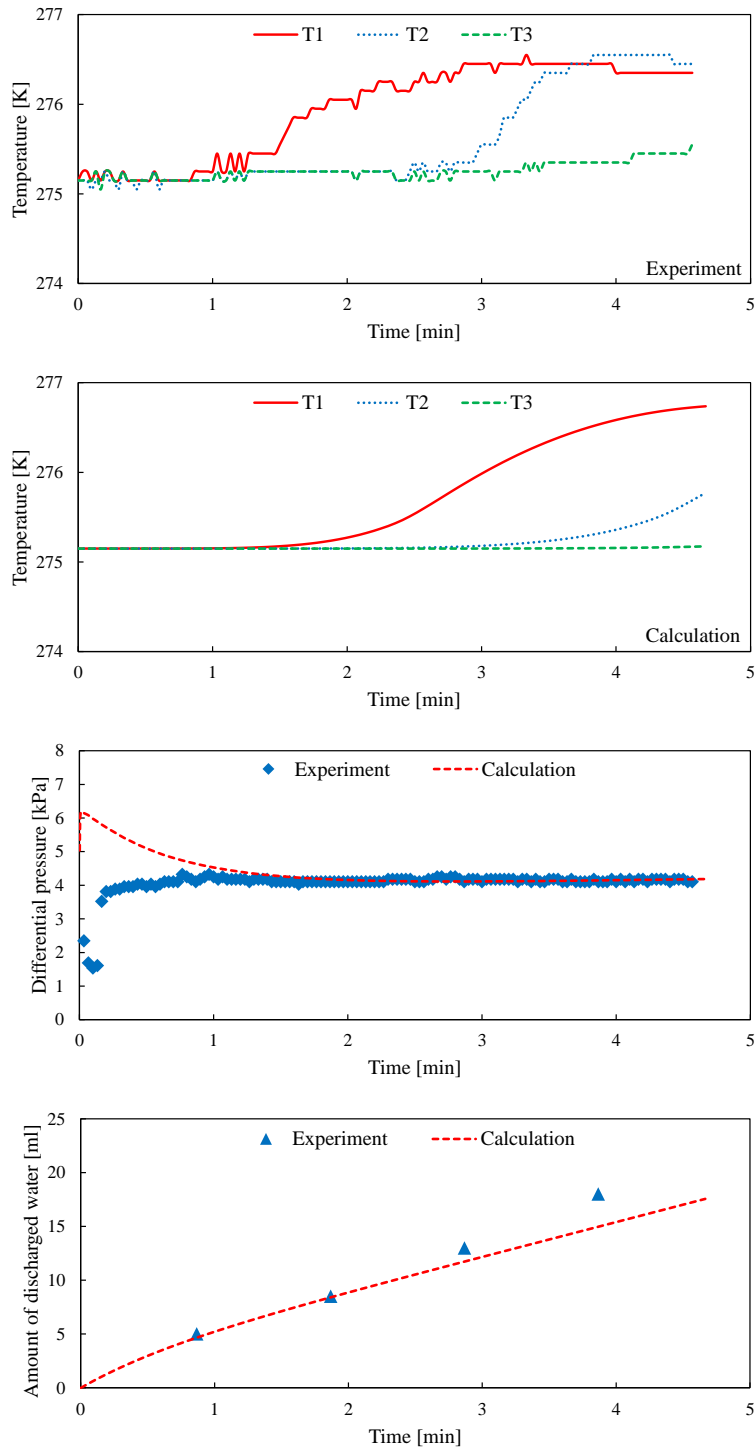
Fig. 3- 30 The comparisons between the calculation results and the experimental data in Case
6G (Induction stage)

(First two) The temperature changes detected at T1~T3

(Third) The differential pressure between the inlet and outlet of the reaction vessel

(Fourth) The amount of discharged water from the outlet of the reaction vessel
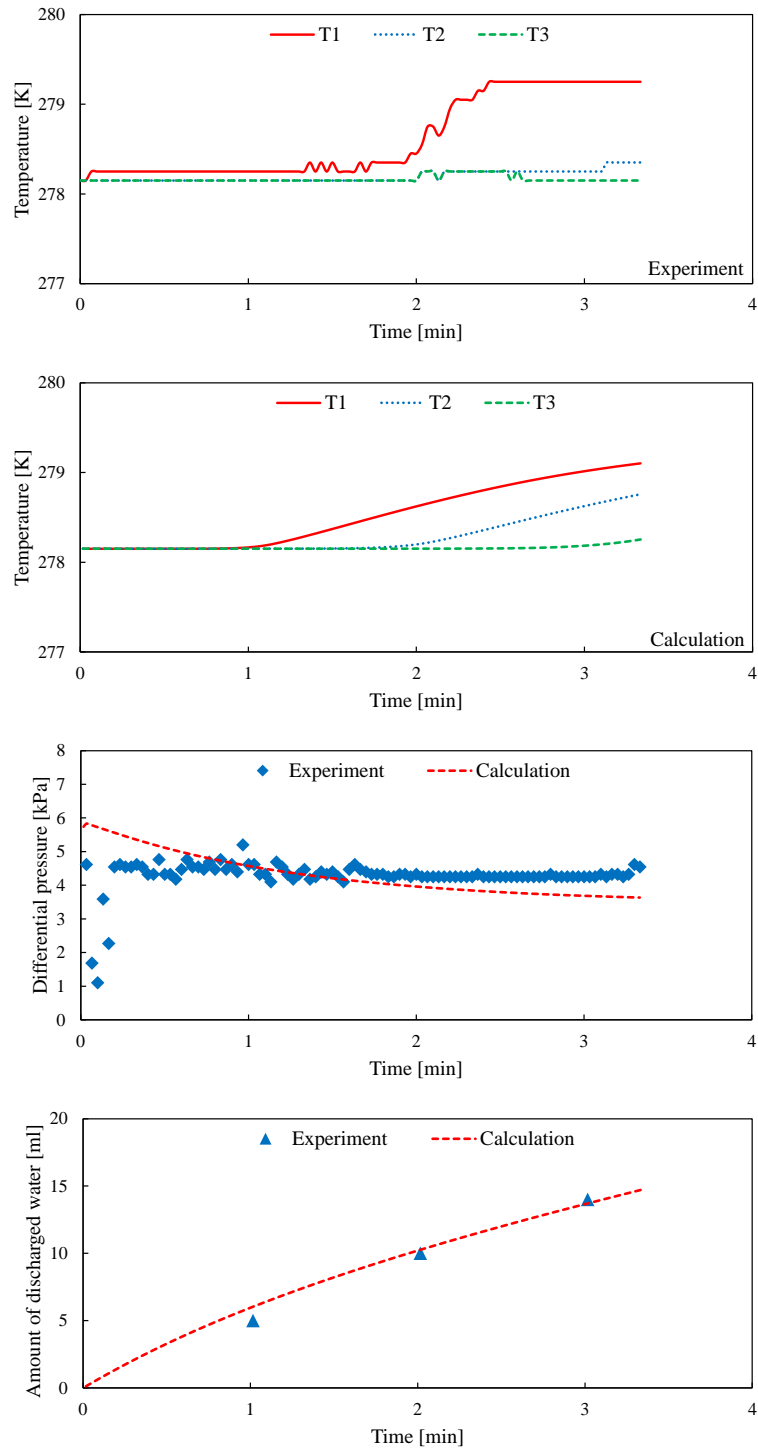
Fig. 3- 31 The comparisons between the calculation results and the experimental data in Case
7A (Induction stage)

(First two) The temperature changes detected at T1~T3

(Third) The differential pressure between the inlet and outlet of the reaction vessel

(Fourth) The amount of discharged water from the outlet of the reaction vessel
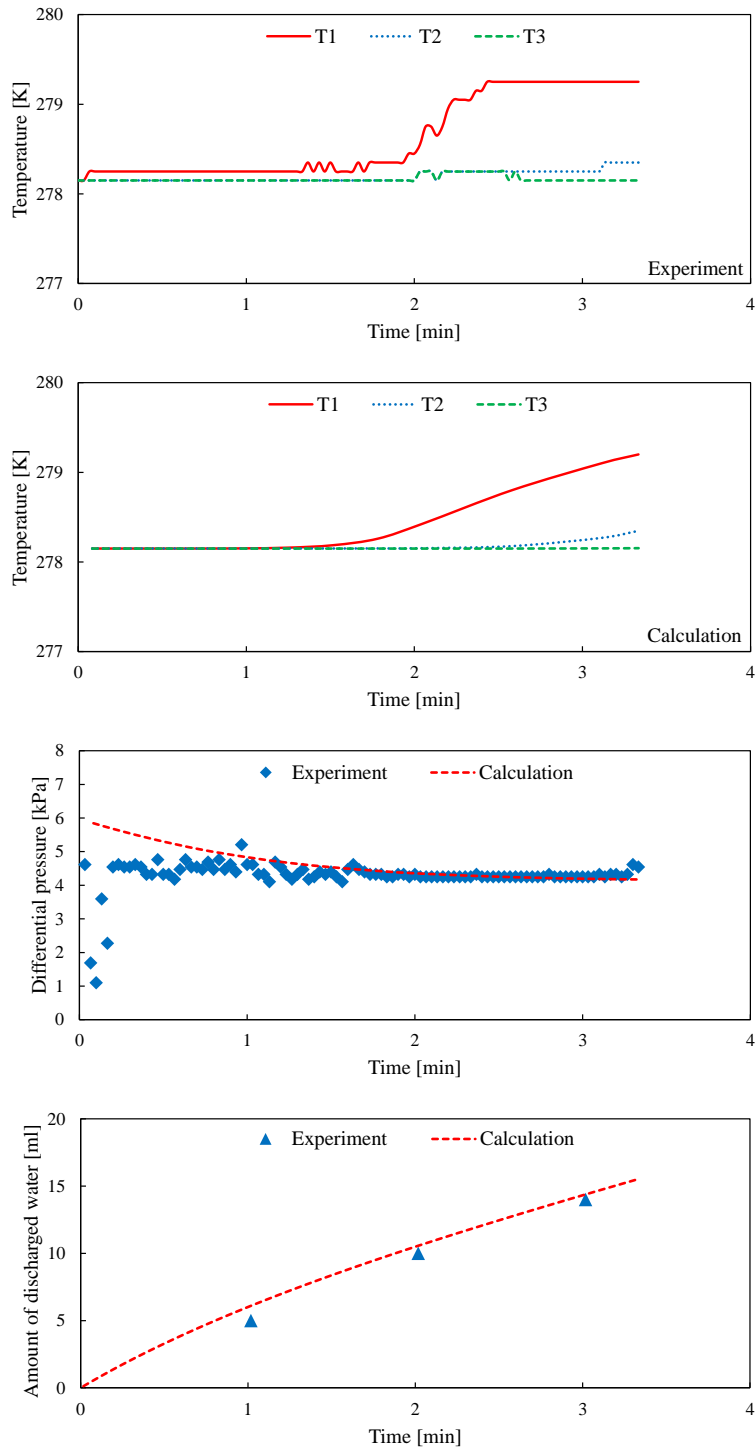
Fig. 3- 32 The comparisons between the calculation results and the experimental data in Case 7B (Induction stage)

(First two) The temperature changes detected at T1~T3

(Third) The differential pressure between the inlet and outlet of the reaction vessel

(Fourth) The amount of discharged water from the outlet of the reaction vessel
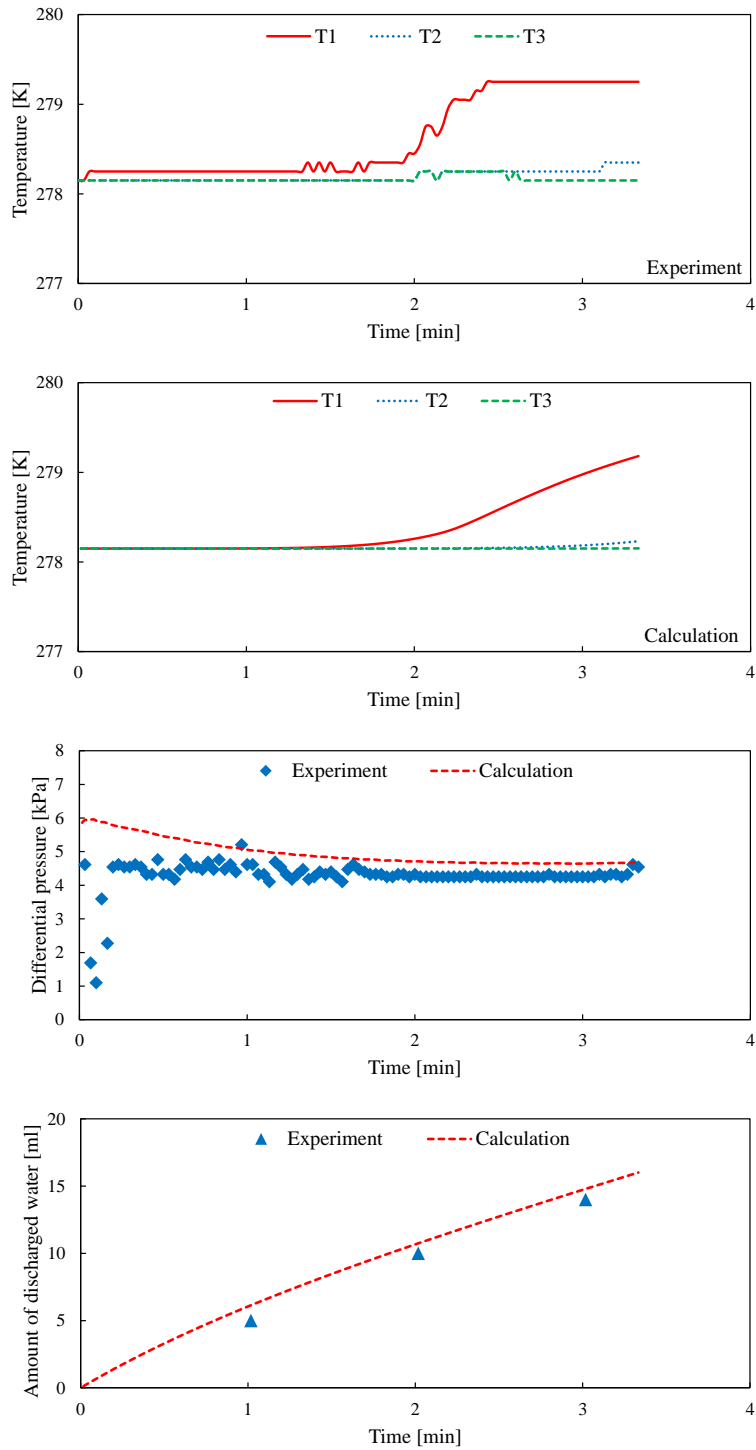
Fig. 3- 33 The comparisons between the calculation results and the experimental data in Case
7C (Induction stage)

(First two) The temperature changes detected at T1~T3

(Third) The differential pressure between the inlet and outlet of the reaction vessel

(Fourth) The amount of discharged water from the outlet of the reaction vessel

91
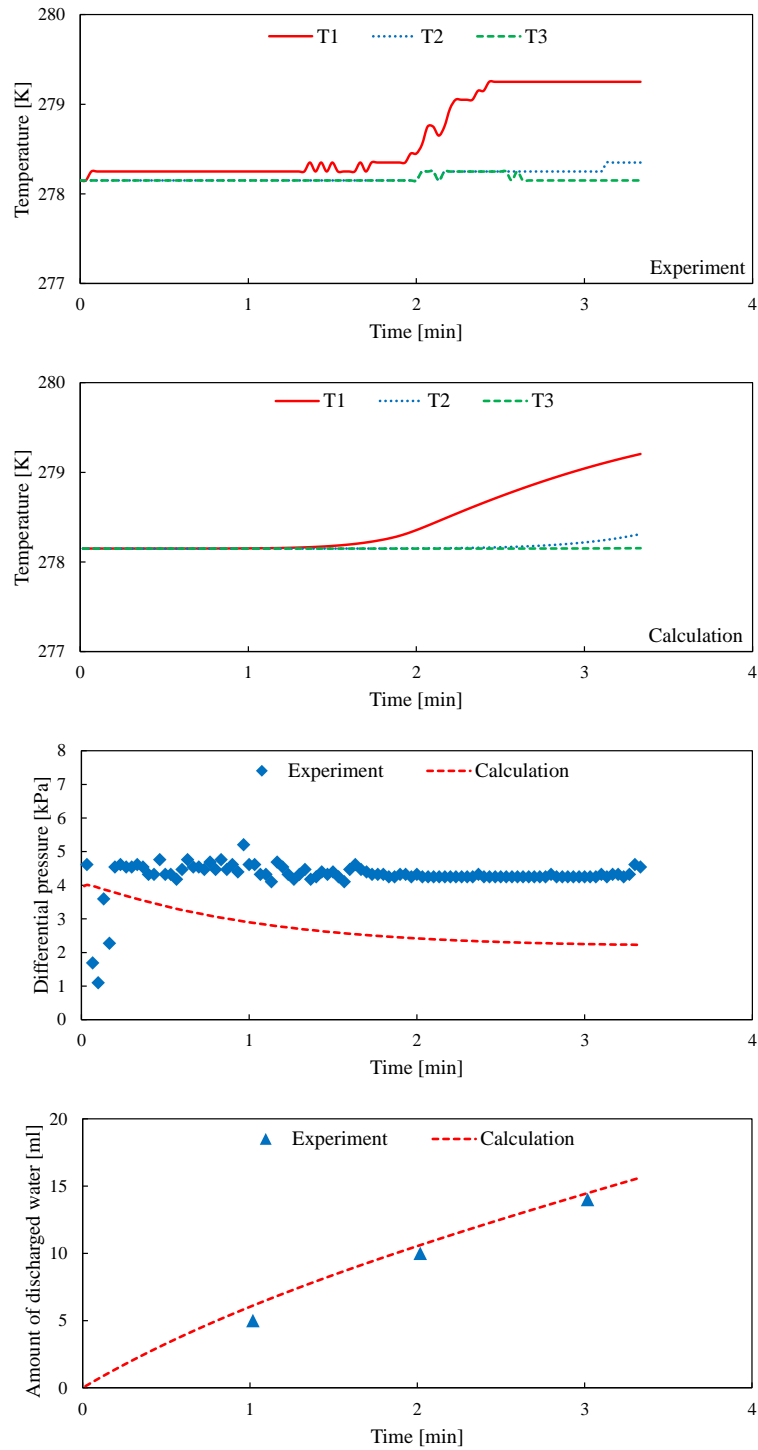
Fig. 3- 34 The comparisons between the calculation results and the experimental data in Case 7D (Induction stage)

(First two) The temperature changes detected at T1~T3

(Third) The differential pressure between the inlet and outlet of the reaction vessel

(Fourth) The amount of discharged water from the outlet of the reaction vessel
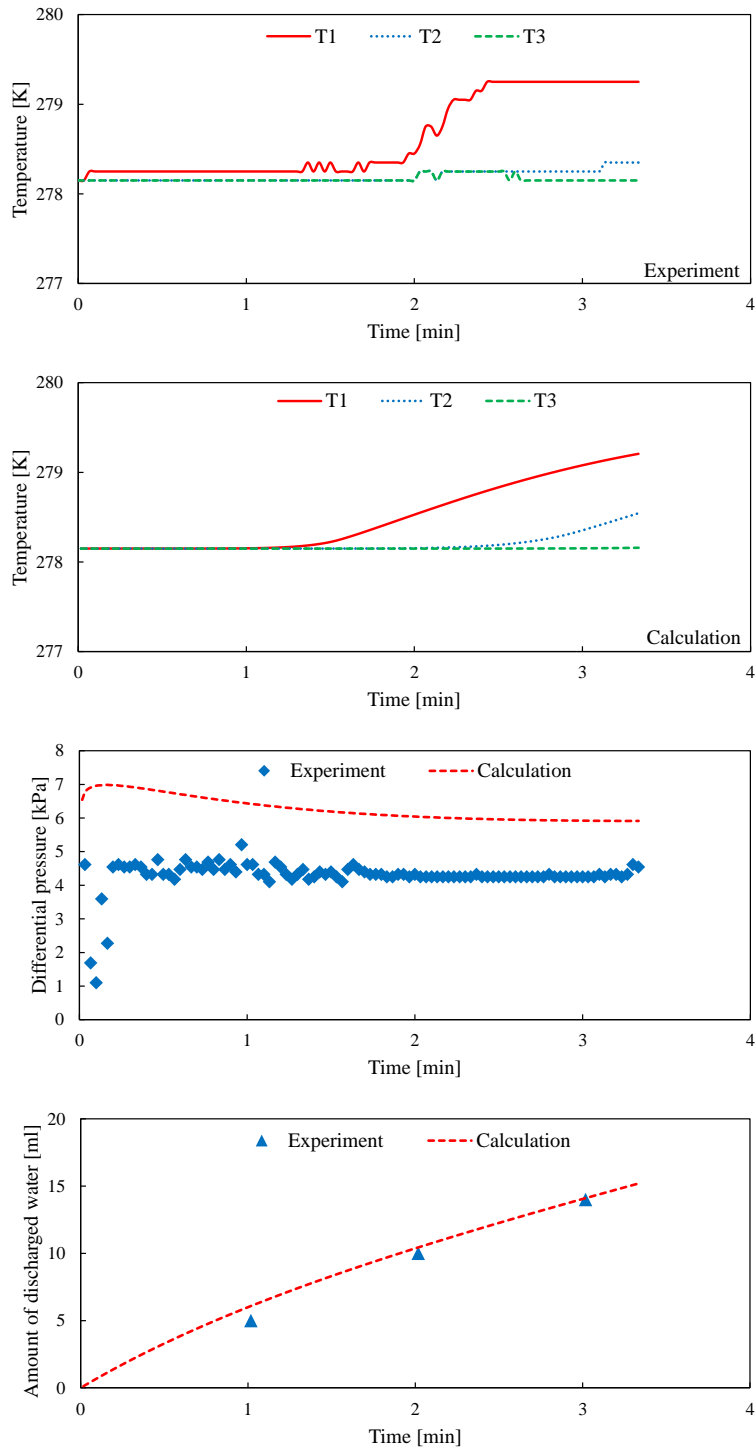
Fig. 3- 35 The comparisons between the calculation results and the experimental data in Case 7E (Induction stage)

(First two) The temperature changes detected at T1~T3

(Third) The differential pressure between the inlet and outlet of the reaction vessel

(Fourth) The amount of discharged water from the outlet of the reaction vessel
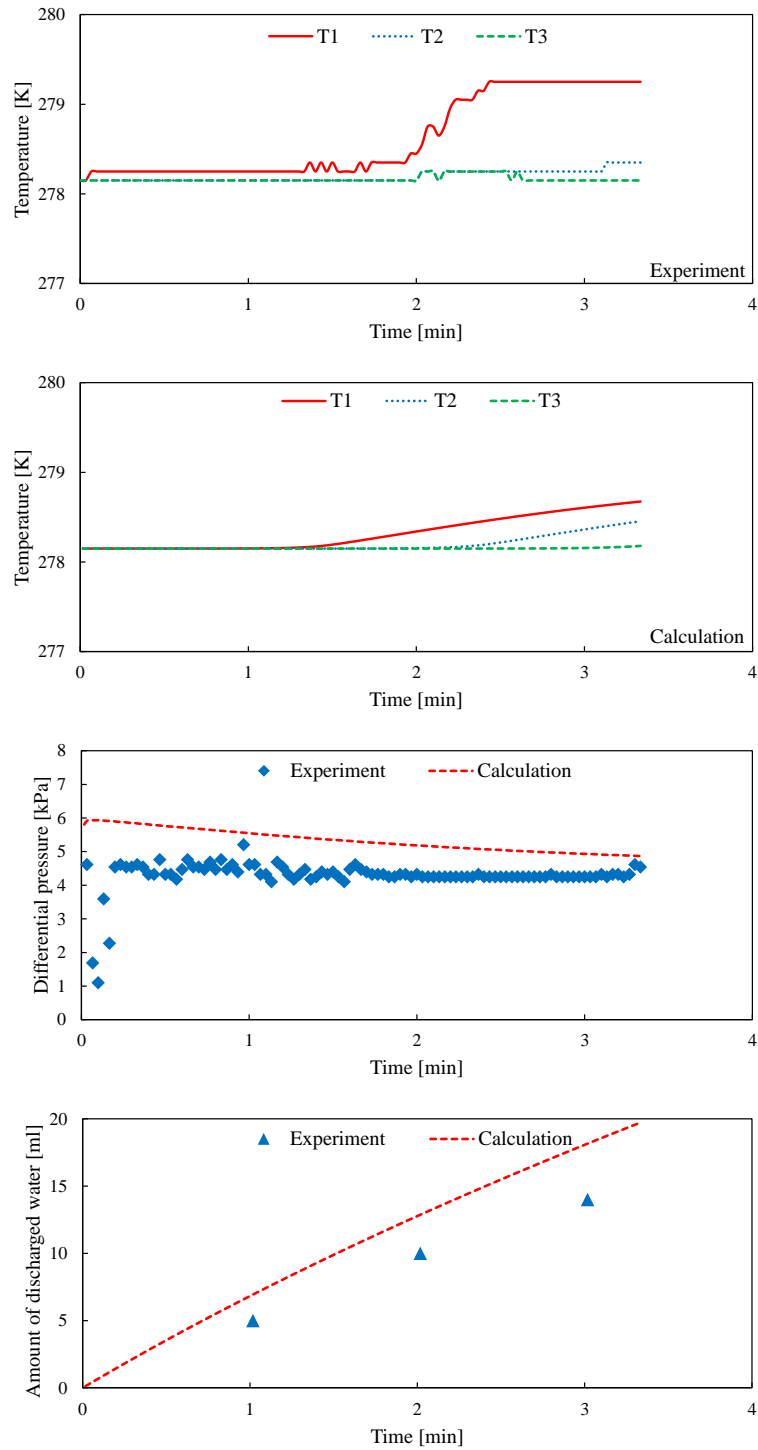
Fig. 3- 36 The comparisons between the calculation results and the experimental data in Case 7F

(Induction stage)

(First two) The temperature changes detected at T1~T3

(Third) The differential pressure between the inlet and outlet of the reaction vessel

(Fourth) The amount of discharged water from the outlet of the reaction vessel
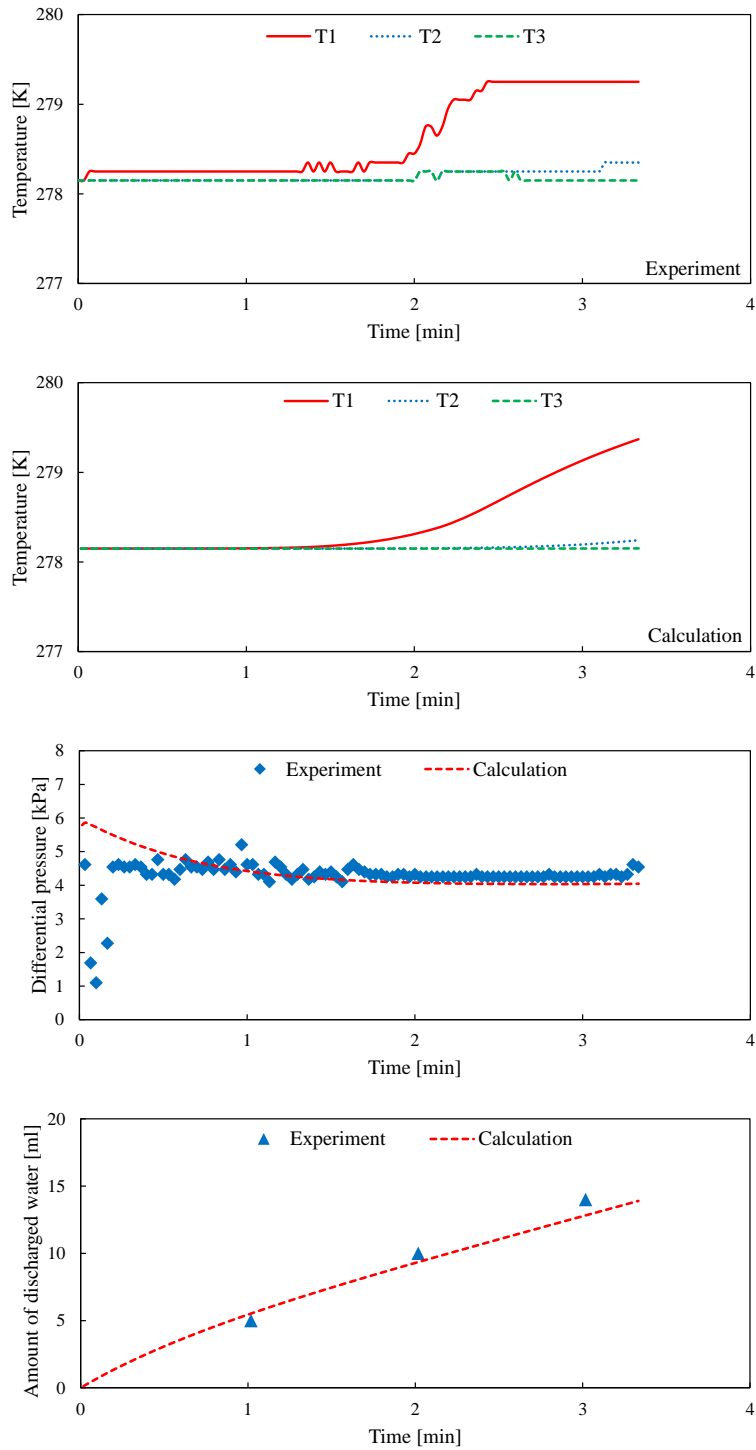
Fig. 3- 37 The comparisons between the calculation results and the experimental data in Case
7G (Induction stage)

(First two) The temperature changes detected at T1~T3

(Third) The differential pressure between the inlet and outlet of the reaction vessel

(Fourth) The amount of discharged water from the outlet of the reaction vessel
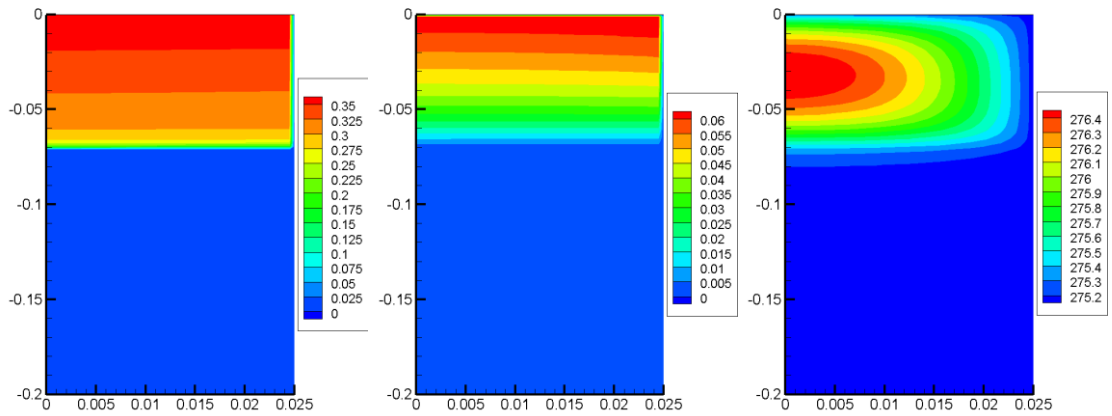
Fig. 3- 38 The contour maps of CO_2 gas saturation, CO_2 mass fraction in the aqueous phase, and

temperature at the end of the induction stage in Case 6B

(Left) The contour map of CO_2 gas saturation [m^3/m^3]

(Middle) The contour map of CO_2 mass fraction in the aqueous phase [kg/kg]

(Right) The contour map of temperature [K]
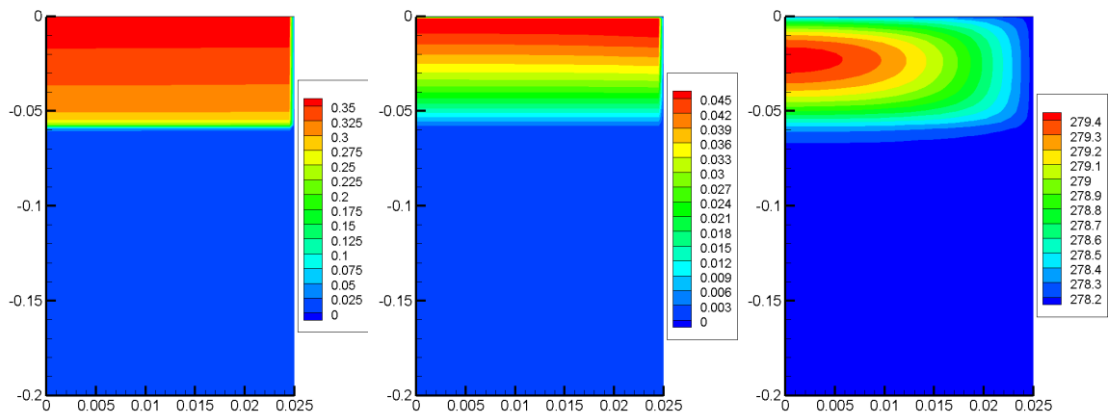
Fig. 3- 39 The contour maps of CO_2 gas saturation, CO_2 mass fraction in the aqueous phase, and

temperature at the end of the induction stage in Case 7B

(Left) The contour map of CO_2 gas saturation [m^3/m^3]

(Middle) The contour map of CO_2 mass fraction in the aqueous phase [kg/kg]

(Right) The contour map of temperature [K]

3.2.3.2 Sensitivity analysis on unknown parameters for CO₂ hydrate formation

As mentioned in Section 2.2, unknown parameters for CO_2 hydrate formation are included in the rupture ratio models on the gas front and behind the gas front, as well as in the modified permeability reduction model, which are α in Equation (2-37), β in Equation (2-57), and N in Equation (2-65), respectively.

Besides, since there is gas-liquid two-phase flow in the sand sediment in Case 6 and Case 7, the full version of the inclusive model for CO_2 hydrate formation as proposed in Equation (2-24) is used for the numerical simulations of CO_2 hydrate formation in the sand sediment.

Likewise, first, preliminary simulations are conducted in order to understand the difference between the calculation results and the experimental data, and predict the ranges of the unknown parameters. Then, accurate simulations are conducted in order to carry out the sensitivity analysis, and obtain the optimum values for the unknown parameters.

As a result, the fitting parameters of α (0.1 s, 1.0 s, and 4.0 s), β ($5.0{\times}10^9$ m^{-2}, $5.0{\times}10^{10}$ m^{-2}, and $5.0{\times}10^{11}$ m^{-2}), and N (3, 13, and 15.5): i.e. total seven combinations of Case 6(7)H ~ Case 6(7)N are selected in this study. The simulation conditions for the sensitivity analysis on unknown parameters for CO_2 hydrate formation are listed in Table 3-7.

In addition, the comparisons between the calculation results and the experimental data in Case 6H ~ Case 6N and Case 7H ~ Case 7N are shown in Fig. 3-40 ~ Fig. 3-46 and Fig. 3-47 ~ Fig. 3-53, respectively. For all these figures, the first two ones represent the temperature changes detected at T1 ~ T7, the third ones represent the differential pressure between the inlet and outlet of the reaction vessel, and the fourth ones represent the amount of discharged water from the outlet of the reaction vessel, respectively.

Table 3- 7 The simulation conditions for the sensitivity analysis on unknown parameters for
CO_2 hydrate formation with gas-liquid two-phase flow

		β [m^{-2}]		
		5.0×10^9	5.0×10^{10}	5.0×10^{11}
α [s] ($N=15.5$)	0.1		Case 6(7)K	
	1.0	Case 6(7)H	Case 6(7)I	Case 6(7)J
	4.0		Case 6(7)L	
N [-] ($\alpha=1.0$)	3		Case 6(7)M	
	13		Case 6(7)N	
	15.5	(Case 6(7)H)	(Case 6(7)I)	(Case 6(7)J)

① Sensitivity analysis on the coefficient β in the rupture ratio model behind the gas front

As shown in Case 6(7)H (Fig. 3-40 and Fig. 3-47), Case 6(7)I (Fig. 3-41 and Fig. 3-48), and Case 6(7)J (Fig. 3-42 and Fig. 3-49), β is varied from 5.0×10^9 m^{-2} to 5.0×10^{11} m^{-2}, while α and N are fixed at 1.0 s and 15.5, respectively. As can be seen in the figures, the timings of the temperature rises detected at T1 ~ T7 are delayed in the calculation results of Case 6H and Case 7H rather than those in the experimental data. On the other hand, in Case 6J and Case 7J, the timings of the temperature rises become earlier in the calculation than those in the experiments. The reason is mentioned in Section 3.1.3, which is with the increase of β, the rupture ratio on the hydrate film behind the gas front x_2 drops more sharply, causing the part of CO_2 hydrate formation at the fresh surface to be depressed. As a result, the amount of hydrate formation becomes less, and the amount of free gas which pushes the water out of the sand sediment becomes more. Meanwhile, the gas flow velocity also increases, causing the gas to be discharged from the outlet of the reaction vessel earlier than the experiments. This is also the reason that the increasing speeds of the amount of discharged water are much larger than the experiments, especially in Case 6J. On the contrary, if β is set to be a smaller value, such as 5.0×10^9 m^{-2}, more CO_2 hydrate forms in the sand sediment, consuming a large amount of gas and causing the gas flow velocity to decrease. Therefore, the differential pressure in the calculation exceeds that in the experiment, while the amount of discharged water becomes less in Case 6H and Case 7H.

Besides, the value of β fitted in this section is much smaller than that fitted in Section 3.1.3, because the sand sediment is water-unsaturated, and the initial water saturation is 0.62 m^3/m^3 in that case. According to Equation (2-55), the gas-liquid interfacial area behind the gas front increases with the decrease of water saturation, so the gas-liquid interfacial area at the beginning

of the calculations in Section 3.1.3 should be much larger than that in this section. As a result, in order to promote hydrate formation rate in the water-saturated sand sediment, the rupture ratio x_2 cannot drop too sharply, which means a much smaller value of β is preferable in this section.

② Sensitivity analysis on the coefficient α in the rupture ratio model on the gas front

   As shown in Case 6(7)I (Fig. 3-41 and Fig. 3-48), Case 6(7)K (Fig. 3-43 and Fig. 3-50), and Case 6(7)L (Fig. 3-44 and Fig. 3-51), α is varied from 0.1 s to 4.0 s, while β and N are fixed at 5.0×10^{10} m^{-2} and 15.5, respectively. However, little differences can be seen in these figures. The reason is that the amount of CO_2 hydrate formation on the gas front is very small, because the gas saturation in the computational cells including the gas front is very low. Besides, after hydrate forms on the gas front, it is moving with the gas front, and have no influence on the permeability reduction as mentioned in Section 2.2.3, as well as no influence on the gas flow velocity. Therefore, the calculation results of temperature, differential pressure, and the amount of discharged water are almost the same between Case 6(7)I, Case 6(7)K, and Case 6(7)L, even with the range of α varied from 0.1 s to 4.0 s.

③ Sensitivity analysis on the reduction exponent N in the modified permeability reduction model

   As shown in Case 6(7)I (Fig. 3-41 and Fig. 3-48), Case 6(7)M (Fig. 3-45 and Fig. 3-52), and Case 6(7)N (Fig. 3-46 and Fig. 3-53), N is varied from 3 to 15.5, while β and α are fixed at 5.0×10^{10} m^{-2} and 1.0 s, respectively. From the third figures, it can be seen that the differential pressure rises significantly with the increase of N. When N is set to be a small value, the permeability reduction due to hydrate formation is not obvious according to Equation (2-65). So the gas front moves fast and arrives at the outlet of the reaction vessel earlier, pushing more water out of the sand sediment. As a result, the calculation results of the differential pressure are smaller in Case 6M and Case 7M, while the amount of discharged water is much larger and closer to the experiments. However, in order to replicate the differential pressure rise due to the blockage of the gas flow, a larger value of N, such as 15.5, is much more appropriate in this study.

④ Parameter-fitting results and discussions

Based on the sensitivity analysis on the unknown parameters for CO_2 hydrate formation, the optimum values of α, β, and N are determined as 1.0 s, 5.0×10^{10} m^{-2}, and 15.5, respectively, as the figures shown in Case 6I and Case 7I where the calculation results show good consistency with the experimental data. In addition, contour maps of CO_2 hydrate saturation S_H, CO_2 gas saturation S_G, total hydrate formation rate Q_H, hydrate formation rate on the gas front Q_{H1}, hydrate formation rate on the hydrate film behind the gas front Q_{H2}, hydrate formation rate on the surface of the sand particles behind the gas front Q_{H3}, and temperature T with time in Case 6I and Case 7I are shown in Fig. 3-54 ~ Fig. 3-60 and Fig. 3-61 ~ Fig. 3-67, respectively.

After the induction stage, CO_2 hydrate suddenly forms on the gas front and in the water-unsaturated zone behind the gas front in short time, resulting in a large amount of CO_2 gas consumption and a very fast shrink in volume. This causes the abrupt pressure drop in the whole reaction vessel. However, in the calculation, the pressure at the outlet of the reaction vessel is set to be fixed and cannot change with time. This is the reason that the differential pressure drops below zero at the beginning of CO_2 hydrate formation and, then, recovers in both the two cases, as shown in Fig. 3-41 and Fig. 3-48. Compared with the experimental data, the timings of the temperature rises detected at T3 ~ T7 are delayed in Case 6I, mainly because the flow resistance in the sand sediment is so large that gas flow has been slowed. However, the temperature jumps detected at T1 ~ T7 caused by CO_2 hydrate formation heat are replicated and confirmed by calculations. Besides, the calculated amount of discharged water is a little less than the experimental data in both the two cases, because most of the water forms hydrate or remains in the sand sediment as irreducible water instead of being discharged.

At the late stage of CO_2 gas injection, especially in Case 6I, obvious elevation of differential pressure can be seen both from the experimental data and the calculation result. This may be because solid hydrate occupies the pore space of the sand sediment, resulting in the blockage of the gas flow, as will be explained later using the contour maps of CO_2 hydrate saturation.

As shown in Fig. 3-54 and Fig. 3-61, CO_2 hydrate mainly distributes near the boundary of the reaction vessel, whose temperature is set to be constant to simulate the temperature-controlled boundary of the reaction vessel bathed in the cooling unit. As mentioned before, the temperatures detected at T1 ~ T7 rise after the induction stage mainly due to CO_2 hydrate formation heat and, then, start to drop down when the cooling effect of the temperature-controlled boundary becomes dominant, causing the temperature near the boundary to be lower than that in the center of the

sand sediment, as shown in Fig. 3-60 and Fig. 3-67. According to the equilibrium curve for CO_2 hydrate formation as shown in Fig. 2-4, hydrate equilibrium pressure drops with the decrease of temperature, resulting in the reduction of hydrate equilibrium fugacity. For this reason, the driving force of hydrate formation near the boundary is much larger than that in the center, leading to the large hydrate formation rate near the boundary, as shown in Fig. 3-56 and Fig. 3-63.

However, unlike Case 7I (Fig. 3-61), main CO_2 hydrate distribution zone is not next to the boundary but has some distance, as shown in Case 6I (Fig. 3-54). This is because CO_2 hydrate saturation is much higher in Case 6I than in Case 7I. When CO_2 hydrate forms horizontally on the upper outer side of the sand sediment at the beginning of hydrate formation, the solid hydrate occupies the pore space of the sand sediment, causing the sharp permeability reduction and forcing the gas phase to flow towards the center, as shown in Fig. 3-55. Therefore, CO_2 hydrate forms gradually at the gas-liquid interface between the aqueous phase remained on the outer side of the sand sediment and the gas phase forced to flow towards the center, resulting in the vertical distribution of CO_2 hydrate saturation near the boundary of the reaction vessel in Case 6I, as shown in Fig. 3-54.

In Fig. 3-57 and Fig. 3-64, it can be seen that hydrate formation rate on the gas front Q_{H1} is very small, mainly because the gas saturation in the computational cells including the gas front is very low, as shown in Fig. 3-55 and Fig. 3-62. Therefore, hydrate formation rate on the gas front Q_{H1} has little contribution to the total hydrate formation rate Q_H, which also agrees with the parameter-fitting results of α as explained before.

On the other hand, as shown in Fig. 3-58 and Fig. 3-65, hydrate formation rate on the hydrate film behind the gas front Q_{H2} is dominant in the total hydrate formation rate Q_H, which contributes to CO_2 hydrate saturation greatly near the boundary, and causes the permeability reduction significantly, resulting in the blockage of the gas flow. Besides, as can be seen in Fig. 3-59 and Fig. 3-66, hydrate formation rate on the surface of the sand particles behind the gas front Q_{H3} is also very small, and has little contribution to the total hydrate formation rate Q_H.

To sum up, the simulation results suggest that the total hydrate formation rate Q_H is large near the boundary, and CO_2 hydrate mainly distributes near the boundary of the reaction vessel due to the cooling effect of the temperature-controlled boundary. Besides, it is also indicated that hydrate formation rate on the hydrate film behind the gas front Q_{H2} makes the most important contribution to the large CO_2 hydrate saturation near the boundary, while on the contrary, hydrate formation rates on the gas front Q_{H1} and on the surface of the sand particles behind the gas front

Q_{H3} only have a very small contribution to CO_2 hydrate saturation in the sand sediment. Therefore, the sharp permeability reduction of the sand sediment may mainly be caused by the part of CO_2 hydrate formation on the hydrate film behind the gas front, which is likely to exist between the sand particles, occupying the pore space of the sand sediment and resulting in the blockage of the gas flow.

In the future, the simulator developed in this study is expected to be applied to the numerical simulations of CO_2 hydrate formation in the real-scale sand sediment in the ocean for sub-seabed CO_2 storage. In that case, the sizes of the cells may be hundred or thousand times larger than those used in the lab-scale sand sediment such as in this study. However, hydrate formation rate on the hydrate film behind the gas front Q_{H2} may still be dominant, and hydrate formation rate on the gas front Q_{H1} may still not be important. The reason is that Q_{H1} is mainly determined by the part of hydrate formation rate at the fresh surface (rupture), as shown in the first term on the right side of Equation (2-26), where the rupture ratio x_1 has played an important part; while the growth rate of the hydrate film hardly has any contributions to Q_{H1}, as shown in the second term on the right side of Equation (2-26). In the process of CO_2 gas injection into the real-scale sub-seabed sand sediment, as the gas front moves, the gas phase velocity U_G drops gradually due to the blockage of the gas flow, causing the rupture ratio x_1 which is proportional to U_G, to become much and much smaller as shown in Equation (2-37). As a result, hydrate formation rate at the fresh surface (rupture) has been depressed, leading to a small Q_{H1}. This suggests that even in the real-scale numerical simulations, Q_{H2} should still be much larger than Q_{H1}, which agrees with the calculation results obtained in this study. Therefore, it is safe to say that the simulator developed in this study can be applied to the real-scale numerical simulations directly.

At last, it is worth mentioning that the experiments conducted by Inui [1-18] were completed at the moment when gas was discharged from the outlet of the reaction vessel. Therefore, compared with Case 6I, the calculation results of Case 7I are much closer to the actual situation of the experiment, because the gas front arrives at the outlet of the reaction vessel at the end of the calculation, as shown in Fig. 3-64. In the future work, improvements should be made to make the calculation results of both the two cases much more accurate and closer to the actual situation of the experiments.

102
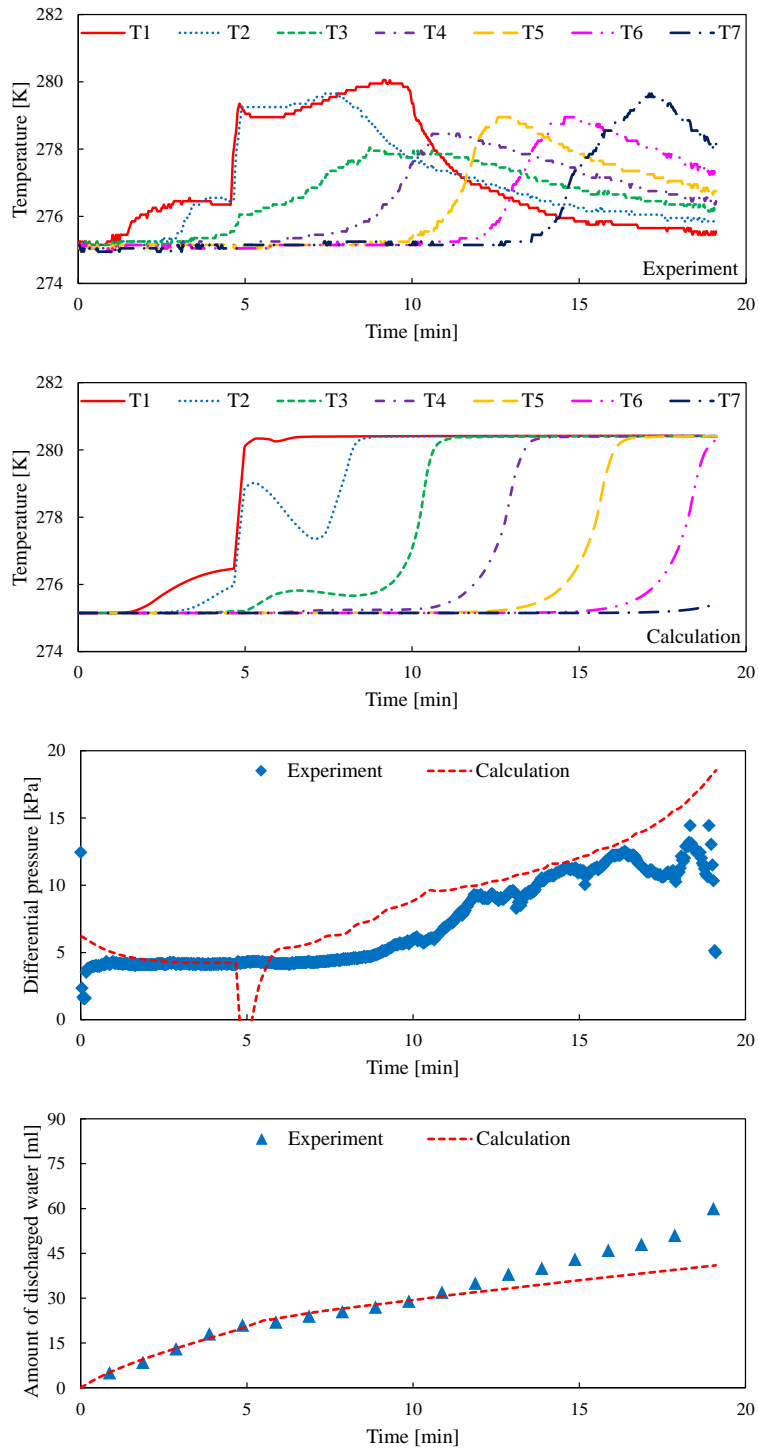
Fig. 3- 40 The comparisons between the calculation results and the experimental data in Case
6H

(First two) The temperature changes detected at T1~T7

(Third) The differential pressure between the inlet and outlet of the reaction vessel

(Fourth) The amount of discharged water from the outlet of the reaction vessel
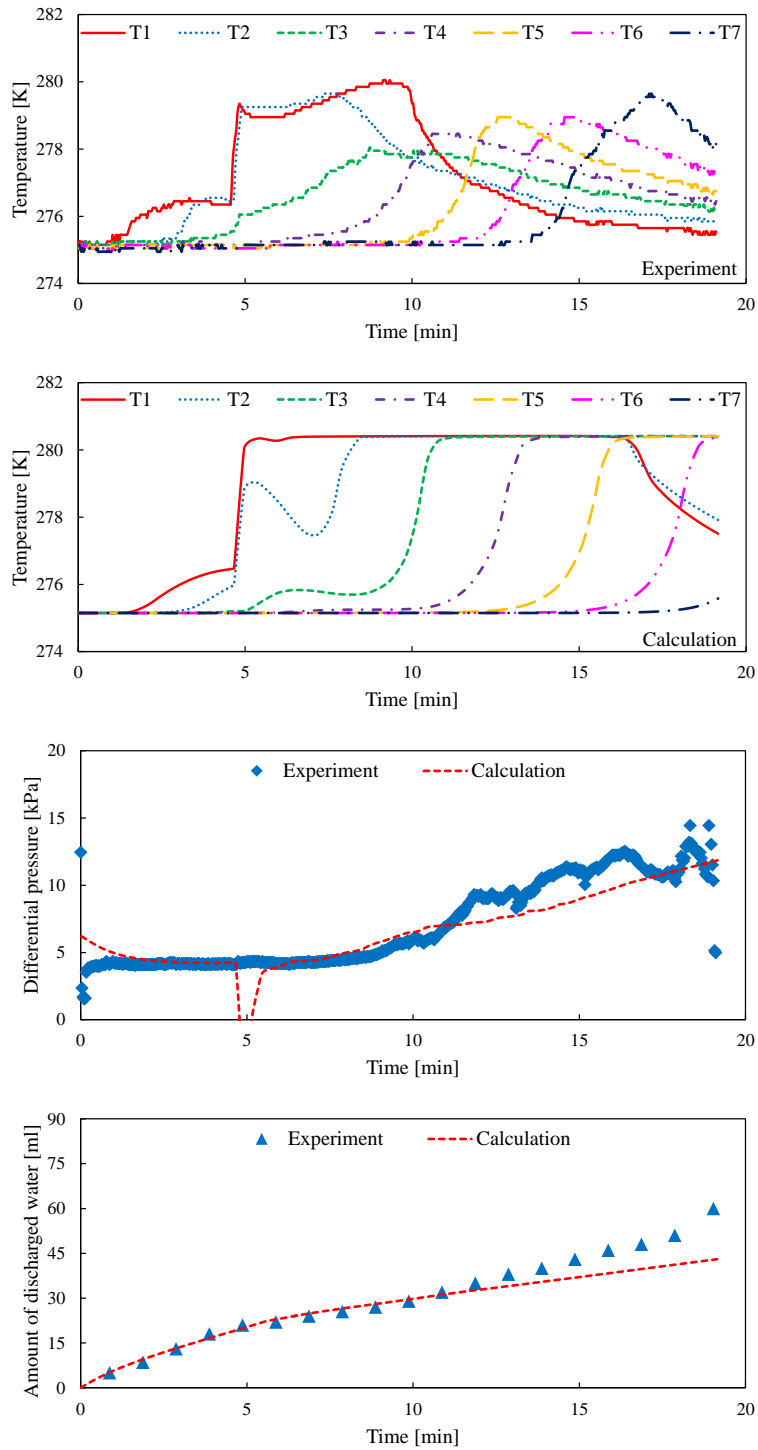
Fig. 3- 41 The comparisons between the calculation results and the experimental data in Case 6I

(First two) The temperature changes detected at T1~T7

(Third) The differential pressure between the inlet and outlet of the reaction vessel

(Fourth) The amount of discharged water from the outlet of the reaction vessel
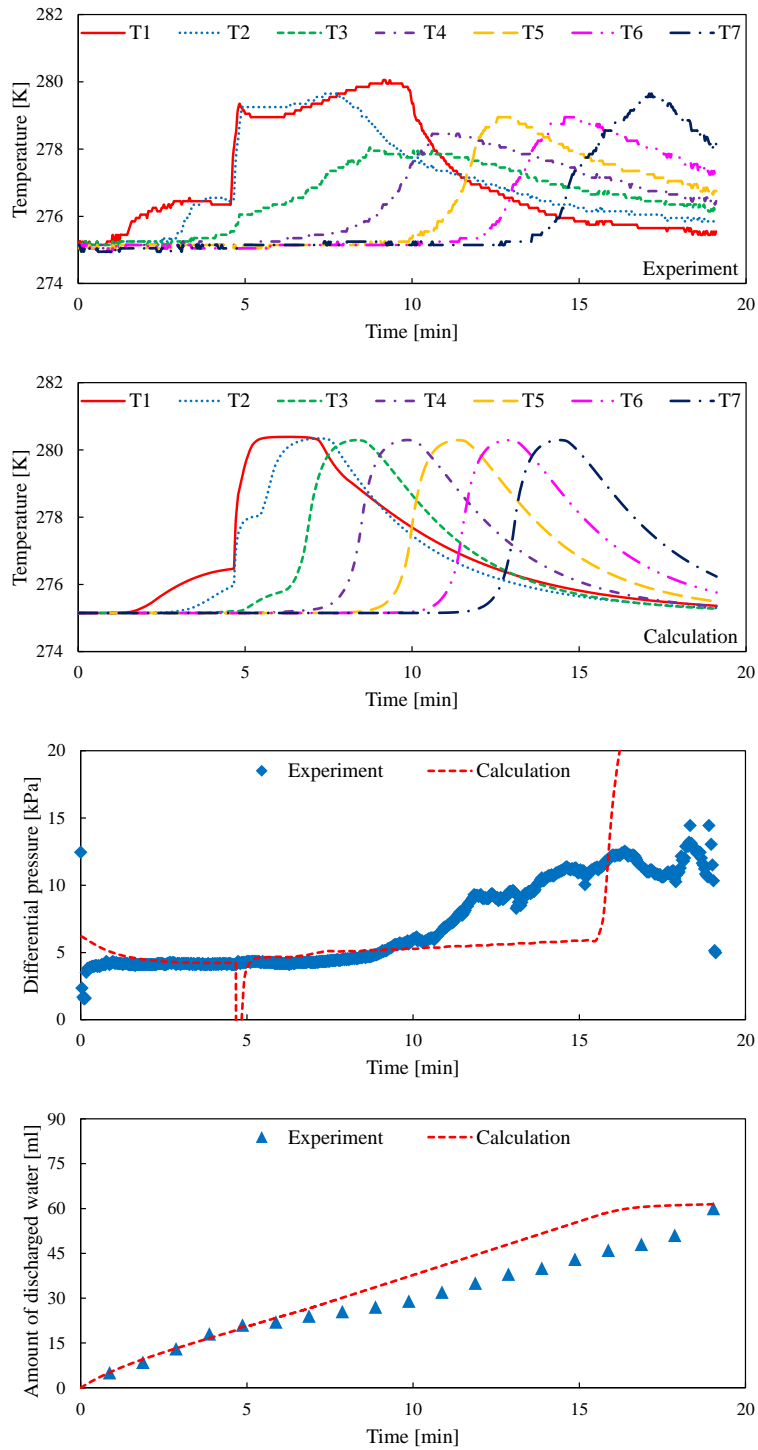
Fig. 3- 42 The comparisons between the calculation results and the experimental data in Case 6J

(First two) The temperature changes detected at T1~T7

(Third) The differential pressure between the inlet and outlet of the reaction vessel

(Fourth) The amount of discharged water from the outlet of the reaction vessel
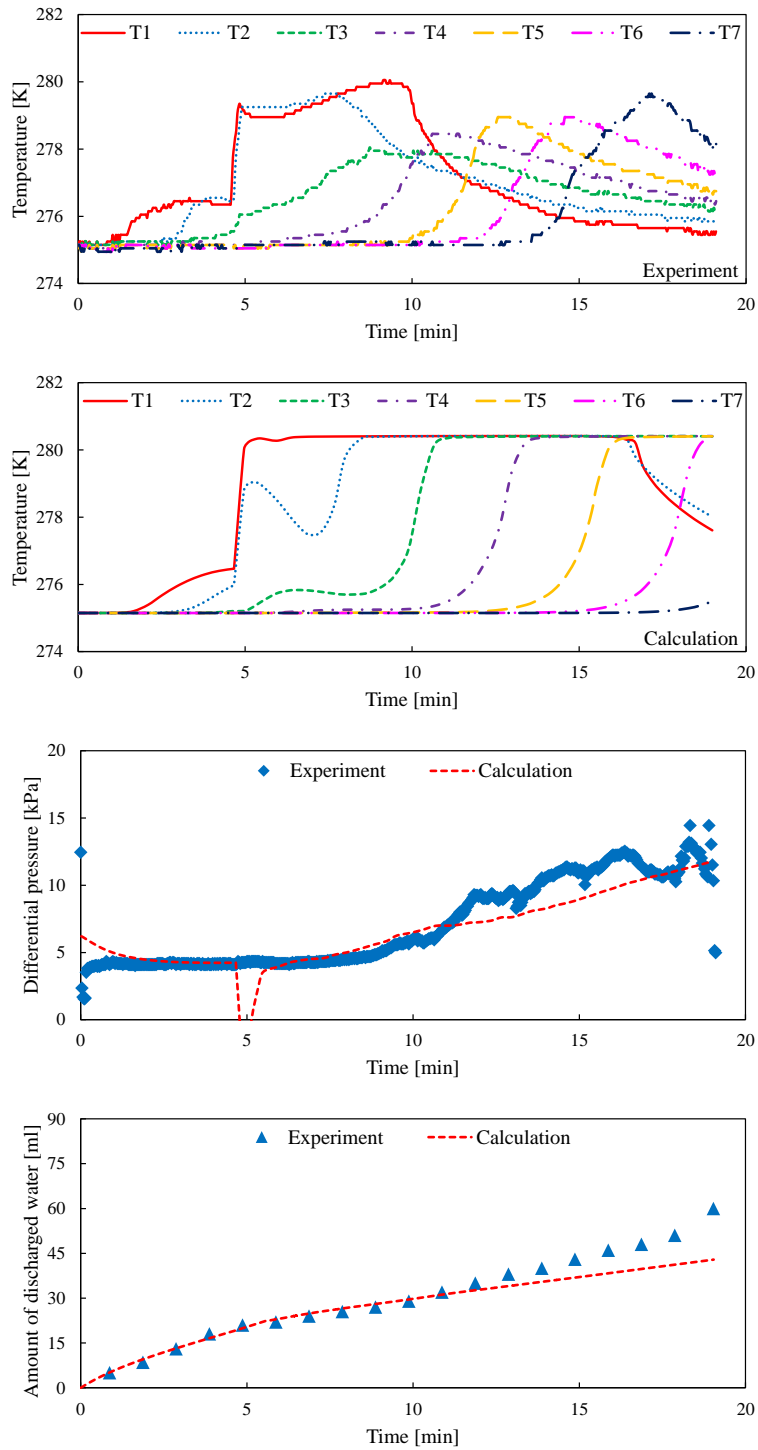
Fig. 3- 43 The comparisons between the calculation results and the experimental data in Case
6K

(First two) The temperature changes detected at T1~T7

(Third) The differential pressure between the inlet and outlet of the reaction vessel

(Fourth) The amount of discharged water from the outlet of the reaction vessel
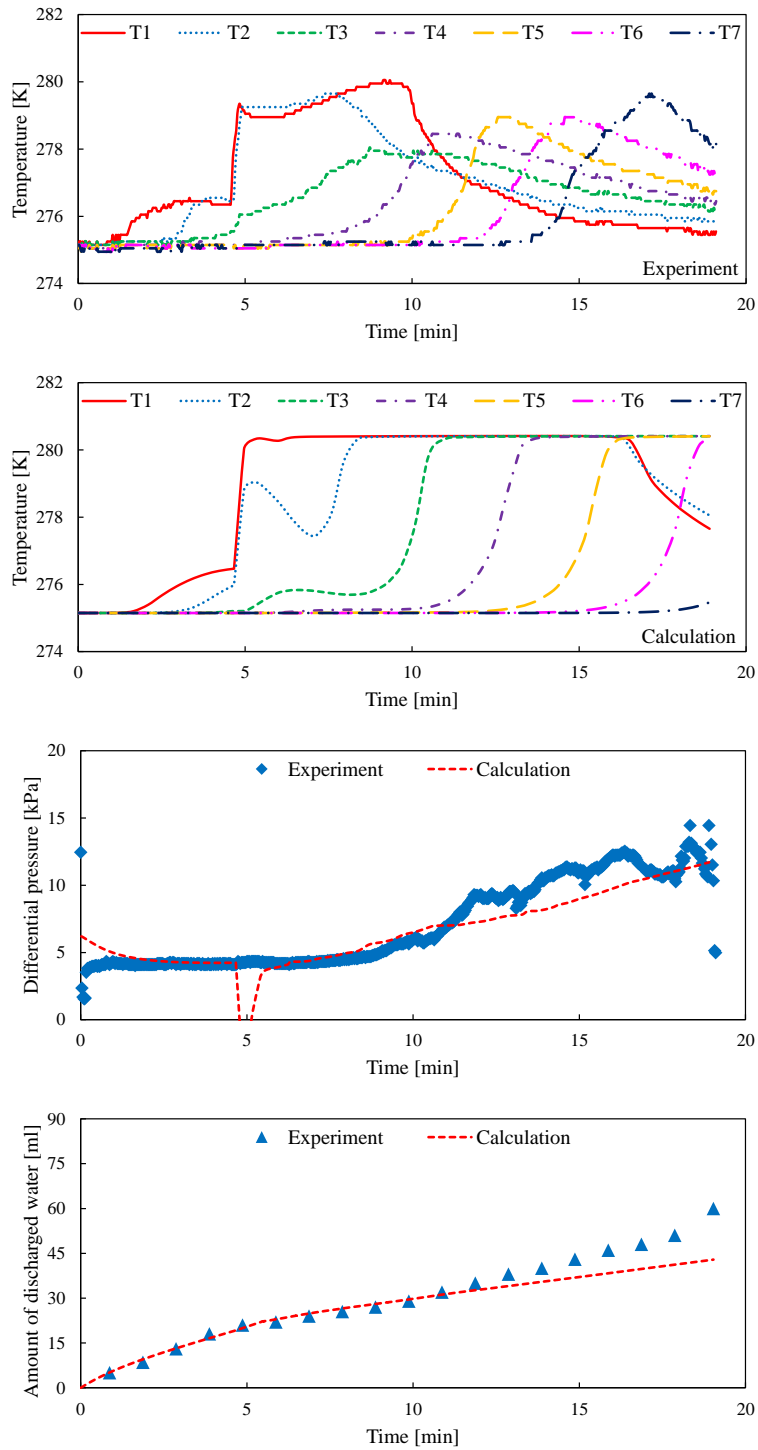
Fig. 3- 44 The comparisons between the calculation results and the experimental data in Case 6L

(First two) The temperature changes detected at T1~T7

(Third) The differential pressure between the inlet and outlet of the reaction vessel

(Fourth) The amount of discharged water from the outlet of the reaction vessel
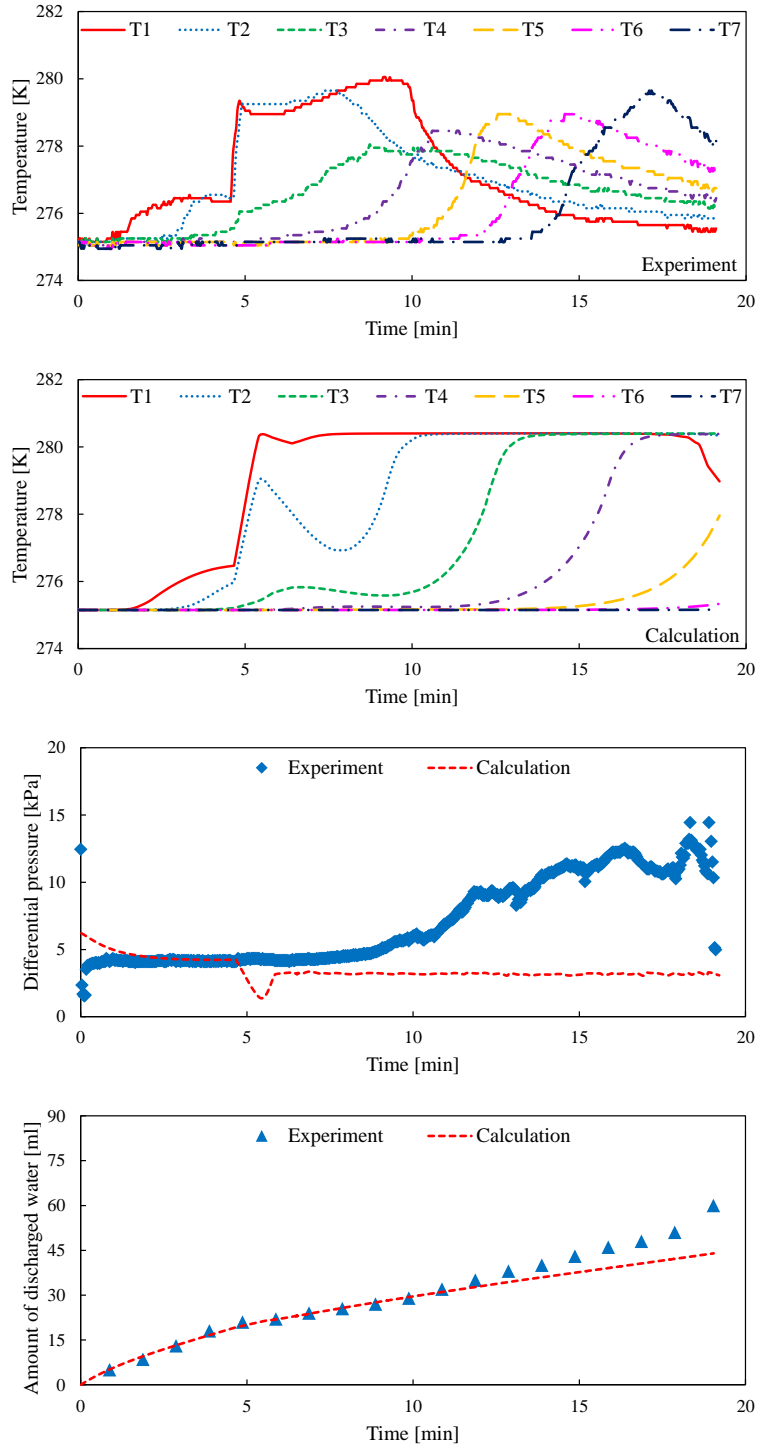
Fig. 3- 45 The comparisons between the calculation results and the experimental data in Case 6M

(First two) The temperature changes detected at T1~T7

(Third) The differential pressure between the inlet and outlet of the reaction vessel

(Fourth) The amount of discharged water from the outlet of the reaction vessel
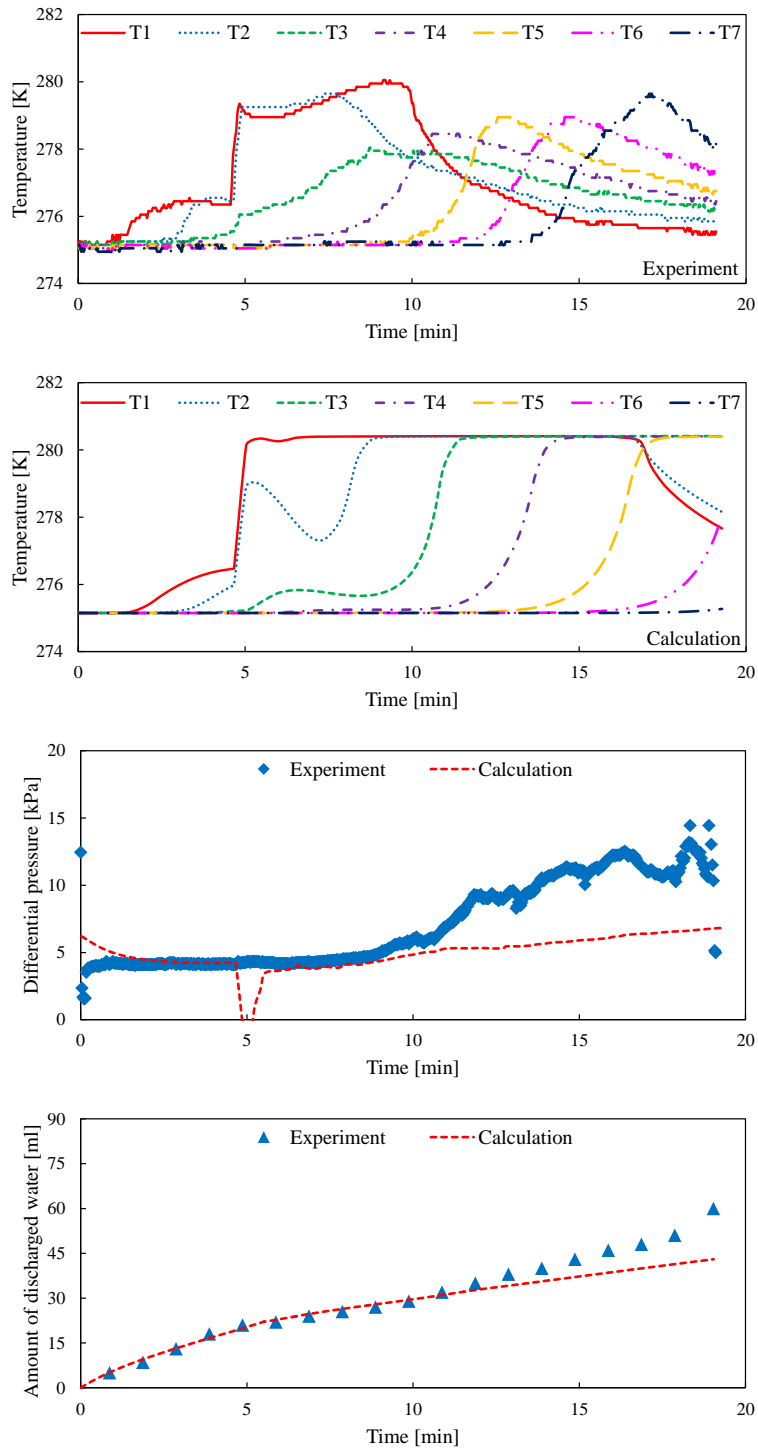
Fig. 3- 46 The comparisons between the calculation results and the experimental data in Case
6N

(First two) The temperature changes detected at T1~T7

(Third) The differential pressure between the inlet and outlet of the reaction vessel

(Fourth) The amount of discharged water from the outlet of the reaction vessel
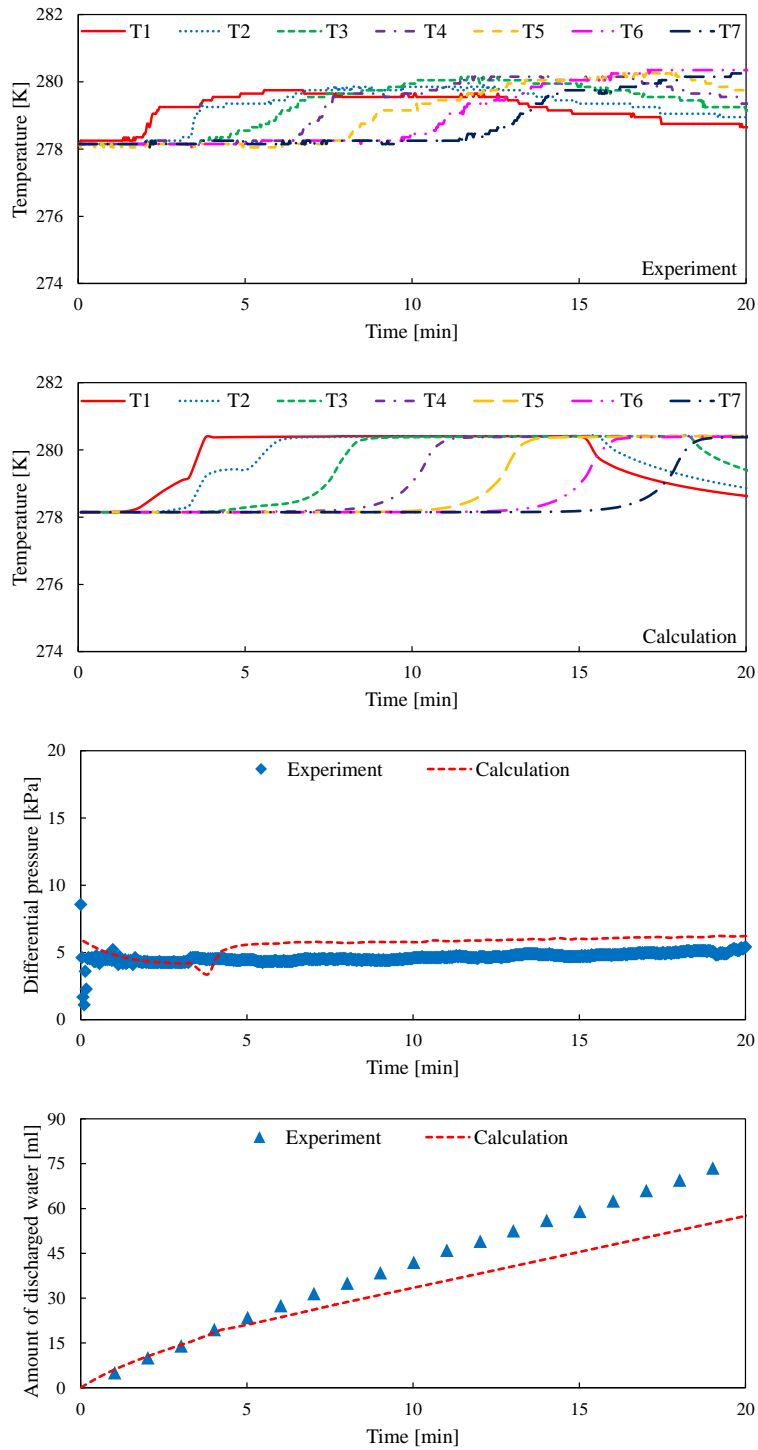
Fig. 3- 47 The comparisons between the calculation results and the experimental data in Case 7H

(First two) The temperature changes detected at T1~T7

(Third) The differential pressure between the inlet and outlet of the reaction vessel

(Fourth) The amount of discharged water from the outlet of the reaction vessel
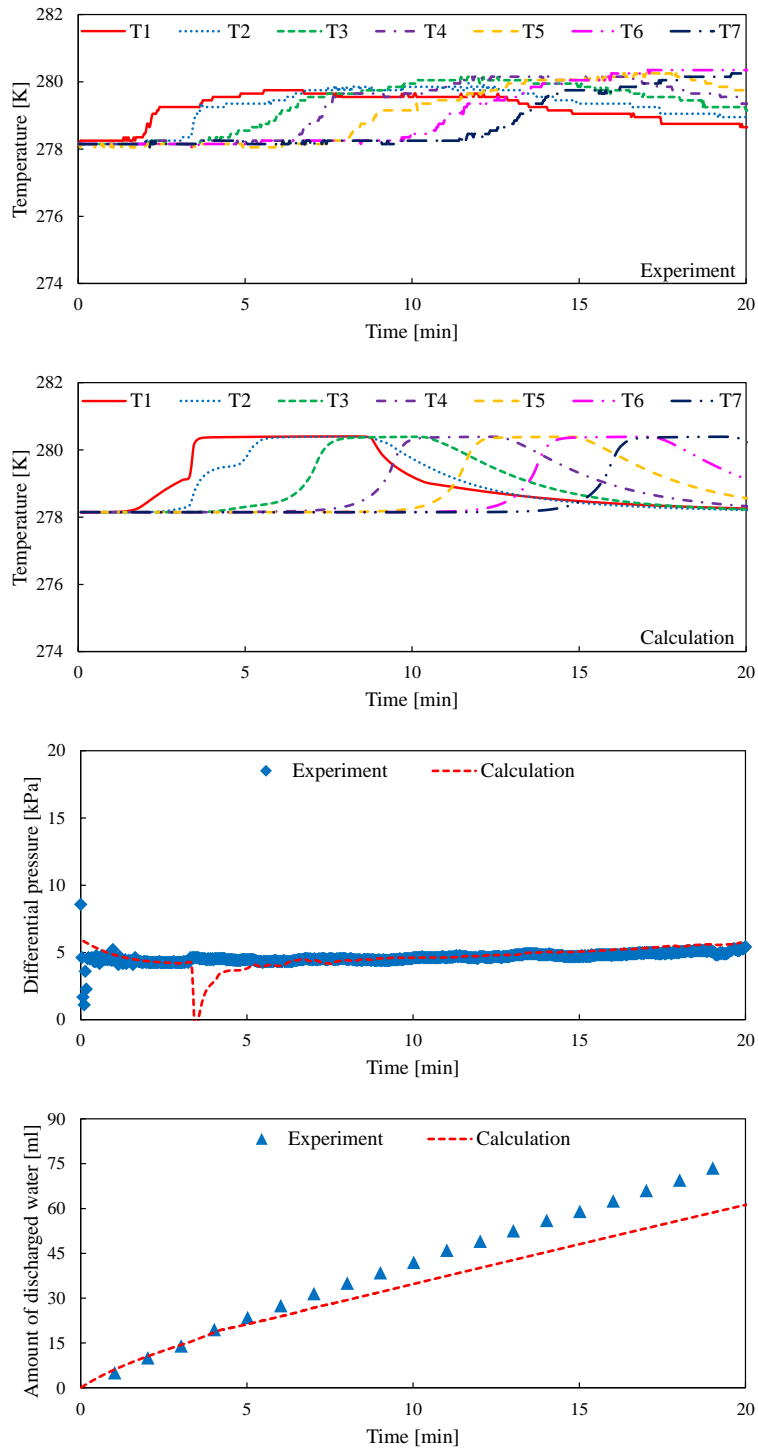
Fig. 3- 48 The comparisons between the calculation results and the experimental data in Case 7I

(First two) The temperature changes detected at T1~T7

(Third) The differential pressure between the inlet and outlet of the reaction vessel

(Fourth) The amount of discharged water from the outlet of the reaction vessel
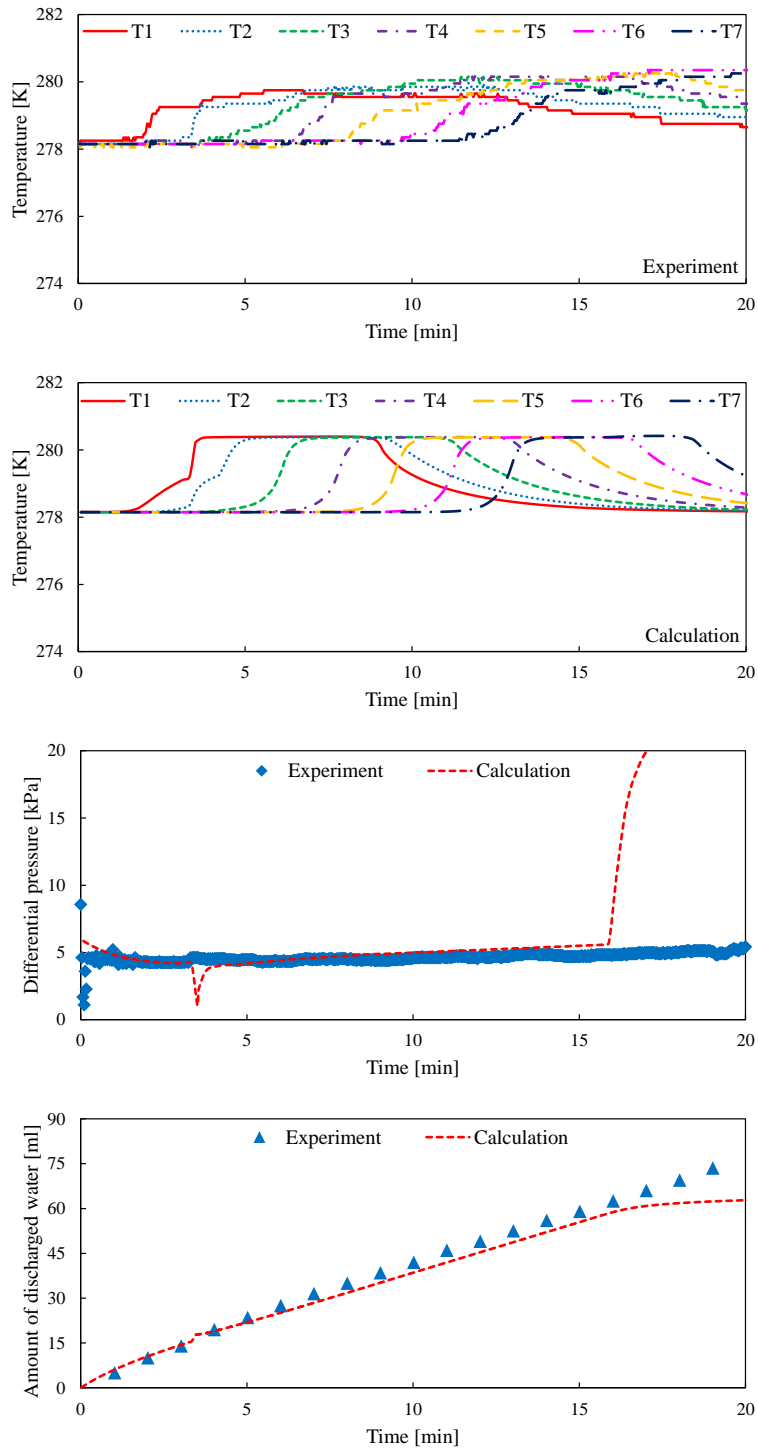
Fig. 3- 49 The comparisons between the calculation results and the experimental data in Case 7J

(First two) The temperature changes detected at T1~T7

(Third) The differential pressure between the inlet and outlet of the reaction vessel

(Fourth) The amount of discharged water from the outlet of the reaction vessel
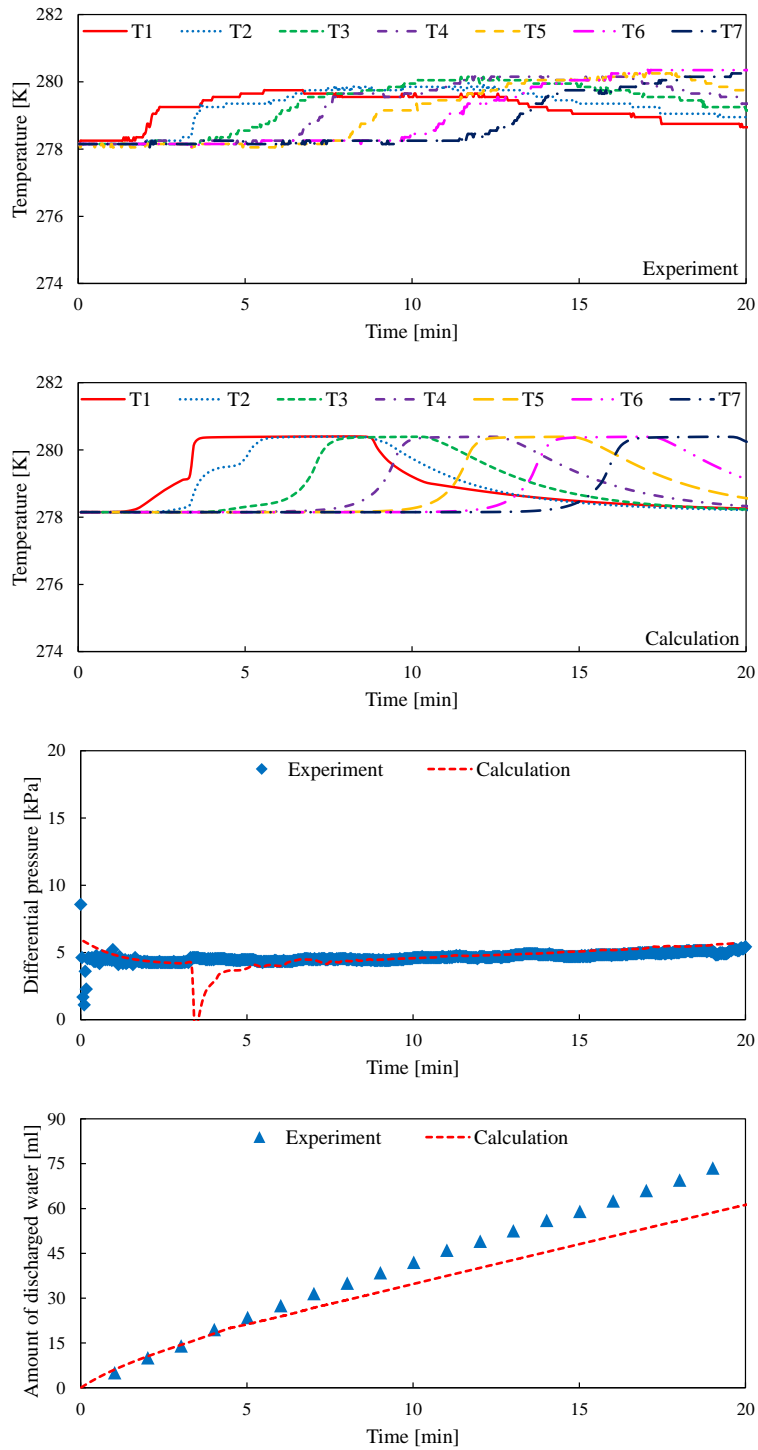
Fig. 3- 50 The comparisons between the calculation results and the experimental data in Case
7K

(First two) The temperature changes detected at T1~T7

(Third) The differential pressure between the inlet and outlet of the reaction vessel

(Fourth) The amount of discharged water from the outlet of the reaction vessel

113
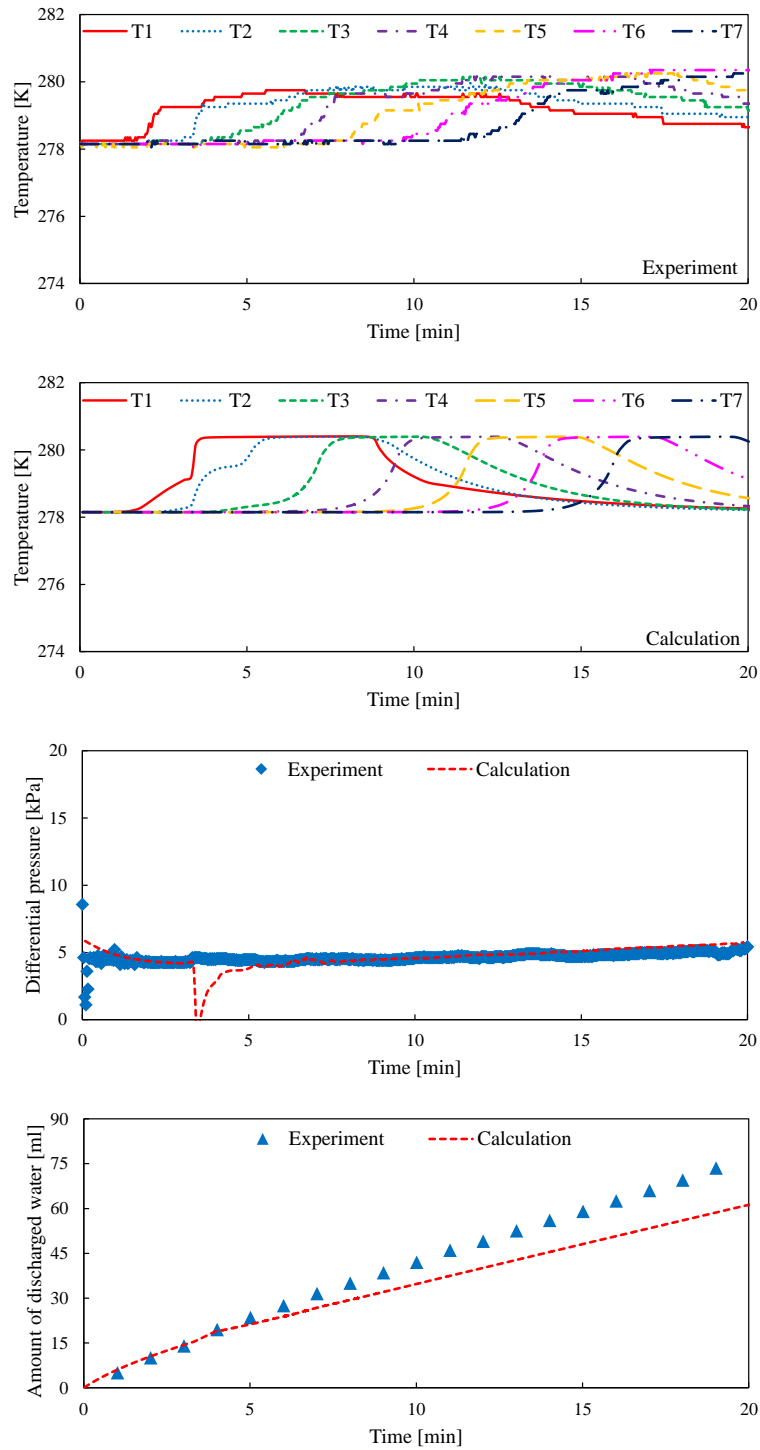
Fig. 3- 51 The comparisons between the calculation results and the experimental data in Case
7L

(First two) The temperature changes detected at T1~T7

(Third) The differential pressure between the inlet and outlet of the reaction vessel

(Fourth) The amount of discharged water from the outlet of the reaction vessel
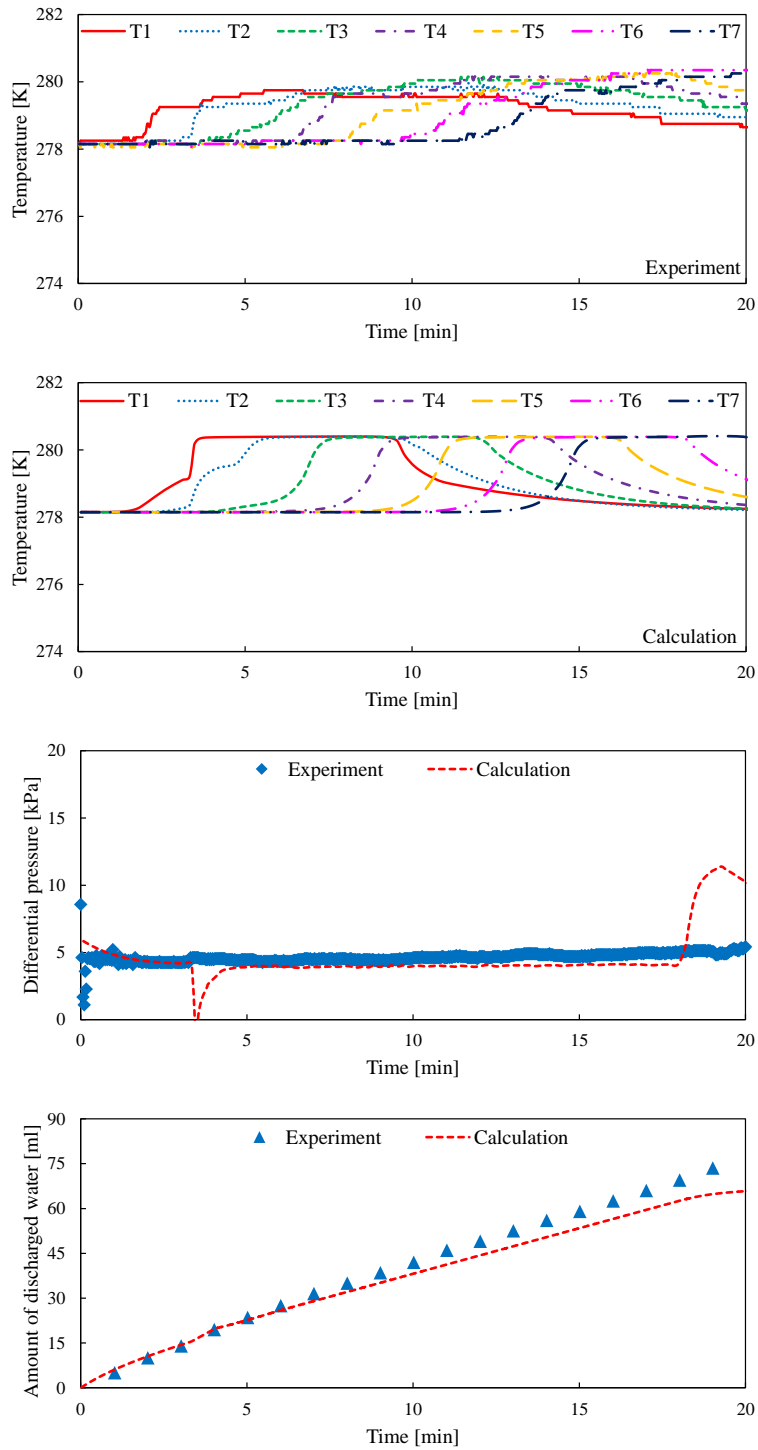
Fig. 3- 52 The comparisons between the calculation results and the experimental data in Case
7M

(First two) The temperature changes detected at T1~T7

(Third) The differential pressure between the inlet and outlet of the reaction vessel

(Fourth) The amount of discharged water from the outlet of the reaction vessel
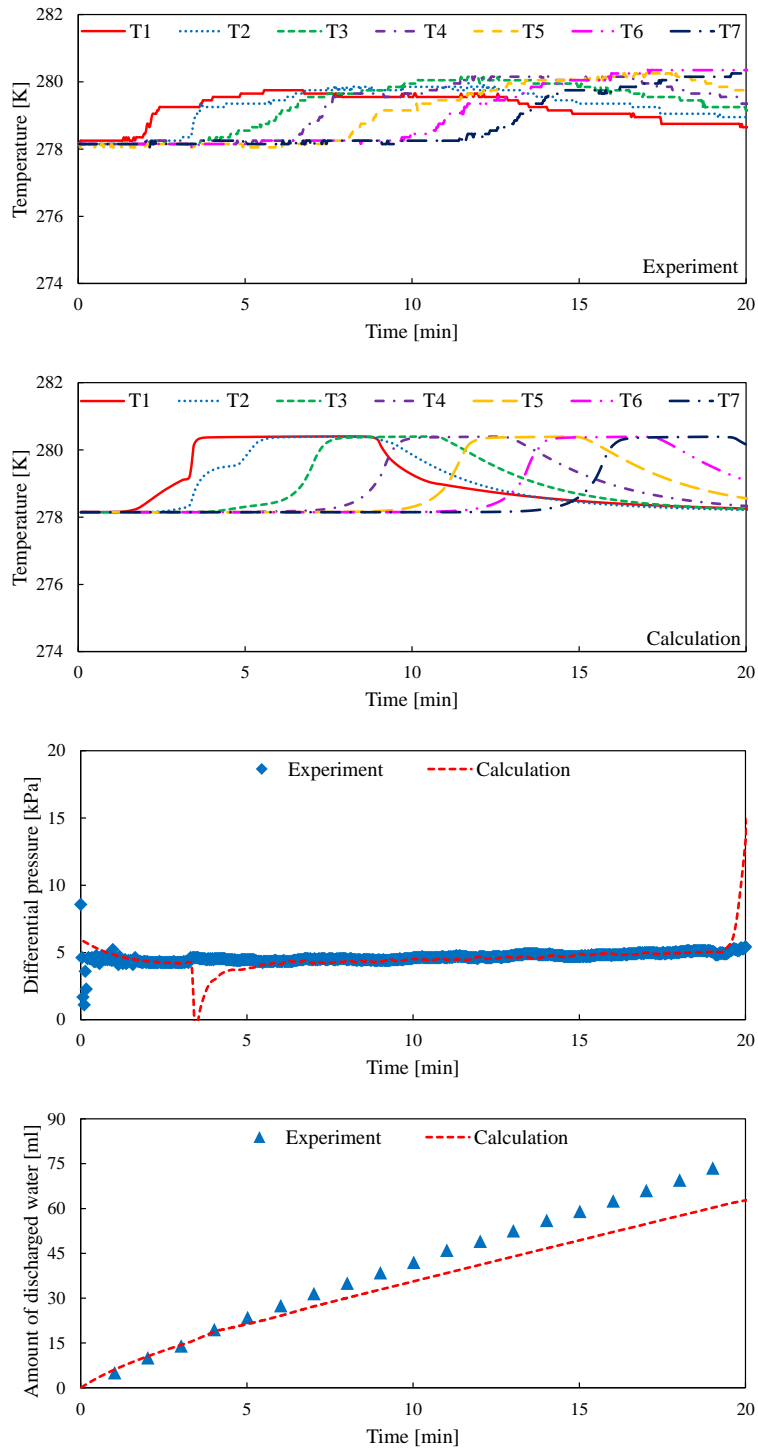
Fig. 3- 53 The comparisons between the calculation results and the experimental data in Case
7N

(First two) The temperature changes detected at T1~T7

(Third) The differential pressure between the inlet and outlet of the reaction vessel

(Fourth) The amount of discharged water from the outlet of the reaction vessel
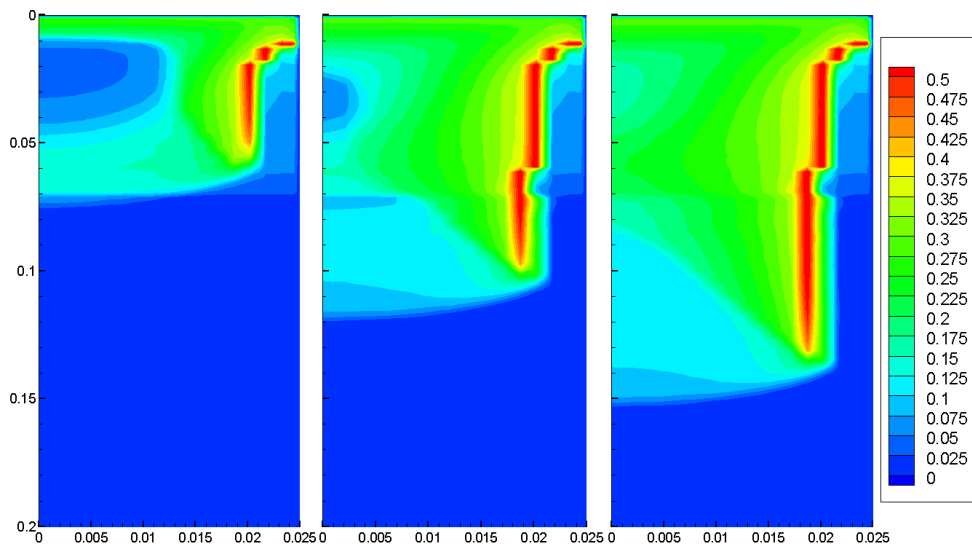
Fig. 3- 54 The contour maps of CO_2 hydrate saturation S_H [m³/m³] with time in Case 6I
(Left: 10 min; Middle: 15 min; Right: End time)
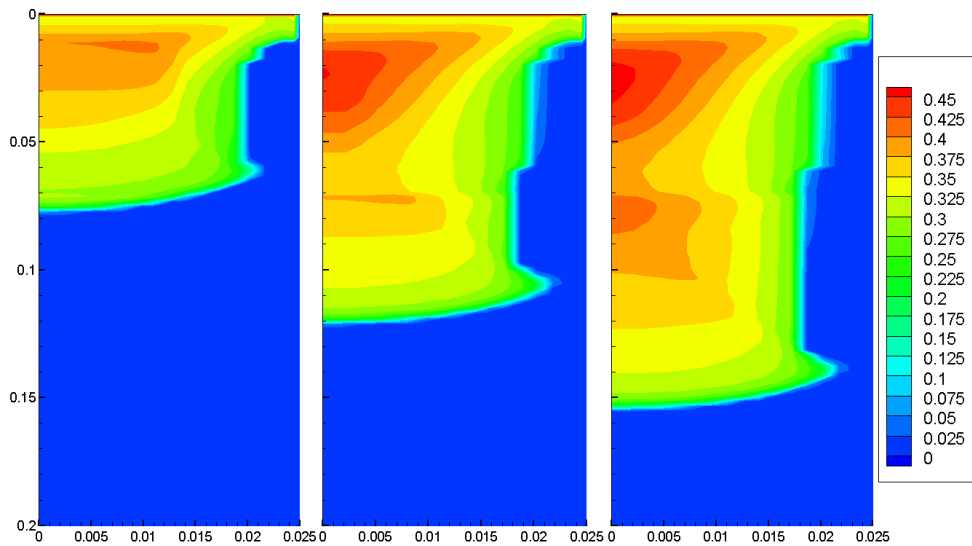
Fig. 3- 55 The contour maps of CO_2 gas saturation S_G [m³/m³] with time in Case 6I
(Left: 10 min; Middle: 15 min; Right: End time)
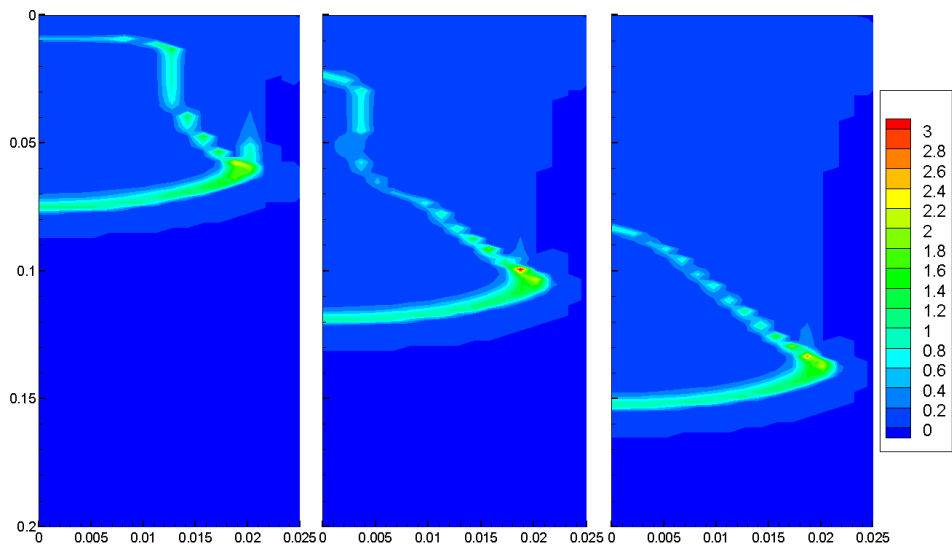
Fig. 3- 56 The contour maps of total hydrate formation rate Q_H [kg/m³/s] with time in Case 6I

(Left: 10 min; Middle: 15 min; Right: End time)
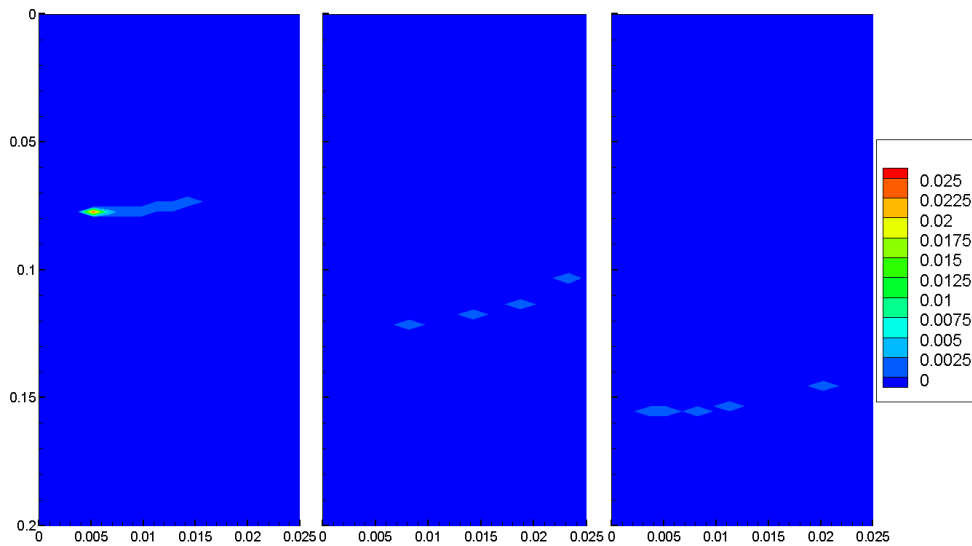
Fig. 3- 57 The contour maps of hydrate formation rate on the gas front Q_{H1} [kg/m³/s]

with time in Case 6I

(Left: 10 min; Middle: 15 min; Right: End time)
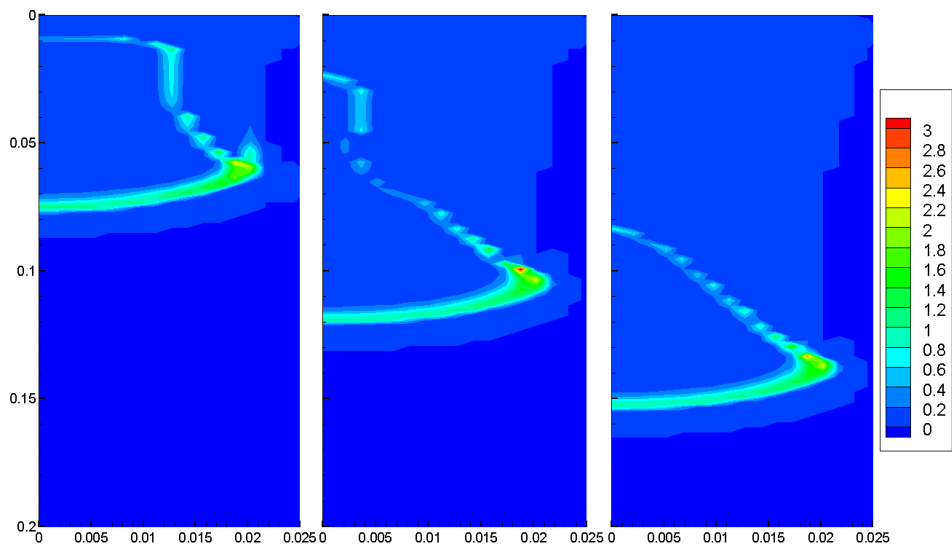
Fig. 3- 58 The contour maps of hydrate formation rate on the hydrate film behind the gas front

Q_{H2} [kg/m³/s] with time in Case 6I

(Left: 10 min; Middle: 15 min; Right: End time)
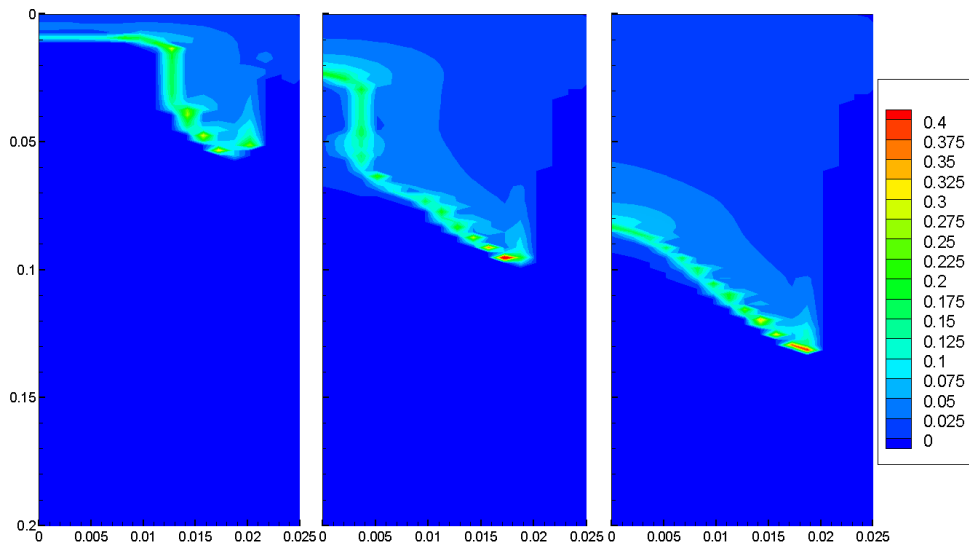
Fig. 3- 59 The contour maps of hydrate formation rate on the surface of the sand particles

behind the gas front Q_{H3} [kg/m³/s] with time in Case 6I

(Left: 10 min; Middle: 15 min; Right: End time)
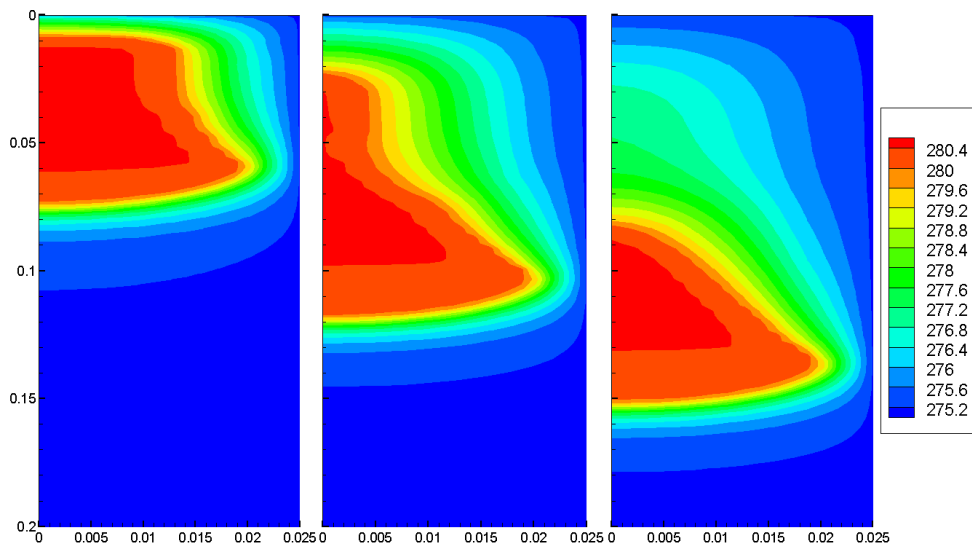
Fig. 3- 60 The contour maps of temperature T [K] with time in Case 6I

(Left: 10 min; Middle: 15 min; Right: End time)
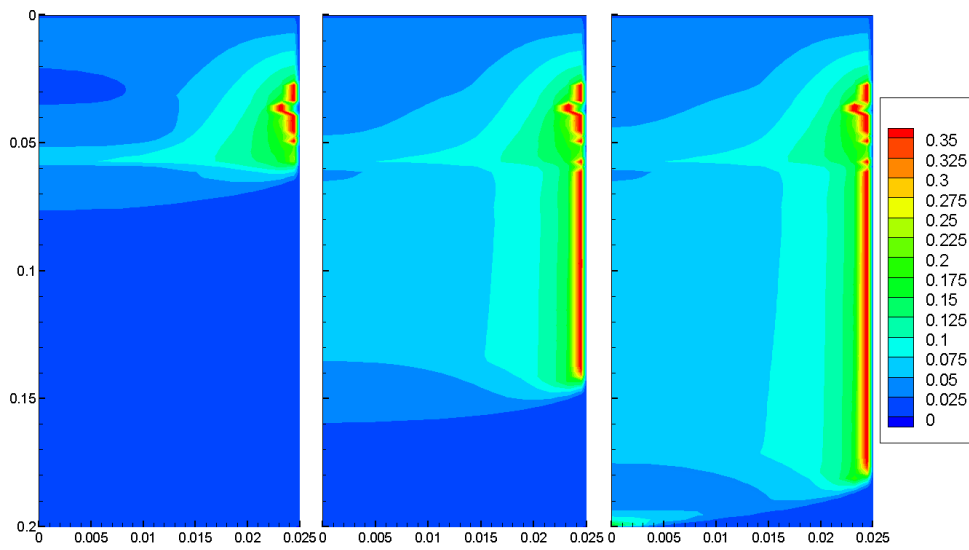
Fig. 3- 61 The contour maps of CO_2 hydrate saturation S_H [m^3/m^3] with time in Case 7I
(Left: 10 min; Middle: 15 min; Right: End time)
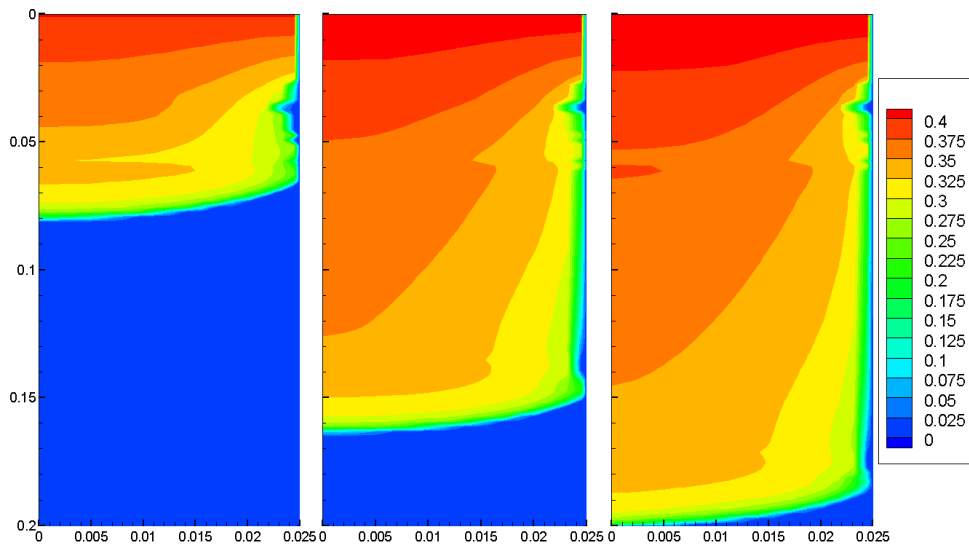
Fig. 3- 62 The contour maps of CO_2 gas saturation S_G [m^3/m^3] with time in Case 7I
(Left: 10 min; Middle: 15 min; Right: End time)
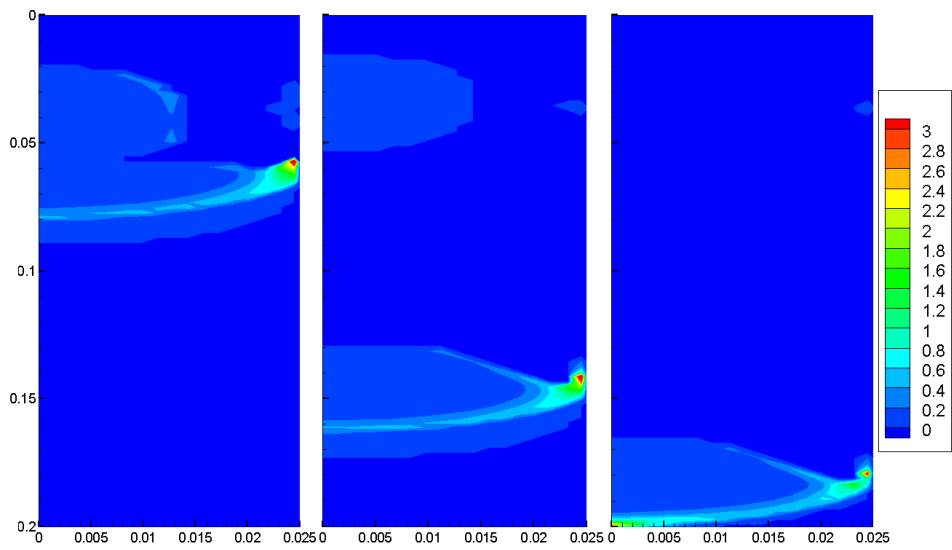
Fig. 3- 63 The contour maps of total hydrate formation rate Q_H [kg/m³/s] with time in Case 7I

(Left: 10 min; Middle: 15 min; Right: End time)
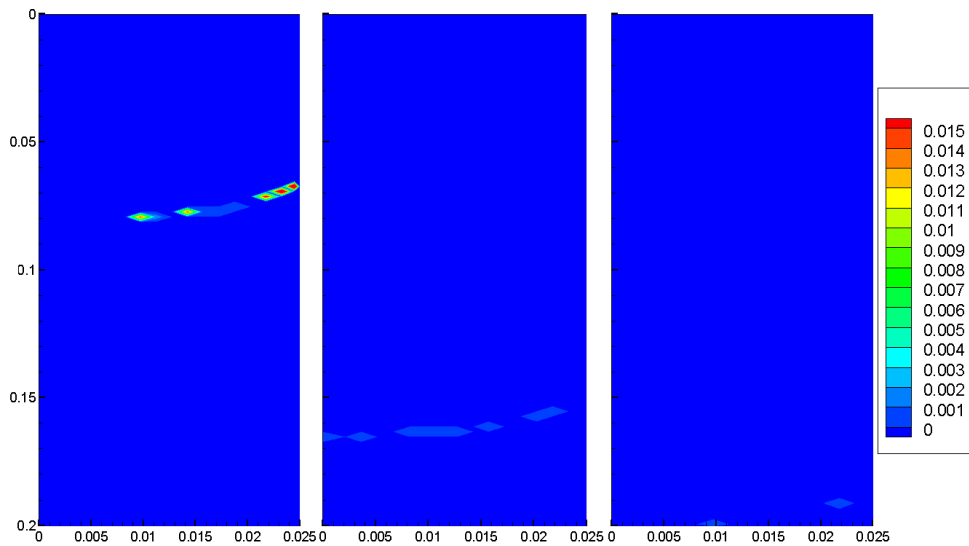
Fig. 3- 64 The contour maps of hydrate formation rate on the gas front Q_{H1} [kg/m³/s]

with time in Case 7I

(Left: 10 min; Middle: 15 min; Right: End time)
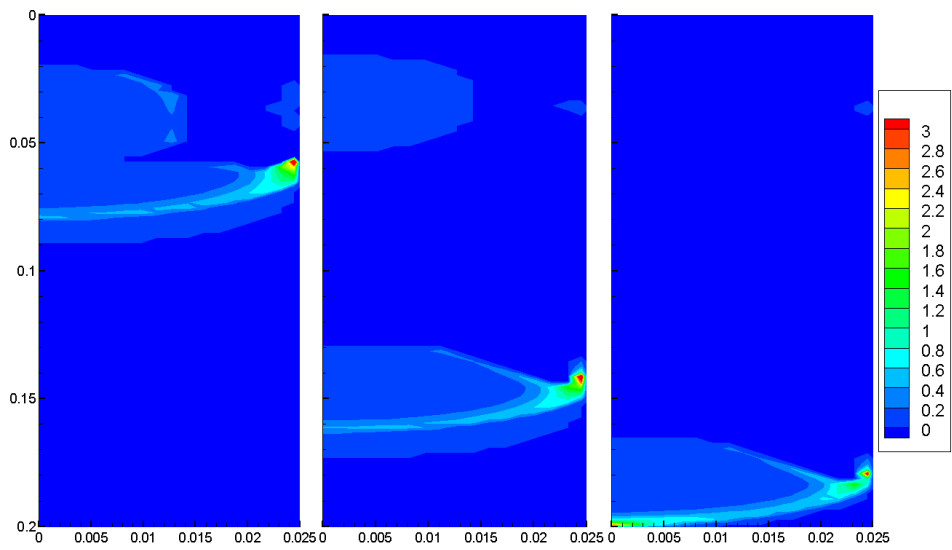
Fig. 3- 65 The contour maps of hydrate formation rate on the hydrate film behind the gas front

Q_{H2} [kg/m³/s] with time in Case 7I

(Left: 10 min; Middle: 15 min; Right: End time)
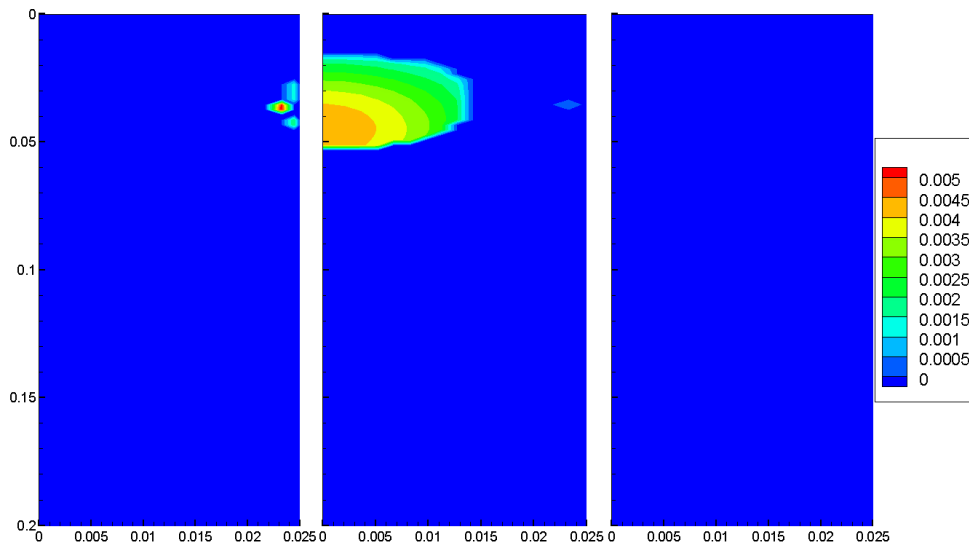
Fig. 3- 66 The contour maps of hydrate formation rate on the surface of the sand particles

behind the gas front Q_{H3} [kg/m³/s] with time in Case 7I

(Left: 10 min; Middle: 15 min; Right: End time)
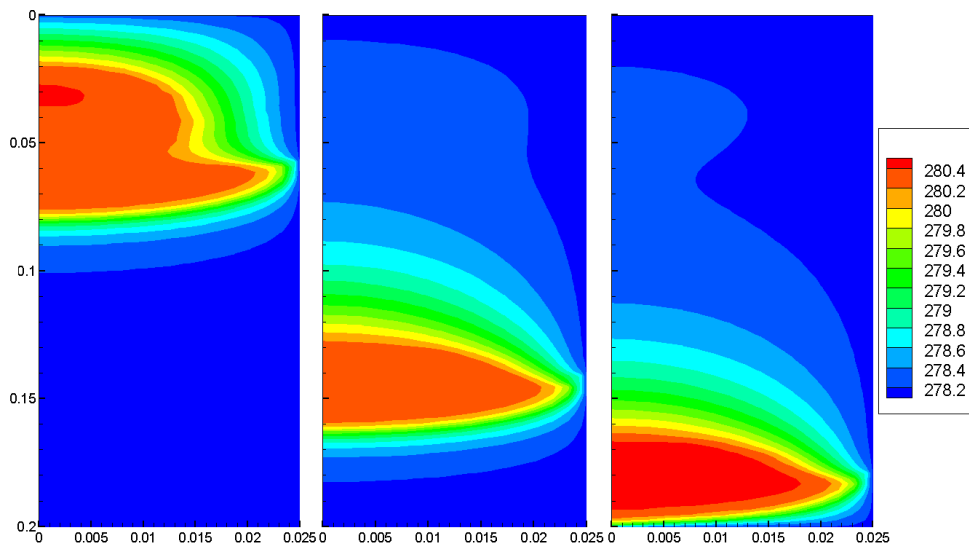
Fig. 3- 67 The contour maps of temperature T [K] with time in Case 7I

(Left: 10 min; Middle: 15 min; Right: End time)

3.3 Summary

In this chapter, numerical simulations of CO_2 hydrate formation in the sand sediment without and with gas-liquid two-phase flow are conducted, respectively, using the inclusive model for CO_2 hydrate formation proposed in this study. The calculation results agree with the experimental data, so that unknown model parameters in the numerical simulator are determined by parameter-fitting. The summary of the unknown model parameters fitted in this study are shown in Table 3-8.

In the next chapter, validation of the inclusive model for CO_2 hydrate formation will be carried out using the model parameters determined in this chapter.

Table 3- 8 The summary of the unknown model parameters fitted in this study

Extracted from	Name of the unknown model parameter	Symbol	Unit	Value	Universality	Other value sources
CO$_2$ hydrate formation without gas-liquid two-phase flow	Intrinsic rate constant of CO$_2$ hydrate formation	k_f	mol/m^2/Pa/s	$k_f = k_0 \exp\left(-\dfrac{\Delta E}{RT}\right)$ $k_0 = 1.73 \times 10^{13}$ mol/m^2/Pa/s $\Delta E = 115.6$ kJ	Universal (the same order as Clarke and Bishnoi [3-5])	Inui [1-18], Takahashi et al. [1-19]
	CO$_2$ diffusion constant in the hydrate film	k_d	mol/m/Pa/s	3.30×10^{-18}	Universal	Inui [1-18], Takahashi et al. [1-19]
	Rupture ratio coefficient behind the gas front	β	m^{-2}	$1.0 \sim 8.0 \times 10^{13}$	Universal (under non-flow condition)	Takahashi et al. [1-19]
CO$_2$ hydrate formation with gas-liquid two-phase flow (Induction stage)	Relative permeability model exponent	n_{rG}	—	8	Universal (the same order as Sakamoto et al. [2-7])	Nakashima [1-20]
	Capillary pressure model exponent	n_{P_c}	—	0.1	Universal (the same order as Sakamoto et al. [2-7])	Nakashima [1-20]
	CO$_2$ mass transfer coefficient	k_t	m/s	1.5×10^{-7}	Dependent on the physical properties of the fluid	Inui [1-18], Nakashima [1-20]
CO$_2$ hydrate formation with gas-liquid two-phase flow (Formation stage)	Rupture ratio coefficient on the gas front	α	s	1.0	Dependent on the shape of the sand particle	Originality
	Rupture ratio coefficient behind the gas front	β	m^{-2}	5.0×10^{10}	Universal (under the condition of gas-liquid two-phase flow)	Nakashima [1-20]
	Permeability reduction exponent	N	—	15.5	Universal (the same order as Masuda et al. [2-17])	Inui [1-18], Nakashima [1-20], Yu et al. [1-22]

4 VALIDATION OF THE INCLUSIVE MODEL FOR CO₂ HYDRATE FORMATION

In Chapter 3, unknown parameters in the models have been determined by parameter-fitting. In this chapter, in order to validate the inclusive model for CO_2 hydrate formation proposed in this study, numerical simulations of CO_2 hydrate formation in the lab-scale sediment by liquid CO_2 injection are conducted using the model parameters determined in the last chapter, and the calculation results are compared with the experimental data of CO_2 hydrate formation in the lab-scale sediment by liquid CO_2 injection.

4.1 Experimental Outline of CO₂ Hydrate Formation in the Lab-scale Sediment by Liquid CO₂ Injection

In this section, experiments of CO_2 hydrate formation in the lab-scale sediment by liquid CO_2 injection carried out by Li et al. [4-1] are introduced at first. Then, based on the experiments, simulations of CO_2 hydrate formation in the lab-scale sediment by liquid CO_2 injection under the experimental conditions are conducted by the numerical simulator using the model parameters determined in Chapter 3 in order to validate the inclusive model for CO_2 hydrate formation proposed in this study.

4.1.1 Experimental apparatus and procedures

The experimental apparatus used by Li et al. [4-1] mainly consisted of a reaction vessel, a cooling unit, fluid injection and discharge parts. The schematic diagram of the experimental apparatus is shown in Fig. 4-1. The reaction vessel was made of stainless steel (high-pressure vessel) with the internal diameter of 49.5 mm and the depth of 250 mm. In order to measure the temperature changes with time in the sediment, three sets of thermocouples (total ten thermocouples, hereinafter referred to as TC.1 ~ TC.10) were placed inside the reaction vessel with the interval of 35 mm vertically and 120º horizontally, among which TC.1 ~ TC.5 were placed at the center of the reaction vessel, and TC.6 ~ TC.10 were placed at the locations which were 10 mm far from the center of the reaction vessel. Besides, TC.2/TC.6, TC.3/TC.7/TC.9, and TC.4/TC.8/TC.10 were at the same height, respectively. In addition, liquid CO_2 was injected into the center of the reaction vessel through an L-shape steel tube directly, the inlet of which was 8 mm higher than TC.2/TC.6. The locations and distributions of the ten thermocouples in the reaction vessel are shown in Fig. 4-2.
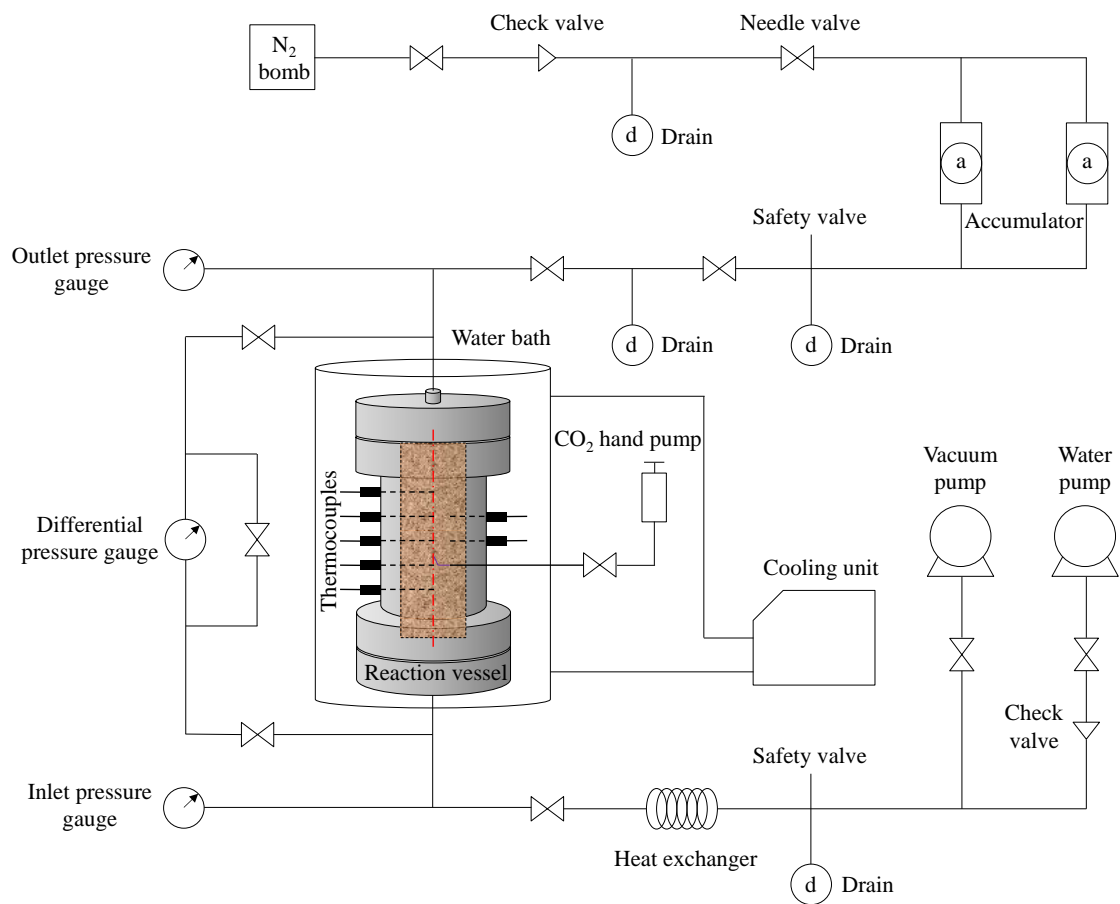
Fig. 4- 1 The schematic diagram of the experimental apparatus for CO_2 hydrate formation in the lab-scale sediment by liquid CO_2 injection [4-1]
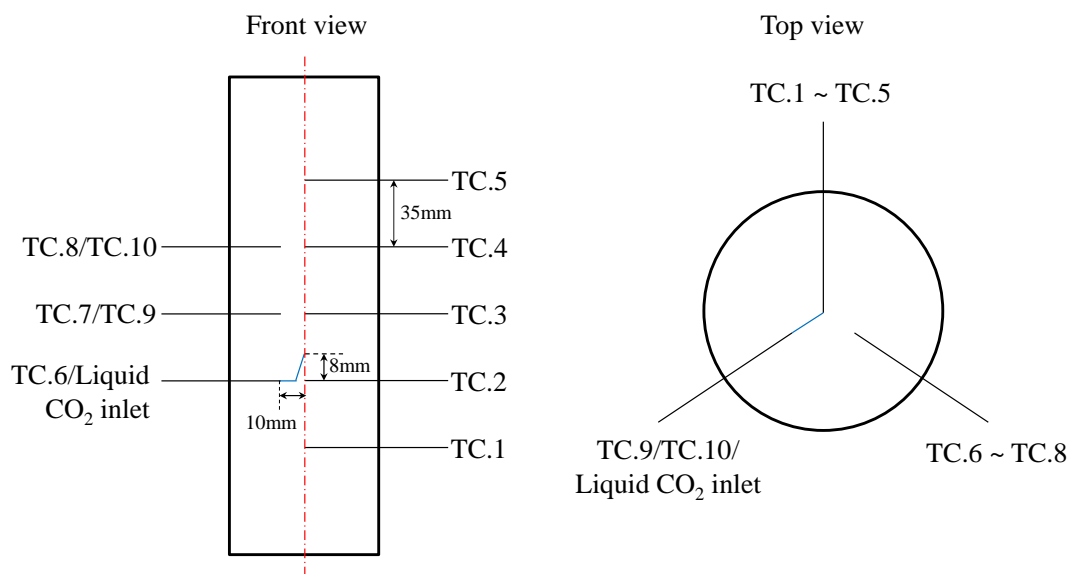
Fig. 4- 2 The locations and distributions of the ten thermocouples in the reaction vessel [4-1]

The experimental procedures are summarized in brief according to Li et al. [4-1], with the illustration of the experimental apparatus as below.

1) First, water-saturated sediment was prepared by filling glass beads (BZ-02) and pure water into the reaction vessel. Besides, in order to eliminate the air bubbles inside the sediment, the reaction vessel was beaten lightly with a wooden hammer in the side during the glass beads filling.

2) After the sediment was set up, the reaction vessel was bathed in the cooling unit at the experimental temperature. Then, water was injected from the bottom of the reaction vessel at a constant rate by the water pump to elevate the pressure inside the reaction vessel to be much higher than the experimental value.

3) After the valve at the bottom of the reaction vessel was closed, obvious pressure drop was observed due to the compression of the residual air.

4) The water injection process was repeated until no obvious pressure drop was observed inside the reaction vessel.

5) After the pressure in the accumulators were adjusted to the experimental pressure by the N_2 gas bomb, the accumulator valves were opened to set the pressure inside the reaction vessel to be the experimental value.

6) Liquid CO_2 was supplied from the CO_2 hand pump into the spiral tube bathed in the cooling unit. Thus, a certain amount of liquid CO_2 was injected from the spiral tube into the reaction vessel. Then, the valves of the CO_2 hand pump and the accumulators were closed, and the measurements were started.

7) CO_2 hydrate formation was confirmed by the temperature rises detected at the ten thermocouples placed inside the reaction vessel.

8) After two hours since hydrate formation, the drain valve was opened to decrease the pressure of the reaction vessel to the atmosphere pressure. After dissociating the formed hydrate in the reaction vessel, one cycle of the experiments was completed.

4.1.2 Initial experimental conditions

The initial experimental conditions for two experimental cases – Case 8 and Case 9 are listed in Table 4-1.

Table 4- 1 Initial experimental conditions for Case 8 and Case 9 [4-1]

		Case 8	Case 9
Initial temperature	[K]	281.35	282.35
Initial pressure	[MPa]	9.0	9.0
Liquid CO_2 injection amount	[Nml]	33	33
Average liquid CO_2 injection rate	[kg/s]	7.227×10^{-4}	7.538×10^{-4}
End time of induction stage	[min]	2.5	4.0
End time of formation stage	[min]	25.0	25.0

4.2 Simulation Outline of CO₂ Hydrate Formation in the Lab-scale Sediment by Liquid CO₂ Injection

In this section, the simulation outline of CO_2 hydrate formation in the lab-scale sediment by liquid CO_2 injection is explained in detail, including physical parameters, computational mesh, and initial simulation conditions.

4.2.1 Physical parameters

The physical parameters of stainless steel and CO_2 hydrate are the same as those listed in Table 3-2. Besides, as mentioned before, the reaction vessel was filled with glass beads (BZ-02), whose physical parameters are listed in Table 4-2.

Table 4- 2 Physical parameters of glass beads (BZ-02)

	Density [kg/m³]	Specific heat [J/kg/K]	Thermal conductivity [W/m/K]	Diameter [m]
Glass beads (BZ-02)	2.5×10^3	8.37×10^2	0.94	$0.117 \sim 0.250 \times 10^{-3}$

4.2.2 Computational mesh

The computational mesh used for numerical simulations of CO_2 hydrate formation in the lab-scale sediment by liquid CO_2 injection in this study is also designed as an axisymmetric cylinder with the radius of 24.75 mm and the height of 250 mm, simulating the lab-scale sediment. Along the radial direction, it is divided into 17 cells, of which 16 cells have a length of 1.5 mm and 1 cell has a length of 0.75 mm (only for the outermost cell). On the other hand, along the height

direction, it is divided into 125 cells equally with a height of 2.0 mm.

Besides, a thin layer of cells which represents the stainless steel is placed around the cells of the calculation domain either with a length of 0.1 mm or a height of 0.1 mm, respectively. The pressure and temperature in these cells are set to be constant and cannot change with time in order to simulate the reaction vessel bathed in the cooling unit. Therefore, a total number of 2286 cells (18 cells in the radial direction and 127 cells in the height direction) is used for the computational mesh in Case 8 and Case 9.

As mentioned before, liquid CO_2 was injected into the center of the reaction vessel through the L-shape steel tube directly, so a particular cell at the depth of 152 mm next to the axis is used as the liquid injection cell to simulate liquid CO_2 injection. Besides, in order to simulate the upward liquid CO_2 flow caused by the L-shape steel tube as shown in Fig. 4-2, a set of five cells around the liquid injection cell is treated as the stainless steel cells, whose physical properties are the same as those located on the boundary of the calculation domain. In addition, two cells in the top stainless steel layer next to the axis are set to be water-saturated with constant pressure and temperature in order to represent the water discharging point at the top of the reaction vessel with a diameter of 6 mm. However, it is worth mentioning that in the experiments, the valve at the outlet of the reaction vessel was only opened during liquid CO_2 injection, and closed after the process of liquid CO_2 injection was finished. So the two cells used for the water discharging point are only active during the induction stage. On the other hand, during the formation stage, these two cells are set to be normal stainless steel cells just like the other ones. The schematic diagram of the computational mesh is shown in Fig. 4-3.
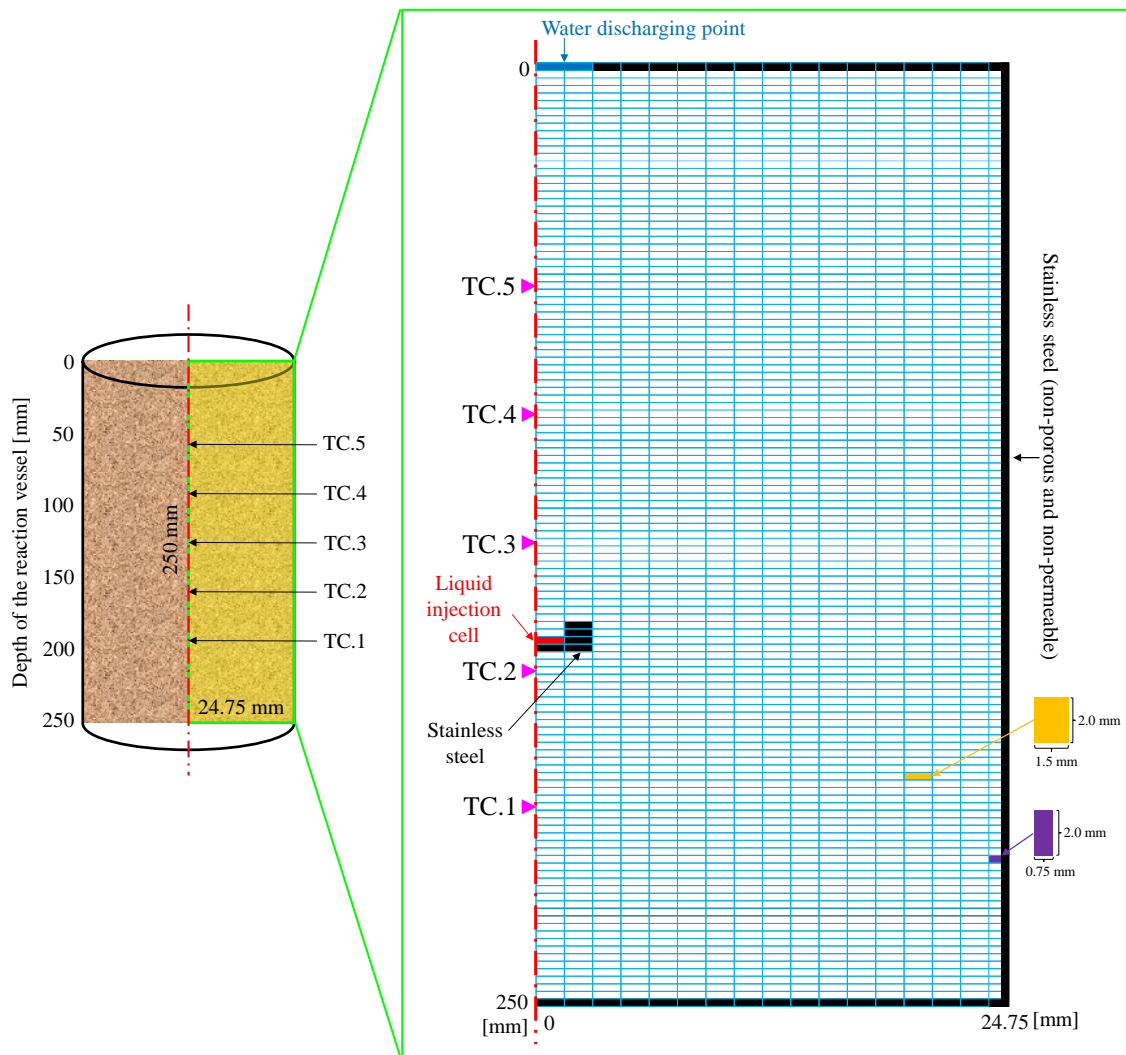
Fig. 4- 3 The schematic diagram of the computational mesh for CO_2 hydrate formation in the lab-scale sediment by liquid CO_2 injection

4.2.3 Initial simulation conditions

The porosity and absolute permeability of the sediment are determined by the experimental data obtained by Li et al. [4-1], set as 0.373 and 8.64×10^{-12} m^2, respectively, in this study. Besides, as mentioned in Section 3.2.2.3, the initial water saturation in the sediment is set as 0.99 m^3/m^3 in order to avoid the calculation termination during the simulation.

On the other hand, since liquid CO_2 was injected into the reaction vessel instead of CO_2 gas in Case 8 and Case 9, the physical properties of the injection fluid have changed greatly. However, unlike CO_2 gas, researches on the physical properties of liquid CO_2 are limited. Therefore, most of the physical properties of liquid CO_2 (such as density, viscosity, thermal conductivity, etc.)

used in this study are determined by the linear fitting of the experimental data obtained from the open literature (Vesovic et al. [4-2], Span and Wagner [4-3], Fenghour et al. [4-4], etc.).

In addition, the initial time step is set as 0.01 s. Meanwhile, the induction stages (before CO_2 hydrate formation) are set as 2.5 min and 4.0 min for Case 8 and Case 9, respectively, as listed in Table 4-1, and the formation stages (during CO_2 hydrate formation) are set as 22.5 min and 21.0 min for Case 8 and Case 9, respectively.

4.3 Simulation Results and Discussions

In this section, numerical simulations of CO_2 hydrate formation in the lab-scale sediment by liquid CO_2 injection are conducted using the model parameters determined in Chapter 3 in order to validate the inclusive model for CO_2 hydrate formation proposed in this study.

Like Case 6 and Case 7, the calculation processes also includes two stages: the induction stage (including only the process of liquid-liquid two-phase flow) and the formation stage (including only the process of CO_2 hydrate formation).

During the induction stage, liquid CO_2 was injected into the reaction vessel by the CO_2 hand pump, so the injection rates were actually not constant in the experiments. However, in the simulations, average liquid CO_2 injection rates, as listed in Table 4-1, are used instead, which may cause slight errors for the calculations of liquid-liquid two-phase flow during the induction stage.

Besides, for the mutual solubilities of liquid CO_2 and water, the solubility of water in liquid CO_2 is smaller than that of liquid CO_2 in water by a factor of 10, and the lower the temperature is, the smaller the value of the solubility of water in liquid CO_2 becomes (King et al. [4-5]). Since liquid CO_2 is only slightly soluble in water, it is reasonable to treat the liquid CO_2 – water system as a one-sided solubility system, with liquid CO_2 as the solute and water as the solvent according to Teng and Yamasaki [4-6]. Therefore, only liquid CO_2 dissolution into the aqueous phase is considered in this study, and the dissolution rate is also described by Equation (2-14). However, CO_2 mass transfer coefficient k_t in Equation (2-14) is actually not a constant, but should be a function of Reynolds number Re and Schmidt number Sc (Hirai et al. [4-7], Someya et al. [4-8], etc.), which are both defined by the density and viscosity of the fluid. Since the injection fluid has changed from CO_2 gas to liquid CO_2 in Case 8 and Case 9, the physical properties of the fluid have also changed significantly. Therefore, the value of k_t as listed in Table 3-8, which is

determined as 1.5×10^{-7} m/s by parameter-fitting in Chapter 3, may not be able to be adopted in these two cases, and need to be re-determined accordingly. In this section, a much smaller value of 0.2×10^{-7} m/s, which is almost one order smaller than that in Chapter 3, is used for the numerical simulations of liquid-liquid two-phase flow in the sediment.

After the process of liquid CO_2 injection was finished, the valve at the outlet of the reaction vessel was closed. Therefore, CO_2 hydrate formed in a closed system like that in Case 1 ~ Case 5. Besides, since there is no movable liquid front during the formation stage in Case 8 and Case 9, $\delta = 0$ is adopted to the inclusive model for CO_2 hydrate formation as proposed in Equation (2-24), which can be simplified as Equation (3-1). Moreover, as listed in Table 3-8, the rupture ratio coefficient behind the gas front β is determined separately for CO_2 hydrate formation in the sand sediment without and with gas-liquid two-phase flow in Chapter 3, and the order of β is determined as 10^{13} m^{-2} (1.0×10^{13} ~ 8.0×10^{13} m^{-2} in Case 1 ~ Case 5) under non-flow condition. Therefore, in this section, a median value of 5.0×10^{13} m^{-2} is adopted to β for the numerical simulations of CO_2 hydrate formation in the lab-scale sediment without liquid-liquid two-phase flow.

The comparisons between the calculation results and the experimental data in Case 8 and Case 9 are shown in Fig. 4-4 and Fig. 4-5, respectively. For all these figures, the left three ones represent the temperature changes detected at TC.1 ~ TC.10 in the experiments, and the right two ones represent the temperature changes detected at TC.1 ~ TC.10 in the calculations.

As shown in the left three figures of Fig. 4-4 and Fig. 4-5, during the induction stage, small temperature rises due to the dissolution heat of liquid CO_2 in the aqueous phase are detected at TC.2, TC.3, TC.7, and TC. 9. This indicates that after injection, most of the liquid CO_2 flows upward due to the L-shape steel tube, and the liquid CO_2 phase may have reached as far as the location between TC.3 and TC.4 in the experiments. However, in the right two figures, small temperature rises are detected not only at the thermocouples mentioned above, but also at TC.4, TC.5, TC.6, TC.8, and TC.10, which means the liquid CO_2 phase has reached as far as the location of TC.5 (the top thermocouple placed in the reaction vessel), and the distribution of liquid CO_2 in the sediment at the end of the induction stage is much broader in the calculations than that in the experiments. This may be caused by the interfacial area model used in this numerical simulator. As mentioned in Section 2.1.4, the interfacial area model proposed by Molly et al. [2-11] describes a linear correlation of gas-liquid interfacial area and water saturation, so it may not be able to be adopted to the case of liquid-liquid two-phase flow. However, models about liquid-liquid interfacial area have not been found in the open literature, so in the numerical simulations of

liquid CO_2 injection into the lab-scale sediment in this chapter, the model proposed by Molly et al. [2-11] still has to be used for the calculations of liquid-liquid interfacial area. This compromise may lead to the overestimation of the interfacial area in the calculations, causing liquid CO_2 to flow much faster, and dissolve into the aqueous phase through the liquid-liquid interface much more than the experiments.

Another possible reason for the broader distribution of liquid CO_2 in the sediment in the calculations may be related to the relative permeability models used in this study (Brooks and Corey models [2-4]), which cause the liquid CO_2 flow to move much faster in the calculations than that in the experiments. As mentioned before, Brooks and Corey models [2-4] were proposed for the relative permeability of the gas-liquid two-phase flow, and no open literature has been found to prove that these relative permeability models can be adopted in the case of liquid-liquid two-phase flow such as liquid CO_2 and water in this study. Therefore, the relative permeability models used for liquid-liquid two-phase flow in this chapter need to be reconsidered in order to slow down the liquid CO_2 flow and improve the calculation results.

On the other hand, during the formation stage, CO_2 hydrate forms in the sediment without liquid-liquid two-phase flow. Likewise, obvious temperature jumps due to CO_2 hydrate formation heat are detected at TC.2, TC.3, TC.7, and TC. 9 in the experiments, as shown in the left three figures of Fig. 4-4 and Fig. 4-5. However, extra temperature jumps are also detected at TC.4, TC.5, TC.6, TC.8, and TC.10, as shown in the right two figures, because the liquid CO_2 phase has already reached the locations of these thermocouples at the end of the induction stage in the calculations, and starts to form hydrate as soon as the formation stage begins. Besides, for the calculation of hydrate formation rate on the hydrate film behind the liquid front Q_{H2} as shown in Equation (3-2), which contributes to the temperature rises in the sediment significantly, the gas-liquid interfacial area model proposed by Molly et al. [2-11] as mention above is also adopted by compromise. This may also lead to some errors in the calculations.

Comparing the calculation results with the experimental data in Case 8 and Case 9, as shown in Fig. 4-4 and Fig. 4-5, it can be seen that the calculation results of the temperature changes detected at TC.4, TC.5, TC.6, TC.8, and TC.10, which increase greatly in the whole calculation period, fail to match the experimental data due to broader distribution of liquid CO_2 in the sediment in the calculations than that in the experiments. However, the temperature changes detected at TC.2, TC.3, TC.7, and TC. 9 in the experiments, which are all the thermocouples near the liquid CO_2 inlet, are replicated and confirmed by calculations successfully, which validates the inclusive model for CO_2 hydrate formation proposed in this study to some extent.

Moreover, no obvious temperature rise is detected at TC.1 either in the experiments or in the calculations in Case 8 and Case 9, as shown in Fig. 4-4 and Fig. 4-5. This means the liquid CO_2 phase does not reach the location of TC.1 which is far below the liquid CO_2 inlet. Therefore, it is considered that the stainless steel cells placed around the liquid injection cell have been proved to be effective on simulating the upward liquid CO_2 flow caused by the L-shape steel tube.

In addition, contour maps of CO_2 hydrate saturation, liquid CO_2 saturation, total hydrate formation rate, hydrate formation rate at the fresh surface (rupture), hydrate formation rate at the liquid-liquid interface of the existing hydrate film (the growth of the hydrate film), and temperature with time in Case 8 and Case 9 are extracted in order to figure out how hydrate forms and distributes in the sediment, as shown in Fig. 4-6 ~ Fig. 4-11 and Fig. 4-12 ~ Fig. 4-17, respectively.

As shown in Fig. 4-6 and Fig. 4-12, CO_2 hydrate mainly distributes near the boundary of the reaction vessel, whose temperature is set to be constant to simulate the temperature-controlled boundary of the reaction vessel bathed in the cooling unit. Besides, as can be seen in Fig. 4-7 and Fig. 4-13, at the end of the induction stage, liquid CO_2 distributes at the depth of 0.03 ~ 0.17 m in the reaction vessel, which covers the location range of TC.2 ~ TC.10. Then, as soon as the formation stage begins, CO_2 hydrate forms in the sediment with a very large hydrate formation rate in short time (Fig. 4-8 and Fig. 4-14), resulting in the temperature rises detected at TC.2 ~ TC.10 at the early stage of the formation stage, as shown in Fig. 4-11 and Fig. 4-17. At this moment, the total hydrate formation rate is mainly contributed by hydrate formation rate at the fresh surface: i.e. hydrate formation from the rupture occurring on the existing hydrate film, as shown in Fig. 4-9 and Fig. 4-15. Then, with the decrease of the rupture ratio x_2, hydrate formation rate at the fresh surface drops sharply. On the contrary, hydrate formation rate at the liquid-liquid interface of the existing hydrate film: i.e. the growth of the hydrate film becomes dominant, as shown in Fig. 4-10 and Fig. 4-16. However, the growth rate of the hydrate film is extremely small due to the insufficiency of the driving force: i.e. the fugacity difference. Therefore, the temperature in the sediment cannot maintain at a high value, and drops gradually with time, as shown in Fig. 4-11 and Fig. 4-17.

At last, from the contour maps, it can also be seen that the difference between the calculation results and the experimental data is due to the broader distribution of liquid CO_2 in the sediment in the calculations, which causes the extra temperature rises detected at TC.4, TC.5, TC.6, TC.8, and TC.10, as shown in Fig. 4-4 and Fig. 4-5.
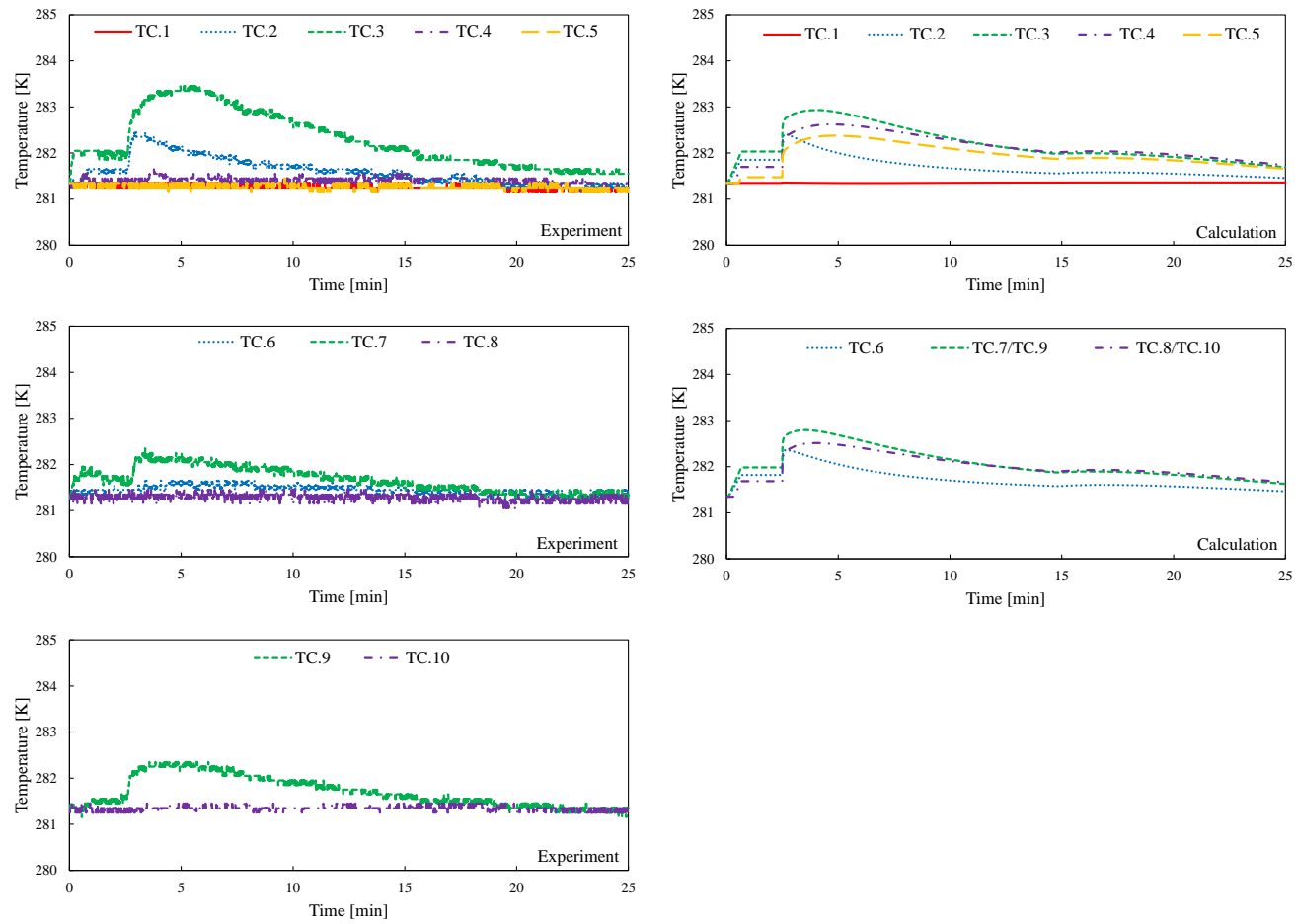
Fig. 4- 4 The comparisons between the calculation results and the experimental data in Case 8

(Left three) The temperature changes detected at TC.1 ~ TC.10 in the experiment

(Right two) The temperature changes detected at TC.1 ~ TC.10 in the calculation
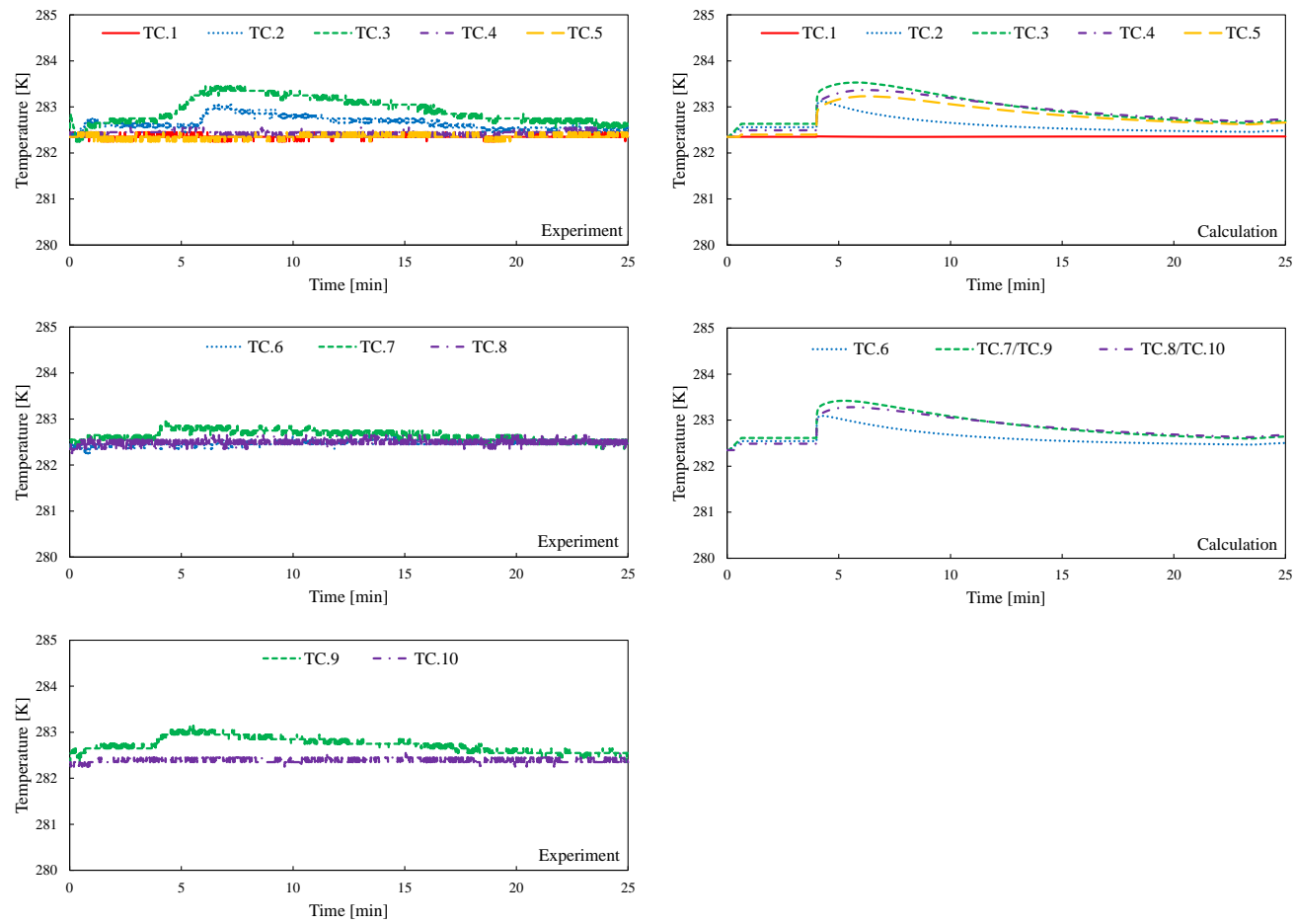
Fig. 4- 5 The comparisons between the calculation results and the experimental data in Case 9

(Left three) The temperature changes detected at TC.1 ~ TC.10 in the experiment

(Right two) The temperature changes detected at TC.1 ~ TC.10 in the calculation
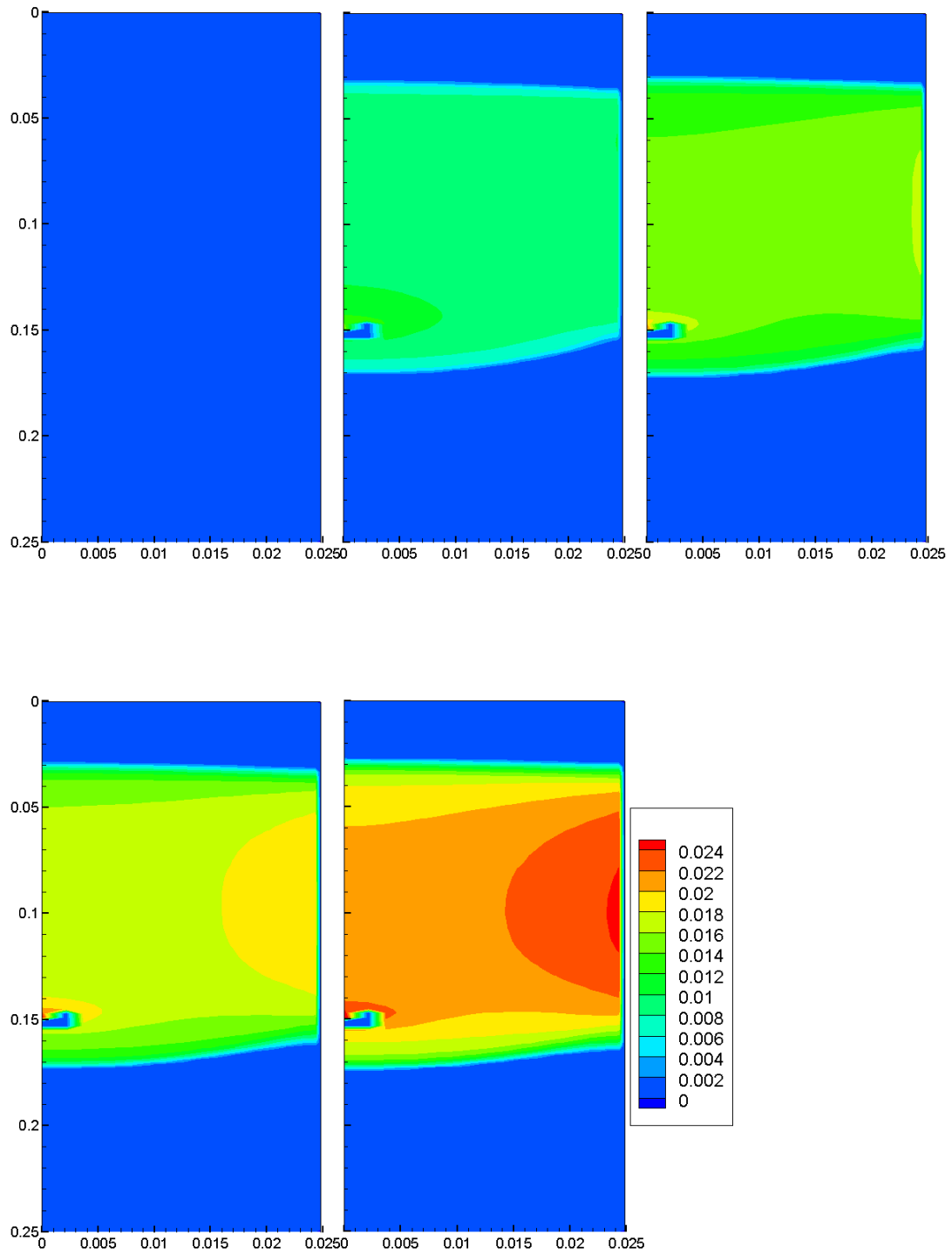
Fig. 4- 6 The contour maps of CO_2 hydrate saturation [m^3/m^3] with time in Case 8

(Top three: 2.5 min, 5 min, 10 min; Bottom two: 15 min, End time)

139
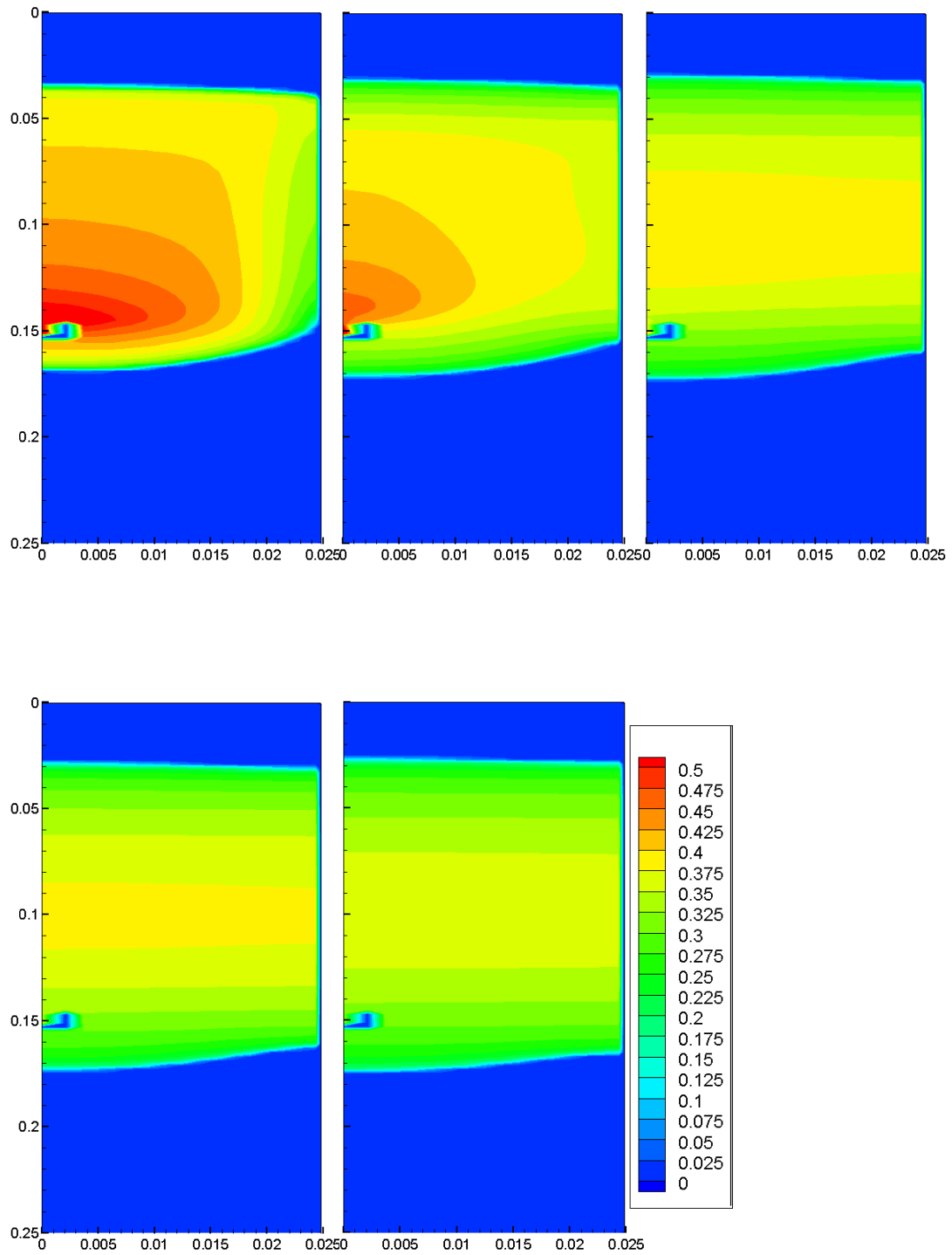
Fig. 4- 7 The contour maps of liquid CO_2 saturation [m^3/m^3] with time in Case 8

(Top three: 2.5 min, 5 min, 10 min; Bottom two: 15 min, End time)
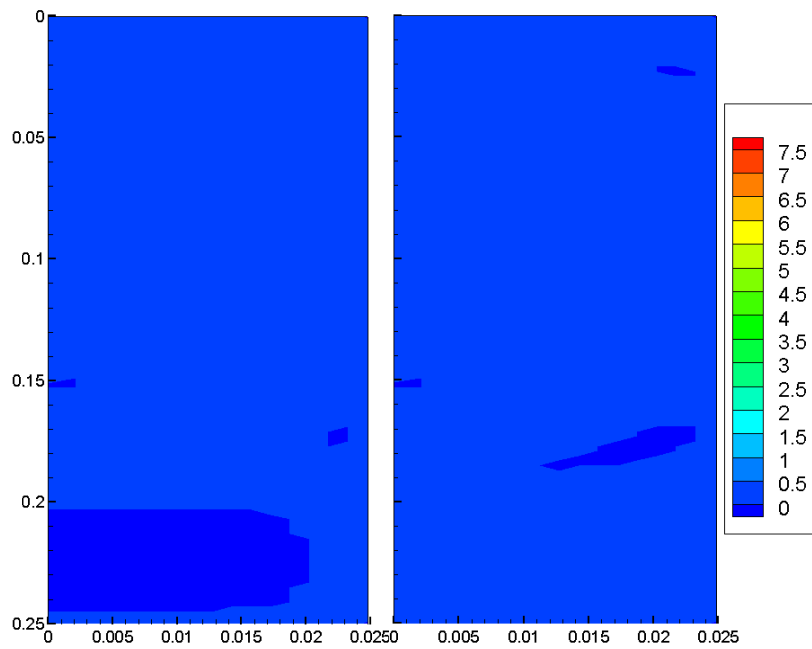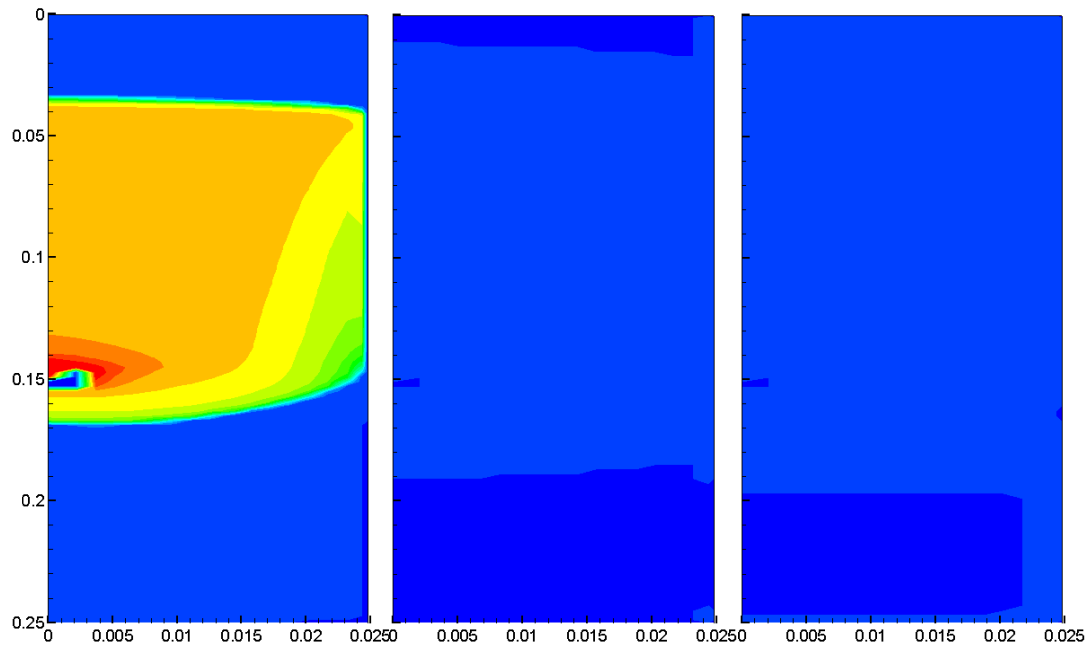
Fig. 4- 8 The contour maps of total hydrate formation rate [kg/m^3/s] with time in Case 8

(Top three: 2.5 min, 5 min, 10 min; Bottom two: 15 min, End time)
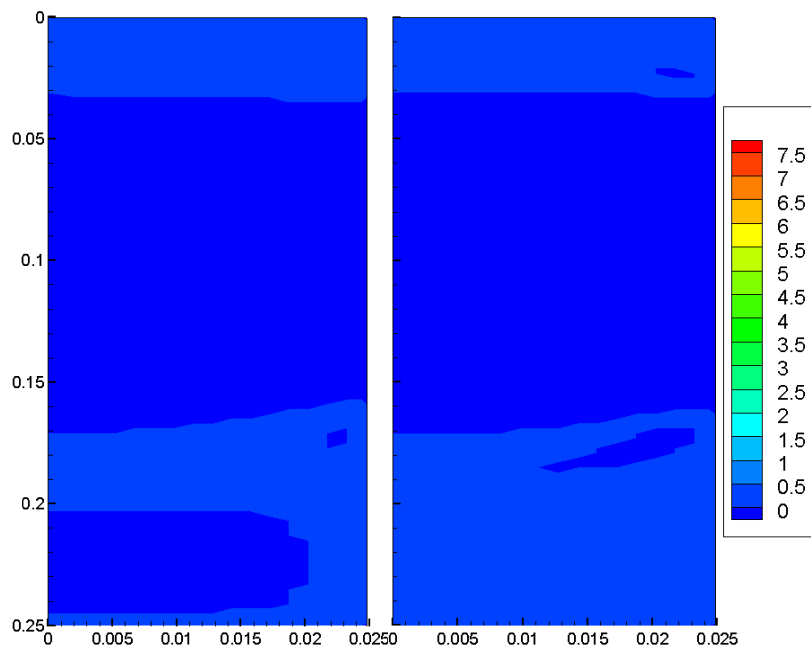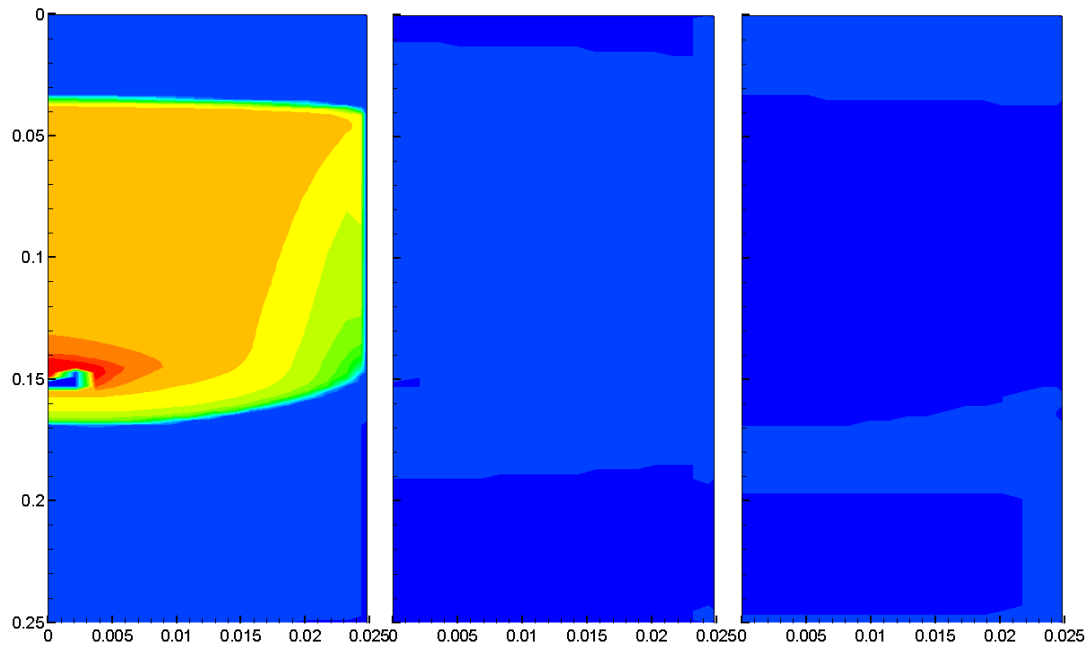
Fig. 4- 9 The contour maps of hydrate formation rate at the fresh surface (rupture) [kg/m^3/s]

with time in Case 8

(Top three: 2.5 min, 5 min, 10 min; Bottom two: 15 min, End time)
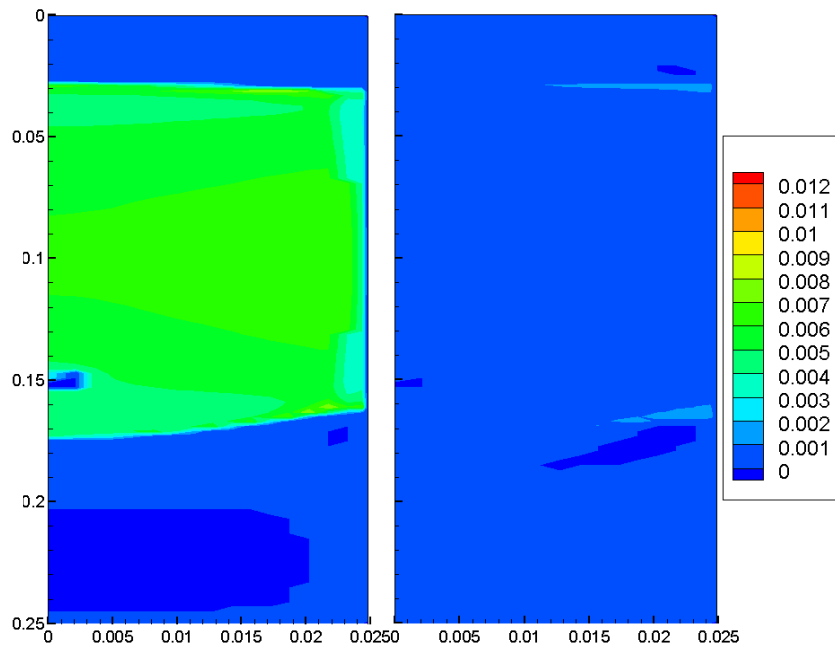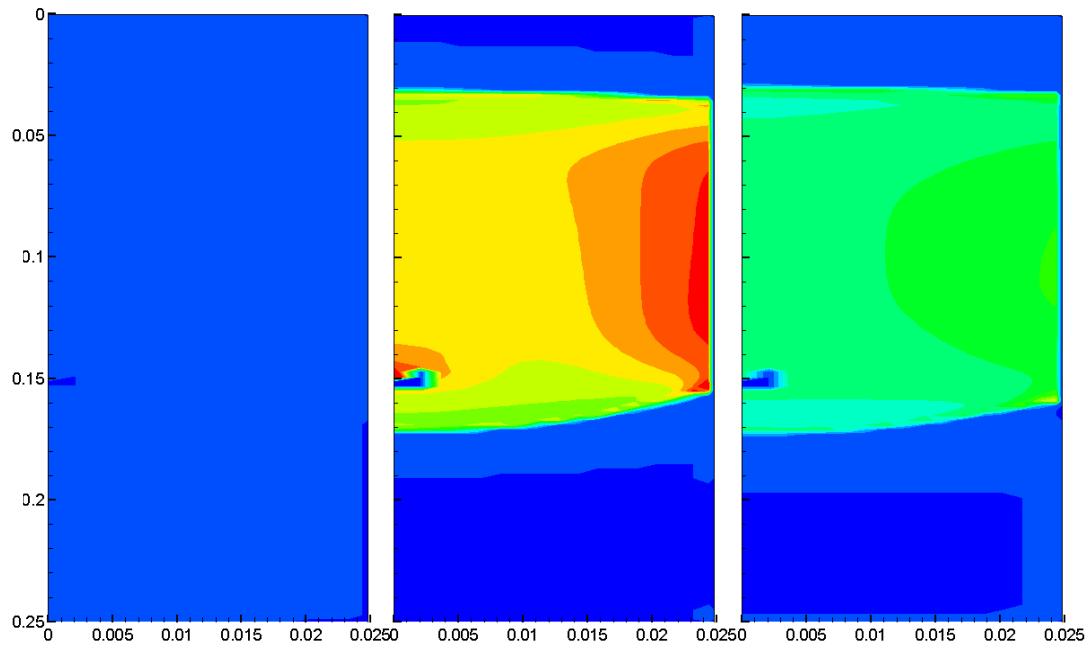
Fig. 4- 10 The contour maps of hydrate formation rate at the liquid-liquid interface of the existing hydrate film (the growth of the hydrate film) [kg/m^3/s] with time in Case 8 (Top three: 2.5 min, 5 min, 10 min; Bottom two: 15 min, End time)
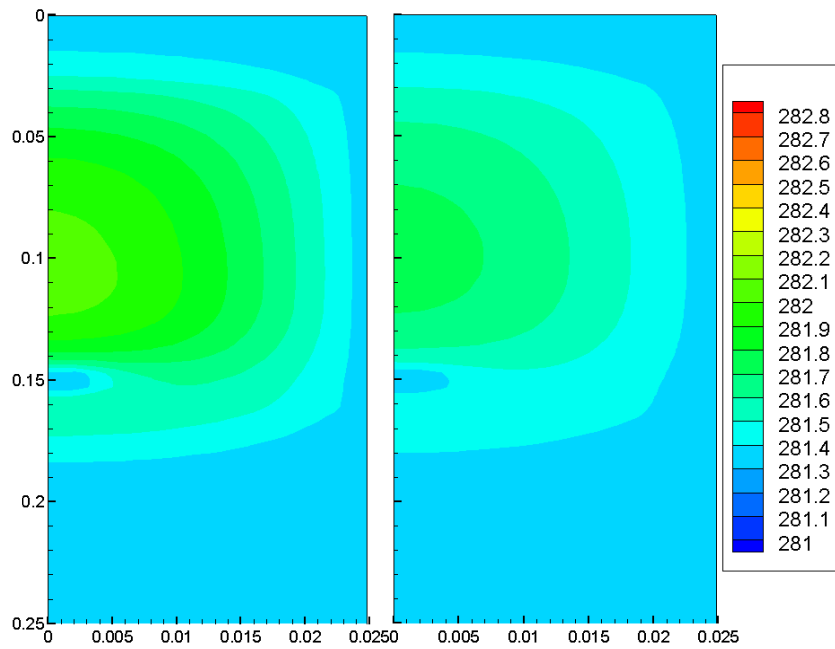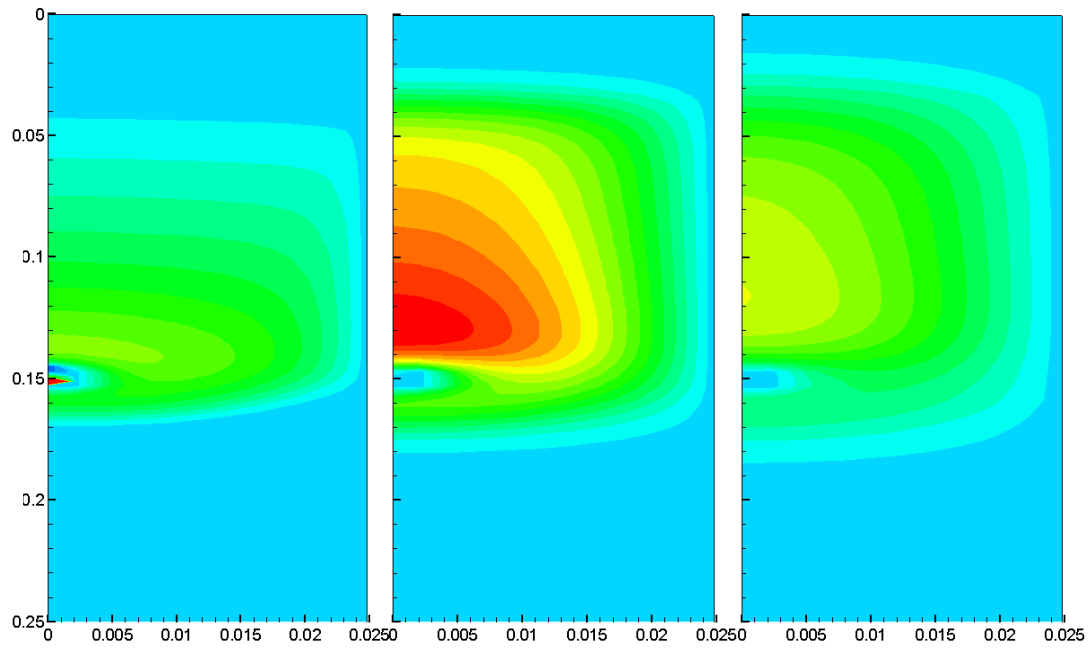
Fig. 4- 11 The contour maps of temperature [K] with time in Case 8
(Top three: 2.5 min, 5 min, 10 min; Bottom two: 15 min, End time)
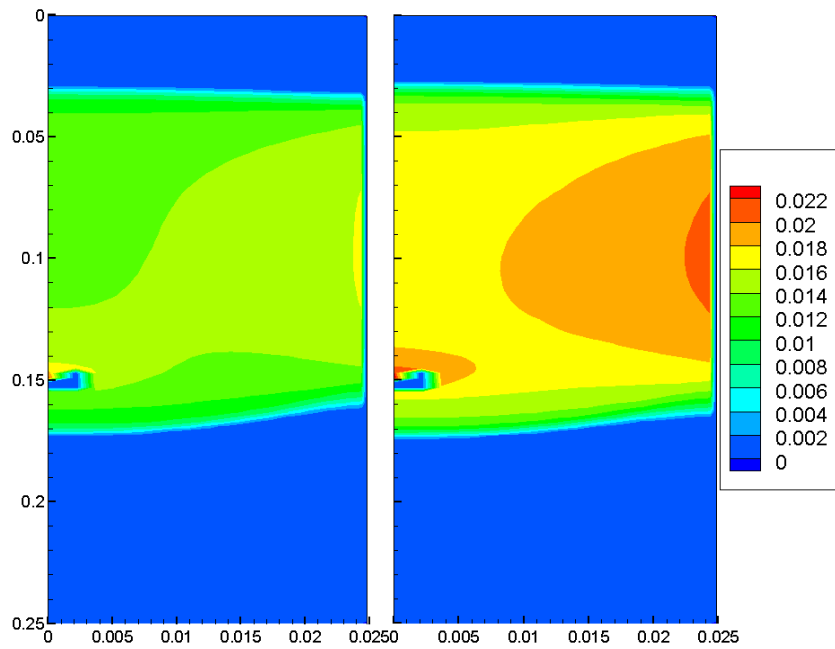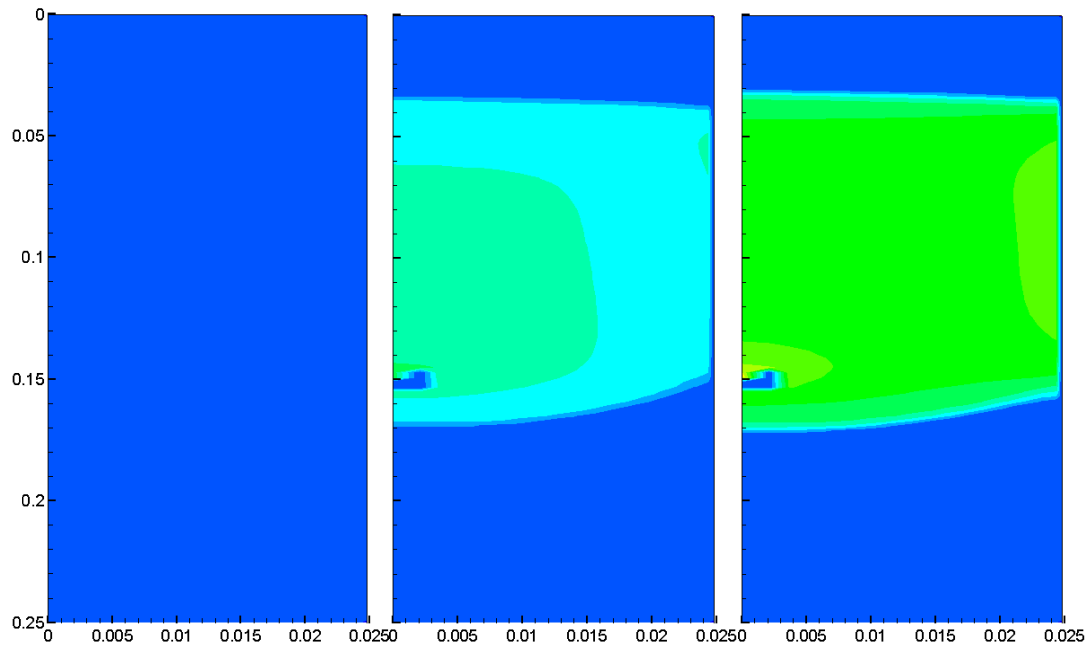
Fig. 4- 12 The contour maps of CO$_2$ hydrate saturation [m^3/m^3] with time in Case 9

(Top three: 4 min, 5 min, 10 min; Bottom two: 15 min, End time)
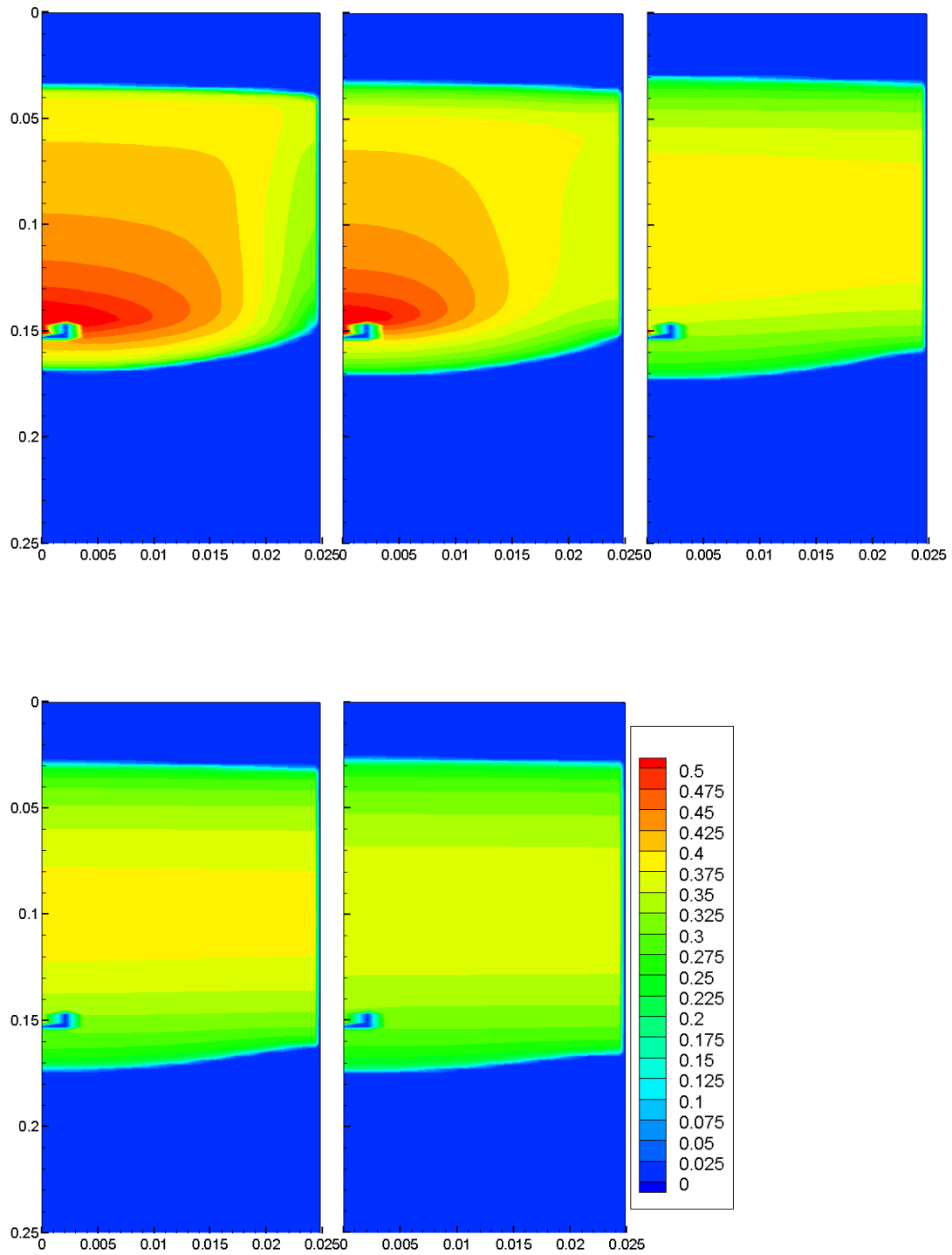
Fig. 4- 13 The contour maps of liquid CO_2 saturation [m^3/m^3] with time in Case 9
(Top three: 4 min, 5 min, 10 min; Bottom two: 15 min, End time)
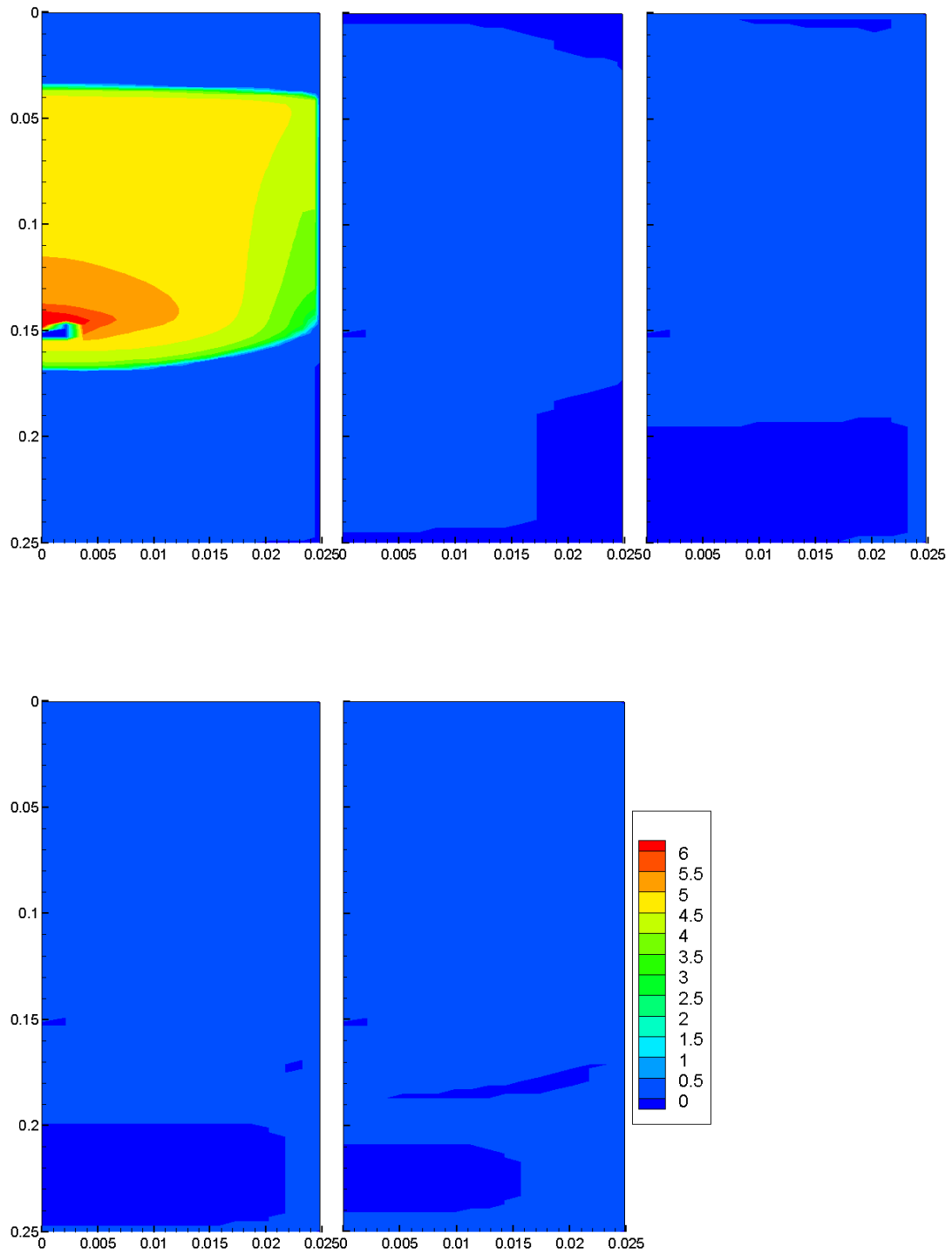
Fig. 4- 14 The contour maps of total hydrate formation rate [kg/m³/s] with time in Case 9
(Top three: 4 min, 5 min, 10 min; Bottom two: 15 min, End time)
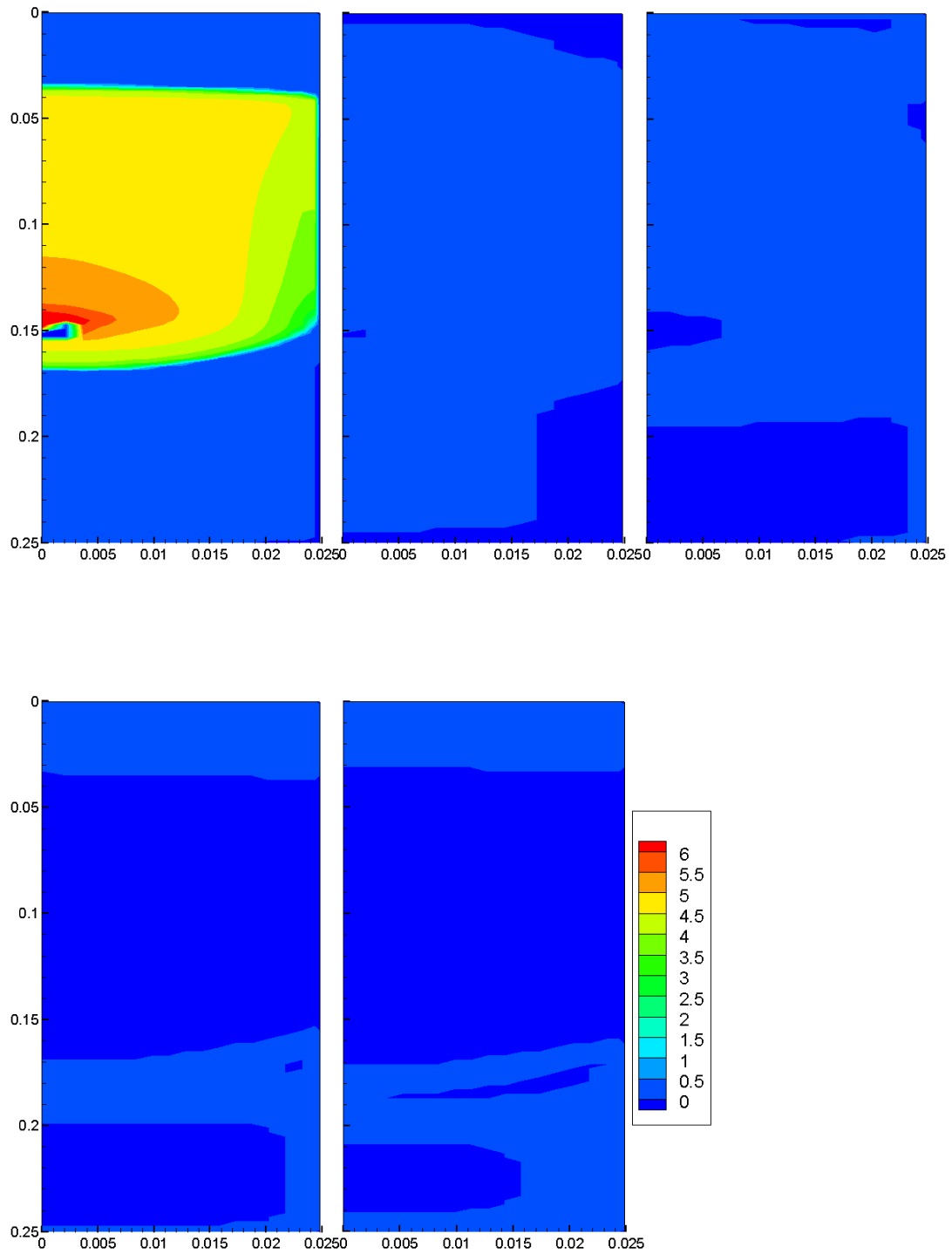
Fig. 4- 15 The contour maps of hydrate formation rate at the fresh surface (rupture) [kg/m^3/s]

with time in Case 9

(Top three: 4 min, 5 min, 10 min; Bottom two: 15 min, End time)

148
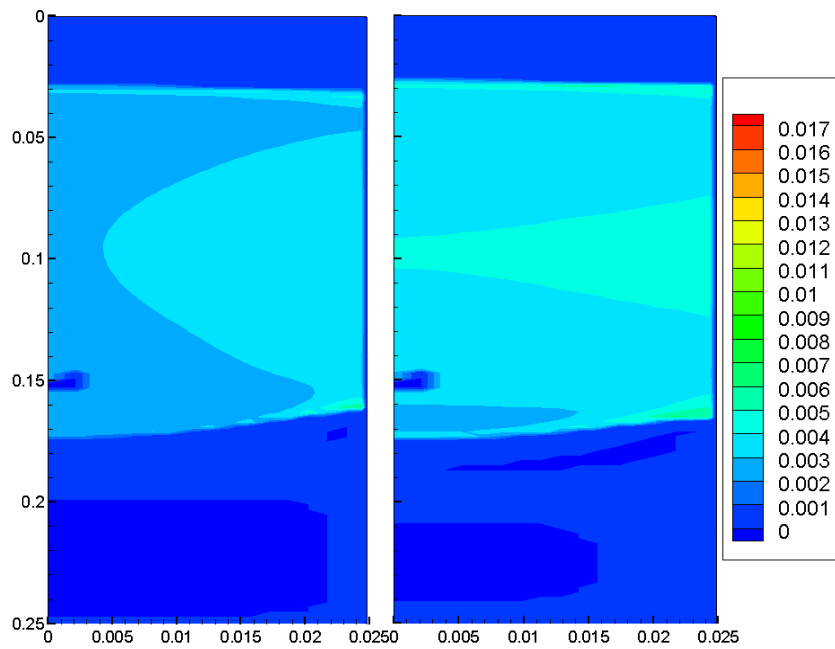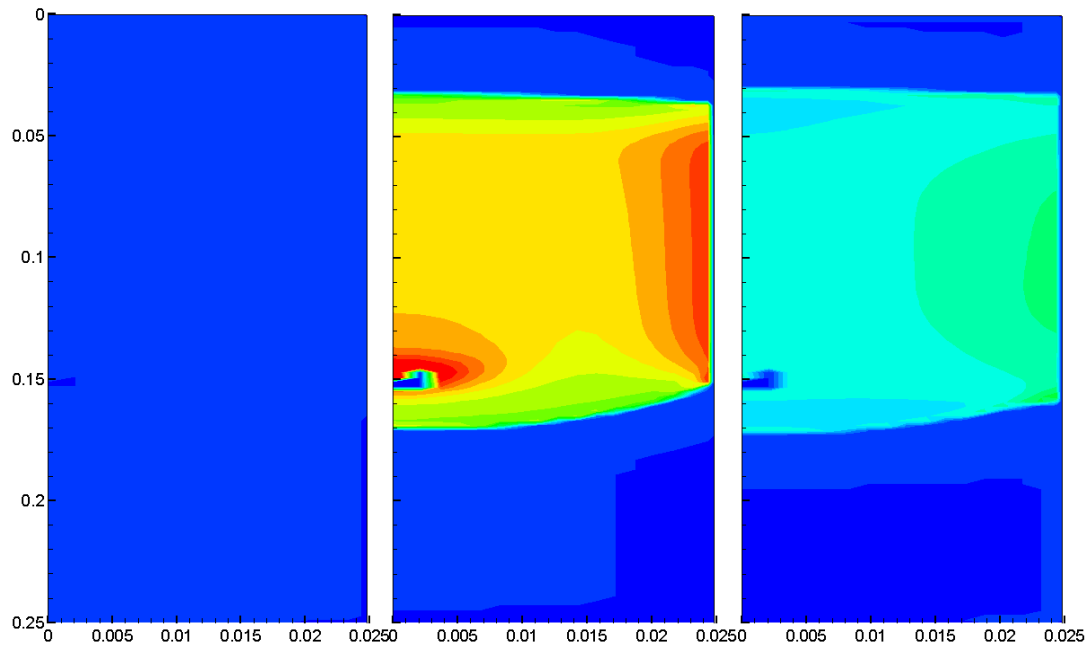
Fig. 4- 16 The contour maps of hydrate formation rate at the liquid-liquid interface of the existing hydrate film (the growth of the hydrate film) [kg/m^3/s] with time in Case 9 (Top three: 4 min, 5 min, 10 min; Bottom two: 15 min, End time)

149
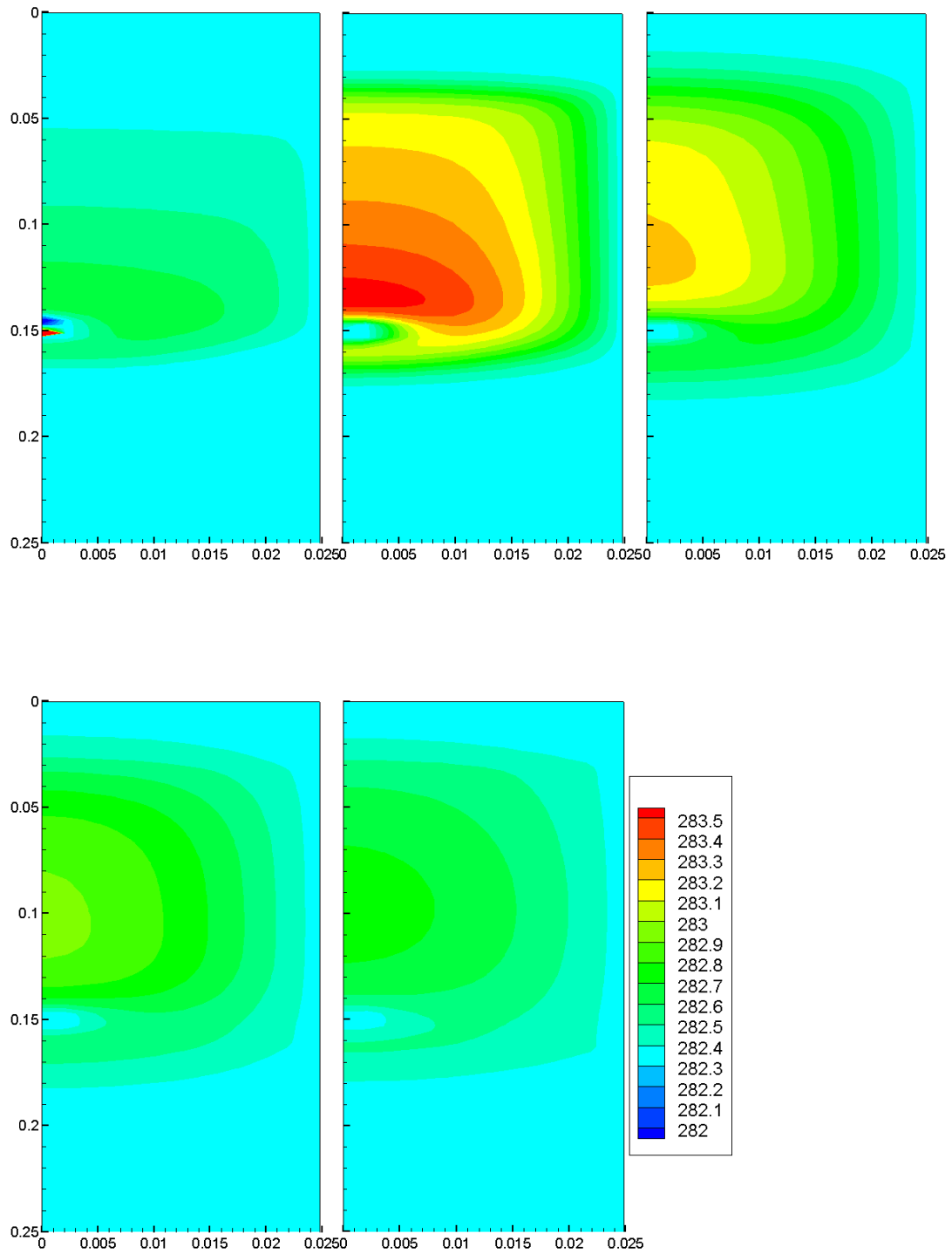
Fig. 4- 17 The contour maps of temperature [K] with time in Case 9

(Top three: 4 min, 5 min, 10 min; Bottom two: 15 min, End time)

4.4 Summary

In this chapter, numerical simulations of liquid CO_2 injection and CO_2 hydrate formation in the lab-scale sediment without liquid-liquid two-phase flow under the experimental conditions have been conducted using the model parameters determined in Chapter 3, and the inclusive model for CO_2 hydrate formation proposed in this study has been validated by the experimental results of CO_2 hydrate formation in the lab-scale sediment by liquid CO_2 injection to some extent.

In the next chapter, conclusions for the whole study will be drawn, and suggestions for the future work will be made.

5 CONCLUSIONS AND SUGGESTIONS

In this chapter, based on the analysis of the simulation results, conclusions for the whole study are drawn, and suggestions for the future work are made.

5.1 Conclusions for the Whole Study

Beyond the traditional methods for CO_2 capture and storage (onshore and shallow offshore storages) at present, two promising technologies: i.e. CO_2 storage in the deep saline aquifers using the sealing effect of gas hydrate (hydrate sealing) and CO_2 storage in the sub-seabed sand sediment in the form of gas hydrate (hydrate storage), have come into the limelight, and may even be expected to become the main stream for CCS some day in the future. Therefore, in order to evaluate the potential and feasibility of hydrate sealing and hydrate storage, it is important to understand CO_2 hydrate formation behavior in the sub-seabed sand sediment by providing precise assessment of hydrate formation rate.

In this study, first, previous studies on kinetic models for CO_2 hydrate formation in the sand sediment are literally reviewed, which are considered to be insufficient to describe the complex process of CO_2 hydrate formation in the sand sediment, and need to be improved. Therefore, an inclusive model for CO_2 hydrate formation is proposed in this study in order to figure out hydrate formation morphologies, which are classified by locations in the sand sediment: i.e. on the gas front, on the hydrate film behind the gas front, and on the surface of the sand particles behind the gas front. Then, the processes of gas-liquid two-phase flow and CO_2 hydrate formation in the sand sediment under the experimental conditions are analyzed using a numerical simulator which incorporates this newly proposed hydrate formation model. Simulation results are compared with the experimental data, so that unknown parameters in the models are determined by parameter-fitting.

Simulation results suggest that the total hydrate formation rate is large near the boundary of the reaction vessel, and CO_2 hydrate mainly distributes near the boundary of the reaction vessel due to the cooling effect of the temperature-controlled boundary. Besides, it is also indicated that CO_2 hydrate formation on the hydrate film behind the gas front makes the most important contribution to the high CO_2 hydrate saturation near the boundary; while on the contrary, CO_2 hydrate formation on the gas front and on the surface of the sand particles behind the gas front only have a very small contribution to CO_2 hydrate saturation in the sand sediment. Therefore, a possible conclusion can be drawn on the basis of the analysis above that the sharp permeability reduction

of the sand sediment is mainly caused by the part of CO_2 hydrate formation on the hydrate film behind the gas front, which is likely to exist between the sand particles and occupy the pore space of the sand sediment, resulting in the blockage of the gas flow.

Besides, in order to validate the inclusive model for CO_2 hydrate formation proposed in this study, numerical simulations of CO_2 hydrate formation in the lab-scale sediment by liquid CO_2 injection are conducted using the model parameters determined in this study. Although extra temperature rises are detected at some thermocouples due to the broader distribution of liquid CO_2 in the sediment in the calculations than that in the experiments, the temperature changes detected at the thermocouples near the liquid CO_2 inlet have been replicated and confirmed by calculations successfully, which validates the inclusive model for CO_2 hydrate formation to some extent.

5.2 Suggestions for the Future Work

The δ switch used to determine whether the gas front exists in a computational cell or not, has a great influence on hydrate formation rate on the gas front. However, the method for the determination of δ proposed in this study can only be adopted to two-dimensional computational mesh (such as the axisymmetric mesh used in this study). For the use of three-dimensional computational mesh, a much more appropriate method should be introduced.

Besides, unlike the rupture ratio model on the gas front proposed in this study, which can be explained both physically and geometrically, the rupture ratio model behind the gas front adopted from Takahashi et al. [1-19] can only be explained physically, but not geometrically. For the accurate evaluation of the rupture ratio behind the gas front, a new model which can be explained both physically and geometrically should be reconsidered.

Moreover, since the amount of hydrate formation on the gas front is found to be very small by calculations, it is considered to have no influence on the permeability reduction of the sand sediment, and the permeability reduction coefficient K_{H1} is treated as 1 in this study. However, if the amount of hydrate formation on the gas front is found to be large by calculations in the future work, its influence on the permeability reduction should be taken into account as well, and a model used for the determination of K_{H1} is expected.

In addition, for the validation of the inclusive model proposed in this study, the experimental

results are only replicated and confirmed by calculations to some extent due to the lack of experimental data and models about the physical properties of liquid CO_2 in the open literature, as well as the inappropriate use of the gas-liquid interfacial area model in the liquid CO_2 – water system. Besides, the process of CO_2 hydrate formation in the reaction vessel is under non-flow condition in the validation experiments, and the δ switch is set to be 0 in the calculations, so the full version of the inclusive model has not been validated completely. Therefore, in order to validate the inclusive model for CO_2 hydrate formation proposed in this study systematically, experiments of CO_2 hydrate formation in the lab-scale sand sediment by continuous CO_2 gas injection at constant rates are suggested in the future work.

At last, it is worth mentioning that the final purpose of this study is to evaluate the potential and feasibility of hydrate sealing and hydrate storage. In order to achieve this purpose, numerical simulations of CO_2 hydrate formation in the real-scale sub-seabed sand sediment in the ocean need to be conducted in the future work using the numerical simulator developed in this study. However, the calculation time may become expansive due to the increase of the cell numbers in the computational mesh. Therefore, efforts should be made to shorten the calculation time by using the proper cell size in the real-scale calculation domain.

REFERENCES

[1-1] Pachauri, R.K., Meyer, L.A., et al., 2014. Climate Change 2014: Synthesis Report. IPCC, Geneva, Switzerland, *Intergovernmental Panel on Climate Change*.

[1-2] Hulme, M., Lu, X., Turnpenny, J., et al., 2002. Climate change scenarios for the Unite Kingdom: the UKCIP02 scientific report. Norwich: Tyndall Centre for Climate Change Research, School of Environmental Sciences, University of East Anglia.

[1-3] Parry, M., Canziani, O., Palutikof, J., Linden, P., Hanson, C., 2007. Summary for Policymakers. In: Climate Change 2007: Impacts, Adaptation and Vulnerability*, Intergovernmental Panel on Climate Change.*

[1-4] Bachu, S., 2015. Review of CO_2 storage efficiency in deep saline aquifers. *Int. J. Greenh. Gas Con.*, 40, 188-202.

[1-5] Gunter, W.D., Bachu, S., Benson, S., 2004. The role of hydrogeological and geochemical trapping in sedimentary basins for secure geological storage of carbon dioxide. *In: Geological Society of London*, *Special Publication*, 233(1), 129-145.

[1-6] Yang, F., Bai, B., Tang, D., Shari, D.N., David, W., 2010. Characteristics of CO_2 sequestration in saline aquifers. *Petrol. Sci.*, 7(1), 83-92.

[1-7] De Silva, G.P.D., Ranjith, P.G., Perera, M.S.A., 2015. Geochemical aspects of CO_2 sequestration in deep saline aquifers: A review. *Fuel*, 155, 128-143.

[1-8] Drange, H., Alendal, G., Johannessen, O.M., 2001. Ocean release of fossil fuel CO_2: a case study. *Geophys. Res. Lett.*, 28(13), 2637-2640.

[1-9] Tohidi, B., Yang, J., Salehabadi, M., Anderson, R., Chapoy, A., 2010. CO_2 hydrates could provide secondary safety factor in subsurface sequestration of CO_2. *Environ. Sci. Technol.*, 44(4), 1509-1514.

[1-10] Koide, H., Takahashi, M., Tsukamoto, H., 1995. Self-trapping mechanisms of carbon dioxide in the aquifer disposal. *Energy Convers. Mgmt.*, 36(6-9), 505-508.

[1-11] Inui, M., Sato, T., Komai, T., Kagemoto, H., 2011. Experiments and numerical simulations of hydrate formation in sand sediment simulating sub-seabed CO_2 storage in the form of gas hydrate. *Journal of MMIJ*, 127(4-5), 194-201 (in Japanese).

[1-12] Englezos, P., Kalogerakis, N., Dholabhai, P.D., Bishnoi, P.R. 1987. Kinetics of formation of methane and ethane gas hydrates. *Chem. Eng. Sci.*, 42(11), 2647-2658.

[1-13] Skovborg, P., Rasmussen, P., 1994. A mass transport limited model for the growth of methane and ethane hydrates. *Chem. Eng. Sci.*, 49(8), 1131-1143.

[1-14] Herri, J.M., Gruy, F., Pic, J.S., Cournil, M., Cingotti, B., Sinquin, A., 1999. Interest of in situ turbidimetry for the characterization of methane hydrate crystallization: application to the study of kinetic inhibitors. *Chem. Eng. Sci.*, 54(12), 1849-1858.

[1-15] Herri, J.M., Pic, J.S., Gruy, F., Cournil, M., 1999. Methane hydrate crystallization

mechanism from in situ particle sizing. *A.I.Ch.E. Journal*, 45(3), 590-602.

[1-16] Gnanendran, N., Amin, R., 2004. Modelling hydrate formation kinetics of a hydrate promoter-water-natural gas system in a semi-batch spray reactor. *Chem. Eng. Sci.*, 59(18), 3849-3863.

[1-17] Ribeiro, C.P., Lage, P.L.C., 2005. Gas-liquid direct-contact evaporation: a review. *Chem. Eng. Technol.*, 28(10), 1081-1107.

[1-18] Inui, M., 2011. Feasibility study on CO_2 sub-seabed storage in the form of gas hydrate. *Doctoral Dissertation: the University of Tokyo* (in Japanese).

[1-19] Takahashi, T., Sato, T., Inui, M., Hirabayashi, S., Brumby, P.E., 2012. Modeling of CO_2-hydrate formation at the gas-water interface in sand sediment. *Chem. Eng. Technol.*, 35(10), 1751-1758.

[1-20] Nakashima, T., 2013. Development of the three-dimensional numerical simulator for sub-seabed CO_2 storage in the form of gas hydrate. *Master Dissertation: the University of Tokyo* (in Japanese).

[1-21] Moridis, G.J., Kowalsky, M.B., Pruess, K., 2008. TOUGH+HYDRATE v1.0 User's Manual: A Code for the Simulation of System Behavior in Hydrate-Bearing Geologic Media. LBNL-0149E.

[1-22] Yu, T., Nakashima, T., Sato, T., Inui, M., 2014. Numerical simulation of CO_2 hydrate formation in lab-scale sand sediment. *Proc. 8th International Conference on Gas Hydrate, Beijing, China*.

[2-1] van Genuchten, M.T., 1980. A closed-form equation for predicting the hydraulic conductivity of unsaturated soils. *Soil Sci. Soc. Am. J.*, 44(5), 892-898.

[2-2] Milly, P.C.D., 1982. Moisture and heat transport in hysteretic inhomogeneous porous media: A matric-head based formulation and a numerical model. *Water Resour. Res.*, 18(3), 489-498.

[2-3] Stone, H.L., 1970. Probability model for estimating three-phase relative permeability. *J. Petrol. Technol.*, 22(2), 214-218.

[2-4] Corey, A.T., 1954. The interrelation between gas and oil relative permeabilities. *Producers Monthly*, 19, 38-41.

[2-5] Sakamoto, Y., Komai, T., Kawabe, Y., Tenma, N., Yamaguchi, T., 2004. Formation and dissociation behavior of methane hydrate in porous media - Estimation of permeability in methane hydrate reservoir, Part 1. *Shigen-to-Sozai*, 120(2), 85-90 (in Japanese).

[2-6] Rutqvist, J., Moridis, G.J., Grover, T., Silpngarmlert, S., Collett, T.S., Holdich, S.A., 2012. Coupled multiphase fluid flow and wellbore stability analysis associated with gas production from oceanic hydrate-bearing sediments. *J. Petrol. Sci. Eng.*, 92-93, 65-81.

[2-7] Sakamoto, Y., Suzuki, Y., Tanaka, A., Tenma, N., Haneda, H., Komai, T., Yamaguchi, T., 2011. Simulation study of a laboratory-scale experiment for flow behavior of supercritical CO_2 in

porous media. *Journal of MMIJ*, 127(10-11), 622-634 (in Japanese).

[2-8] Ott, H., Berg, S., Oedai, S., 2012. Displacement and mass transfer of CO_2/brine in sandstone. *Energy Procedia*, 23, 512-520.

[2-9] National Astronomical Observatory. Chronological Scientific Tables 2010. Maruzen Co., Ltd., 2009.

[2-10] Hoeg, S., Scholer, H.F., Warnatz, J., 2004. Assessment of interfacial mass transfer in water-unsaturated soils during vapor extraction. *J. Contam. Hydrol.*, 74(1-4), 163-195.

[2-11] Molly, S.C., Katherine, H.H., Ross, M.L., 2008. X-ray microtomography determination of air-water interfacial area-water saturation relationships in sandy porous media. *Environ. Sci. Technol.*, 42(8), 2949-2956.

[2-12] Carman, P.C., 1938. Fundamental principle of industrial filtration (A critical review of present knowledge). *Trans. Inst. Chem. Eng.*, 16, 168-188.

[2-13] Fuller, E.N., Ensley, K., Giddings, J.C., 1969. Diffusion of halogenated hydrocarbons in helium. The effect of structure on collision cross sections. *J. Phys. Chem.*, 73(11), 3679-3685.

[2-14] Millington, R.J., Quirk, J.P., 1961. Permeability of porous solids. *Trans. Faraday Soc.*, 57, 1200-1207.

[2-15] Riazi, M.R., Whiton, C.H., 1993. Estimating diffusion coefficients of dense fluids. *Ind. Eng. Chem. Res.*, 32(12), 3081-3088.

[2-16] Wilke, C.R., Chang, P., 1955. Correlation of diffusion coefficients in dilute solutions. *A.I.Ch.E. Journal*, 1(2), 264-270.

[2-17] Masuda, Y., Kurihara, M., Ohuchi, H., Sato, T., 2002. A field-scale simulation study on gas productivity of formations containing gas hydrates. *Proc. 4th International Conference on Gas Hydrate, Yokohama, Japan*.

[2-18] Chung, T.H., Ajlan, M., Lee, L.L., Starling, K.E., 1988. Generalized multiparameter correlation for nonpolar fluid transport properties. *Ind. Eng. Chem. Res.*, 27(4), 671-679.

[2-19] O'Sullivan, M.J., Bodvarsoson, G.S., Pruess, K., Blakeley, M.R., 1985. Fluid and heat flow in gas-rich geothermal reservoirs. *Society of Petroleum Engineers Journal*, 25(2), 215-226.

[2-20] Falta, R.W., Pruess, K., Finsterle, S., Battistelli, A., 1995. T2VOC User's Guide. *Lawrence Berkeley Laboratory Report*, LBL-36400.

[2-21] Kamath, V.A., 1984. Study of heat transfer characteristics during dissociation of gas hydrates in porous media. *Ph.D. Dissertation*, Univ. of Pittsburgh, Pittsburgh, PA.

[2-22] Himmelblau, D.M., Babb, A.L., 1959. Reaction rate constants by radioactive tracer techniques. *Ind. Eng. Chem.*, 51(11), 1403-1408.

[3-1] Konno Y., Oyama, H., Nagao, J., Masuda, Y., Kurihara, M., 2010. Numerical analysis of the dissociation experiment of naturally occurring gas hydrate in sediment cores obtained at the Eastern Nankai trough, Japan. *Energy & Fuels*, 24(12), 6353-6358.

[3-2] Ikegawa, Y., 2007. Estimation by experiments and its analysis for thermal stimulation of methane hydrate using exothermic reaction of CO_2 hydrate formation. *Japan Society of Civil Engineers*, 63(4), 206-215 (in Japanese).

[3-3] Aya, I., Yamane, K., Nariai, H., 1997. Solubility of CO_2 and density of CO_2 and hydrate at 30 MPa. *Energy*, 22(2-3), 263-271.

[3-4] Gupta, A., Kneafsey, T.J., Moridis, G.J., 2006. Composite thermal conductivity in a large heterogeneous porous methane hydrate. *J. Phys. Chem. B*, 110(33), 16384-16392.

[3-5] Clarke, M.A., Bishnoi, P.R., 2005. Determination of the intrinsic kinetics of CO_2 gas hydrate formation using in situ particles size analysis. *Chem. Eng. Sci.*, 60(3), 695-709.

[4-1] Li, Y.R., Someya, S., Yu, T., 2015. CO_2 sequestration under an artificial impermeable layer with clathrate hydrate in sediments. *Proc. 9th International Symposium on Measurement Techniques for Multiphase Flow, Sapporo, Japan*.

[4-2] Vesovic, V., Wakeham, W.A., Olchowy, G.A., Sengers, J.V., Watson, J.T.R., Millat, J., 1990. The transport properties of carbon dioxide. *J. Phys. Chem. Ref. Data*, 19(3), 763-808.

[4-3] Span, R., Wagner, W., 1996. A new equation of state for carbon dioxide covering the fluid region from the triple-point temperature to 1100 K at pressures up to 800 MPa. *J. Phys. Chem. Ref. Data*, 25(6), 1509-1596.

[4-4] Fenghour, A., Wakeham, W.A., Vesovic, V., 1998. The viscosity of carbon dioxide. *J. Phys. Chem. Ref. Data*, 27(1), 31-44.

[4-5] King, M.B., Mubarak, A., Kim, J.D., Bott, T.R., 1992. The mutual solubilities of water with supercritical and liquid carbon dioxide. *J. Supercrit. Fluid.*, 5(4), 296-302.

[4-6] Teng, H., Yamasaki, A., 1998. Solubility of liquid CO_2 in synthetic sea water at temperatures from 278 K to 293 K and pressures from 6.44MPa to 29.49 MPa, and densities of the corresponding aqueous solutions. *J. Chem. Eng. Data*, 43(1), 2-5.

[4-7] Hirai, S., Okazaki, K., Tabe, Y., Hijikata, K., 1997. Mass transport phenomena of liquid CO_2 with hydrate. *Waste Manage.*, 17(5-6), 353-360.

[4-8] Someya, S., Chen, B., Nishio, M., Okamoto, K., Uchida, T., 2000. Visualization of the dissolution of a CO_2 droplet into pure/sea water. *Visualization*, 20(77), 44-51 (in Japanese).

ACKNOWLEDGEMENTS